

## ABSTRACT

Title of Document:                   RANDOM NETWORKS OF ONE-DIMENSIONAL CONDUCTIVE NANOMATERIALS: FABRICATION, PROPERTIES, AND APPLICATIONS.

Colin Daniel Preston, Doctor of Philosophy,  
2014

Directed By:                         Professor Liangbing Hu, Department of  
Materials Science and Engineering

Random networks of one-dimensional conductive nanomaterials are unique structures that exhibit nominal properties useful in flexible thin-film electronics; however, a greater understanding of these properties is necessary to enable high performance device functionality. This thesis presents a comprehensive investigation into the various mechanisms that determine certain characteristics of random networks composed of either carbon nanotubes or silver nanowires. In Chapter 1 we outline the motivation and structure of the dissertation. In Chapter 2, we explore the properties of carbon nanotube spray-coatings, and their application as conductive electrodes for various devices. In this chapter, an ink composed of originally grown nanotubes with a tailored wall number is demonstrated to enable spray-coatings with conductivities reaching 2100 S/cm, which is the highest conductivity for spray-coated carbon nanotube random networks from surfactant-free inks. In Chapter 3, we introduce a synthesis

technique to form a new nanostructure of boron-doped few walled carbon nanotubes directed at lowering the bulk resistivity of the nanotube growth yield. An investigation into the structure, morphology, and composition of the boron-doped nanotubes is conducted and compared to undoped few walled nanotubes from the previous chapter. In Chapter 4, we explore the properties of random networks of originally grown Ag NWs and their application towards transparent conducting electrodes for thin-film solar cells. The impact of transmission haze in transparent conducting electrodes is investigated, which provides evidence that the current performance metric of transparent conducting electrodes is insufficient at evaluating their performance in thin-film solar cell devices. In Chapter 5, we expound upon our evidence that transmission haze is a beneficial property for transparent conducting electrodes in thin-film solar cells by introducing a novel Ag NW paper hybrid network that form a transparent conducting electrode with exceptional properties. The combined high transmittance, low sheet resistance, and high transmission haze measured and studied in this new Ag NW paper structure suggests that is the highest performing transparent conducting electrode for thin-film solar cells. In Chapter 6, we consider the impact of this dissertation on the current thin-film technology. Future experiments that may supplement the results in this thesis were also suggested in this chapter.

RANDOM NETWORKS OF ONE-DIMENSIONAL CONDUCTIVE  
NANOMATERIALS: FABRICATION, PROPERTIES, AND APPLICATIONS.

By

Colin Daniel Preston.

Dissertation submitted to the Faculty of the Graduate School of the  
University of Maryland, College Park, in partial fulfillment  
of the requirements for the degree of  
Doctor of Philosophy  
2014

Advisory Committee:  
Professor Liangbing Hu, Chair  
Professor John Cumings  
Dr. Vince Ballarotto  
Professor Oded Rabin  
Professor Mario Dagenais, Dean's Representative

© Copyright by  
Colin Daniel Preston  
2014

## Acknowledgements

I would like to first and foremost thank the continued support and belief from my advisor Prof. Liangbing Hu. It has certainly been an incredible journey through the years; to be among the first graduate student researchers advised by Prof. Hu and to write the first thesis representative of his research group is truly an honor. I will always appreciate his mentorship and time dedicated to my graduate tenure, and will forever try to emulate the perseverance, enthusiasm, and creativity he demonstrated as my advisor.

I would like to thank the constant assistance, cooperation, and camaraderie of the Bing Research Group members, especially Xiaogang Han, Hongli Zhu, and Jiayu Wan who have been with me on this journey from the very beginning. I would also like to thank and wish the best of luck to Jaiqi Dai, Zhen Liu, Steven Lacey, and all the other group members that will further the reputation of the Bing Research Group. I would finally like to thank all the international students I had the privilege of working with and hope to cross paths with again, in particular Oeyvind Vaaland, Zhiqiang Fang, Yuanyuan Li, Fei Shen, and Zhen Bao.

I would also like to acknowledge the incredible support from my collaborators at the Laboratory for Physical Science (LPS) as well as many of the faculty members and graduate researchers at the University of Maryland. In particular I would like to thank Prof. John Cumings for his guidance and time dedicated to my research efforts over the past couple years, as well as the invaluable support from Vince Ballarotto at the LPS. I would like to thank the constant assistance from John Bavier and Da Song at the LPS from Prof. John Cumings group. I would like to thank Prof. Jeremy Munday and his research group for their collaboration, in particular Joseph Murray and Yunlu Xu.

Finally, I could not be where I am without the loving support of my parents Meg and Steve, and from my siblings Ben, Greg, and Kathryn. You are all a constant inspiration to me. To Katrina, thank you for your tireless patience and belief in me over the past few years; I couldn't have done this without you.

# Table of Contents

Acknowledgements.....	ii
Table of Contents.....	iv
List of Tables.....	vi
List of Figures.....	vii
List of Abbreviations.....	xvii
Chapter 1: Background.....	1
1.1 Introduction to Random Networks of One-Dimensional Materials.....	1
1.2 Properties of the Conductive Random Network.....	1
1.2.1 Electrical properties of random network.....	3
1.2.2 Optical properties of random network.....	3
1.2.2 Mechanical properties of random network.....	4
1.3 Applications of a Conductive Network.....	4
1.4 Solution-based Scalable Manufacturing.....	6
1.5 Thesis Structure.....	7
Chapter 2: Surfactant-Free Carbon Nanotube Inks for Spray Coatings with High Conductivity.....	12
2.1 Carbon nanotube properties.....	12
2.1.1 Carbon nanotube structure.....	12
2.1.2 Carbon nanotube electrical properties.....	14
2.1.3 Carbon nanotube optical properties.....	19
2.2 Carbon nanotube electrode fabrication.....	21
2.2.1 Carbon nanotube synthesis.....	21
2.2.2 Percolation theory.....	24
2.2.3 Carbon nanotube ink formation.....	28
2.2.4 Carbon nanotube electrode formation.....	31
2.3 Few-walled Carbon Nanotubes.....	33
2.4 Experimental Method.....	35
2.5 Results and Discussion.....	39
2.5.1 CVD growth yield of FWNTs.....	39
2.5.2 IPA-based FWNT ink fabrication.....	44
2.5.3 Comparing ink dispersion properties to spray-coated film properties.....	50
2.6 Conclusion.....	61
Chapter 3: Chemical Vapor Deposition Synthesis of Boron Doped Few-Walled Carbon Nanotubes.....	62
3.1 Boron-Doped Carbon Nanotubes.....	62
3.1.1 Substitutional doping mechanism.....	63
3.1.2 Projected change in electrical properties.....	63
3.2. Synthesis of Boron-doped FWNTs.....	65
3.3 Results and Discussion.....	67
3.3.1 Structure, morphology, and composition of B-FWNTs.....	67
3.3.2 Impact of purification on BFWNT spray-coating properties.....	87
3.4 Summary.....	104

Chapter 4: Haze of Transparent and Conductive Silver Nanowire Electrodes.....	105
4.1 Silver nanowire transparent electrodes .....	105
4.1.1 Optical properties of silver nanowires .....	105
4.1.2 Optoelectronic performance of Ag NW TCEs.....	106
4.2 Silver nanowire transparent electrode fabrication .....	109
4.2.1 Silver nanowire synthesis .....	109
4.2.2 Silver nanowire electrode formation.....	112
4.3 Transmission haze in TCEs .....	114
4.3.1 Mie theory of diffuse light scattering.....	116
4.3.2 Measuring transmission haze of TCEs .....	118
4.4 Experimental Method.....	120
4.5 Results and Discussion .....	123
4.5.1. Comparing the figure of merit of Ag NW TCEs. ....	130
4.5.2. Comparing the Ag NW TCE haze factor to the figure of merit.....	131
4.5.3. Thin-film CZTS solar cells .....	134
4.6 Conclusion .....	143
Chapter 5: Silver Nanowire Transparent Paper-based Electrode with High Transmission Haze .....	144
5.1 Paper Substrates for Transparent Electrodes .....	144
5.2 Synthesis of Transparent Paper with High Haze .....	149
5.3 Transparent Paper Properties .....	155
5.3.1 Optical properties of transparent paper.....	155
5.3.2 Mechanical properties of transparent paper .....	164
5.4 Smooth Transparent Paper for Conductive Electrode .....	167
5.5 Experimental Method.....	169
5.6 Results and Discussion .....	173
5.6.1 Optoelectronic performance.....	173
5.6.2 Haze properties .....	177
5.6.3 Photovoltaic light absorption simulation .....	182
5.7 Conclusion .....	186
Chapter 6: Conclusion and Outlook.....	187
6.1 Thesis Summary.....	187
6.2 Impact and Future Works.....	188
Bibliography .....	193



## List of Tables

Table 2.1: Acid reflux parameters, the zeta-potential of the refluxed FWNTs in water, and the film conductivity of spray-coated FWNT films from various IPA-based inks.

Table 3.1: The atomic ratio of boron to carbon of the BFWNTs as derived from the EELS measurement in Figure 3.6.

Table 3.2: The atomic ratio of boron to carbon of the BFWNTs as derived from the EELS measurement in Figure 3.7.

Table 3.3: Characteristic features of Raman spectra for BFWNT samples synthesized under various source solutions and CVD growth temperatures, such as the wavenumber of the D-band, the wavenumber of the G-band, the wavenumber of the D'-band, and the ratio of the D-band peak intensity to the G-band peak intensity.

Table 3.4: A comparison of spray-coated film properties formed from IPA-based inks containing BFWNTs that are synthesized via a CVD conducted at a 850 °C growth temperature with a 2.0 atm% boron source solution containing an ethanol/methanol mixture as a solvent with a 1:1 weight ratio. Each of the BFWNT growths were purified at 500 °C and washed in 100 mL of boiling methanol for 1 hour. Growth BFWNT(2) was dispersed in IPA after being refluxed in a 10 M HNO<sub>3</sub> solution for 2 hours while BFWNT(1) was suspended in IPA without being refluxed. The sheet resistance was measured with a four-point probe while the thickness was measured with a profilometer.

Table 3.5: A comparison of the characteristic properties of the Raman spectra in Figure 3.20; BFWNT (i) representing the as grown BFWNTs (Figure 3.20a), BFWNT (ii) representing the BFWNTs that were purified at 500 °C (Figure 3.20b), and BFWNT (iii) representing the BFWNTs that were purified at 625 °C (Figure 3.20c).

Table 3.6: The spray-coated film properties formed from IPA-based inks containing BFWNTs that were synthesized via a CVD conducted at a 850 °C growth temperature with a 2.0 atm% boron source solution containing an ethanol/methanol mixture as a solvent with a 1:1 weight ratio. The BFWNT growth was purified at 625 °C, washed in 100 mL of boiling methanol for 1 hour, and dispersed in IPA following a reflux in a 10 M HNO<sub>3</sub> solution for 2 hours.

Table 4.1) The tabulated data of the CZTS concentration in solution versus the absorbance of that solution at 500 nm.

Table 5.1: Mechanical properties of transparent paper, regular paper, and PET measured by the tensile strength test in Figure 5.16.

## List of Figures

Figure 1.1: A scanning electron microscope (SEM) image taken by a Hitachi SU-70 SEM of Ag NWs grown with a seed-mediated growth process, dispersed in a methanol ink solution, and then vacuum filtered into a random network.

Figure 1.2: An SEM image taken by a ZEISS (LEO) 1550VP SEM of CNTs grown with a chemical vapor deposition process spray-coated into a random network with an airbrush.

Figure 1.3: Examples of flexible thin-film devices that may utilize random networks of one-dimensional nanostructures, such as thin-film solar cells, flexible batteries, and flexible touchscreens.

Figure 1.4: Examples of solution-based deposition techniques that may fabricate random networks of one-dimensional nanomaterials from inks; these examples include spray coating, inkjet printing, spin coating, Meyer-rod coating, vacuum filtration, and dip coating. Each of these techniques may quickly assemble conductive random networks from inks containing dispersed one-dimensional conductive nanostructures onto a myriad of substrate surfaces.

Figure 1.5: Flow-chart illustrating chapter titles of this dissertation, and the distribution of research foci towards different random networks.

Figure 2.1: The index  $(n,m)$  determines the chirality of the CNT and the circumference  $C_h$ . The geometrical outline on the hexagonal lattice that forms a (4,3) CNT is depicted by the red parallel lines that must be rolled into seamless contact with each other. Examples of armchair and zigzag chiralities are also denoted on the hexagonal lattice. This figure was printed from Hierold, C., et al., "Carbon Nanotube Devices: Properties, Modeling, Integration and Applications." Advanced Micro & Nanosystems, Vol. 8, Wiley-VCH, 2008.

Figure 2.2: Hexagonal Brillouin zone of graphene with the high-symmetry points  $\Gamma$ ,  $K$ , and  $M$ , and the reciprocal lattice vectors  $\mathbf{k}_1$  and  $\mathbf{k}_2$ . This figure is printed from Reich, S. et al. "Carbon Nanotubes: Basic Properties and Physical Concepts," Wiley-VCH, 2004.

Figure 2.3: ((a) The band structure of graphene from hexagonal cones in the vicinity of the Fermi energy, which is cut into slices of allowed states when rolled graphene is rolled into carbon nanotubes. The resulting band structure of the nanotubes is (b) semiconducting or (c) metallic. (d) The determination of whether a tube is semiconducting or metallic may be made based on the chiral indices  $(n,m)$  of the nanotube.

Figure 2.4: Ab initio calculation of electronic bandstructure for metallic and semiconducting nanotubes with varying chiralities, which demonstrates the close

symmetry of the density of states (DOS) on either side of the Fermi energy. This figure was printed from A. Rubio, Appl. Phys. A, 1999.

Figure 2.5: A Raman spectrum of a single walled nanotube with a diameter of 1.38 nm with the characteristic wavenumbers where peaks representing the RBM, D-band, and G-band are found. This figure is printed from A. M. Rao et al., Science, 1997.

Figure 2.6: Chemical vapor deposition tube furnace setup for growth of carbon nanotubes described in this chapter. The carbon feedstock gas ( $\text{CH}_4$ ), carrier gas (Ar), and ramping gas ( $\text{H}_2$ ) are controlled by digital flow meters that monitor the flow rates into the tube furnace. The furnace hosts a quartz tube with a 2-inch diameter with three heating zones. The exhaust from the tube furnace is channeled to a glove box ventilator in the laboratory.

Figure 2.7: Sheet resistance as a function of the aspect ratio ( $L/D$ ) and area fraction of rods in nanowire films with a constant diameter of  $D = 50$  nm with an average contact resistance of  $R_c = 2$  k $\Omega$ . The top schematic illustrates two percolation networks of monodisperse rods with nanowire area fractions at or above the area fraction critical limit for percolation ( $AF_c$ ). This figure was printed from Mutiso et al., ACS Nano, 2013.

Figure 2.8: Schematic of a six fiber structure with relatively small aspect ratio and a two fiber structure with a relatively high aspect ratio. It is assumed that the contact resistance dominates the percolation across each structure, with the distance the charges travel assumed equal. The corresponding resistor representation of each structure is found below the fiber configuration.

Figure 2.9: A schematic diagramming the surface functional groups attached to the nanotube surface during a nitric acid ( $\text{HNO}_3$ ) reflux, including carboxyl groups (-COOH), carbonyl groups (C=O), and hydroxyl groups (-OH).

Figure 2.10: Attenuated total reflectance FTIR absorption spectra of pristine multi-walled nanotubes, purified multi-walled nanotubes after thermal oxidation, and acid treated multi-walled nanotubes. The characteristic peaks of oxygenated graphene groups by the acid reflux are labeled along with the corresponding wavenumber. This image is printed from R. Yudianti et al., Carbon, 2011.

Figure 2.11: A schematic illustrating a spray coating mechanism of a carbon nanotube ink onto a heated glass substrate with an airbrush. The air brush atomizes a carbon nanotube solution at a fixed air pressure of approximately 200 psi and a fixed distance of approximately 4 inches from the substrate surface heated by a hot plate. The pressure and distance from the surface determine the droplet size that deposits on the glass while the ink solvent and surface temperature determine the evaporation rate of the ink coating.

Figure 2.12: An image of the pink catalyst solution and the resulting brown powder catalyst after a combustion synthesis method.

Figure 2.13: TEM images of powder catalyst particles at various magnifications.

Figure 2.14: An image of the powder catalyst inserted into the quartz boat that is inserted into the tube furnace for the chemical vapor deposition growth of carbon nanotubes

Figure 2.15: A schematic illustrating the base growth carbon decomposition process that enables the formation of FWNTs emanating from the catalyst particles: (a) melted metal nanoparticles embedded in a catalyst powder and are exposed to the carbon source; (b) carbon decomposes into metal nanoparticles from the pyrolysis of the hot methane gas during the CVD growth until the solubility limit of the metal nanoparticles is reached and carbon precipitates out into a graphitic cap on the catalyst particle; (c) carbon continues to precipitate out of nanoparticle to form nanotubes with diameters smaller than catalyst particle size, which are stabilized by the rapid decomposition of carbon into the catalyst and rapid diffusion through the nanoparticle. This mechanism explains the formation of FWNTs as opposed to larger diameter MWNTs.

Figure 2.16: Pristine growth yield of the CVD process outlined in Section 2.4, which is visible by the transformation of the brown catalyst into a black powder composed of carbon nanotubes and amorphous carbon after the growth.

Figure 2.17: TEM images at various magnifications of pristine yield of CVD growth. The morphology, dispersion of wall numbers, and nanostructure of the resulting nanotubes is clearly depicted, as well as a presence of amorphous carbon that collects on the tube surface.

Figure 2.18: A thermogravimetric analysis spectrum of the pristine yield of the CVD growth, which was conducted in air by a Shimadzu TGA at a ramping rate of 2 °C per minute. The mass loss of the sample up to approximately 150 °C is due to the evaporation of water from the powder sample and due to the stabilization of the balance.

Figure 2.19: A schematic illustrating how bundled nanotubes may be dispersed by attaching carboxyl groups to their surface in order to counteract the intrinsic van der Waals forces.

Figure 2.20: An image of the HNO<sub>3</sub> bath solution that hosts the acid reflux conducted to functionalize the surface of the carbon nanotubes.

Figure 2.21: Raman spectra of carbon nanotube samples immediately after the CVD growth, after purification of the growth yield by thermal oxidation, and after the purified nanotube yield is refluxed in HNO<sub>3</sub>.

Figure 2.22: A FTIR spectrum of the HNO<sub>3</sub> refluxed nanotubes with the characteristic peaks of successful surface functionalization of carboxyl groups to the outer walls labeled.

Figure 2.23: (a) An as-grown FWNT suspension in IPA at 0.6 mg/mL, (b) an example of a spray-coated FWNT film from an as-grown FWNT suspension in IPA, and (c) a spray-coated as-grown FWNT film surface.

Figure 2.24: (a) A functionalized FWNT suspension in IPA at 0.6 mg/mL, (b) an example of a spray-coated FWNT film from a functionalized FWNT suspension in IPA, and (c) a spray-coated functionalized FWNT film surface.

Figure 2.25 A schematic of the dynamic light scattering setup within a Malvern Zetasizer. An incident laser pulsed by a mirror oscillating at 320 Hz is scattered by the nanotubes in the dilute solution hosted within the capillary chamber of the sample cuvette. The scattered beam is combined with the pulsed reference beam redirected by the oscillating mirror at an interferometer, which determines the shift in frequency between the scattered and reference beam. The motion of nanotubes is controlled by their response to an electric field applied by the cuvette electrodes, which rapidly fluctuates to generate numerous mobility measurements that are automatically averaged by the Malvern Zetasizer software.

Figure 2.26: SEM images of spray-coated FWNT films from (a) sample A and (b) sample D, as detailed in Table 2.1.

Figure 3.1: The theoretical LDOS associated with a  $BC_3$  island (encircled region) plotted with the LDOS associated with a pure carbon island of the same radius, located far away from the B atoms as depicted in the unfolded tube model to the right (to reform the tube A has to be joined with A' and B with B', respectively).

Figure 3.2: A schematic of experimental setup for the in-growth substitutionally doped B-FWNT synthesis via a solution-injected CVD method

Figure 3.3: Growth yield of B-FWNTs in quartz sample holder.

Figure 3.4: FTIR of secondary phase from growth yield after a) initial growth and b) oxidation at 500 °C.

Figure 3.5: TEM images of B-FWNTs at various magnifications.

Figure 3.6: An EELS spectrum measured at the point indicated at the point on the nanotube in the STEM inset image. The background and EELS cross-section are demarked by the red and green spectra, respectively.

Figure 3.7: An EELS spectrum measured at the point indicated at the point on the nanotube near the catalyst in the STEM inset image. The background and EELS cross-section are demarked by the red and green spectra, respectively.

Figure 3.8: (a-b) Electron-energy loss spectra measured along the B-FWNT at various locations on the line depicted in the STEM image. (c) The resulting concentration of

boron at the locations along the EELS line scan of the nanotube in the STEM measurement is given by the bar graph, with the x-axis representing the location of the EELS scan.

Figure 3.9: TEM images depicting the solution-injected CVD growth yield of BFWNTs with a lower growth temperature of 750 °C at various magnifications

Figure 3.10: TEM images depicting the solution-injected CVD growth yield of BFWNTs with a higher methanol content in the source solution of 3:1 methanol to ethanol at various magnifications.

Figure 3.11: (a) Raman spectrum of as-grown B-FWNTs, grown at 850 °C with 1:1 methanol/ethanol, (b) Raman spectrum of as-grown B-FWNTs, grown at 750 °C with a 1:1 methanol/ethanol source solution, and (c) Raman spectrum of as-grown B-FWNTs, grown at 850 °C with 3:1 methanol/ethanol in the source solution.

Figure 3.12: (a) TGA of B-FWNT grown at 850 °C with a 1:1 methanol to ethanol source solution, Growth 1 and (b) a TGA of B-FWNT grown at 850 °C with a 3:1 methanol to ethanol source solution, Growth 3.

Figure 3.13: TEM with various magnifications of the morphology of wavy B-FWNTs, which clearly demonstrates fluctuations in the inner and outer diameters of the nanotubes.

Figure 3.14: SEM images at various magnifications of spray-coated BFWNT films following a reflux of the nanotubes in 10 M HNO<sub>3</sub> for about 2 hours. Image were taken at high contrast in order to illuminate the BFWNTs along with the presence of a seemingly amorphous secondary phase.

Figure 3.15: ATR-FTIR spectrum of Growth 1 BFWNTs with the wavenumber of prevalent peaks labeled.

Figure 3.16: FTIR spectrum generated from an ATR measurement of grey “ash” from Growth 1 of the CVD synthesis of BFWNTs as depicted in Figure 3.3.

Figure 3.17: FTIR spectrum generated from an ATR measurement of grey “ash” from Growth 1 of the CVD synthesis of BFWNTs after an oxidation at 500 °C for 1 hour.

Figure 3.18: SEM images of spray-coated surface of methanol-washed BFWNTs refluxed in 10 M HNO<sub>3</sub> for 2 hours and dispersed in IPA at an approximate concentration of 0.6 mg/mL.

Figure 3.19: FTIR spectrum generated from an ATR measurement of Growth 1 of the CVD synthesis of BFWNTs after an oxidation at 500 °C for 1 hour.

Figure 3.20: Raman spectra of BFWNTs that were synthesized via a CVD conducted at a 850 °C growth temperature with a 2.0 atm% boron source solution containing an

ethanol/methanol mixture as a solvent with a 1:1 weight ratio (a) as grown, and that were purified at (b) 500 °C and (c) 625 °C.

Figure 3.21: TEM images of BFWNTs synthesized via a CVD conducted at a 850 °C growth temperature with a 2.0 atm% boron source solution containing an ethanol/methanol mixture as a solvent with a 1:1 weight ratio.

Figure 4.1: Plots of the transmittance and coverage density with respect to sheet resistance for networks of (a) long Ag NWs (19  $\mu\text{m}$ ) purchased from Blue nano and (b) short Ag NWs (11  $\mu\text{m}$ ) purchased from Nanogap compared to ITO and fluorine doped tin oxide (FTO). Non-linear curve fits of the experimental data for the transmittance and coverage density are also plotted for each of the short and long nanowire samples. This figure is printed from Sepulveda-Mora, et al., J. of Nanomaterials, 2012.

Figure 4.2: (a) A TEM image of silver seeds for nanowire growth (inset demonstrating the crystal planes). This image was printed from Sun et al., Nanoscale, 2010.<sup>[19]</sup> (b) A schematic of a silver nanowire seed mediated growth reaction where the silver seed solution that act as nucleation sites for titrated silver ions ( $\text{Ag}^+$ ). The simultaneous formation of silver bromide ( $\text{AgBr}$ ) from the addition of a competing salt ( $\text{KBr}$ ) in the seed solution tapers the nucleation of silver ions on the seed particles in order to monitor the diameter. The presence of ethylene glycol (EG) perpetuates the one-dimensional propagation of nanowire growth by bonding to the (100) planes of the nanowire.

Figure 4.3: Images of the (a) seed solution before the titration of  $\text{AgNO}_3$  and (b) the solution after the titration of  $\text{AgNO}_3$ , where the translucent yellow seed solution has transformed into a brownish-grey opaque solution.

Figure 4.4: A silver nanowire ink solution in a centrifuge vial.

Figure 4.5: A schematic illustrating the dry-transfer process for fabricating TCEs on a PDMS stamp that delaminates a uniform filtered random network of Ag NWs off its AAO filter.

Figure 4.6: Images that illustrate (a) a vacuum filtered Ag NW network derived from an ink suspension and (b) an example of a dry-transferred electrode random network of Ag NWs on a PDMS substrate.

Figure 4.7: A plot of the photon energy of incident light waves versus the absorption coefficient of silicon that demonstrates thin films of silicon (<1  $\mu\text{m}$ ) are inadequate absorbers of light at their band gap energy.

Figure 4.8: A schematic that demonstrates path length of light propagating through a TCE with high optical haze is longer than for low optical haze, which enables greater light absorption in the conversion layer beneath the TCE in the solar cell stack.

Figure 4.9: Schematic of the 2D simulation setup used to calculate the light scattering behavior at normal incidence from a single silver nanowire with a radius of  $R$ . The center of the nanowire is the origin of the axes. The green box represents a Total Field Scattered Field (TFSF) source with a length of 500 nm in the x-direction. The length is chosen according to the average spacing between Ag NW as calculated from SEM images.

Figure 4.10: A schematic illustrating the experimental mechanism used to measure the transmission haze of a substrate with an integrating sphere and a back reflector; (a) the total diffuse scattering through the substrate is measured by detecting the light that does not transmit through the open window at a  $0^\circ$  angle from the perpendicular axis to the surface of the substrate, (b) the total transmittance through the substrate is measured by placing a white reflecting surface at the back window so as to detect all the light transmitted through the substrate, (c-d) and the experimental error of the system is measured to be subtracted from the data taken.

Figure 4.11: The SEM images of Ag NW; a) percolation network of the film with small diameters, b) display of small Ag NW diameters with little deviation, the diameters are as small as  $\sim 60$  nm, c) percolation network of film with large diameters, d) display of large Ag NW diameters with little deviation, averaged to be  $\sim 150$  nm..

Figure 4.12: Simulation of the transmittance for a large (150nm) and small (60nm) diameter nanowire with (a) TE polarization, (b) TM polarization, and (c) averaged transmission; and the transmission haze simulation for a large (150nm) and small (60nm) diameter nanowire with (d) TE polarization, (e) TM polarization, and (f) averaged haze factor of Ag NW's with different diameters (60nm and 150nm).

Figure 4.13: Simulation of the normalized scattered field intensity versus scattering angle from the axis normal to the silver nanowire with diffuse scattering represented by acute angles ( $0-90^\circ$  and  $270^\circ-360^\circ$ ) and backscattering represented by obtuse angles ( $90-270^\circ$ ) for (a) TE polarization and (b) TM polarization and (c) average of TE and TM for 60 nm and 150 nm diameter silver nanowires. (a) and (b) are in log scale and (c) is in linear scale for clarity.

Figure 4.14: (a) The transmittance spectrum for the various films formed from vacuum filtration of Ag NW dispersions with large diameters ( $\sim 150$  nm), and b) the transmittance spectrum for the various films formed from vacuum filtration of Ag NW dispersions with small diameters ( $\sim 60$  nm).

Figure 4.15: (a) Comparison of experimental transmittance data for a small diameter ( $\sim 60$  nm) Ag NW TCE film with  $R_s = 45 \Omega/\text{sq}$  and a large diameter ( $\sim 150$  nm) Ag NW TCE film with  $R_s = 35 \Omega/\text{sq}$ , and b) haze factor comparison between the same small diameter and large diameter Ag NW TCE films.

Figure 4.16) A schematic of a typical thin-film solar cell stack.



Figure 4.17: The synthesis setup for a fabrication of CZTS nanorods. In a typical synthesis, copper(II) acetylacetonate (0.261g, 1mmol), Zinc acetate (0.091g, 0.5mmol), Tin(IV) acetate (0.177g, 0.5mmol) and TOPO (1.353g, 3.5mmol) were mixed with 10mL of 1-octadecene in a three-neck round-bottom flask and evacuated at room temperature for 30-45mins. The solution was then heated to 240-260°C under an argon atmosphere. At 150- 160°C, a mixture of 0.25mL 1-dodecanethiol and 1.75mL t-dodecanethiol was quickly injected into the flask which resulted in an immediate color change from dark green to wine red and then finally to brown. After injection, the reaction was allowed to proceed for 15-30 minutes with continuous stirring. The nanorod growth was terminated by a removal of the heating mantle and at 80°C, 2–4 ml anhydrous toluene were added to the mixture to quench the reaction.

Figure 4.18: TEM images of CZTS nanorods at different magnifications demonstrating varying degrees of self-alignment (a, b), and a HRTEM image of a CZTS nanorod demonstrating the atomic crystalline structure.

Figure 4.19: A plot of the CZTS concentration in solution versus the absorbance of that solution at 500 nm, and a linear fit of the regression. The slope of the linear regression is calculated to be  $\alpha = 0.02$ , which is the absorption coefficient as calculated by this plot.

Figure 4.20: A plot of the  $(\alpha h\nu)^2$  versus  $h\nu$  that demonstrates a linear fit intercepting the x-axis at approximately 1.43 eV.

Figure 4.21: TEM images of a thin-film composed of CZTS nanorods coated onto a molybdenum sputtered soda lime glass substrate, which is then annealed at 500 °C for 10-15 min in a selenium environment.

Figure 4.22: SEM-EDS spectra at different locations on annealed CZTS thin-film layers, with corresponding SEM images with the scan location marked and tables of the atomic compositions at each scan.

Figure 5.1: A schematic detailing the derivation of wood fibers from trees as well as the hierarchical structure of these wood fibers, which enables cellulose nanofibers and microfibrils to be extracted from the cell wall of the wood fibers.

Figure 5.2: A schematic depicting the random network of nanofibrillated cellulose (NFC) with approximate diameters less than 15 nm as illustrated in the inset TEM image.

Figure 5.3: A schematic of how an opaque porous network of wood fibers with diameters between 10-50  $\mu\text{m}$  is transformed into a transparent substrate with significant diffuse scattering. NFC with diameters between 5-30 nm fill the space within the wood fiber network to create a denser hybrid network from the two cellulose structures that reduces the surface reflection and enhances the transmission through the paper substrate.

Figure 5.4: A schematic illustrating the transformation of a network of microscopic cellulose fibers into a densely packed network by altering the fiber structure.

Figure 5.5: (a) The morphology of original bleached sulfate wood fibers under an optical microscope. Inset is a 0.25 wt% original bleached sulfate wood pulp suspension. (b) The morphology of TEMPO-oxidized wood fibers under an optical microscope. Inset is a 0.25 wt% TEMPO-oxidized wood fiber suspension. SEM images of unzipped TEMPO-oxidized wood fibers (c) and (d) nanofibers on the cell wall of TEMPO-oxidized wood fiber.

Figure 5.6: An image of transparent paper produced from TEMPO-oxidized wood fibers with a diameter of 20 cm.

Figure 5.7: SEM images of the surface of (a) an untreated regular paper substrate and (b) the transparent paper substrate, with the inset magnifying the scale bar to 100  $\mu\text{m}$ .

Figure 5.8: The total transmittance of the transparent paper, nanopaper, and PET substrates.

Figure 5.9: The total diffuse scattering of the transparent paper, nanopaper, and PET substrates measured in Figure 5.9.

Figure 5.10: A schematic illustrating how the angular distribution of the diffusely scattered light is measured, with a rotating detector measuring the intensity of light every two degrees from  $-90 \leq \theta \leq 90^\circ$  to the perpendicular axis of the substrate surface.

Figure 5.11: A polar plot demonstrating the angular distribution of light diffusely scattered by transparent paper for multiple incident angles on the substrate surface by the illumination source.

Figure 5.12: Images of the transmission haze effect on 532 nm light transmitted through (a) PET, (b) glass, and (c) transparent paper onto a target held at a fixed distance from the substrate surface.

Figure 5.13: A plot demonstrating the total diffuse light scattering through a transparent paper substrate with varying thicknesses.

Figure 5.14: A plot demonstrating the total transmittance of light through transparent paper substrates with thicknesses correlating with Figure 5.14.

Figure 5.15: A stress versus strain curve for transparent paper and a regular paper substrate.

Figure 5.16: A schematic demonstrating the change in the number of interfacial bonds between a curved wood fiber and a TEMPO-oxidized flattened cellulose fiber.

Figure 5.17: Schematic of Ag NW network embedded in a nanopaper surface on the transparent paper. (a) Nanofibrillated cellulose was filtered through TEMPO-treated paper to form a smooth surface, (b) with a novel lamination process, a filtered Ag NW network is embedded in the smooth NFC surface, and (c) the final structure is a uniform Ag NW network embedded onto the surface of transparent paper.

Figure 5.18: The transmittance curve for the paper substrate before a Ag NW network is embedded into the surface.

Figure 5.19: Optical image of Ag NW transparent paper.

Figure 5.20: An SEM image of Ag NWs with a diameter of 100 nm.

Figure 5.21: Top view of Ag NW transparent paper demonstrating embedded Ag NW network.

Figure 5.22: An SEM image of the cross-section of Ag NW transparent paper.

Figure 5.23: Total transmittance versus wavelength of Ag NW paper.

Figure 5.24: Figure of merit versus total transmittance for previous TCE reports, ITO, and our Ag NW transparent paper.

Figure 5.25: The tabulated results for the tape test measurement on the Ag NW paper TCE sample. The initial sheet resistance of the sample was measured at 13  $\Omega$ /sq, which increased to 25  $\Omega$ /sq after manually pressing scotch tape down on the sample and peeling it off a total of ten times.

Figure 5.26: The total diffuse transmission haze for (a) ITO on glass, (b) transparent paper, and (c) Ag NW paper.

Figure 5.27: Diffuse scattering angular distribution with arbitrary y-axis units for (a) ITO on glass, (b) transparent paper, and (c) Ag NW paper.

Figure 5.28: Light absorption dependence of a structure including either a TCE with varying optical properties and an absorber layer (a) a 1  $\mu$ m thick Si film, (b) a 50 nm thick GaAs film, and a 50 nm thick CdTe film. Light absorption in these absorbers for a highly transparent ITO TCE and our Ag NW paper TCE are compared as well.

## List of Abbreviations

AAO – Anopore aluminum oxide

AF<sub>(c)</sub> - (critical) area fraction

Ag NW – silver nanowire

ATR – attenuated total reflection

B-FWNT – boron-doped few walled carbon nanotube

CNT – carbon nanotube

CTAB – cetyl trimethylammonium bromide

CVD – chemical vapor deposition

EELS – electron energy loss spectroscopy

FDTD – finite difference time domain

FTIR – Fourier transform infrared spectroscopy

FWNT – few walled carbon nanotube

IPA – isopropanol

ITO – indium tin oxide

MWNT – multi walled carbon nanotube

NFC – nanofibrillated cellulose

PDA – poly(dopamine)

PDMS – polydimethylsiloxane

PEDOT:PSS – poly(3,4-ethylenedioxythiophene) polystyrene sulfonate

PET – polyethylene terephthalate

PV – photovoltaic

PVDF – polyvinylidene difluoride

PVP – polyvinylpyrrolidone

SDBS – sodium dodecyl benzene sulphonate

SDS – sodium dodecyl sulfate

SEM – scanning electron microscopy

SEM-EDS – scanning electron microscope electron dispersive spectroscopy

SWNT – single walled carbon nanotube

TCE – transparent conducting electrode

TE – transverse electric

TEM – transmission electron microscopy

TEMPO – (2,2,6,6-tetramethylpiperidin-1-yl)oxy

TFSF – total field scattered field

TGA – thermogravimetric analysis

TM – transverse magnetic

# Chapter 1: Background

## 1.1 Introduction to Random Networks of One-Dimensional Materials

Networks of randomly arranged one-dimensional nanomaterials offer fertile grounds to grow new thin-film devices with exceptional features. These random networks exhibit unique properties at small thicknesses ( $< 1\mu\text{m}$ ) that diverge from those characteristic of solid thin-films. It is demonstrated that porous three-dimensional networks of one-dimensional nanomaterials induce more light scattering interactions, exhibit lower light absorption, and withstand higher strain than solid thin-films with a similar thickness. Random networks of conducting nanomaterials may also exhibit low sheet resistance and be hybridized with other nanomaterials to augment certain properties. Conductive random networks are therefore unique structures with immense applications in thin-film flexible electronics; however, a greater understanding of their properties is necessary to fully enable high performance thin-film devices. This thesis presents a comprehensive investigation into the various mechanisms that determine the characteristics of random networks of one-dimensional nanomaterials. As a result, some unique device functionalities with novel properties are also demonstrated in this work.

## 1.2 Properties of the Conductive Random Network

The electrical, optical, and mechanical properties of a random network of one-dimensional nanomaterials are determined by three parameters: 1) the nanomaterial composition, 2) the nanomaterial geometry, and 3) the morphology of nanomaterials

within the random network. Figure 1.1 illustrates a random network of silver nanowires (Ag NWs) and Figure 1.2 illustrates a random network of carbon nanotubes (CNTs).

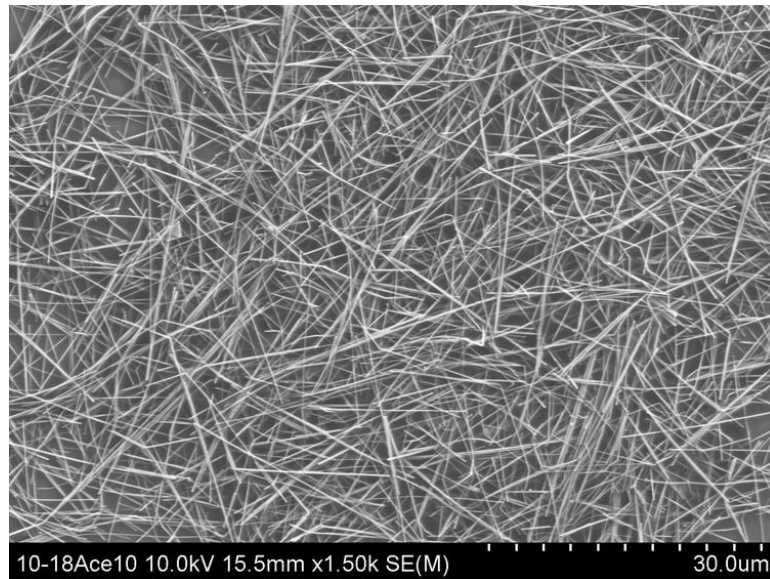


**Figure 1.1)** A scanning electron microscope (SEM) image taken by a Hitachi SU-70 SEM of Ag NWs grown with a seed-mediated growth process, dispersed in a methanol ink solution, and then vacuum filtered into a random network.

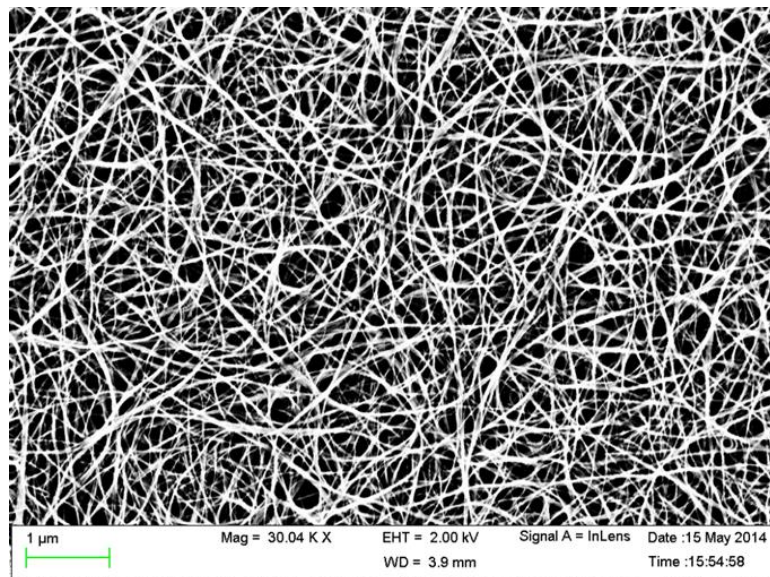


**Figure 1.2)** An SEM image taken by a ZEISS (LEO) 1550VP SEM of CNTs grown with a chemical vapor deposition process spray-coated into a random network with an airbrush.

### 1.2.1 Electrical properties of random network

Conductive one-dimensional nanostructures may form a percolative network for charge transport that exhibits very high conductivity at low thicknesses. Each individual nanostructure acts a metaphorical “highway” to efficiently transport charge along a confined pathway, which subsequently combine to form a web of conducting channels that enable volumetric flow of charge. These channels may be straight nanostructures such as Ag NWs seen in Figure 1.1 or nanostructures with high degrees of curvature such as CNTs seen in Figure 1.2. The low thickness and high porosity of the conductive network promotes other additional beneficial features that are challenging to achieve with solid thin-films, such as high flexibility or high total transmittance. This thesis work seeks to understand the impact factors that determine the formation of highly conductive random networks of Ag NWs or CNTs in conjunction with other desirable unique optical or mechanical properties.

### 1.2.2 Optical properties of random network

In conjunction with a high conductivity, random networks of one-dimensional nanostructures may exhibit nominal optical properties. Silver nanowires in particular are widely demonstrated to form random networks that exhibit high total transmittance and simultaneously a low sheet resistance; however, a unique optical property achievable by these networks is the diffuse light scattering or transmission haze. The length and diameter of individual Ag NWs affect their extinction coefficient and thus dictate their scattering interactions with incident electromagnetic waves, but any understanding of the transmission haze through a random network of Ag NWs or its impact on device functionality is limited. This thesis work seeks to emphasize the importance of



transmission haze in thin-film devices by more fully characterizing and understanding the diffuse light scattering behavior through networks of Ag NWs.

### 1.2.2 Mechanical properties of random network

The geometry of one-dimensional conducting nanomaterials is best defined by their aspect ratio (length:diameter), which not only impacts the electrical and optical properties of a subsequent random network but also the mechanical strength and flexibility of the interwoven channels. The high flexibility of random networks of CNTs and Ag NWs have been thoroughly studied and reported in current literature, and thus will not be primarily investigated in this work.<sup>[2-4, 57, 111, 163, 164]</sup> It is noteworthy, however, that the unique optical and electrical properties of these conductive random networks may be adjoined by their inherent flexibility as well to promote unique device applications.

### 1.3 Applications of a Conductive Network

Thin-film electronics are emerging as a new frontier towards various lightweight, economical, yet high performance devices. Figure 1.3 demonstrates some examples for popular electronic devices that utilize thin-film technology to become lighter and more flexible.

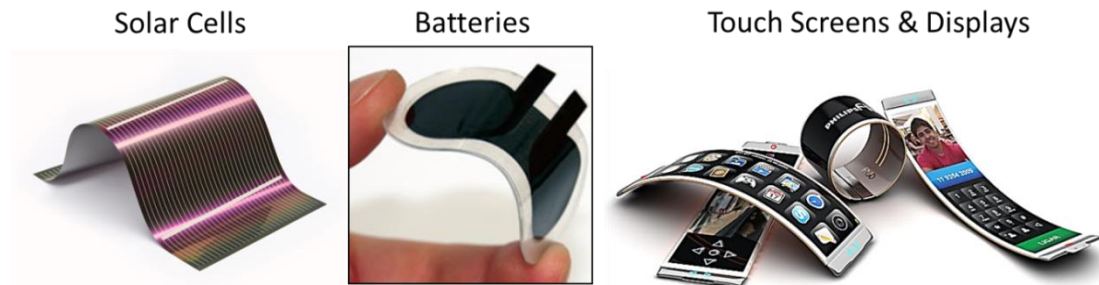


**Figure 1.3)** Examples of flexible thin-film devices that may utilize random networks of one-dimensional nanostructures, such as thin-film solar cells, flexible batteries, and flexible touchscreens.

The devices in Figure 1.2 require conductive layers that may withstand significant repeated mechanical strain and conform to non-planar geometries. Random networks of CNTs or Ag NWs meet these criteria due to the high flexibility of the interwoven network of conducting nanostructures.<sup>[1-5]</sup> Carbon nanotubes may be assembled into random networks to form electrodes that are applicable in a variety of devices such as current collectors in flexible low-cost batteries. Introducing CNT structures with lower intrinsic resistivity and networks with a higher homogeneity of dispersed CNTs will enhance the conductivity of the resulting electrode and thus improve the overall performance of the dependent devices. Flexible transparent conducting electrodes (TCEs) may be formed from random networks of Ag NWs for application in displays, touch-screens, and solar cells. The optoelectronic characteristics of these TCEs must exhibit a low sheet resistance with a high optical transmittance in order to maximize the device performance. The optoelectronic properties of a TCE in a solar cell is of particular importance because transmittances lower than 90% and sheet resistances higher than  $10 \Omega/sq$  results in significant power losses.<sup>[6]</sup> An additional optical property that impacts the power output of thin-film solar cells is diffuse light scattering or transmission haze through the TCE, which enhances light absorption in solar cells by extending the path length of light through the critical conversion layers. Since transmission haze through random networks of Ag NWs is inadequately characterized or understood, new studies are needed to illuminate the mechanism of diffuse light scattering through Ag NW TCEs in order to account for it in the performance evaluation for solar cells. This thesis work seeks to improve both the performance and the scalability of thin-film

devices that incorporate these conductive random networks by simultaneously understanding and improving their electrical and optical properties.

#### 1.4 Solution-based Scalable Manufacturing

There are many fabrication techniques to process the nanostructures into random networks, but solution-based methods are the most versatile and low-cost. Figure 1.4 illustrates various solution-based processes to fabricate thin-films. These processes rely on inks of nanomaterials dispersed in a solution that may be quickly deposited into precise patterns or uniform areas to form devices on a range of substrates. Thin-film devices formed from inks thus enable a rapid assembly of electronic devices on a myriad of substrates useful for various applications. It is critical to ensure an efficient dispersion of nanostructures in solution during the ink formation and to promote a uniform ink coating with good adhesion to the substrate by tuning the printing parameters. In this manner, solution-based fabrication methods may form random networks with ideal electrical, optical, and mechanical properties while improving the scalability of high performance thin-film devices. In this thesis we seek to understand the unique electronic and optical properties of random networks composed of either CNTs or Ag NWs formed from ink-based coating techniques in order to enable the fabrication of thin-film devices with better performance from scalable manufacturing processes.

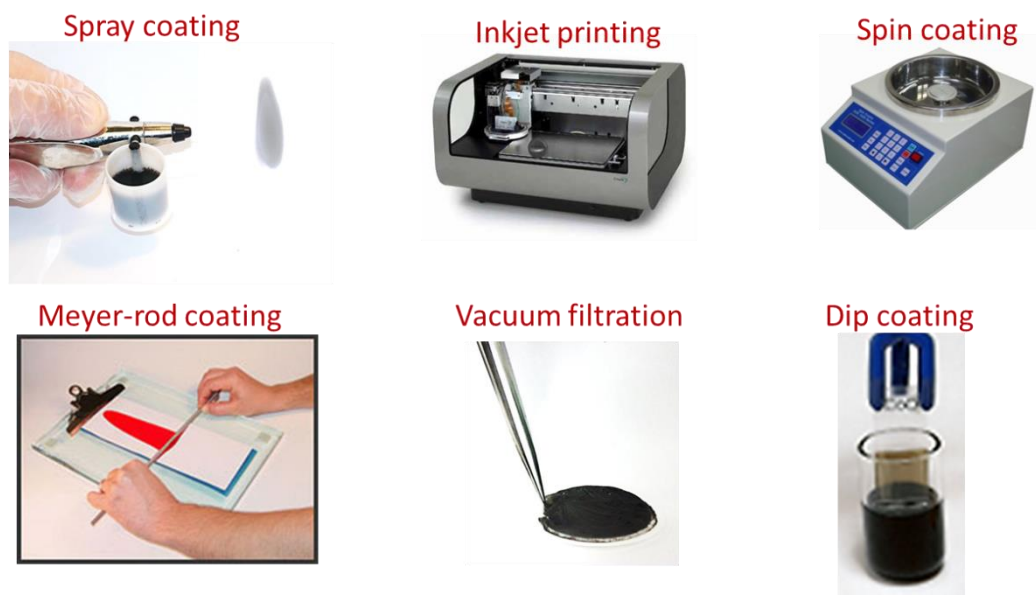


**Figure 1.4)** Examples of solution-based deposition techniques that may fabricate random networks of one-dimensional nanomaterials from inks; these examples include spray coating, inkjet printing, spin coating, Meyer-rod coating, vacuum filtration, and dip coating. Each of these techniques may quickly assemble conductive random networks from inks containing dispersed one-dimensional conductive nanostructures onto a myriad of substrate surfaces.

### 1.5 Thesis Structure

This thesis work investigates random networks formed from different one-dimensional nanostructures. The fundamental properties of the random networks composed of these nanomaterials are studied and optimized to enable unique device functionalities with high performance. Figure 1.5 diagrams the hierarchical structure of this dissertation.

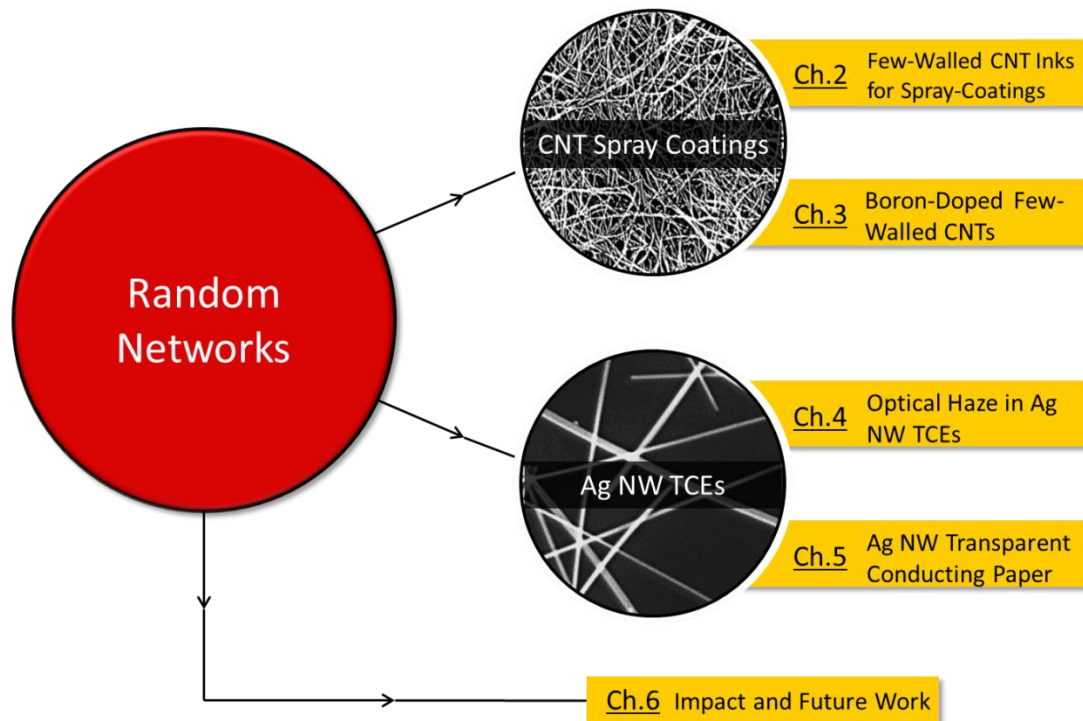


**Figure 1.5)** Flow-chart illustrating chapter titles of this dissertation, and the distribution of research foci towards different random networks.

In Chapter 2, we explore the properties of carbon nanotube spray-coatings, and their application as conductive electrodes for various devices. Carbon nanotubes are one-dimensional structures that may be fabricated through scalable methods and exhibit unique fundamental properties. Spray-coated CNT films offer a simple and printable solution for fabricating low-cost, light-weight, and flexible thin-film electronics. Current nanotube spray inks require either a disruptive surfactant or destructive surface functionalization to stabilize the dispersions at the cost of the electrical properties of the deposited film. It is demonstrated that high purity few-walled carbon nanotubes (FWNTs) may be stabilized in isopropanol after surface functionalization, and that optimizing ink stability dramatically enhances the conductivity of subsequent spray-

coated thin films. We consequently report a surfactant-free FWNT ink that enables spray-coated thin films with conductivities reaching 2100 S/cm, which is the highest conductivity for printed CNT networks without using a surfactant. Zeta-potential measurements are used here to quantify the nanotube ink dispersion quality. These measurements demonstrate a direct positive correlation with the spray-coated film conductivity, the key metric for high performance printed electronics.

In Chapter 3, we introduce a new synthesis technique to form boron-doped FWNTs directed at lowering the bulk resistivity of the nanotube growth yield, and their use in conductive electrodes is investigated. A new synthesis procedure that introduces boron into the carbon lattice during a FWNT growth is investigated and demonstrates successful substitutional boron doping through electron energy loss spectroscopy (EELS) measurements. The growth yield of boron doped FWNTs (B-FWNTs) fabricated under various solution injected CVD conditions is investigated and compared with Raman spectroscopy and thermogravimetric analysis (TGA). An investigation into optimizing the purification of the B-FWNT growth yields is also conducted with Fourier transform infrared spectroscopy (FTIR), TGA measurements, and SEM images. Separate ink solutions were prepared from FWNTs and B-FWNTs, and spray-coated to compare their sheet resistance. Differences in the ink and spray-coating properties for pristine and surface-functionalized B-FWNTs are also investigated.

In Chapter 4, we explore the properties of random networks of Ag NWs and their application towards transparent conducting electrodes (TCEs). As mentioned in Section 1.3, thin-film optoelectronic devices require flexible electrodes with a high transmittance and low sheet resistance. The contemporary performance metric of TCEs is thus

evaluated by its transmittance and sheet resistance. Through a discussion on the percolation theory, the structural and morphological characteristics of a random Ag NW network with a low sheet resistance and a high transmittance are determined. Based on this discussion and a review of previous reports, it is concluded that Ag NWs with a high aspect ratio dispersed in a uniform random network exhibits the highest transmittance at the lowest sheet resistance. The nanowire synthesis, fabrication method of the Ag NW network, and post-fabrication processing methods that enable these properties are reviewed. A discussion on light trapping in thin-film solar cells reveals that transmission haze is an equally important yet disregarded parameter in the performance evaluation of TCEs. The effect of the Ag NW diameter on the transmission haze values in the visible spectrum was investigated using films composed of either small diameters (~60 nm) or large diameters (~150 nm). Finite Difference Time Domain (FDTD) simulations and experimental transmittance data confirm that smaller diameter nanowires form higher performing TCE films according to the current figure of merit. While maintaining near constant transmittance and conductivity for each film, however, it is observed experimentally that films composed of Ag NWs with larger diameters demonstrate a higher haze factor than films with smaller diameters. This confirms FDTD simulations of the haze factor for single nanowires with similarly large and small diameters. This is the first record of transmission haze properties for Ag NWs that are simulated or experimentally measured, and also the first evidence that the current figure of merit for TCEs is insufficient at evaluating their performance in thin-film solar cell devices.

In Chapter 5, we expound upon our evidence that transmission haze is a beneficial property for TCEs in thin-film solar cells by introducing a novel Ag NW paper hybrid

network that form a TCE with exceptional properties. Transparent paper substrates with a smooth surface are introduced by extracting cellulose fibers with micro-sized and nano-sized diameters from the hierarchical structure of paper fibers and integrating them into a random network. The process of extracting these cellulose fibers is explained and a novel transparent paper that possesses both high optical transparency and high haze is investigated. The transmittance and sheet resistance of the resulting Ag NW paper TCE were experimentally measured, and represent the highest reported figure of merit value for solution-based TCEs according to conventional models. It is demonstrated that the hybrid network exhibits good flexibility and a scratch-resistant Ag NW network. The diffuse light scattering properties of the Ag NW paper were also thoroughly investigated through various techniques; the total transmission haze of the hybrid random network and the distribution of diffuse scattering angles through the surface of the network. A simulation that relates the optical properties of TCEs with the light absorption in the conversion layers for various thin-film solar cells demonstrates that the Ag NW paper induces greater light absorption than ITO in several thin-films common in solar cells. The combined high transmittance, low sheet resistance, and high transmission haze measured and studied in this new Ag NW paper structure suggests that it is the highest performing TCE for thin-film solar cells.

In Chapter 6, we consider the impact of this dissertation on the current thin-film technology. We will also outline future works that may enhance our understanding of random networks and realize more unique functionalities for thin-film devices.



## Chapter 2: Surfactant-Free Carbon Nanotube Inks for Spray Coatings with High Conductivity

The carbon nanotube is an intensely studied nanostructure since its discovery in the 1990's by Iijima.<sup>[7]</sup> Due to a similar intrinsic lattice structure to graphene, carbon nanotubes share many of the beneficial electrical, mechanical, and optical properties of graphene; however, their one-dimensionality enable their use in electrodes as conductive channels that form a percolation network. Coupled with the low-cost and availability of carbon, carbon nanotubes make ideal nanostructures to form conducting networks that may act as charge carriers in batteries.<sup>[8,9]</sup> The following subsections review the fundamental characteristics of carbon nanotubes, and the experimental process to form spray-coated networks from carbon nanotube solutions.

### 2.1 Carbon nanotube properties

#### 2.1.1 Carbon nanotube structure

Carbon nanotubes may be regarded as graphitic carbon lattice planes rolled into cylinders. We see in Figure 2.1 the honeycomb hexagonal lattice of graphene with a unit cell described by vectors  $\mathbf{a}_1$  and  $\mathbf{a}_2$  where  $a_0 = 2.461 \text{ \AA}$ . When the graphitic sheet is rolled into a cylinder that seamlessly connects the two red lines in Figure 2.1, the lattice vector  $\mathbf{C} = n\mathbf{a}_1 + m\mathbf{a}_2$  describes the circumference of that resulting nanotube.

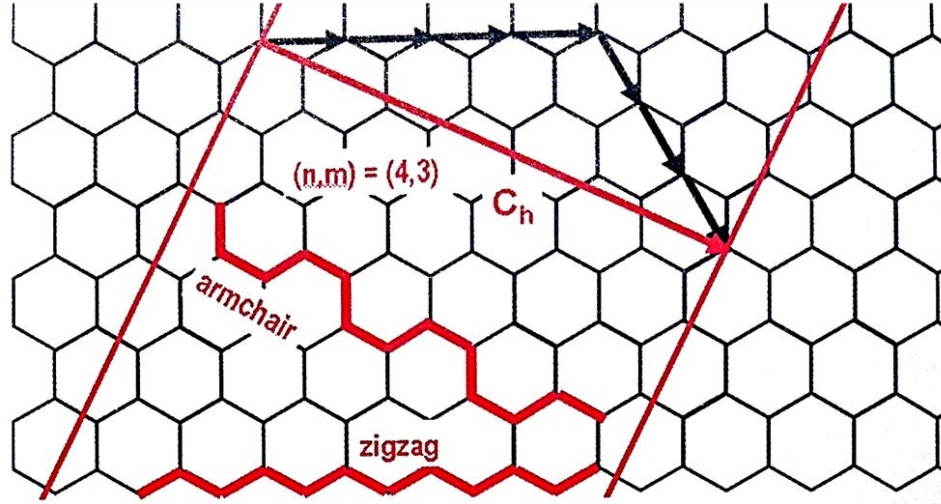


**Figure 2.1)** The index  $(n,m)$  determines the chirality of the CNT and the circumference  $C_h$ . The geometrical outline on the hexagonal lattice that forms a  $(4,3)$  CNT is depicted by the red parallel lines that must be rolled into seamless contact with each other. Examples of armchair and zigzag chiralities are also denoted on the hexagonal lattice. This figure was printed from Hierold, C., et al., Carbon Nanotube Devices: Properties, Modeling, Integration and Applications. Advanced Micro & Nanosystems, Vol. 8, Wiley-VCH, 2008<sup>[10]</sup>

The direction of the chiral vector  $C$  is described by the chiral angle:

$$\cos \theta = \frac{\mathbf{a}_1 \cdot \mathbf{c}}{|\mathbf{a}_1| |\mathbf{c}|} = \frac{n + \frac{m}{2}}{\sqrt{n^2 + nm + m^2}}. \quad (2.1).$$

The diameter of the tube is given by the length of the chiral vector:

$$d = \frac{|\mathbf{c}|}{\pi} = \frac{2.461}{\pi} \sqrt{n^2 + nm + m^2}. \quad (2.2).$$

The translational vector that is directed perpendicular to the chiral vector may be summarized by a translational period  $\mathbf{a}$  that is determined from the chiral indices  $(n,m)$  with  $p$  as their common divisor:

$$\mathbf{a} = \frac{2m+n}{p\mathcal{R}} \mathbf{a}_1 + \frac{2n+m}{p\mathcal{R}} \mathbf{a}_2 \quad (2.3)$$

where  $\mathfrak{R} = 3$  if  $(n - m)/3p$  is equal to an integer, and  $\mathfrak{R} = 1$  otherwise. The height of the rectangular unit cell of the carbon nanotube is thus determined by the magnitude of the translational vector and represents the translational period:

$$a = \frac{\sqrt{3(n^2+nm+m^2)}}{p\mathfrak{R}} a_0 \quad (2.4).$$

The number of carbon atoms in the unit cell of the nanotube  $n_c$  may be determined by the ratio of the cylindrical unit cell surface area to the area of the hexagonal graphene unit cell:

$$h_c = \frac{2(n^2+nm+m^2)}{p\mathfrak{R}} \quad (2.5).$$

Equation represents the number of graphene hexagons in the rectangular unit cell of a carbon nanotube. Since there are two carbon atoms in each graphene hexagon:

$$n_c = \frac{4(n^2+nm+m^2)}{p\mathfrak{R}} \quad (2.6).$$

The carbon nanotube diameter is also related to the quantity of concentric cylindrical cylinders that comprise the structure. Nanotubes composed of one wall are referred to as single-walled carbon nanotubes (SWNTs) and typically have diameters less than 2 nm with lengths that reach into the millimeter range.<sup>[11,12]</sup> Nanotubes with multiple concentric walls in their structure are referred to as multi-walled carbon nanotubes (MWNTs) and exhibit a range of diameters that depend on the exact wall number of the MWNTs.

### 2.1.2 Carbon nanotube electrical properties

The Brillouin zone of SWNTs may be determined from the unit cell, which we may compare to the hexagonal first Brillouin zone of graphene displayed in Figure 2.2. The reciprocal lattice vector corresponds to the translational period  $a$  along the tube axis

(z-axis) with a continuous length  $k_z = 2\pi/a$ . The length of the reciprocal lattice vector along the circumferential axis may be calculated from a zone folding scheme, which gives the following condition: the wave vector  $\mathbf{k}_c$  must have a phase shift of an integer multiple of  $2\pi$  or else it will vanish by interference.

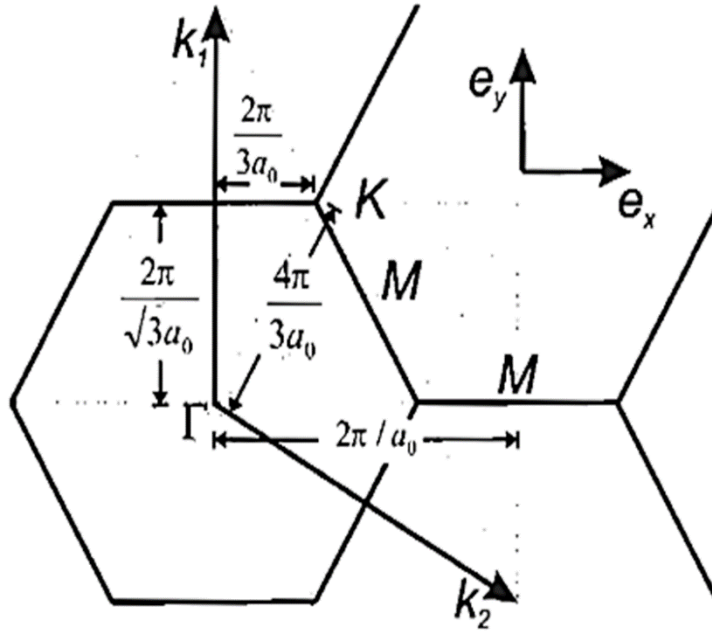


**Figure 2.2)** Hexagonal Brillouin zone of graphene with the high- symmetry points  $\Gamma$ ,  $K$ , and  $M$ , and the reciprocal lattice vectors  $\mathbf{k}_1$  and  $\mathbf{k}_2$ . This figure is printed from Reich, S. et al. Carbon Nanotubes: Basic Properties and Physical Concepts, Wiley-VCH, 2004.<sup>[13]</sup>

The length of the reciprocal lattice vector is thus:

$$k_c = \frac{2\pi}{|c|} \cdot q = \frac{2}{d} \cdot q \quad (2.7)$$

where  $q$  represents an integer bounded by the number of atoms  $n_c$  in the unit cell (since four atoms are required to define a wavelength,  $q \leq n_c/4$  or  $q \leq h_c/2$ ).

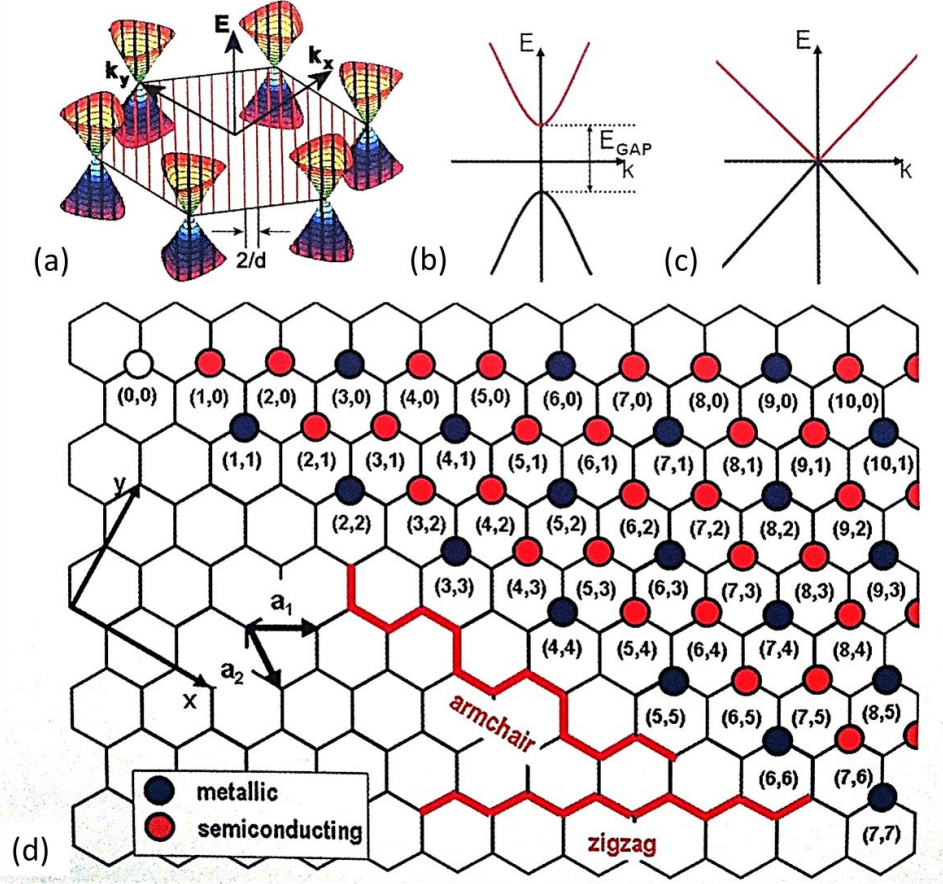


**Figure 2.3** (a) The band structure of graphene from hexagonal cones in the vicinity of the Fermi energy, which is cut into slices of allowed states when rolled graphene is rolled into carbon nanotubes. The resulting band structure of the nanotubes is (b) semiconducting or (c) metallic. (d) The determination of whether a tube is semiconducting or metallic may be made based on the chiral indices  $(n,m)$  of the nanotube.<sup>[10]</sup>

Since the reciprocal lattice vector length around the circumference is quantized by  $q$ , the first Brillouin zone possesses  $h_c$  allowed states along the tube axis demarked by parallel lines spaced  $2/d$  apart in Figure 2.3(a). These lines intersect the allowed wave vectors in the hexagonal first Brillouin zone, which determines whether the nanotube is metallic or semiconducting; if the allowed states do not intersect the  $K$  points there is a bandgap at the Fermi level and the nanotube is a semiconductor (Figure 2.3(b)), if the allowed states intersect the  $K$  points the nanotube is metallic (Figure 2.3(c)). Since the line spacing of

the allowed states is  $2/d$ , the bandgap in semiconducting tubes depends on the diameter. The intersection of allowed states with the  $K$  points is determined by the chiral indices  $(n,m)$ , as illustrated in the Figure 2.3(d). If  $(n - m)/3$  is an integer then allowed  $k_z$  states intersect the  $K$  points and the nanotube is metallic. If  $(n - m)/3$  is not an integer the allowed  $k_z$  states do not intersect the  $K$  points, and the nanotube is semiconducting.

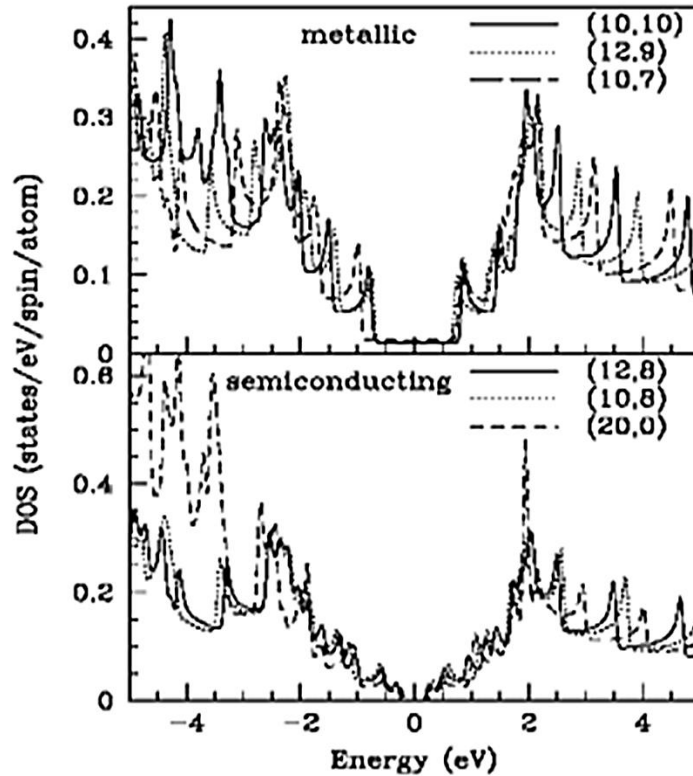


**Figure 2.4)** Ab initio calculation of electronic bandstructure for metallic and semiconducting nanotubes with varying chiralities, which demonstrates the close symmetry of the density of states (DOS) on either side of the Fermi energy. This figure was printed from A. Rubio, Spectroscopic Properties and STM Images of Carbon Nanotubes, Appl. Phys. A 68, 275,1999.<sup>[14]</sup>

The band structure for carbon nanotubes is uniquely different than that for graphene. The energy bands in a two-dimensional solid such as graphene appear as a step-function, where in one-dimensional solids such as nanotubes the bands diverge as

the inverse square of the energy. A band diagram for metallic and semiconducting tubes is demonstrated in Figure 2.4. The equation for the density of states of a carbon nanotube is:

$$g(E, E_q) = \begin{cases} \frac{|E|}{\sqrt{(E^2 - E_q^2)}}, & |E| > |E_q| \\ 0, & |E| < |E_q| \end{cases} \quad (2.8)$$

where  $E$  is the energy state and  $E_q$  is the permitted energy state as determined by the permitted wave vectors  $\mathbf{k}_c \cdot \mathbf{C} = 2\pi q$ . At  $E_q = 0$  we arrive at  $g(E, 0) = 1$ , which refers to metallic tubes and bands that cross at the Fermi energy. All other  $E_q$  for which the density of states peaks, which are referred to as van-Hove singularities, correspond to the diameter of the nanotube:

$$E_q = \frac{ia_0\gamma_0}{\sqrt{3}d} \quad (2.9)$$

where  $i$  represents integers corresponding to metallic (1,3,6...) and semiconducting (1,2,4,5,7...) tubes.

In applications for current collectors in batteries, or simply as conductive electrodes, metallic nanotubes are preferred to semiconductors. The conditions that dictate what chiral indices pertain to metallic tubes predict a third of SWNTs in a nanotube growth yield will be metallic. The structural symmetry of armchair nanotubes ( $n = m$ ) enables the ballistic transport of charges.<sup>[15]</sup> Since MWNTs consist of a range of diameters and chiralities coaxial to each other, the permitted energy states overlap and quench any band gaps formed by semiconducting tubes in the structure. Multi-walled nanotubes with large wall numbers and diameters consequently exhibit metallic behavior; however, the charge flow across a MWNT remains on the outer most tube. Nanotubes

with larger diameters do not exhibit ballistic transport and possess a higher density of scattering phenomena in the carbon lattice that dissipates the charge flow.

### 2.1.3 Carbon nanotube optical properties

Although there are many optical techniques to investigate the structure of carbon nanotubes, Raman spectroscopy is the primary method used in this thesis.

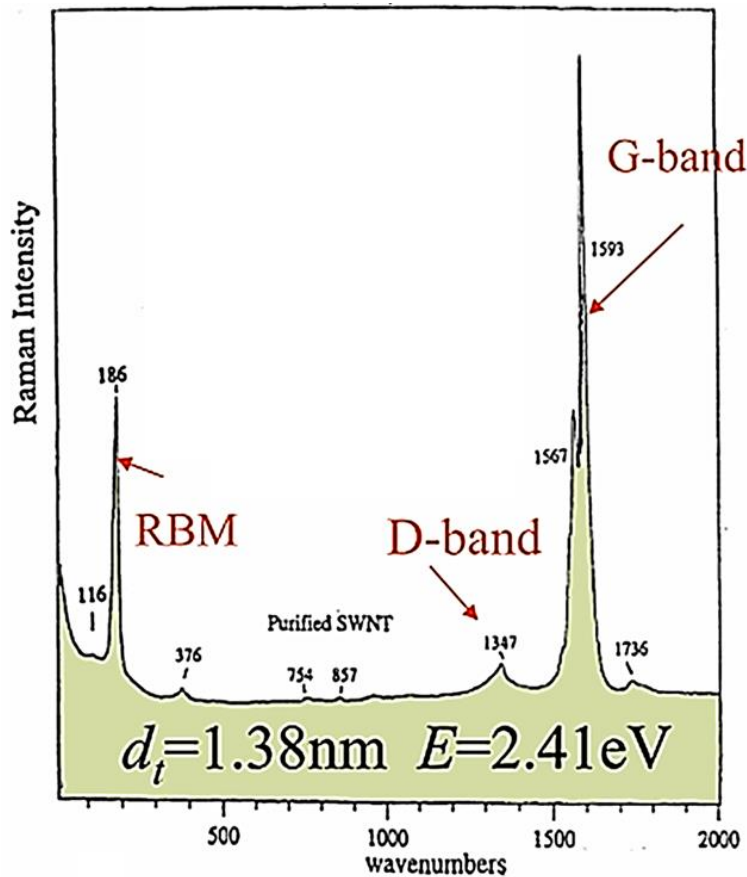


**Figure 2.5)** A Raman spectrum of a single walled nanotube with a diameter of 1.38 nm with the characteristic wavenumbers where peaks representing the RBM, D-band, and G-band are found. This figure is printed from A. M. Rao et al., Science, 1997.<sup>[16]</sup>

Raman spectroscopy measures the inelastic scattering of light by carbon nanotubes. The mechanism of a scattering event is as follows: (1) an electron is excited from the valence energy band to the conduction energy band by absorbing a photon, (2) the excited



electron is scattered by emitting (or absorbing) phonons, and (3) the electron relaxes to the valence band by emitting a photon.<sup>[17]</sup> A Raman scattering spectra is created by plotting the intensity of scattered light as a function of the loss in energy of the scattered frequency from the incident frequency, which diagrams the phonon frequencies of the material. A typical Raman spectrum for a carbon nanotube sample is demonstrated by Figure 2.5.

The most dominant features in Raman spectra of carbon nanotubes, as depicted in the Figure 2.5, are the radial breathing mode (RBM) peaks, the graphitic band (G-band), and the disordered carbon band (D-band) as well as the second overtone of the D-band (G'). The RBM peaks correspond to the vibration of carbon atoms in the radial direction, and occur at frequencies between 120-350  $\text{cm}^{-1}$  for SWNTs with diameters in the range of  $0.7 \text{ nm} < d < 2 \text{ nm}$ . For isolated SWNTs, the relation between the diameter and the RBM peak is reported as  $\omega_{RBM} = 248/d$ .<sup>[18]</sup> This relationship is not accurate for larger diameter SWNTs where the RBM peaks are weak, and for MWNTs where the atomic vibrations from the inner walls convolute the spectra in this frequency range. The G-band represents the tangential mode vibrations of the carbon atoms within the hexagonal lattice along the nanotube, and may contain peaks around 1582  $\text{cm}^{-1}$  that are characteristic of the graphitic structure of the nanotubes. The D-band represents the disorder-induced mode in the graphitic lattice at 1350  $\text{cm}^{-1}$  with its second harmonic G' occurring at roughly twice the D-band frequency. The ratio of the intensities of the D-band and the G-band ( $I_G / I_D$ ) quantifies a metric used to compare the graphitic quality of carbon nanotubes.

## 2.2 Carbon nanotube electrode fabrication

### 2.2.1 Carbon nanotube synthesis

The three primary methods to form CNTs are arc-discharge, laser ablation, and chemical vapor deposition (CVD). The arc-discharge method for forming CNTs involves passing a high current through two graphitic probes to create a spark between them. This causes carbon atoms to disintegrate from the probe discharging the spark due to the high temperatures, and reorder themselves into various carbon nanostructures including CNTs onto a catalyst between the probes. The laser ablation method involves heating a graphitic target in a chamber with a pulsed laser. This causes carbon atoms to disintegrate and reorder into carbon nanostructures including CNTs at cooler areas in the chamber. Compared to these methods, CVD enables the greatest quantity of CNTs to be fabricated per each growth yield and limits the percent of carbonaceous impurities (fullerenes, graphene, and amorphous carbon) in the yield as well. This is due to greater control over the carbon source decomposition and recrystallization into CNTs.

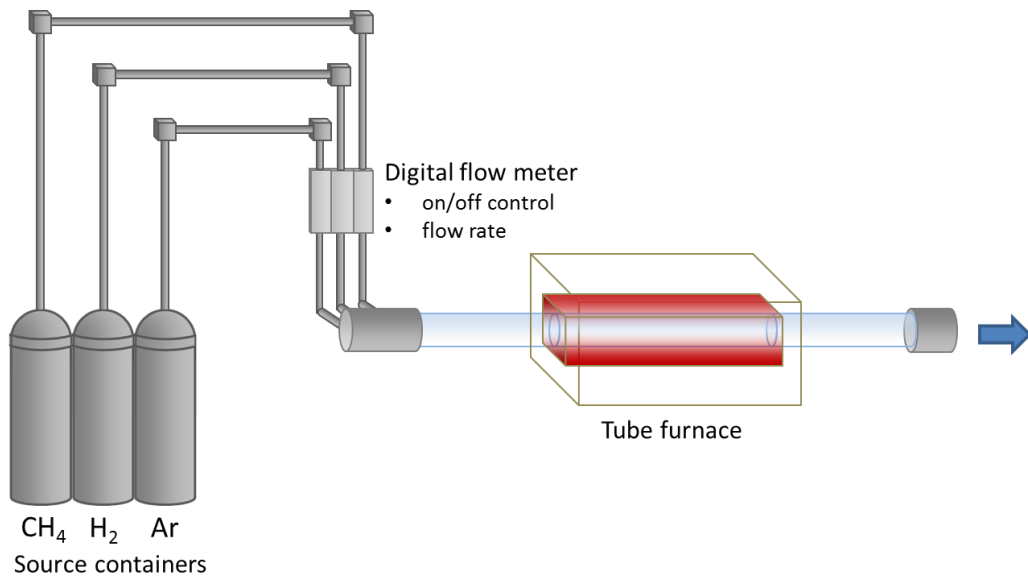


**Figure 2.6)** Chemical vapor deposition tube furnace setup for growth of carbon nanotubes described in this chapter. The carbon feedstock gas ( $\text{CH}_4$ ), carrier gas (Ar), and ramping gas ( $\text{H}_2$ ) are controlled by digital flow meters that monitor the flow rates into the tube furnace. The furnace hosts a quartz tube with a 2-inch diameter with three heating zones. The exhaust from the tube furnace is channeled to a glove box ventilator in the laboratory.

Chemical vapor deposition growth of CNTs is performed in a tube furnace where a carbonaceous gas source is fed to a catalyst with a carrier in a hot environment. A schematic of a typical CVD setup is depicted in Figure 2.6. The CVD growth process is most commonly described by a vapor-liquid-solid mechanism, although an exact description is still unknown.<sup>[68-71]</sup> During the CVD process, solid metal catalysts melt into nanoparticles in the tube furnace upon heating it to the growth temperature in a hydrogen gas environment. After reaching the growth temperature the carbon source is carried into the chamber by an inert gas. The carbonaceous gas will then decompose through pyrolysis into carbon atoms that absorb into the melted catalyst particles. Carbon atoms will continue to absorb into the catalyst particles until reaching a solubility limit at which carbon will then precipitate out. The precipitating carbon atoms form  $\text{sp}^2$  bonds that nucleate CNT growth, which is energetically favorable since ideal nanotubes lack dangling bonds that exist in single graphene layers. This growth continues until the carbon source is quenched and the temperature in the tube furnace is ramped down.

The key parameters that affect the growth yield during CVD and the CNT properties may be separated into two categories: the catalyst properties and the growth conditions in the tube furnace.<sup>[19]</sup> Typical catalysts are composed of Fe, Ni, or Co due to high solubility of carbon in these metals at high temperatures and a high diffusion rate in these metals which enables carbon to quickly precipitate to the particle surface at its

saturation limit. Molybdenum ions may also be added to supplement the production of carbon nanotubes by generating intermediate aromatic species from the carbon source that may contribute to nanotube growth.<sup>[20]</sup> Although the catalyst metals may be sputtered onto a surface to propagate unidirectional growth, a magnesium oxide (MgO) powder may be used as a support to disperse the metal ions and to provide greater surface area for the decomposition of carbon and consequently greater carbon nanotube yields during CVD.<sup>[72]</sup> Although other porous supports may be used such as silica or alumina, MgO may be removed from the growth yield with a simple nitric or hydrochloric acid treatment while silica and alumina require a more dangerous treatment with hydrofluoric acid to be removed. Catalysts that incorporate a MgO support follow a “base-growth” mechanism, where the CNTs propagate out of catalyst particles that remain rooted in the MgO support.

The CVD growth parameters greatly affect the mechanism for which carbon decomposes and precipitates out of the catalyst particles. Higher temperatures, higher gas flow rates, and larger ratios of source to carrier during gas flow attribute to higher decomposition rates of carbon.<sup>[21]</sup> Higher decomposition rates of carbon typically attribute to the formation of single walled carbon nanotubes with smaller diameters. This is because greater rates of carbon feeding to the catalyst stabilize smaller nucleation sites of precipitating carbon that are typically less energetically favorable than larger graphitic caps. Larger rates of carbon decomposition also result in the formation of greater percentages of amorphous carbon or non-tubular graphitic species, which results in more extensive measures to extract CNTs from the CVD growth yield such as thermal or chemical purification methods. The source gas also affects the rate of carbon

decomposition. Methane (CH<sub>4</sub>) may be used as the CVD carbon feeding source gas for both multi-walled and single-walled nanotubes with distinct advantages in both growth procedures; methane generates fewer carbonaceous impurities than acetylene (C<sub>2</sub>H<sub>2</sub>) due to the less rapid production of carbon atoms and is safer than carbon monoxide (CO). The carbon nanotube syntheses included in the reports of this thesis use a CVD procedure with methane as the carbon source.

### 2.2.2 Percolation theory

The percolation theory predicts the following relationship between the conductivity of a film with respect to the density of conducting channels in the three-dimensional network:

$$\sigma \propto (N - N_c)^\alpha \quad (2.10)$$

where  $\sigma$  represents the three-dimensional conductivity,  $\alpha$  represents the conductivity exponent,  $N$  represents the density of conducting channels in the network, and  $N_c$  represents the critical density for percolation of charge across the three-dimensional network.<sup>[22]</sup> For a random distribution of conducting channels, the critical density is given by:

$$l\sqrt{\pi N_c} = 4.236 \quad (2.11)$$

where  $l$  is the length of each conducting channel. We gather from Equation 2.10 and Equation 2.11 that efficient charge percolation across the conductive network is achieved by properly tuning the dimensions of the individual nanomaterials and by forming a high density of conducting channels. Although the sheet resistance of the films with a nanomaterial density at the percolation threshold  $N_c$  is relatively high, increasing the number of channels beyond the threshold dramatically lowers it.<sup>[23]</sup> This behavior is

typical for networks where the contact resistance  $R_s$  across the conducting “sticks” is significantly lower than the resistance  $R_j$  across the junctions, such as with Ag NW and CNT networks.<sup>[24]</sup> The relation between the conductivity and the channel density is theorized as Equation 1 with  $\alpha \approx 1.3 - 2$  when the density of channels is  $N_c < N < 2N_c$ . The conductivity exponent  $\alpha$  depends on the ratio  $\frac{R_j}{R_s}$  as well as the length of the nanomaterials; larger  $\frac{R_j}{R_s}$  values and longer lengths form conductivity exponents that more closely approach  $\alpha = 2$ .<sup>[24-26]</sup> As we see from Equation 2.11, longer channel lengths also decrease the critical number density  $N_c$  of nanomaterials necessary to interconnect them into a conductive network within a fixed electrode volume. Thus the nanomaterial lengths dictate the connectivity of the conducting channels across the network, which is described by the number of conducting channels and the number of junctions necessary to form a complete percolative network.

An additional metric that further elucidates the impact the length has on the sheet resistance of a percolative nanomaterial network is the area fraction:

$$A_F = NlD \quad (2.12)$$

where  $N$  is the nanomaterial number density,  $l$  is the length of the nanomaterials, and  $D$  is the nanomaterial diameter.<sup>[23,27]</sup> Mutiso et al. demonstrates in Figure 2.7 that at a fixed nanomaterial diameter  $D$  and area fraction  $A_F$ , lower sheet resistances are achieved at greater nanomaterial lengths  $l$ .<sup>[27]</sup> Additional studies theoretically and experimentally demonstrate that larger conducting channel lengths contribute to thin-films with a lower sheet resistance.<sup>[165]</sup> This is directly related to the formation of a percolation network with fewer contacts between channels, which contributes to a lower resistance to charges traveling across the network.<sup>[25]</sup>

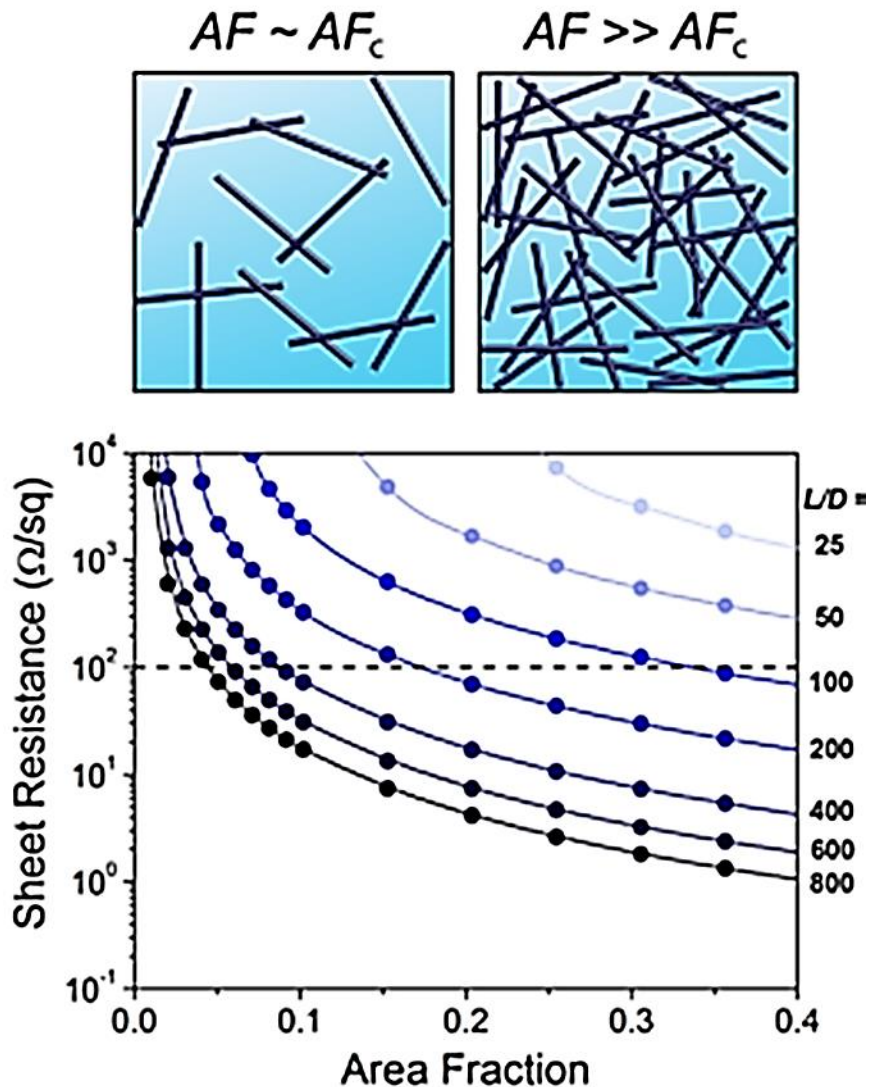


**Figure 2.7)** Sheet resistance as a function of the aspect ratio ( $L/D$ ) and area fraction of rods in nanowire films with a constant diameter of  $D = 50$  nm with an average contact resistance of  $R_c = 2$  k $\Omega$ . The top schematic illustrates two percolation networks of monodisperse rods with nanowire area fractions at or above the area fraction critical limit for percolation ( $AF_c$ ). This figure was printed from Mutiso et al., ACS Nano, 2013<sup>[27]</sup>

Even at large number densities within the percolation region, networks consisting of long nanomaterials demonstrate smaller sheet resistances due to fewer channel junctions required to complete the charge transport across the network, as illustrated in Figure 2.8.

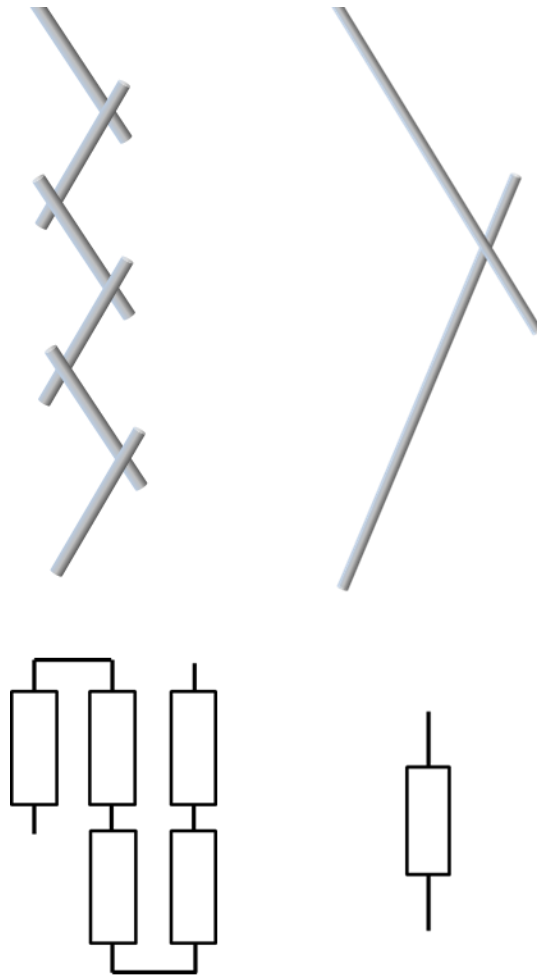


**Figure 2.8)** Schematic of a six fiber structure with relatively small aspect ratio and a two fiber structure with a relatively high aspect ratio. It is assumed that the contact resistance dominates the percolation across each structure, with the distance the charges travel assumed equal. The corresponding resistor representation of each structure is found below the fiber configuration.<sup>[25]</sup>

It is further reported that nanomaterials agglomerated into bundles act as singular nanomaterials with larger diameters than the individual structures. This coagulation of the nanomaterials reduces the number of parallel conducting channels across the percolation network, and increases the sheet resistance of the electrode.<sup>[28,29]</sup>



### 2.2.3 Carbon nanotube ink formation

As we discussed in Section 2.2.2, percolation networks have the highest conductivity when the conducting channels are at the highest aspect ratio and are uniformly dispersed across the electrode. Carbon nanotubes possess many attractive van der Waals forces inherent to their graphitic structure and aspect ratio; therefore, carbon nanotubes exhibit a strong propensity to agglomerate into bundles with diameters much larger than the individual tubes during their synthesis. Dispersing these bundles in solution is important for preserving the optimal high aspect ratio of the carbon nanotubes and the percolation network uniformity in the electrode.<sup>[28]</sup>

The techniques to disperse CNTs in solution may be separated into two categories: mechanical and chemical processes. The most popular mechanical method is ultra-sonication of the CNT solution. Ultra-sonicators generate acoustic waves in the ink solution that form bubbles on the surface of the CNT bundles, and the cavitation of these bubbles releases energy that expel individual nanotubes from the bundles.<sup>[30-32]</sup> Ultra-sonication may generate the acoustic waves in a water bath or at greater amplitudes with a vibrating probe. Ultra-sonication only temporarily separates the exfoliated nanotubes once the acoustic waves are removed from the ink solution if there is nothing to oppose the van der Waals forces from recombining the nanotubes into bundles.<sup>[33]</sup>

Additional measures that permanently separate the exfoliated nanotubes in solution are introduced through two chemical methods: the addition of a surfactant polymer to the CNT solution and the attachment of functional groups to the surface of the CNTs. Surfactants are polar polymers that form micelles around the individual carbon nanotubes or intercalate themselves between the carbon nanotubes in solution, which

causes the separation and repulsion of CNTs from one another in solution. Typical surfactant molecules used in ink solutions are sodium dodecyl sulfate (SDS), sodium dodecyl benzene sulfonate (SDBS), and hexadecyltrimethylammonium bromide (CTAB).<sup>[34]</sup> The dispersion of CNTs by surfactants in solution are stable for long periods of time and enable very uniform coatings.

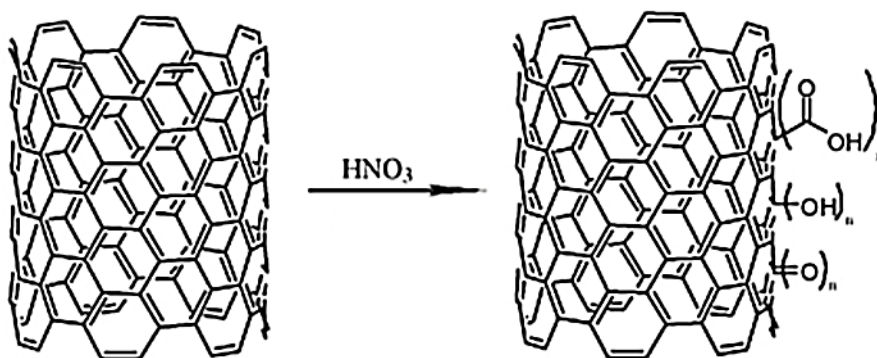


**Figure 2.9)** A schematic diagramming the surface functional groups attached to the nanotube surface during a nitric acid ( $\text{HNO}_3$ ) reflux, including carboxyl groups ( $-\text{COOH}$ ), carbonyl groups ( $\text{C}=\text{O}$ ), and hydroxyl groups ( $-\text{OH}$ ).

Another chemical method is to attach functional groups to the surface of carbon nanotube outer walls. This is most commonly conducted by boiling the carbon nanotubes in a strongly acidic ( $\text{HCl}$ ,  $\text{HNO}_3$ ,  $\text{HSO}_4$ ) aqueous solution. In the acid reflux, oxygen groups covalently bond with carbon at open sites on the nanotube surface, as seen in Figure 2.9. These sites either exist as preexisting lattice defects, tube end caps, or where strained carbon bonds were broken during the acid reflux.<sup>[35]</sup> The acid reflux attaches carboxyl ( $\text{COOH}$ ) groups to the sidewalls of the carbon nanotubes, which ionize in an aqueous solution to enhance the electrostatic potential around each nanotube. The resulting repulsive forces between the electronegative carbon nanotube surfaces in solution stabilize the nanotube suspension without the presence of a surfactant Since the

degree of strain in the curved carbon lattice scales inversely with tube diameter, SWNTs are more reactive to sidewall functionalization than MWNTs.<sup>[36]</sup> Despite the lower intrinsic reactivity than SWNTs, MWNTs typically have a greater density of defects across the lattice structure, which act as openings for surface functionalization. The attachment of surface functional groups, however, is predicated on the presence of defect sites or the destruction of carbon bonds in the nanotube lattice to enable carboxyl bonds to form. Sustained acid refluxing therefore inflicts damage to the nanotube lattice of the outer shell that disrupts their intrinsic conductivity and builds amorphous carbon deposits in the solution.<sup>[37]</sup>

Fourier transform infrared spectroscopy (FTIR) is often used to characterize the efficacy of an acid reflux to attach functional groups to the nanotube sidewall.<sup>[38]</sup> FTIR measurements are taken by splitting a broad infrared source with an interferometer incident on a sample, and then deciphering the absorption/transmission spectra from the interference pattern via a Fourier transform by the device software. The peaks in an FTIR absorption spectrum indicate unique chemical bonds in the sample with vibrational modes that match optical frequencies emitted by the infrared source, as seen in Figure 2.10. Several studies have investigated and confirmed characteristic absorption peaks that are representative of carbon bonds in the lattice, hydroxyl bonds formed at defect sites or with amorphous carbon, and carboxyl bonds formed after an acid reflux.<sup>[39,40]</sup>

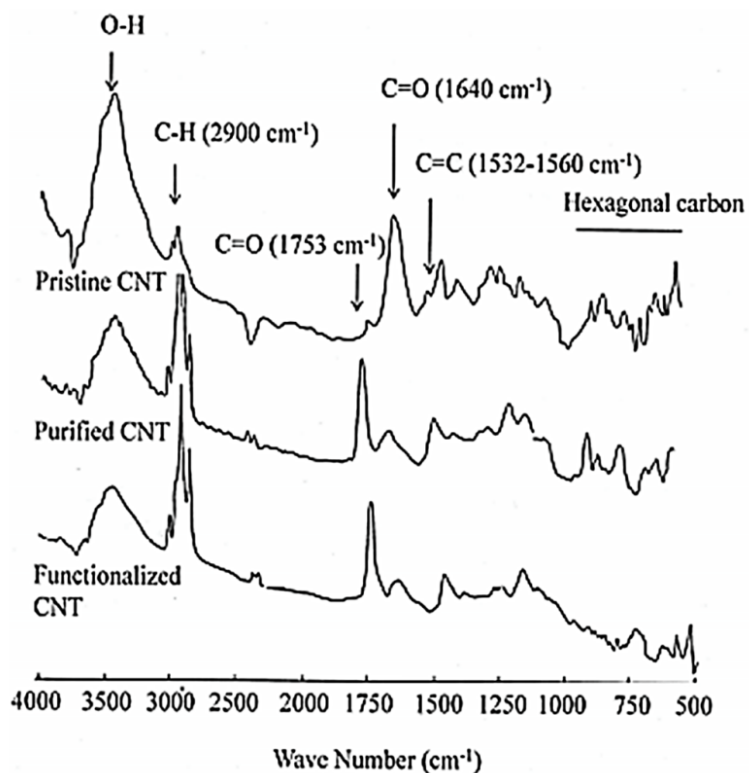


**Figure 2.10)** Attenuated total reflectance FTIR absorption spectra of pristine multi-walled nanotubes, purified multi-walled nanotubes after thermal oxidation, and acid treated multi-walled nanotubes. The characteristic peaks of oxygenated graphene groups by the acid reflux are labeled along with the corresponding wavenumber. This image is printed from. R. Yudianti et al., Carbon, 2011.<sup>[38]</sup>

#### 2.2.4 Carbon nanotube electrode formation

Conducting electrodes may be formed by carbon nanotube networks through various ink deposition methods such as Meyer rod coating, vacuum filtrations, ink-jet printing, spin coating, and dip coating. Spray-coating is an additional deposition method with the following advantages: (1) enables highly precise coating patterns, (2) capable of uniformly coating large surface areas, and (3) not restricted to flat coating surfaces.<sup>[41,42]</sup> A schematic of a spray-coating setup is depicted in Figure 2.11.

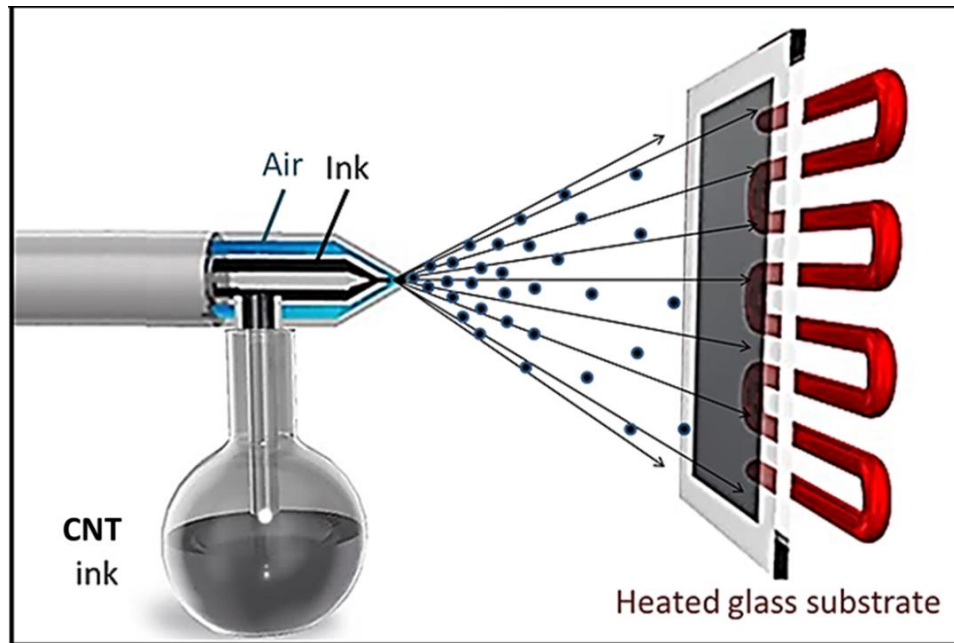


**Figure 2.11)** A schematic illustrating a spray coating mechanism of a carbon nanotube ink onto a heated glass substrate with an airbrush. The air brush atomizes a carbon nanotube solution at a fixed air pressure of approximately 200 psi and a fixed distance of approximately 4 inches from the substrate surface heated by a hot plate. The pressure and distance from the surface determine the droplet size that deposits on the glass while the ink solvent and surface temperature determine the evaporation rate of the ink coating.

The coating properties are primarily determined by the ink parameters; the ink solvent, the nanotube concentration in the ink, and the dispersion forces between the nanotubes in solution.<sup>[42]</sup> Solvents that form droplets with low surface tension are preferable for spray-coatings because they enable better wetting of the substrate. Droplets with a high surface tension also evaporate faster at the edges, which leads to the flow of solvent from the middle of a droplet to the edges in pursuit of thermal equilibrium. This leaves rings of coagulated carbon nanotubes on the coated surface, which compromises the uniformity of the random carbon nanotube network.<sup>[43]</sup> Inks that have higher concentrations of carbon nanotubes also prevent coagulation due to faster evaporation of the solvent from the film coating.

The amount of resistance to nanotubes agglomerating within the droplets during drying is also determined by the strength of permanent dispersion forces applied in the ink making process. Although surfactant polymers are effective stabilizers of carbon nanotube dispersion in solution, they are insulating and disrupt the charge percolation across the nanotube network, and therefore must be removed from the electrodes after deposition.<sup>[44,45]</sup> Current methods to remove surfactants from deposited electrodes are not entirely effective and often damage the film coating.<sup>[46]</sup> Inks of surface functionalized carbon nanotubes do not form electrodes with disruptive impurities that need to be removed, yet are typically more stable in dilute solutions.<sup>[47]</sup> Forming stable carbon nanotube ink solutions and fabricating uniform spray-coatings, therefore, require independent parameterization to optimize the conductivity of carbon nanotube electrodes.

### 2.3 Few-walled Carbon Nanotubes

The wall number of carbon nanotubes has a dramatic impact on their properties and thus on their fabrication into conductive percolation networks. In the case of single-walled carbon nanotubes, their small diameters and typically long lengths in CVD syntheses promote efficient percolation across a conductive network. The conductivity of this network also relies on the uniformity of the CNT network, which can be degraded when large nanotube bundles are present in the dispersion.<sup>[22]</sup> Spray coating is a uniquely precise and practical method for printing conformal thin films with large surface areas useful for lightweight and flexible electronics; uniform spray-coated CNT films are dependent on optimizing the ink stability of individual CNTs. In order to achieve stable CNT inks without the use of disruptive and insulating surfactants it is required to bind functional groups to the surface of carbon nanotube sidewalls to separate highly resistive

tube bundles and promote a homogenous ink dispersion.<sup>[37, 48-51]</sup> Since SWNTs consists of only one graphitic layer rolled into a cylinder, dispersing SWNTs in solution via surface functionalization requires cautious parameterization of the acid reflux concentration and duration. Typically the damage inflicted to the SWNT carbon lattice by the acid reflux renders a high density of structural defects that deteriorate the ballistic charge transport across the tube, and often digests long tubes into smaller sections. Multi-walled nanotubes offer robustness during an acid reflux that SWNTs lack; the outer walls host the surface functionalization while the inner walls remain intact. The aspect ratio of multi-walled carbon nanotubes is usually limited by a large outer-diameter (< 100 nm) that stunts its length during the CVD growth. Due to the higher graphitic surface area, the defect density in MWNTs is greater than SWNTs. The resistance across MWNTs is consequently greater than SWNTs because of a higher number of scattering phenomena across the outer wall. The sheet resistance across a percolative network of MWNTs is also greater due to the significantly lower aspect ratio than SWNTs. Also, surface functionalized CNTs are most easily dispersed in water or organic solvents,<sup>[51,52]</sup> but low vapor pressure solvents, like water, have a pronounced coffee-ring effect,<sup>[43]</sup> while fast-drying solvents are associated with toxic vapors that inhibit large-scale production.<sup>[42]</sup> The question remains, therefore, of how to form a stable CNT ink with an innocuous solvent without inhibiting the conductivity of spray-coated thin films.

Recent reports demonstrate that few-walled carbon nanotubes, defined as possessing a wall number between two and six, exhibit the robustness of multi-walled nanotubes while maintaining the optimal electrical conductivity and graphitic quality of single walled nanotubes.<sup>[39, 53-57]</sup> The electrical properties of FWNTs, furthermore, do not

diminish after surface functionalization of the outer tubes since the structural integrity of the inner tubes is unaltered. To further support the utility of the FWNT structure for spray-coated films, this study explores the relationships between the electrical conductivity of the spray-coated FWNT films, and the rheological properties of FWNTs dispersed in a surfactant-free ink solution. Here, we introduce a surfactant-free ink of surface functionalized FWNTs dispersed in pure isopropanol (IPA) that produces high conductivity spray-coated films.

#### 2.4 Experimental Method

A catalyst composed of nanoparticles with a Co:Mo:MgO composition of 1:0.5:100 is formed through a combustion synthesis,<sup>[56, 58]</sup> as depicted in Figure 2.12.

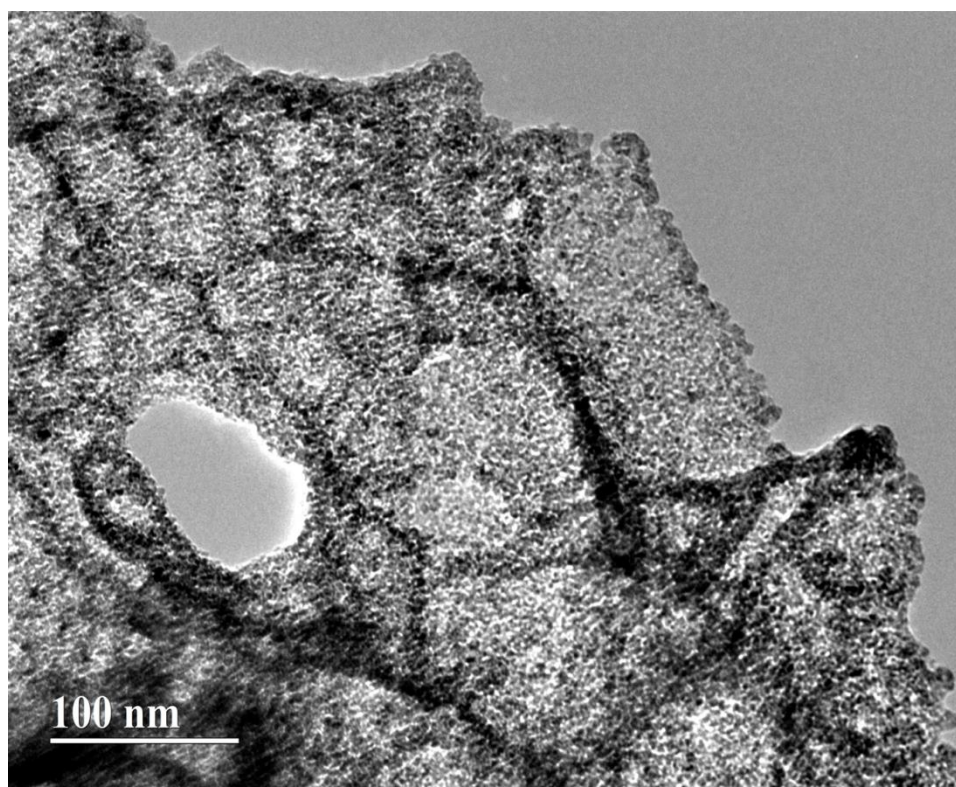


**Figure 2.12)** An image of the pink catalyst solution and the resulting brown powder catalyst after a combustion synthesis method.

The pink solution in Figure 2.12 is the liquid catalyst solution consisting of controlled concentrations of cobalt nitrate ( $\text{Co}(\text{NO}_3)_2$ ), ammonium molybdate ( $(\text{NH}_4)_2\text{MoO}_4$ ), magnesium nitrate ( $\text{MgNO}_3$ ), citric acid, and glycine. The formation of MgO particles



with imbedded Co:Mo nanoparticles is then facilitated via a glycine-nitrate combustion; the precursor solution is gradually heated to a combustion temperature, at which the solution erupts into the catalyst particles shown in Figure 2.12 as the brown powder. It is clear from this image that large yields of catalyst powder may be generated by each combustion synthesis. Catalyst particles are depicted in the transmission electron microscopy (TEM) images in Figure 2.13, which were taken with a JEOL 2100 LaB<sub>6</sub> TEM.



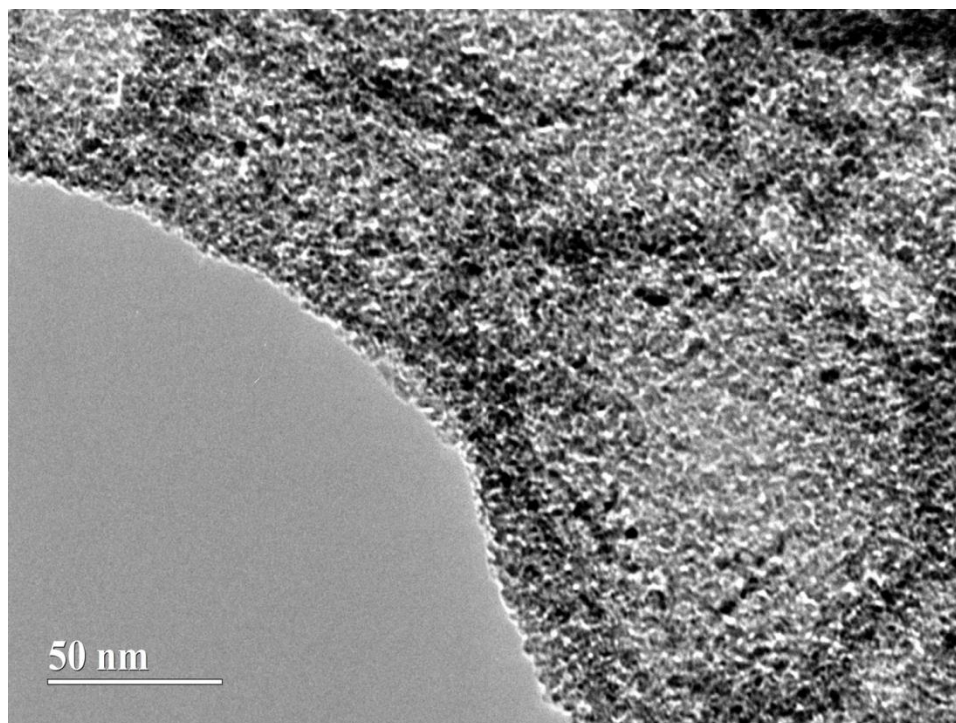


**Figure 2.13)** TEM images of powder catalyst particles at various magnifications.



**Figure 2.14)** An image of the powder catalyst inserted into the quartz boat that is inserted into the tube furnace for the chemical vapor deposition growth of carbon nanotubes.

It is clear from the TEM images in Figure 2.13 that the catalyst particles promote a high yield of carbon nanotubes by providing a high surface area for the decomposition of carbon during the CVD growth. The average catalyst nanoparticle size is less than 5 nm. Approximately 60-80 mg of the powder catalyst is loaded onto a 1-inch quartz boat and inserted into a tube furnace for each CVD growth of the FWNTs, as seen in Figure 2.14. The furnace is first ramped from room temp to 850 °C in H<sub>2</sub> and then held at a constant temperature of 850 °C for 45 min while a methane mixture is introduced at a flow rate of CH<sub>4</sub>/H<sub>2</sub> = 1600/400 sccm. After a growth time of 30min the furnace is cooled for 2hr to reach close to room temperature. The decomposition rate of carbon under these growth conditions oversaturates the catalyst particles, which enables the formation of nanotubes with diameters smaller than the catalyst particle by stabilizing smaller nucleation sites. This mechanism is depicted in Figure 2.15, as proposed by Qian et al.<sup>[56]</sup>

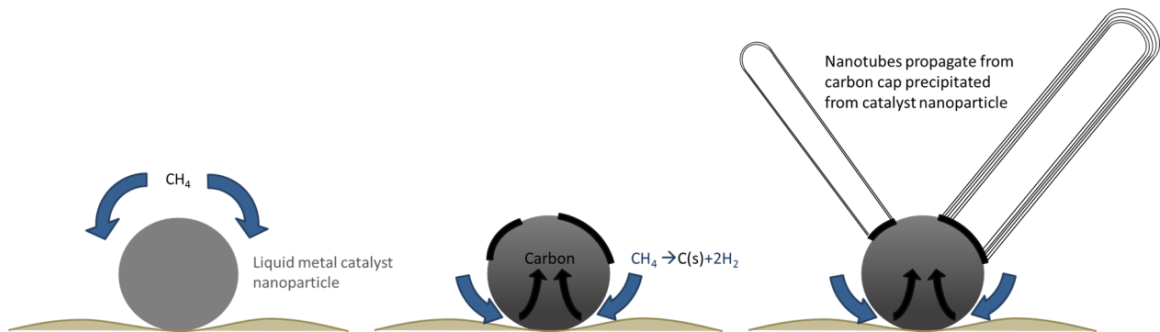
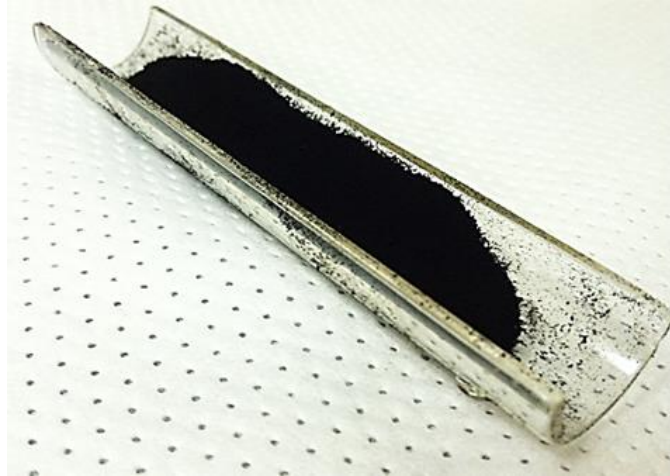


**Figure 2.15)** A schematic illustrating the base growth carbon decomposition process that enables the formation of FWNTs emanating from the catalyst particles: (a) melted metal nanoparticles embedded in a catalyst powder and are exposed to the carbon source; (b) carbon decomposes into metal nanoparticles from the pyrolysis of the hot methane gas during the CVD growth until the solubility limit of the metal nanoparticles is reached and carbon precipitates out into a graphitic cap on the catalyst particle; (c) carbon continues to precipitate out of nanoparticle to form nanotubes with diameters smaller than catalyst particle size, which are stabilized by the rapid decomposition of carbon into the catalyst and rapid diffusion through the nanoparticle. This mechanism explains the formation of FWNTs as opposed to larger diameter MWNTs.

## 2.5 Results and Discussion

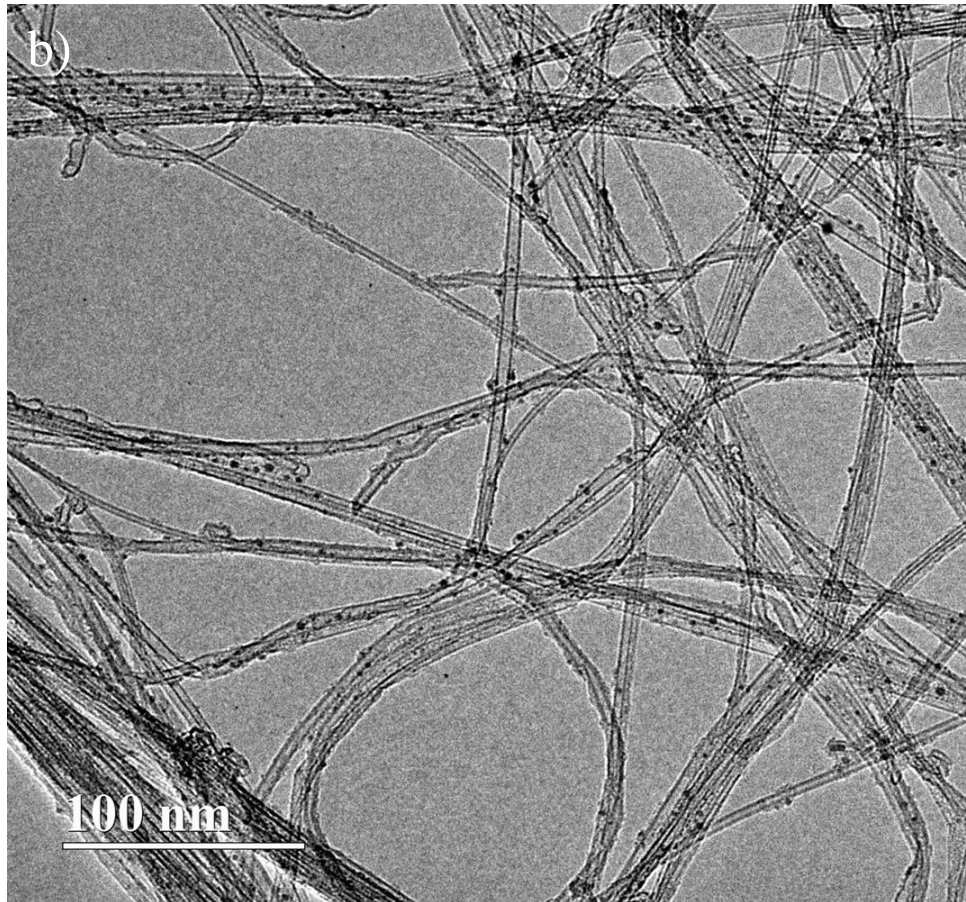
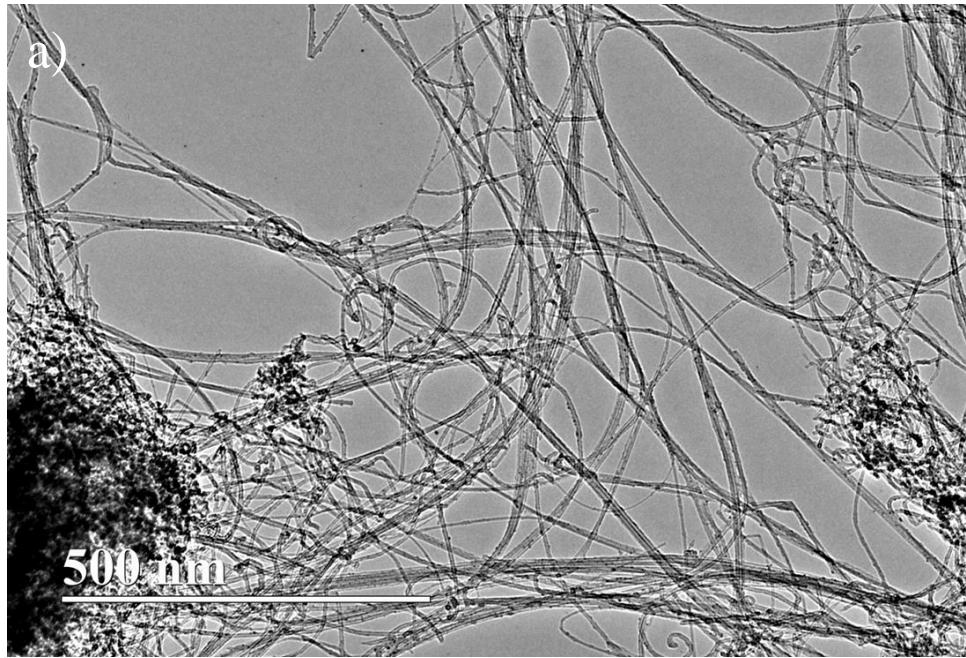
### 2.5.1 CVD growth yield of FWNTs

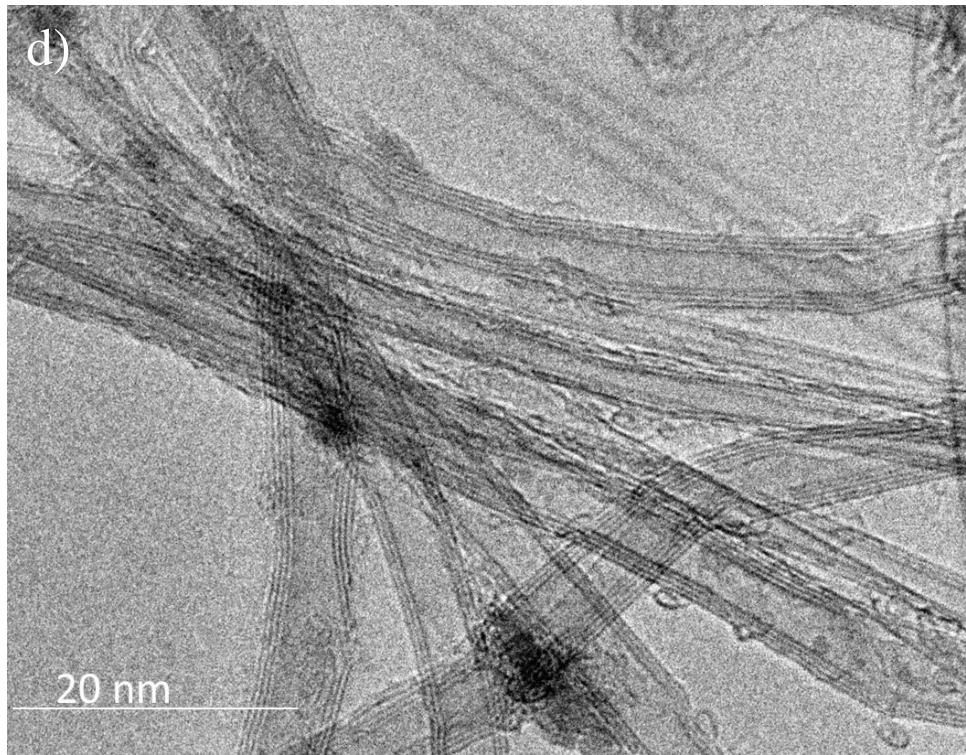
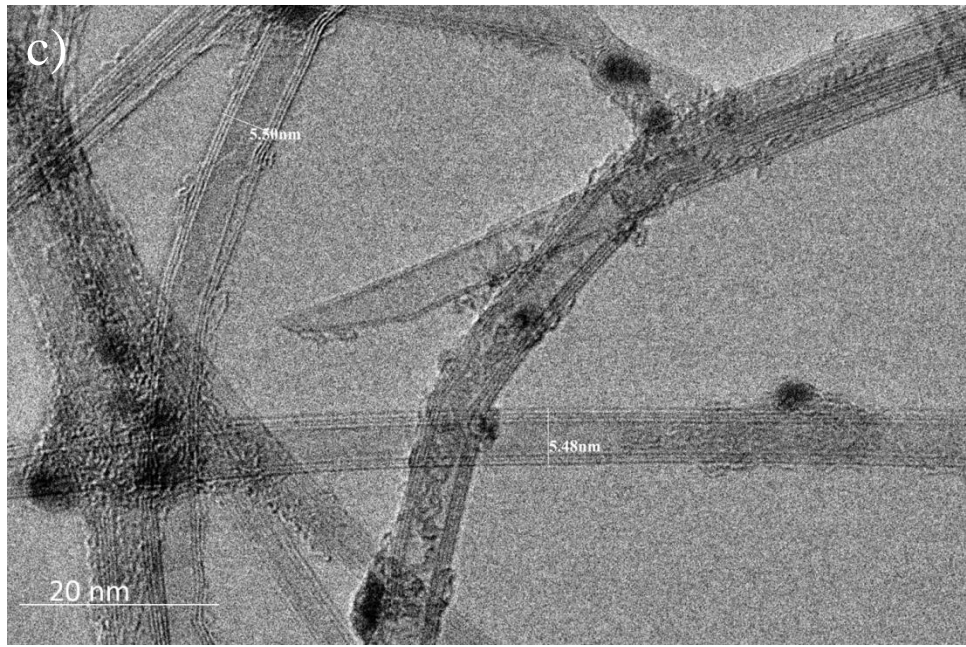
The CVD growth yield produced from the method outline in the previous section is pictured in Figure 2.16.



**Figure 2.16)** Pristine growth yield of the CVD process outlined in Section 2.4, which is visible by the transformation of the brown catalyst into a black powder composed of carbon nanotubes and amorphous carbon after the growth.

As compared to the image of the catalyst powder in Figure 2.12 and Figure 2.13, the resulting growth yield from the CVD process is clearly visible by the catalyst turning a solid black color. It should be noted that the brown catalyst particles are preserved in the growth yield; however, the CVD results in each particle to be encompassed by carbon nanostructures propagating out of the catalyst powder, resulting in the overall black color. Multiple TEM images of the growth yield at various magnifications are depicted in Figure 2.17.





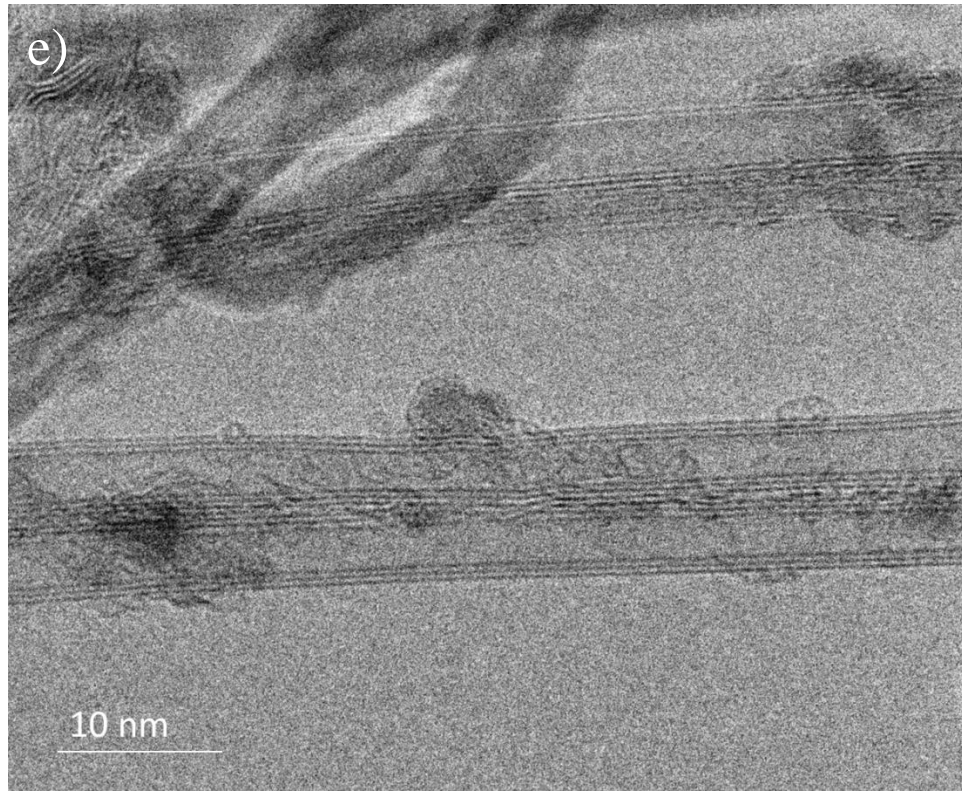


**Figure 2.17)** TEM images at various magnifications of pristine yield of CVD growth. The morphology, dispersion of wall numbers, and nanostructure of the resulting nanotubes is clearly depicted, as well as a presence of amorphous carbon that collects on the tube surface.

Figure 2.17(a) illustrates carbon nanotubes with a high aspect ratio propagating from a cluster of catalyst particles. Figure 2.17(b) demonstrates that although these nanotubes may coagulate into bundles of several nanotubes, evidence of individually separated nanotubes is clearly observable. These nanotubes clearly possess a high aspect ratio with few morphological characteristics such as kinks or sharp bends that indicate structural defects. Attached to the surface of the nanotubes are particles of amorphous carbon impurities that are also produced during the CVD growth. Figure 2.17(c-e) depict TEM images that clearly demonstrate the carbon nanotubes possess wall numbers between 2-5 with diameters between 4-8 nm. These FWNTs possess very few structural defects in the

form of kinks or vacancies in the graphitic structure, according to the TEM images in Figure 2.17. It may be concluded from these images, therefore, that the CVD growth process outlined in Section 2.4 is successful in fabricating FWNTs.

In order to eradicate the carbonaceous impurities in the CVD growth yield, an oxidation of the yield in the tube furnace may be conducted. Thermogravimetric analysis measures the mass loss versus time and temperature of a sample in an oxidizing environment like air, which may be used to visualize distinct structural phases such as amorphous carbon that are present in the final CVD growth yield. Figure 2.18 illustrates the mass loss spectrum after oxidizing the CVD growth yield depicted in Figure 2.16.

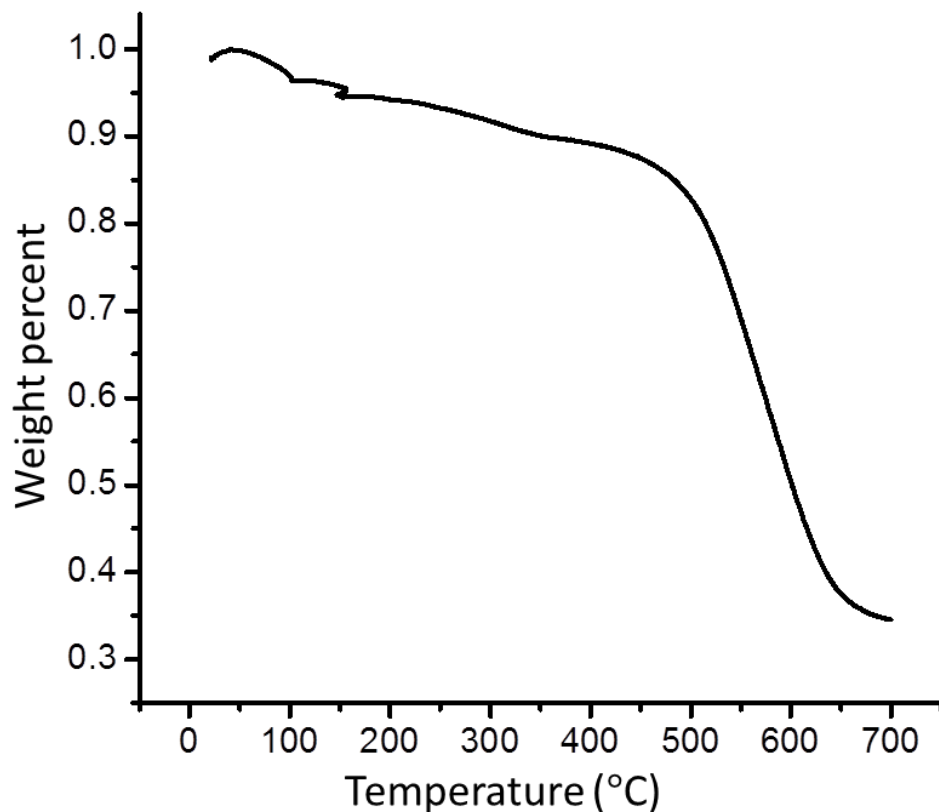


**Figure 2.18)** A thermogravimetric analysis spectrum of the pristine yield of the CVD growth, which was conducted in air by a Shimadzu TGA at a ramping rate of 2 °C per minute. The mass loss of the sample up to approximately 150 °C is due to the evaporation of water from the powder sample and due to the stabilization of the balance.



The mass loss spectrum in Figure 2.18 depicts specific carbon phases that oxidize at various temperature ranges. Up to approximately 150 °C we see an erratic mass loss regression, which is most likely due to the evaporation of water from the sample as well as a slight disruption in the linear temperature ramping. The distinct phase between 200-375 °C is due to amorphous carbon since it is less thermally stable than graphitic carbon. The major mass loss regression from 400-700 °C is due to the oxidation of carbon nanotubes. The remaining weight percent of the yield is due to the remaining catalyst that does not burn off during the temperature ramping. The composition of the CVD growth yield measured in Figure 2.18 is thus approximately 4 wt% water, 5 wt% amorphous carbon, 56 wt% graphitic carbon, and 35 wt% catalyst. According to this analysis the approximate weight percent of amorphous carbon with respect to the total carbon content in the growth yield is 8.2 wt%. The oxidation purification step of the growth yield was therefore conducted at 575 °C for 1 hr in the tube furnace in order to remove not only the amorphous carbon but any defective nanotubes or nanotube fragments that may be present in the growth yield.

### 2.5.2 IPA-based FWNT ink fabrication

After the as-grown FWNTs are thermally oxidized, a nitric acid (HNO<sub>3</sub>) reflux is conducted to dissolve the catalyst from the FWNT yield and to functionalize the outer walls of the FWNTs with carboxyl groups so that they may disperse in solution.<sup>[33,35,37,52]</sup> A schematic of the dispersion mechanism is illustrated in Figure 2.19.

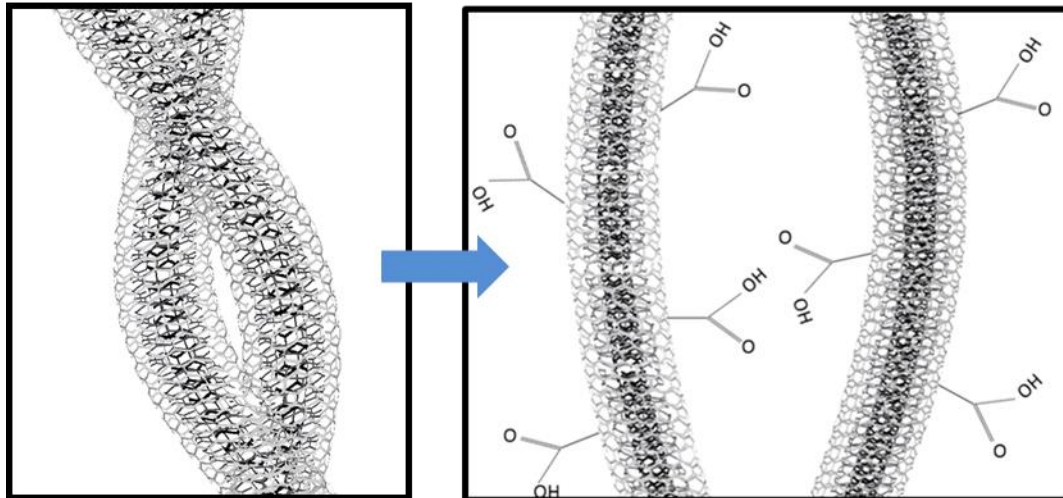


**Figure 2.19)** A schematic illustrating how bundled nanotubes may be dispersed by attaching carboxyl groups to their surface in order to counteract the intrinsic van der Waals forces.

In an aqueous solution, the carboxyl groups dissociate into  $\text{COO}^-$  on the sidewalls and  $\text{H}^+$  in solution, which would promote the formation of a double layer by aligning water molecule dipoles with the charged surface groups. Such double layers are a common path toward highly stable inks in aqueous solutions.<sup>[59]</sup> Water-based nanotube ink solutions, however, leave “coffee rings” and non-uniform coating layers when sprayed on substrates.<sup>[42,60]</sup> A scalable nanotube ink must be composed of a solvent that ensures a uniform spray-coating, yet also prevents nanotube agglomerations without the benefit of strong aqueous dipoles. Isopropanol is a volatile solvent with a lower toxicity than methanol or other organic solvents, and thus may operate as a high performance solvent for spray coating applications. Nevertheless, IPA retains a small molecular polarity, and the dispersion of nanotubes in IPA will depend on the quantity of attached surface charge groups and their effectiveness to align IPA’s weaker molecular dipoles. As depicted in the TEM images in Figure 2.17, the FWNTs grown from the CVD method are bundled together, but the functional groups added during the  $\text{HNO}_3$  reflux cause them to repel

each other and disperse homogenously in solution. The acid reflux setup is shown in Figure 2.20.



**Figure 2.20)** An image of the HNO<sub>3</sub> bath solution that hosts the acid reflux conducted to functionalize the surface of the carbon nanotubes.

Raman spectroscopy is a common method to characterize the FWNT growth quality and their purification, as well as to confirm the surface functionalization.<sup>[17,61]</sup> A Raman spectra comparison of the as-grown tubes and the purified tubes was conducted with an H-J-Y Microscope using a 633 nm laser, and is presented in Figure 2.20.

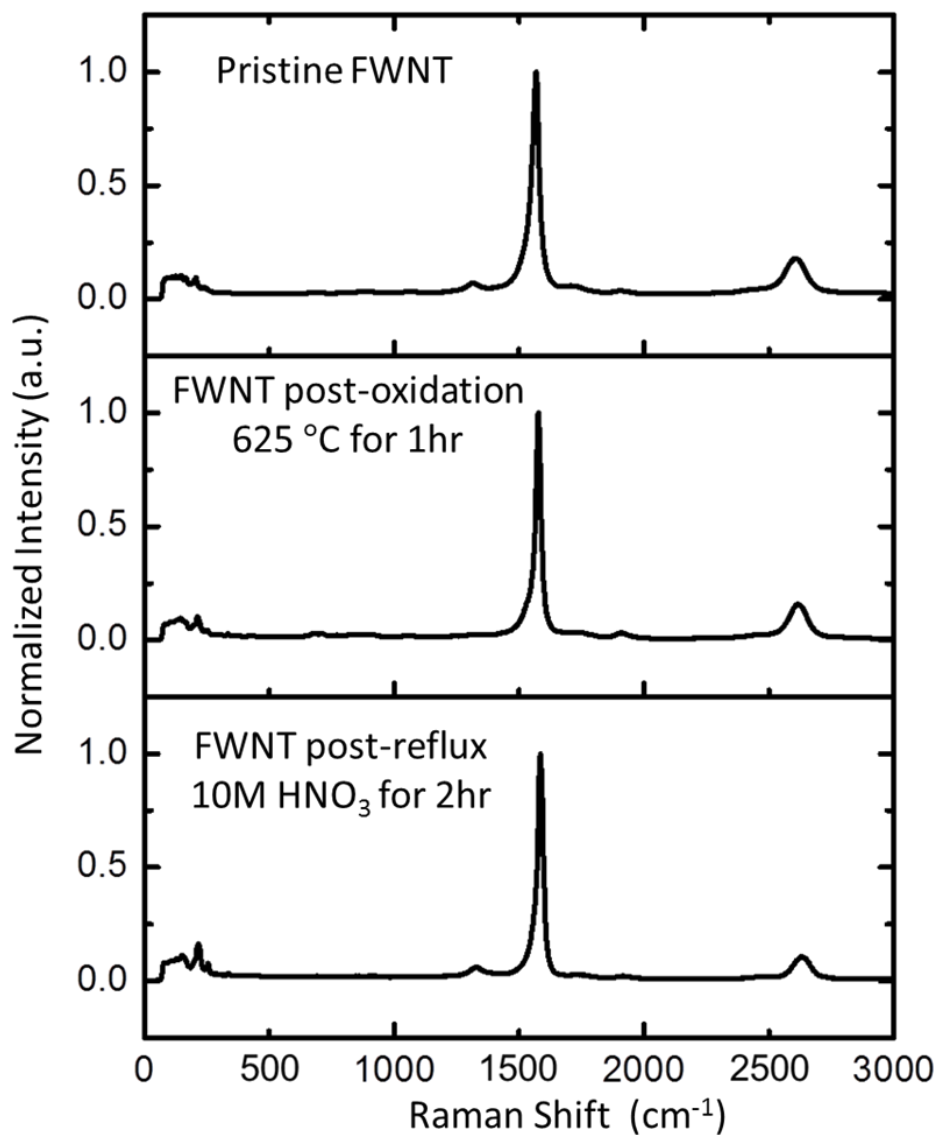


**Figure 2.21)** Raman spectra of carbon nanotube samples immediately after the CVD growth, after purification of the growth yield by thermal oxidation, and after the purified nanotube yield is refluxed in HNO<sub>3</sub>.

As we see in Figure 2.21, the as-grown FWNT samples display a low intensity ratio ( $I_D/I_G = 0.071$ ) between the disordered carbon band (D-band) at  $\sim 1317 \text{ cm}^{-1}$  and the graphitic carbon band (G-band) at  $\sim 1575 \text{ cm}^{-1}$ . This further confirms the CVD process yields high purity CNTs with few structural defects or impurities, as indicated by the TEM images. Upon thermally oxidizing the as-grown FWNT samples at  $625 \text{ }^\circ\text{C}$ , a

decrease in the intensity of the D-band is observed while the G-band remains strong ( $I_D/I_G = 0.025$ ), which together confirm the selective elimination of the amorphous carbon originating from the CVD growth. The D-band intensity increases again once the oxidized FWNTs are refluxed in  $\text{HNO}_3$ . The reemergence of the D-band is caused by the introduction of defects to the outer walls when  $\text{C}=\text{C}$  covalent bonds break and allow carboxyl groups ( $\text{COOH}$ ) to form during surface functionalization with  $\text{HNO}_3$ . The  $I_D/I_G$  ratio remains lower than the as-grown yield after the acid reflux ( $I_D/I_G = 0.061$ ). This implies that the graphitic structure of the FWNTs is not compromised by the surface functionalization because the inner-tubes remain structurally intact. Each Raman spectrum in Figure 2.21 is normalized relative to its G-band intensity. There are also slight shifts in the radial breathing modes (RBMs,  $100\text{-}300\text{ cm}^{-1}$ ), first after thermally oxidizing the as-grown tubes, and then again after refluxing the purified tubes in acid, but determining a conclusive explanation for these shifts is beyond the scope of this study due to the complicated nature of RBMs in multi-walled tubes.<sup>[28,30]</sup>

Further examination of the surface functionalization is conducted through Fourier transform infrared spectroscopy, which elucidates the covalent bonds present in the FWNT sample. Figure 2.22 presents the FTIR absorption spectrum of the  $\text{HNO}_3$  refluxed FWNTs taken with an Attenuated Total Reflection (ATR) measurement by a Thermo Nicolet FT-Raman Spectrometer.

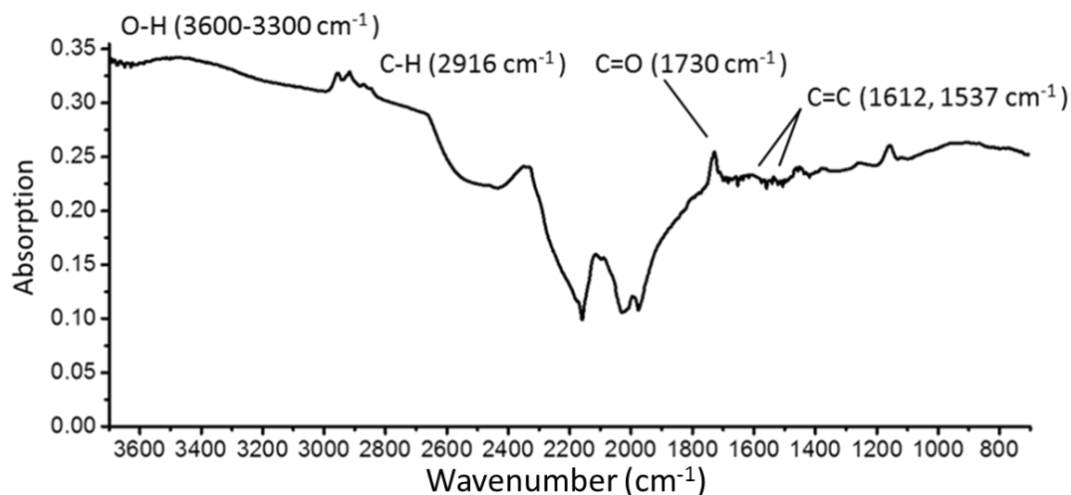
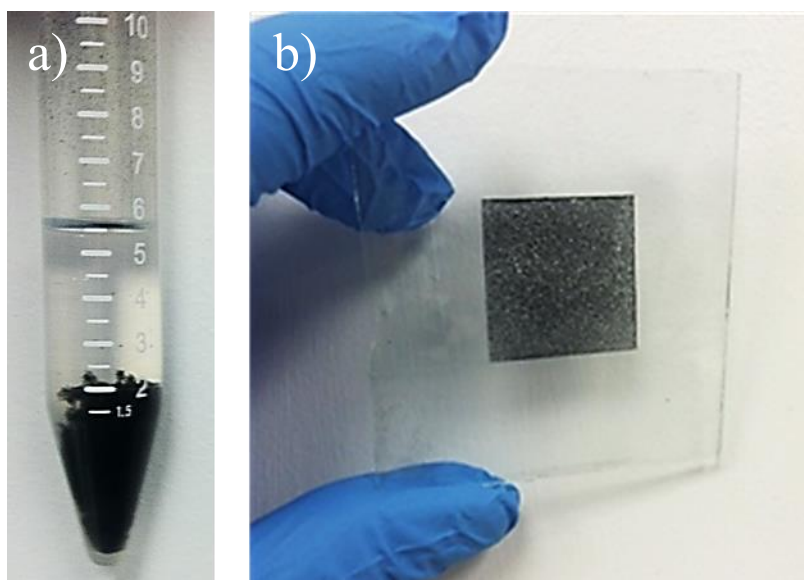


**Figure 2.22)** A FTIR spectrum of the HNO<sub>3</sub> refluxed nanotubes with the characteristic peaks of successful surface functionalization of carboxyl groups to the outer walls labeled.

An Attenuated Total Reflection of the Fourier Transform Infrared Spectrum (ATR-FTIR) is a technique that utilizes an evanescent wave formed by the total internal reflection by a crystal with a high refractive index such as germanium (Ge) that hosts a powdered sample. This specific technique is helpful for measuring the absorption spectrum of highly absorbing samples due to the small penetration depth of the incident beam into the sample. It is clear from Figure 2.22 that the refluxed FWNTs contain peaks characteristic of carboxyl (C=O) bonds and hydroxyl bonds (O-H), characteristic of the HNO<sub>3</sub> surface functionalization illustrated in the schematic in Figure 2.19. The presence of vibrational phonon modes that correspond with graphitic sp<sup>2</sup> carbon bonds (C=C) is similarly present.<sup>[37,38]</sup> A peak is also present around ~ 2100 cm<sup>-1</sup> due to the ambient environment containing water and CO<sub>2</sub>.<sup>[39,40]</sup> The presence of these characteristic peaks in the FTIR spectrum verifies the successful functionalization of the surface of the FWNTs during the HNO<sub>3</sub> reflux.

### 2.5.3 Comparing ink dispersion properties to spray-coated film properties

Each refluxed FWNT bath solution was filtered with over 500 mL of deionized (DI) water, and then the FWNTs were dispersed in IPA at high concentrations ( $\sim 0.6$  mg/mL) via bath sonication and short periods of probe sonication. The resulting inks were spray-coated with an airbrush (A470M airbrush at 200 kPa of argon) onto 100 mm<sup>2</sup> area on a cleaned glass substrate heated to 120 °C. Each film thickness is set below 1  $\mu$ m based on the ink concentration and volume of ink sprayed on the fixed area. Examples of as-grown FWNT dispersions in IPA and FWNTs functionalized with carboxyl groups through a HNO<sub>3</sub> reflux and then dispersed in IPA are illustrated in Figure 2.23 and Figure 2.24, respectively.



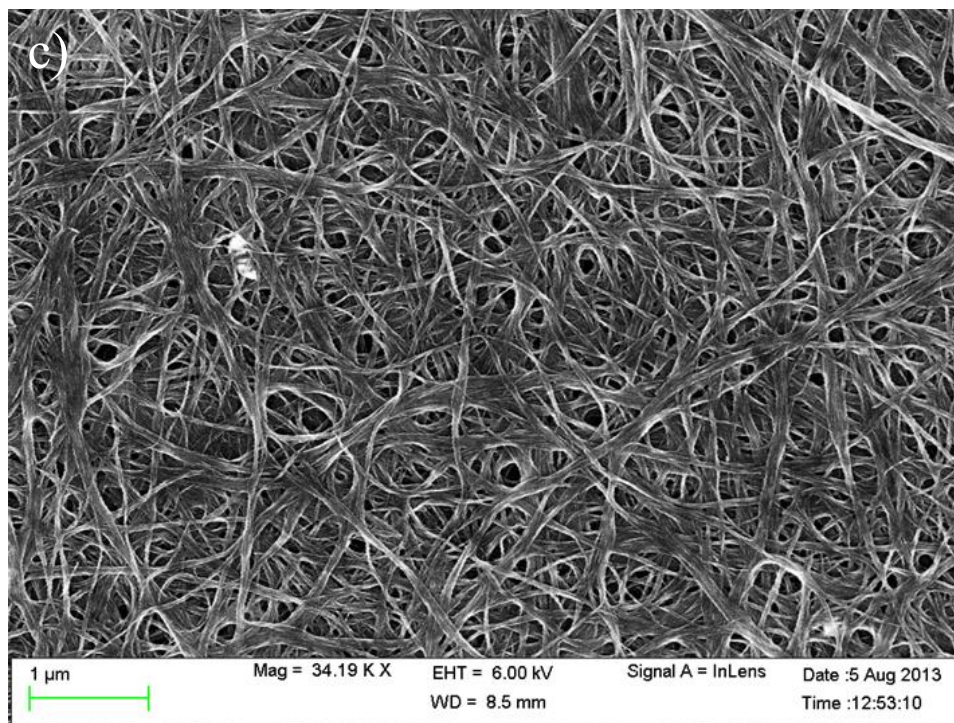


**Figure 2.23** (a) An as-grown FWNT suspension in IPA at 0.6 mg/mL, (b) an example of a spray-coated FWNT film from an as-grown FWNT suspension in IPA, and (c) a spray-coated as-grown FWNT film surface.

We see in Figure 2.23(a) that as-grown tubes aggregate and settle to the bottom of the solution at a concentration of 0.6 mg/mL, resulting in a poor dispersion of the FWNTs. Spray-coating 20-30 mL of the FWNT ink subsequently forms films that are not uniform, as pictured in Figure 2.23(b). The inhomogeneous film coating results in a porous network of aggregated nanotubes, which limits the percolation across the film. These aggregates are further visualized at the microscopic level with a scanning electron microscope (SEM) in Figure 2.23(c). All spray-coated films are imaged with a Hitachi SU-70 SEM. Nanotubes grouped into bundles reaching hundreds of nanometers in diameter are clearly observable in the SEM images of the non-uniform spray-coated films



formed from inks composed of as-grown FWNTs, which limits the conductivity based on the high contact resistance of these bundled

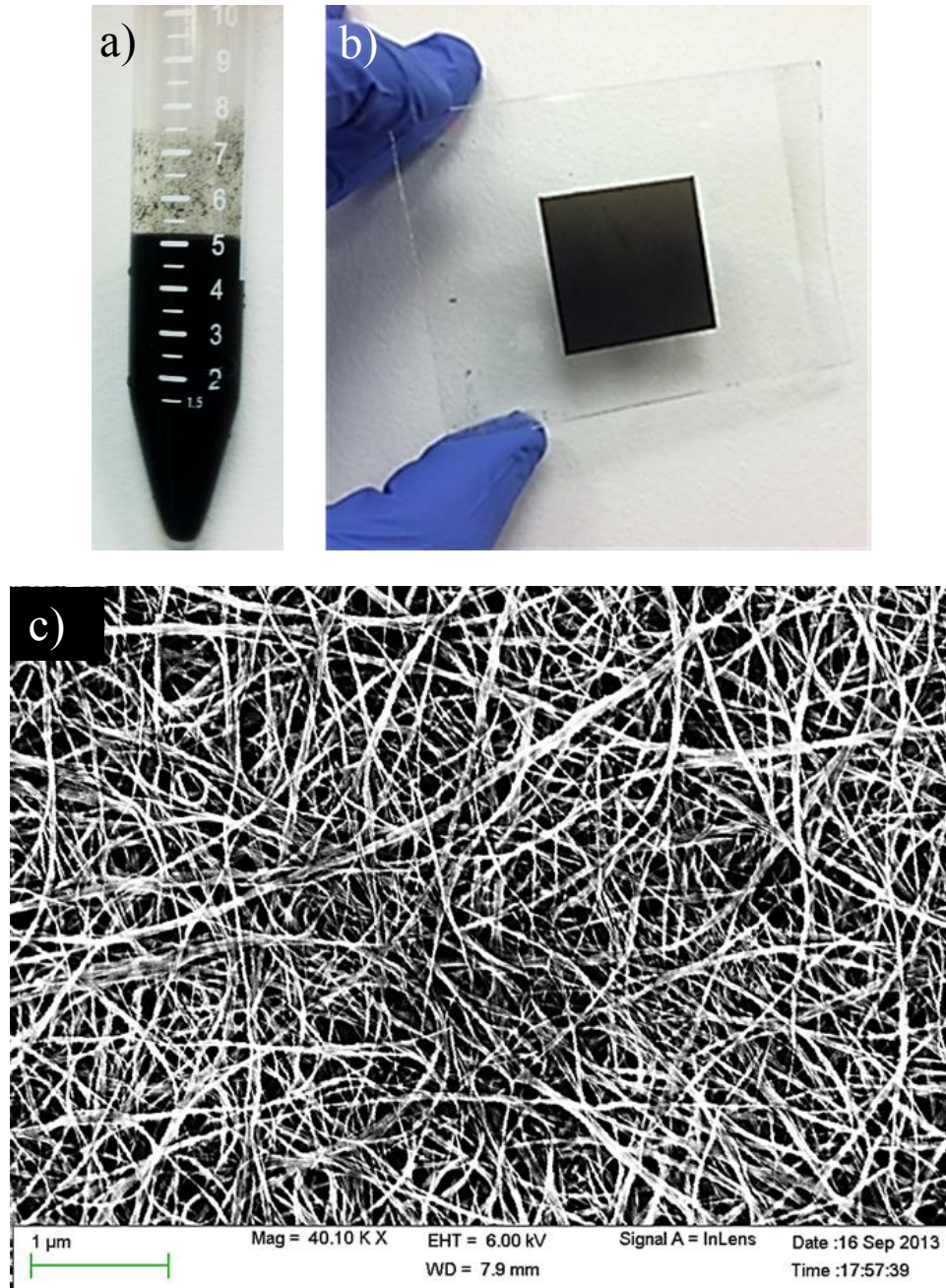


**Figure 2.24)** (a) A functionalized FWNT suspension in IPA at 0.6 mg/mL, (b) an example of a spray-coated FWNT film from a functionalized FWNT suspension in IPA, and (c) a spray-coated functionalized FWNT film surface.

Figure 2.24(a) demonstrates that once the FWNTs are refluxed in 10M HNO<sub>3</sub> for 2hr and then dispersed in IPA, they remain suspended in solution at the same concentration as Figure 2.23(a). This is significant since a colloidal dispersion is achieved at a high concentration, despite the IPA solvent possessing a weak polarity. Achieving a stable dispersion in a volatile solvent with low toxicity enables highly uniform films, shown in Figure 2.24(b), after spray coating the same volume of FWNT ink as shown in Figure 2.23(b). Figure 2.24(c) illustrates an SEM image of a spray-coated film formed from the ink composed of the functionalized FWNT in IPA that displays a uniform network of exfoliated nanotubes. From a comparison of the images of films formed from the two solutions at equal FWNT mass concentrations in IPA, it is thus apparent that functionalized tubes form inks with higher colloidal stability and consequentially more uniform spray coating with fewer resistive bundles.

In order to quantify the dispersive quality of the FWNT inks in solution, the zeta-potential was measured with a dynamic light scattering setup in a Malvern Zetasizer, as illustrated in Figure 2.25.

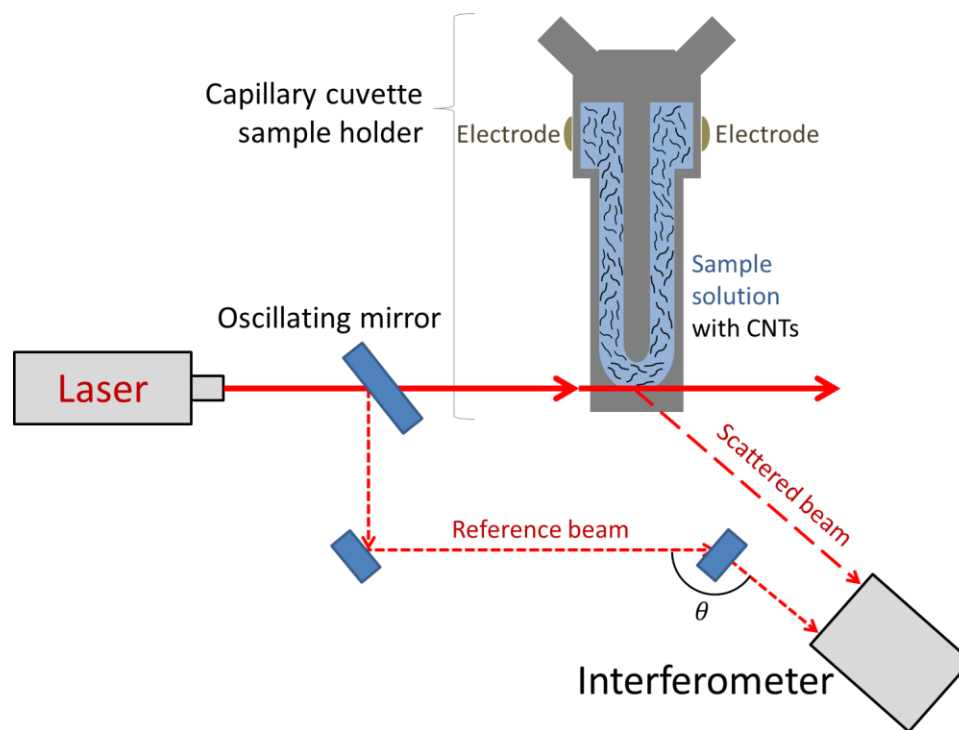


**Figure 2.25)** A schematic of the dynamic light scattering setup within a Malvern Zetasizer. An incident laser pulsed by a mirror oscillating at 320 Hz is scattered by the nanotubes in the dilute solution hosted within the capillary chamber of the sample cuvette. The scattered beam is combined with the pulsed reference beam redirected by the oscillating mirror at an interferometer, which determines the shift in frequency between the scattered and reference beam. The motion of nanotubes is controlled by their response to an electric field applied by the cuvette electrodes, which rapidly fluctuates to generate numerous mobility measurements that are automatically averaged by the Malvern Zetasizer software.

Few-walled nanotubes that are refluxed in  $\text{HNO}_3$  possess carboxyl groups on the surface of their outer walls, which deprotonate in an aqueous solution to form an electrostatic surface potential on the functionalized FWNTs. In the presence of an external electric field, electrostatic repulsion to the negative electrode and simultaneous attraction to the positive electrode induces a force that causes the nanotubes to flow in solution. The electrophoretic velocity of the individual nanotubes in the applied electric field is thus directly related to the strength of their electrostatic field, which consequently offers a useful mechanism to examine the strength of the repulsive forces between the FWNTs in

solution after surface functionalization. The dynamic light scattering experiment diagrammed in Figure 2.25 measures the electrophoretic velocity of the nanotubes flowing to the positive terminal. The positive terminal quickly alternates between the two cuvette electrodes to prevent the nanotubes from agglomerating at one area during the measurement. An incident beam pulsed at a fixed frequency of 320 Hz by an oscillating mirror is scattered by the moving nanotubes, which shifts the frequency of the scattered beam from the incident beam. This frequency shift of the scattered beam from the incident beam is extracted from an interference pattern collected from a reference beam redirected by the oscillating mirror that combines with the scattered beam at a detector. The relation between the shift in frequency ( $\Delta f$ ) and the electrophoretic velocity ( $v$ ) of the nanotubes in solution is given by Equation 2.13:

$$\Delta f = \frac{2v \sin\left(\frac{180-\theta}{2}\right)}{\lambda} \quad (2.13)$$

where  $\lambda = 632.8 \text{ nm}$  is the laser wavelength and  $\theta$  is the scattering angle detected. The electrophoretic velocity that is derived from the frequency shift measurement may be related to the electrophoretic mobility ( $\mu$ ) of the nanotubes, which describes their responsiveness to an applied field:

$$\mu = \frac{v}{E} \quad (2.14)$$

where  $E$  is the magnitude of the applied electric field.

After the surface functionalized FWNTs ionize in water, they emanate an electrostatic field that aligns the dipoles of highly polar solvent molecules like water at a distance directly related to the field strength. The electrophoretic mobility of the nanotubes is related to the electrostatic potential at a spatial boundary at a distance where the solvent molecules cease to be affected by the potential field of the nanotubes. The

strength of the electrostatic potential at this spatial boundary is representative of the dispersive strength between the nanotubes in solution, and is referred to as the zeta-potential ( $\zeta$ ). The zeta-potential is affected by the surface potential of the nanostructures, the polarity of the solvent molecules, and the concentration of the nanostructures in solution. A greater surface potential of the nanostructures and solvent molecules with a higher polarity attribute to stronger repulsive forces between the nanostructures in solution, and thus greater zeta-potentials; however, higher concentrations of nanostructures in solution attribute to smaller spatial separation enabled by the solvent molecules, which lowers reflects in lower zeta-potentials.

The relation between the zeta-potential and electrophoretic mobility of nanostructures in solution has been studied vigorously and theorized for multiple systems.<sup>[52, 62-64]</sup> The Malvern Zetasizer used in this study derives the zeta-potential from the Henry function:<sup>[65, 66]</sup>

$$\mu = \frac{2}{3} \frac{\epsilon \epsilon_0 \zeta}{\eta} F(\kappa d) \quad (2.15)$$

where  $\epsilon$  is the relative permittivity of the solvent,  $\epsilon_0$  is the vacuum permittivity, and  $\eta$  is the solution viscosity. The correction factor  $F(\kappa d)$  is dependent on the Debye length ( $\kappa$ ) and radius of the nanostructure ( $d$ ) where  $\kappa d$  is the ratio of the nanostructure radius to the Debye length. The correction factor reduces the Henry function to two approximations:

$$\mu = \frac{\epsilon \epsilon_0 \zeta}{\eta}; \kappa d \gg 1 \quad (2.16)$$

$$\mu = \frac{2}{3} \frac{\epsilon \epsilon_0 \zeta}{\eta}; \kappa d \ll 1 \quad (2.17).$$

Equation 2.16 represents the Smoluchowski approximation, which is representative of electrophoretic mobility in polar solutions. Equation 2.17 represents the Hunkel approximation, which is representative of electrophoretic mobility in non-polar solutions.

In order to measure the electrophoretic velocity of each individual nanotube, the sample solutions are highly dilute aqueous solutions ( $wt\% \ll 0.01\%$ ). The low concentration of nanotubes in solution helps prevent them from agglomerating during the electrophoretic velocity measurement and the high polarity of the water molecules allows the alignment of the solvent dipoles in the electrostatic potential field of the nanotubes. Samples prepared for zeta-potential measurements were chosen as dilute aqueous solutions as opposed to the IPA-based spray-coated ink solutions with a higher concentration of nanotubes so that a resolute and reproducible measurement of the zeta-potential of each individual tube might be capable. We thus assume that the comparisons between the zeta-potentials for sample solutions composed of nanotubes with varying surface functionalization properties based on the acid reflux parameters are still quite informative about the agglomeration and bundling properties of the IPA-based solutions that disperse the same nanotube samples, despite the measurements being taken in dilute aqueous solutions.

Another assumption made to quantify the zeta-potential from the electrophoretic mobility is that the Smoluchowski approximation applies to the samples since the nanotubes are dispersed in water. Multiple reports indicate that the Smoluchowski approximation is limited to spherical particles with a uniform charge density; however, it is also reported that the Smoluchowski approximation may be used when for uniformly charged rods with high aspect ratios where edge effects may be ignored.<sup>[67]</sup> The exact

mechanism that describes the electrophoretic mobility of the FWNTs is unclear and beyond the scope of this study; therefore we assume near uniform charge distribution across the nanotube surface and a structural rigidity during the electrophoretic movement.

The zeta potentials of various aqueous FWNT ink dispersions with low concentrations ( $\ll 1wt\%$ ) in solution were measured with a Malvern Zetasizer. The various ink dispersions differed in the acid reflux conditions of the purified FWNTs, Varying reflux duration, molar concentrations, and the volume of the bath solution gives a range of zeta potentials of FWNTs in solution. Table 2.1 gives the individual values for the ink dispersions and resulting spray-coated film conductivities.

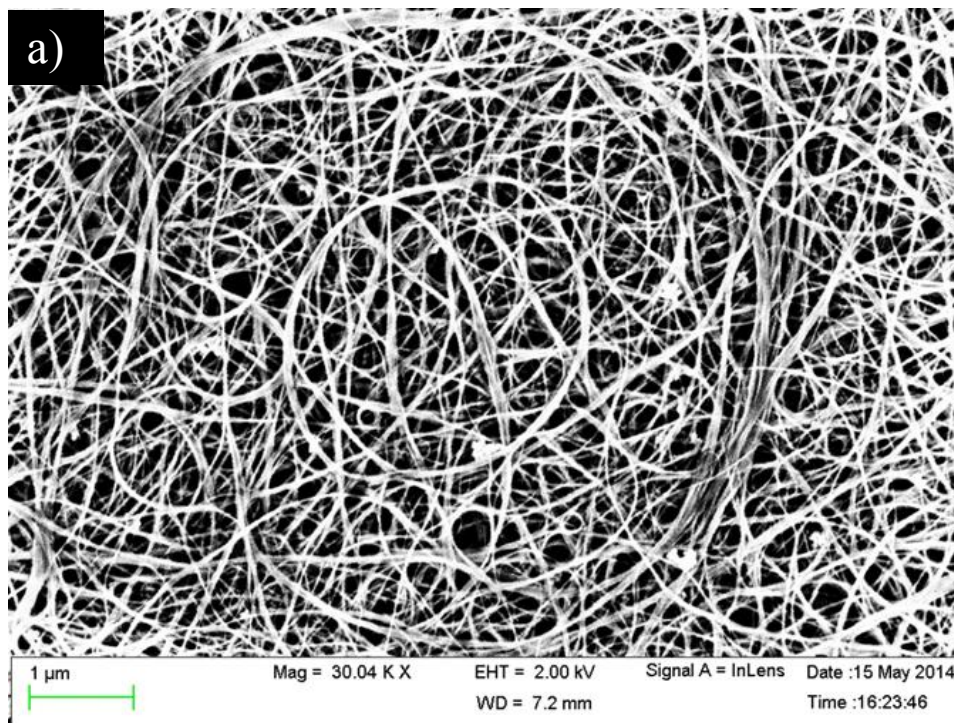
<b>Sample</b>	<b>HNO<sub>3</sub> reflux molarity</b>	<b>HNO<sub>3</sub> reflux time</b>	<b>Ink zeta-potential</b>	<b>Film conductivity</b>
<b>A</b>	<b>6M</b>	<b>2hr</b>	<b>-12.77mV</b>	<b>660 S/cm</b>
<b>B</b>	<b>8M</b>	<b>2hr</b>	<b>-13.26mV</b>	<b>781 S/cm</b>
<b>C</b>	<b>10M</b>	<b>1hr</b>	<b>-13.5mV</b>	<b>944 S/cm</b>
<b>D</b>	<b>10M</b>	<b>2hr</b>	<b>-14.6mV</b>	<b>2105 S/cm</b>

**Table 2.1)** Acid reflux parameters, the zeta-potential of the refluxed FWNTs in water, and the film conductivity of spray-coated FWNT films from various IPA-based inks.

To evaluate the surface charge of the nanotubes and the value of zeta-potential measurements in water, the zeta-potential of each water-based ink was compared to the resulting morphology and electrical conductivity of the spray-coated FWNT film from an IPA-based ink. The highest zeta potential was achieved for a reflux conducted in an 80 mL 10M HNO<sub>3</sub> solution held at 120 °C for 2hrs. The ink dispersion is represented by the

average of three zeta-potential measurements taken with the same water-based solution, while the values of the spray-coated film conductivity were taken from four point probe measurements of the sheet resistance and an average thickness determined by a profilometer step measurement from the substrate to 1.5mm across the sample surface while compensating for the surface roughness. The thickness of all the samples outlined in Table 2.1 are less than 1  $\mu\text{m}$ . It is observed that, as the zeta-potential increases, the film conductivity also increases. In fact, we see that the conductivity becomes dramatically greater with increases in the zeta-potential. We report film conductivity as high as 2100 S/cm, which is the highest reported value for surfactant-free IPA-based CNT inks.

A comparison of the SEM images of the spray-coatings for Sample A and Sample D is presented in Figure 2.26.





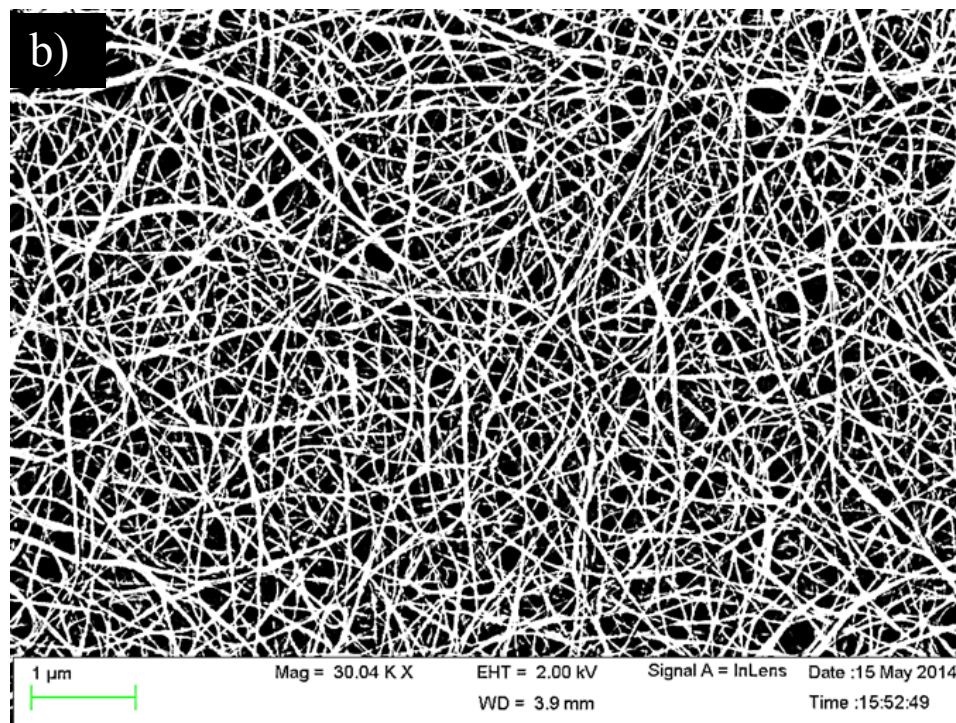


**Figure 2.26)** SEM images of spray-coated FWNT films from (a) sample A and (b) sample D, as detailed in Table 2.1.

We may confirm from the SEM images in Figure 2.26 that greater ink stabilities form more visibly uniform CNT networks with lower degrees of nanotube bundling. Translating film properties solely from the rheological behavior of the ink is difficult due to the many procedural variables that impact spray-coated films.<sup>[42]</sup> However, the clearly observable decrease in nanotube bundle size with films formed from FWNT inks that possess higher dispersion forces and the consequential dramatic enhancement in film conductivity suggest the quantity of repulsive surface groups plays a fundamental if not primary role in maximizing the electrical performance of spray-coated carbon nanotube films formed from weakly polar inks.

## 2.6 Conclusion

We report a novel surfactant-free ink composed of FWNTs dispersed in IPA to form highly conductive spray-coated films. Minimized tube bundling in the spray-coated films through a unique ink engineering process was demonstrated and investigated with various measurements to emphasize that manufacturing stable inks through functionalizing the outer walls of FWNTs forms highly uniform spray-coated films with remarkable conductivity. Through this investigation, we demonstrate a FWNT film with a conductivity of 2100 S/cm, which is the highest for spray-coated films from surfactant-free IPA based inks. Such films with high electrical performance from scalable and printable fabrication methods have unique applications in lightweight or flexible electronics where surfactant removal from an electrode is a primary issue.

## Chapter 3: Chemical Vapor Deposition Synthesis of Boron Doped Few-Walled Carbon Nanotubes

Chemically doping bulk yields of pure carbon nanotubes to control their electrical properties is a well-established technique. Carbon nanotubes in any growth yield display a random variety of chiralities; therefore, it is predicted that the ratio of semiconducting to metallic nanotubes is 2:1. Since semiconducting nanotubes possess a band gap at the Fermi level in the band structure, the overall conductivity across a random network at room temperature is limited by the presence of semiconducting nanotubes. A common method to lower the resistance of semiconducting  $sp^2$  carbon structures is to shift the Fermi level into the valence band by adding p-type charge carriers. Although this technique is demonstrated on SWNTs and MWNTs with large outer diameters ( $> 20\text{nm}$ ), no reports on chemical doping as a means to lower the bulk resistivity of FWNTs exist. The following chapter introduces a novel CVD process to safely grow boron-doped FWNTs (B-FWNTs), and explores the fundamental properties of these new nanomaterials.

### 3.1 Boron-Doped Carbon Nanotubes

The stability of any alterations to the band structure of carbon nanotubes depends on the doping mechanism. Impurities that are absorbed onto the surface of the nanotubes may only temporarily alter the band structure because they may detach at high temperatures.<sup>[73, 74]</sup> The most stable p-doping procedure is to substitute an impurity into the  $sp^2$  carbon lattice, which is only achievable with boron due to its similar size as the carbon atom. Impurity atoms any smaller than boron or larger than nitrogen induce too

much strain between the neighboring covalent carbon bonds to be successfully integrated into the lattice. Substitutional boron-doping of carbon nanotubes may be achieved through different processes with varying effects on the nanotube properties.

### 3.1.1 Substitutional doping mechanism

The procedures to substitute boron atoms into the carbon nanotube lattice may be separated into two categories: 1) in-growth doping methods and 2) post-synthetic doping methods. In-growth methods include a concentration of boron in the carbon source during the synthesis of nanotubes; these methods include arc-discharge, pulsed-laser ablation, and chemical vapor deposition. Post-synthetic processes substitute boron into the carbon lattice after the carbon nanotubes are grown. In-growth doping methods typically effect all the nanotubes in the bulk yield, whereas post-synthetic procedures are limited to tubes with open vacancies.<sup>[75]</sup> In order to influence a greater yield of carbon nanotubes, post-synthetic processes are typically conducted at high temperatures in a diborane ( $B_2O_3$ ) environment. This disintegrates carbon from the nanotube lattice by forming carbon monoxide, which allows boron to be substituted into the vacant site.<sup>[76]</sup> In-growth substitutional doping methods are therefore more advantageous because they do not require any post-growth disintegration of the carbon lattice and form doped nanotubes with a safer single synthesis process.

### 3.1.2 Projected change in electrical properties

The arrangement and concentration of boron atoms in the carbon lattice during in-growth doping procedures has been studied extensively for SWNTs and MWNTs in order to elucidate the varying effects on the band structure. Theoretical models of the band

structure of zig-zag SWNTs demonstrate the expected behavior of greater concentrations of boron in the carbon lattice of graphene promote greater shifts of the Fermi level into the valence band.<sup>[77-80]</sup> Although boron concentrations in the carbon lattice may reach as high as 15-25 atm% in post-synthetic substitutional doping methods,<sup>[81]</sup> McGuire et. al demonstrates that boron concentrations above 3 atm% impede the formation of SWNTs nanotubes during the growth process.<sup>[82, 83]</sup>

The behavior of in-growth boron doping in MWNTs is significantly different than in SWNTs.<sup>[9, 12, 13]</sup> Carroll et al. demonstrates that in-growth boron doping procedures of MWNTs arrange themselves into islands of  $BC_3$  nanodomains with varying sizes. Figure 3.1 illustrates the theorized localized density of states (LDOS) of the  $BC_3$  island superimposed by the LDOS of the metallic (6,6) nanotube the island is embedded in.

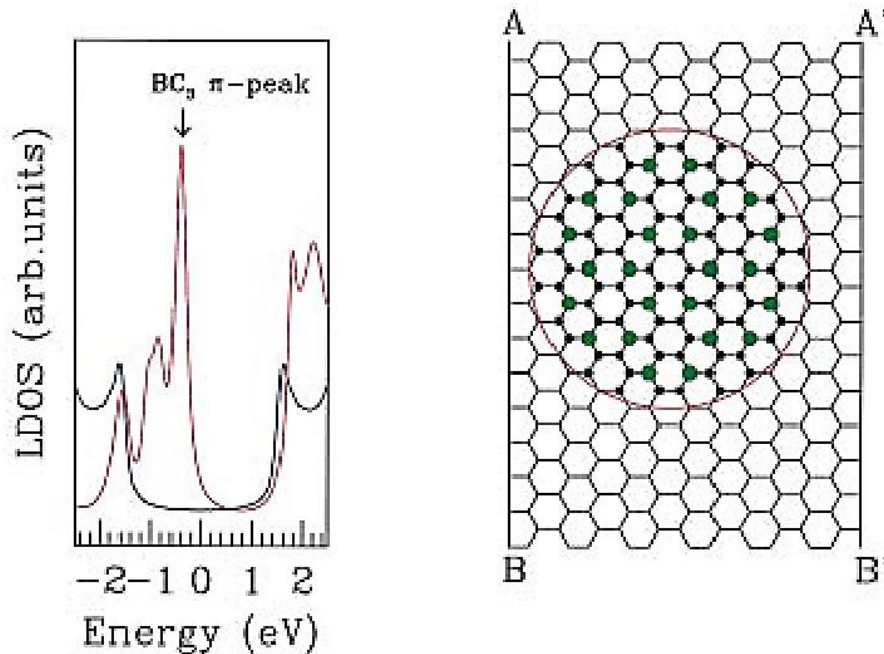


**Figure 3.1** The theoretical LDOS associated with a  $BC_3$  island (encircled region) plotted with the LDOS associated with a pure carbon island of the same radius, located far away from the B atoms as depicted in the unfolded tube model to the right (to reform the tube A has to be joined with A' and B with B', respectively).<sup>[85]</sup>

The formation of  $\text{BC}_3$  nanodomains in the carbon lattice instigates the alignment of the carbon nanotube and the  $\text{BC}_3$  Fermi levels, which gives rise to the strong acceptor peak attributed to the  $\text{BC}_3$  just below the Fermi level of the nanotube. A small increase in the density of p-type impurity atoms thus dramatically improves the conductivity of the nanotubes at room temperature due to this assembly into  $\text{BC}_3$  domains.<sup>[84]</sup> Wei et al. demonstrates an intrinsic resistivity of boron-doped MWNTs an order of magnitude lower than undoped tubes.<sup>[86]</sup> Although these  $\text{BC}_3$  domains are also reported to form in highly doped (>15 atm%) SWNTs with post-synthetic methods,<sup>[81]</sup> in-growth doping methods do not permit these high concentrations. Since the contribution of  $\text{BC}_3$  domains to the overall band structure of the nanotubes differs greatly from individual atomic substitutions of boron across the carbon lattice, understanding the exact mechanism that describes how the boron atoms are integrated into the CNT is important to comprehend any change in their electrical properties.

### 3.2. Synthesis of Boron-doped FWNTs

In Chapter 2 we discussed a CVD method to synthesize high yields of FWNTs with a low defect density from a Co:Mo catalyst embedded in a MgO support. The structural properties are primarily attributed to the composition of the catalyst; therefore, in-growth substitutional doping of boron into the lattice of FWNTs was facilitated with a similar carbon source decomposing onto the same powder catalyst. Ishii et al. demonstrate a CVD process to grow boron-doped FWNTs (B-FWNTs) with a solution of boric acid dissolved in methanol pumped into the furnace as the source solution.<sup>[87]</sup> Although the carbon source utilized to grow FWNTs previously in Chapter 2 was methane, alcohol solutions have been demonstrated as successful sources for FWNT

growth.<sup>[88]</sup> Reports also indicate that the growth yield of CNTs from pure methanol solutions is low compared to mixtures with ethanol.<sup>[58]</sup> This is due to a greater atomic decomposition of carbon from ethanol as opposed to methanol; however, the amount of carbonaceous impurities is tapered with higher concentrations of methanol in the source solution. The optimal solution based carbon source to grow B-FWNTs thus stems from a mixture of ethanol and methanol hosting a low concentration of boric acid. Figure 3.2 depicts a schematic of the experimental setup for the in-growth substitutionally doped B-FWNTs synthesized in this study.

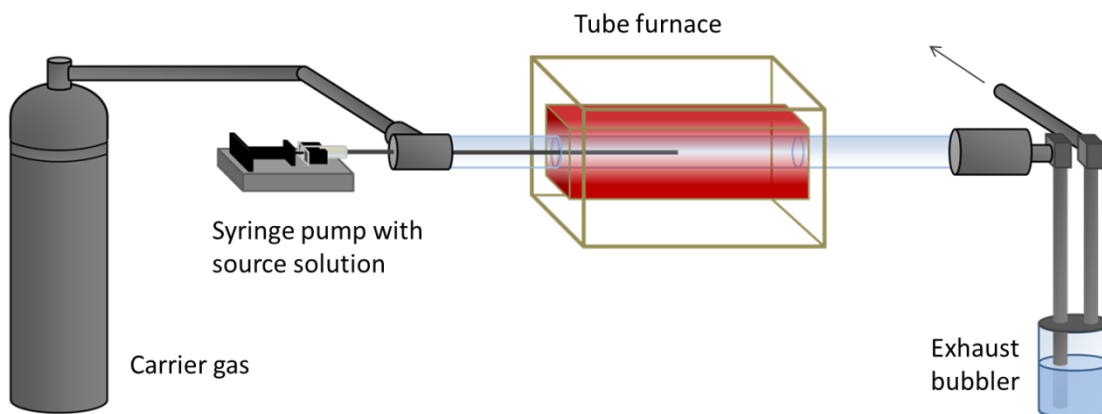


**Figure 3.2)** A schematic of experimental setup for the in-growth substitutionally doped B-FWNT synthesis via a solution-injected CVD method. The carbon feedstock is provided by a syringe pump injecting an alcohol mixture containing dissolved boric acid at a slow rate with a carrier gas into the tube furnace. The growth is conducted in the tube furnace with the exhaust passed through a water bubbler.

As seen in Figure 3.2, a syringe pump carrying the source solution inserts a needle into the tube furnace suspended over the powdered catalyst. A carrier gas composed of Ar/H<sub>2</sub> is used to ramp the temperature and set the flow rate of the vaporized source during the growth. An exhaust bubbler is attached as a precaution to dilute any acid vapor that may condense away from the furnace.

### 3.3 Results and Discussion

#### 3.3.1 Structure, morphology, and composition of B-FWNTs

The Co:Mo:MgO catalyst for the CVD growth is synthesized through a combustion method with a ratio of 1:0.5:100, which is outlined in Chapter 2. The source solution for the CVD growth of the B-FWNTs is prepared by dissolving boric acid in a 1:1 methanol + ethanol mixture so as to contain 2 atm% boron. After the furnace is ramped to 850 °C the source solution is injected into the furnace via the syringe pump at 20 mL/hr for 33 minutes with Ar flowing at 1600 sccm as the carrier gas. Figure 3.3 depicts a CVD growth yield of the B-FWNTs under these conditions.

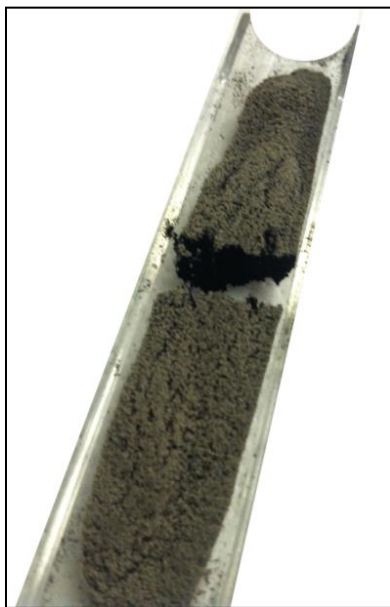
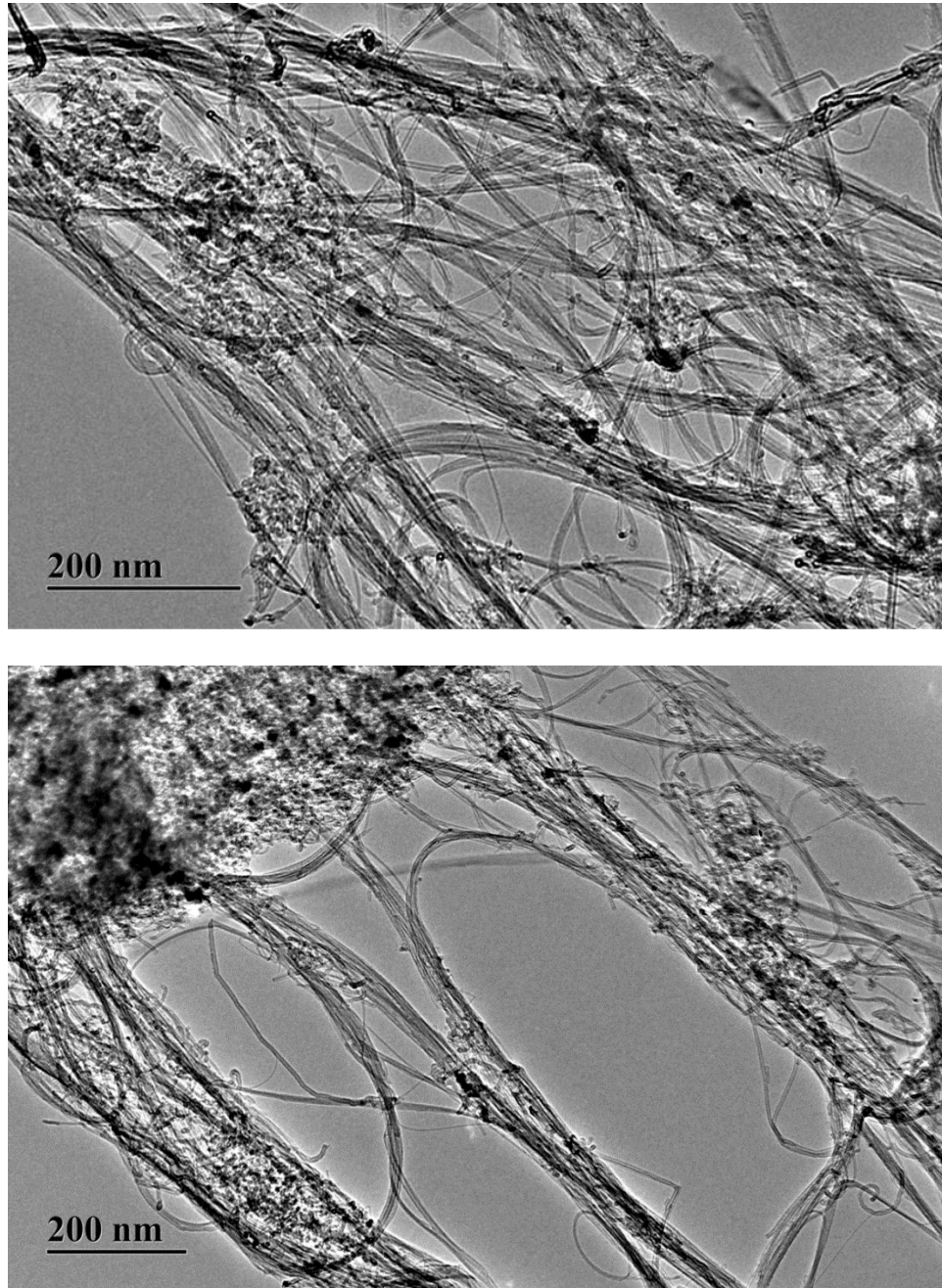


**Figure 3.3)** Growth yield of B-FWNTs in quartz sample holder. The black powder is the carbon nanotubes, while the grey powder covering it is a secondary phase.

The CVD growth yield demonstrates significant nanotube formation with large lengths extending several microns with varying degrees of bundling and curvatures. The

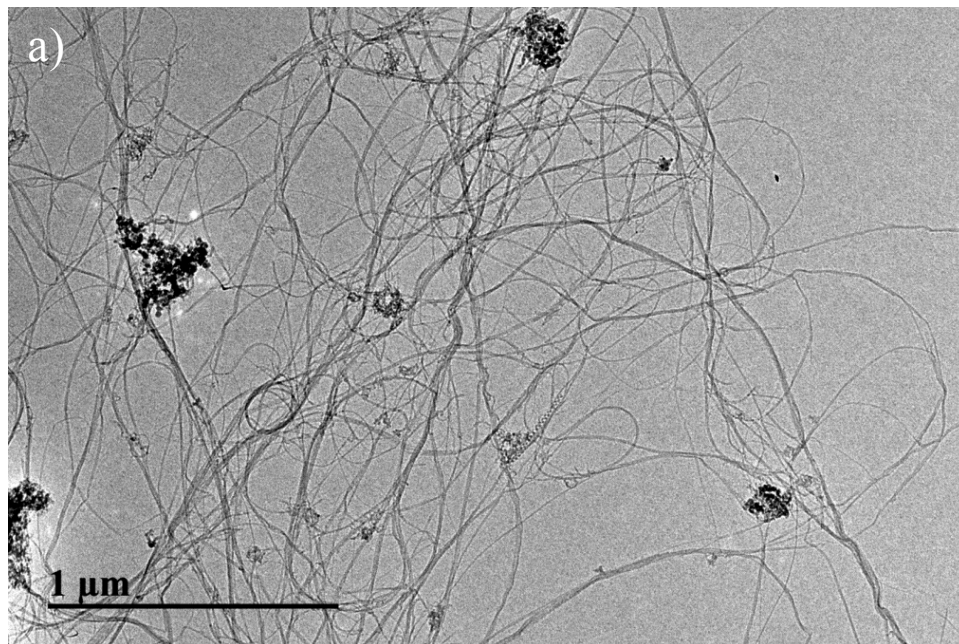


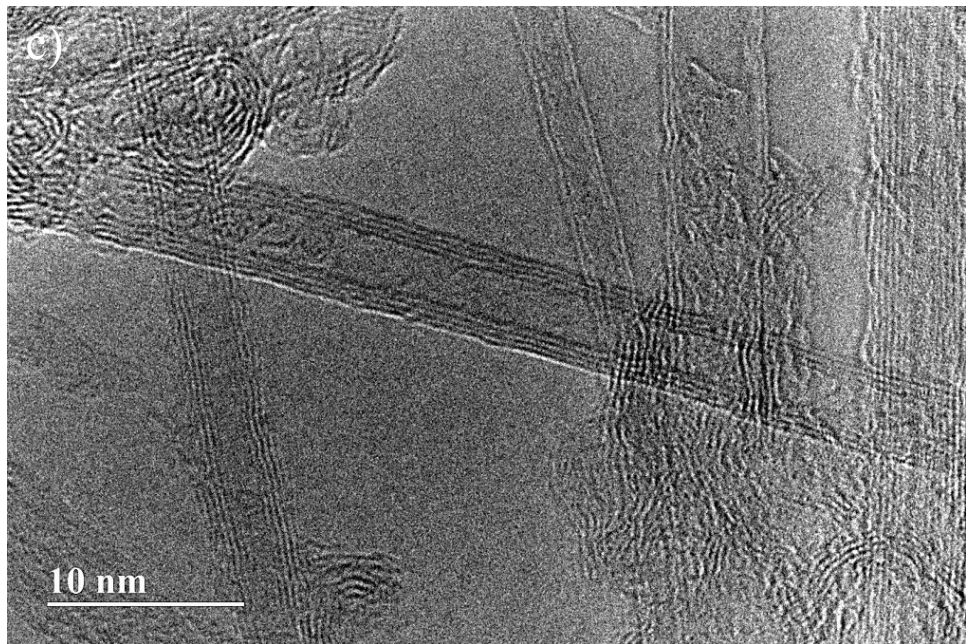
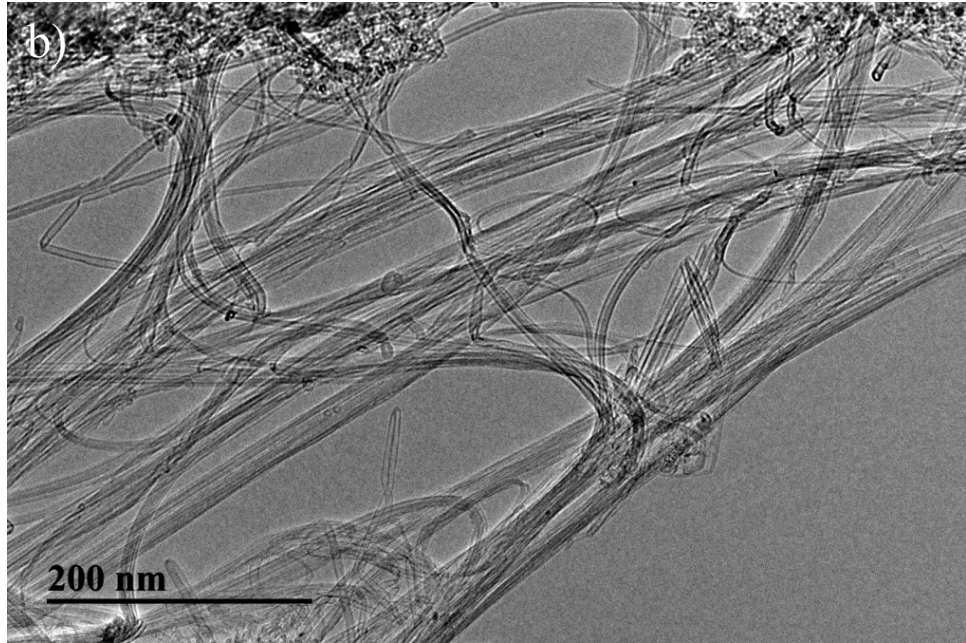
morphology and dimensions of the as-grown nanotubes are depicted in Figure 3.4. Figure 3.5 illustrates the same nanotubes following a thermal purification step for 1 hr at 500 °C.



**Figure 3.4)** TEM images of BFWNTs produced via a CVD conducted at a 850 °C growth temperature with a 2.0 atm% boron source solution containing an ethanol/methanol mixture as a solvent with a 1:1 weight ratio.

It is clear from Figure 3.5(a) that the nanotubes maintain a high aspect ratio with small bundle sizes no more than several nanotubes. The particles intermingling with the nanotubes are residual catalyst particles from the growth yield. Figure 3.5(b) demonstrates that the nanotubes have very few structural defects such as kinks or stunted growths. Since these nanotubes are grown to possess few morphological defects with a high aspect ratio, it is clear that the CVD growth process fabricates high quality nanotubes from the Co:Mo:MgO catalyst despite a new carbon source and the presence of concentrations of boron in that source. Figure 3.5(c) and Figure 3.5(d) demonstrate that the wall number of the nanotubes fits within the range of FWNTs, demonstrating that the growth process successfully fabricates FWNTs with a source solution that includes boron. The dark outlines in these HRTEM images are the concentric graphitic walls of the CNT. Figure 3.5(c) displays several nanotubes with wall numbers ranging from 2 to 7, as well as a presence of defective nanotubes. Figure 3.5(d) demonstrates a nanotube with a wall number of 5 that has no obvious structural defects.





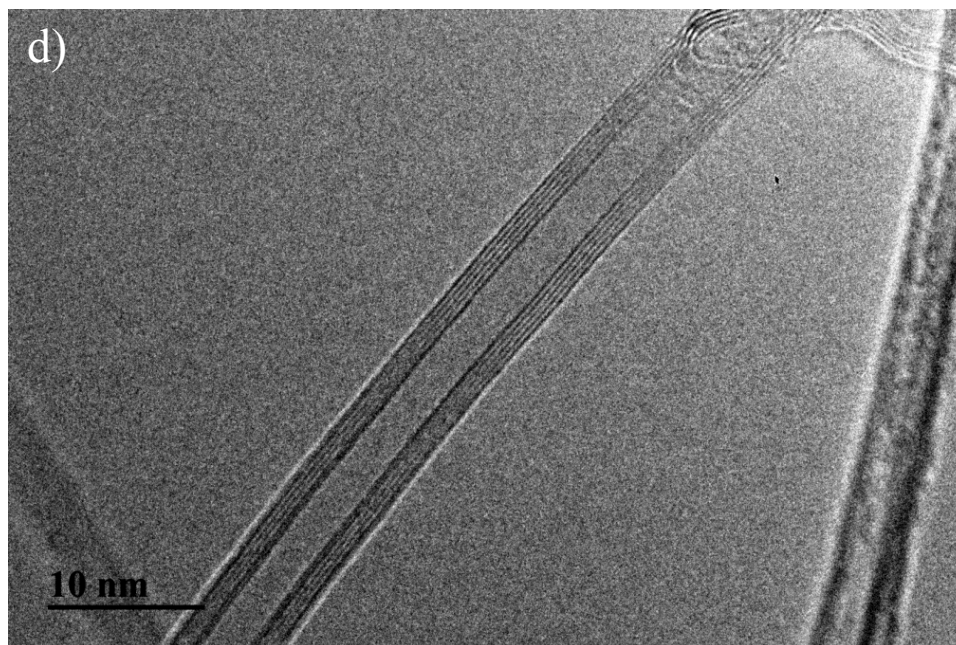


**Figure 3.5)** TEM images of B-FWNTs produced from a CVD conducted at a 850 °C growth temperature with a 2.0 atm% boron source solution containing an ethanol/methanol mixture as a solvent with a 1:1 weight ratio after thermal purification at 500 °C at various magnifications.

In order to confirm that the FWNTs fabricated by this new growth process successfully includes boron in the carbon lattice, Electron Energy Loss Spectroscopy (EELS) was conducted on the as-grown CNT sample. As transmitted electrons move through the sample they may be inelastically scattered, which forms an energy-loss spectrum. The excitation of inner shell electrons by a transmitted electron gives rise to ionization edges in the energy-loss spectrum, which reflect binding energies that are mostly hundreds or thousands of electron volts. Since core-electron binding energies differ for each element and each type of shell, the ionization edges can be used to identify which elements are present in the specimen. Figure 3.6 displays an energy-loss spectrum of the FWNTs as measured by EELS.

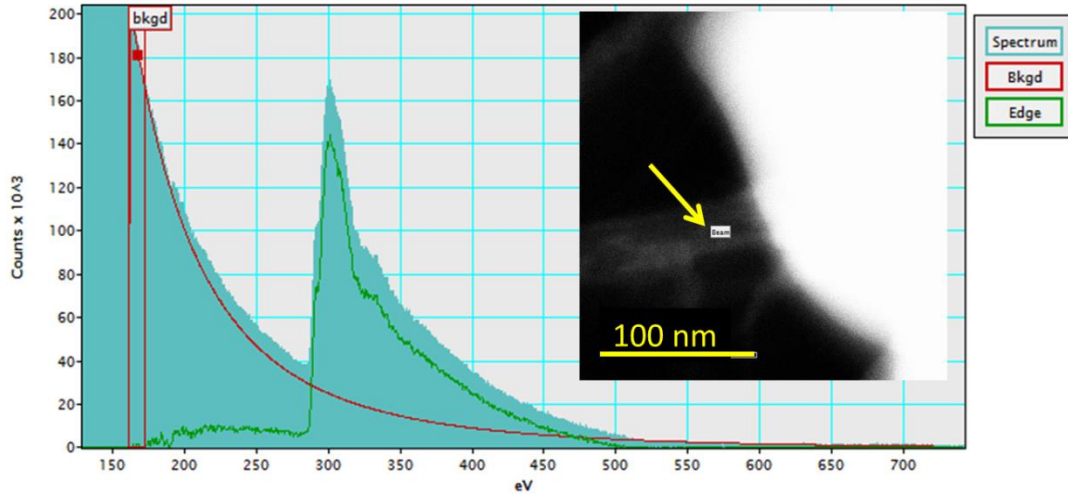


**Figure 3.6)** An EELS spectrum measured at the point indicated at the point on the nanotube in the STEM inset image. The background and EELS cross-section are demarked by the red and green spectra, respectively.

The ionization edges of boron and carbon are marked on the energy-loss spectrum of the carbon nanotube; the ionization edge of the boron atom is located at 188 eV and the ionization edge of the carbon atom is located at 284 eV, with each representing the excitation of 1s electrons in the K-shell to a  $\pi^*$  orbital in the hybridized  $sp^2$  network.<sup>[101]</sup>

The inset of Figure 3.6 depicts the scanning-transmitted electron microscopy image that marks the scanning site on a nanotube for the EELS measurement at the arrow. The bright white material that the nanotube emanates out from is an agglomeration of catalyst particles. Once the background of the energy-loss spectrum is extracted and subtracted, the cross-section of the energy-loss spectra  $\sigma_K$  and the intensities at the ionization edge  $I_K$  for each element may be quantified. The number of atoms per unit area that contribute to the K-edge may be quantified as:

$$N = \frac{I_K}{\sigma_K I_T} \quad (3.1)$$

with  $I_T$  representing the total transmitted intensity of the electron beam. The ratio of  $N$  for each element in the spectrum gives an atomic ratio of the elements in that scanning area. The atomic ratio of boron to carbon derived from the EELS measurement in Figure 3.6 is given by Table 3.1.

Element	Atomic Ratio (1/Counts)	Atomic Percent (%)
Boron (B)	$0.03 \pm 0.004$	2.78
Carbon (C)	$1.00 \pm 0.000$	97.22

**Table 3.1)** The atomic ratio of boron to carbon of the BFWNTs as derived from the EELS measurement in Figure 3.6.

The quantified atomic percent of boron within the FWNT measured by EELS demonstrates the success of the in-growth CVD doping method. The atomic percent of boron in the nanotube was found to be greater at EELS scan points closer to the catalyst agglomeration, as demonstrated in Figure 3.7 and Table 3.2.

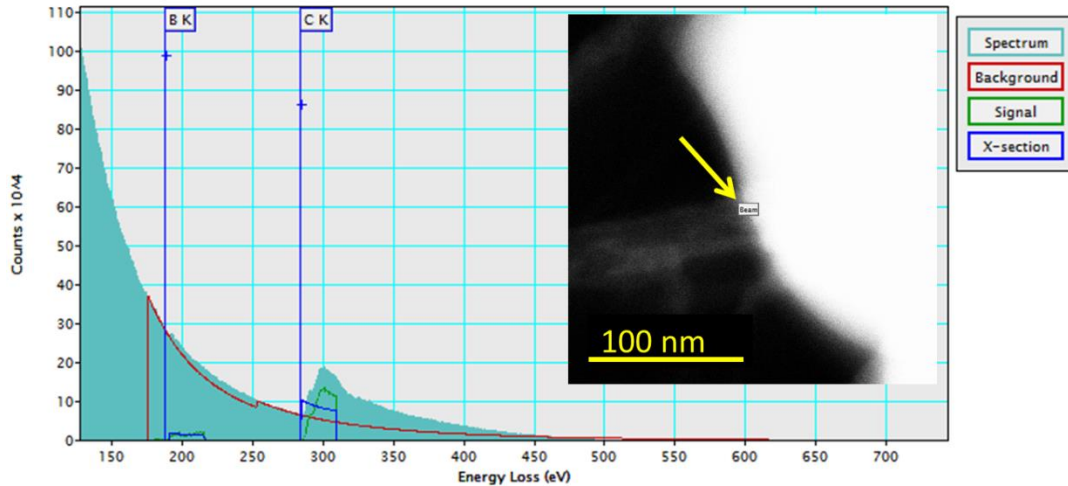


**Figure 3.7)** An EELS spectrum measured at the point indicated at the point on the nanotube near the catalyst in the STEM inset image. The background and EELS cross-section are demarked by the red and green spectra, respectively.

<b>Element</b>	<b>Atomic Ratio (1/Counts)</b>	<b>Atomic Percent (%)</b>
Boron (B)	$0.08 \pm 0.011$	7.22
Carbon (C)	$1.00 \pm 0.000$	92.78

**Table 3.2)** The atomic ratio of boron to carbon of the BFWNTs as derived from the EELS measurement in Figure 3.7.

Since the source solution in the CVD growth of the B-FWNTs consists of 3.0 atm% boron, it is expected that the boron content throughout the nanotube to be less than or equal to that if the individual boron atoms are individually substituted into the carbon lattice uniformly. Electron energy loss spectroscopy measurements on a finite point of a nanotube may register boron content greater than 2.0 atm% due to a coincidence that more boron atoms substituted into the lattice in that scanning area or because the boron atoms arrange themselves into  $BC_3$  nanodomains in the carbon lattice during the nanotube growth. In order to better elucidate the behavior of boron substitution in the carbon lattice of the nanotubes EELS measurements were taken in a line scan along the length of a CNT extending out of a cluster of catalyst particles. Figure 3.8 illustrates the energy-loss spectrum taken by EELS along a nanotube depicted in the STEM image.

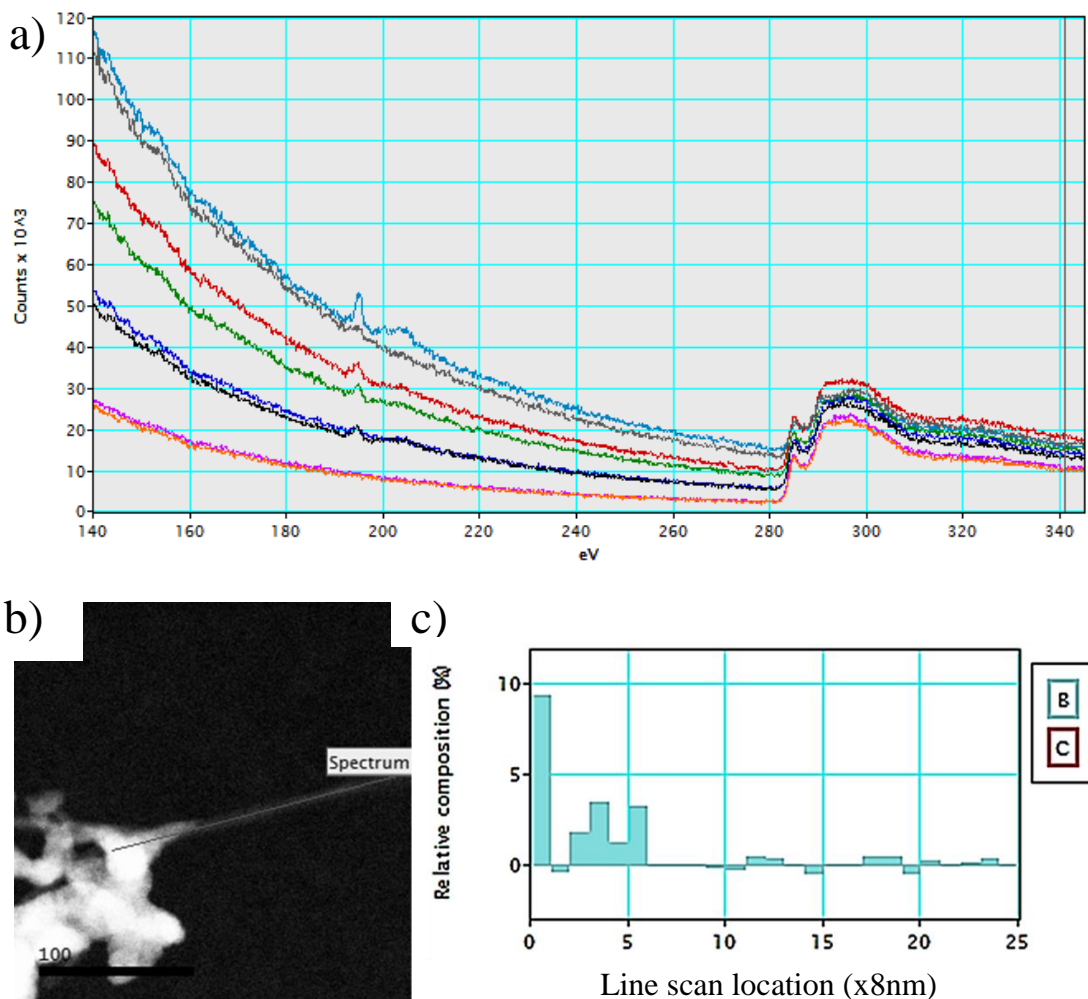


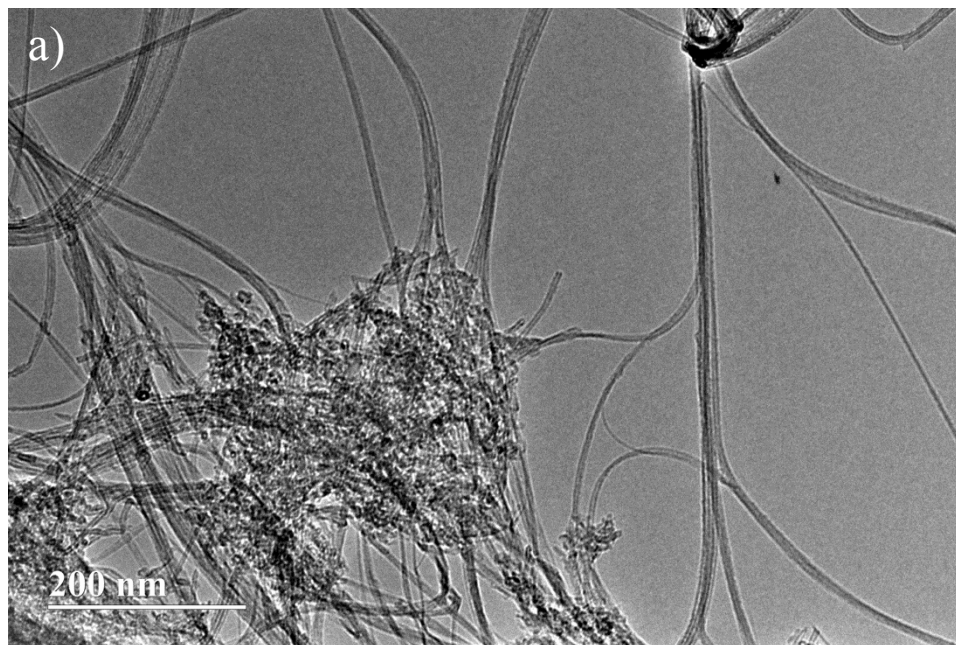
**Figure 3.8)** (a-b) Electron-energy loss spectra measured along the B-FWNT at various locations on the line depicted in the STEM image. (c) The resulting concentration of boron at the locations along the EELS line scan of the nanotube in the STEM measurement is given by the bar graph, with the x-axis representing the location of the EELS scan.

The  $1s \rightarrow \pi^*$  and  $1s \rightarrow \sigma^*$  transitions are clearly visible for carbon with the K-edge at 284 eV.<sup>[102]</sup> The same transitions are detectable for boron with the K-edge at 188 eV for some energy-loss spectra. This indicates varying atomic ratios of B/C across the nanotube. Figure 3.8(c) depicts the relative composition along the line scan of the nanotube in Figure 3.8(b), which shows that there is higher boron content in the nanotubes closer to the catalyst. This agrees with previous reports that boron primarily



substitutes into the carbon lattice near the tube ends during the growth of CNTs.<sup>[103]</sup> Atomic percentages of boron near the end of the CNT range above the 3.0 atm% boron content found in the source solution. This suggests that the boron does not evenly substitute into the carbon lattice throughout the nanotube, but concentrates towards the ends of the nanotubes extending out of the catalyst. This behavior may be indirect evidence for the formation of BC<sub>3</sub> domains as opposed to individual atomic substitutions.

The effect of the growth parameters on the structural characteristics of the B-FWNTs was investigated. Previous reports indicate that reduced growth temperatures during the CVD process form fewer carbonaceous impurities with the CNT yield. To investigate the effect of temperature on the CVD growth process for B-FWNTs, the source solution of 1:1 methanol /ethanol with a 2.0 atm% boron content was introduced to the tube furnace after ramping to 750 °C. Figure 3.9 shows TEM images of this growth yield.



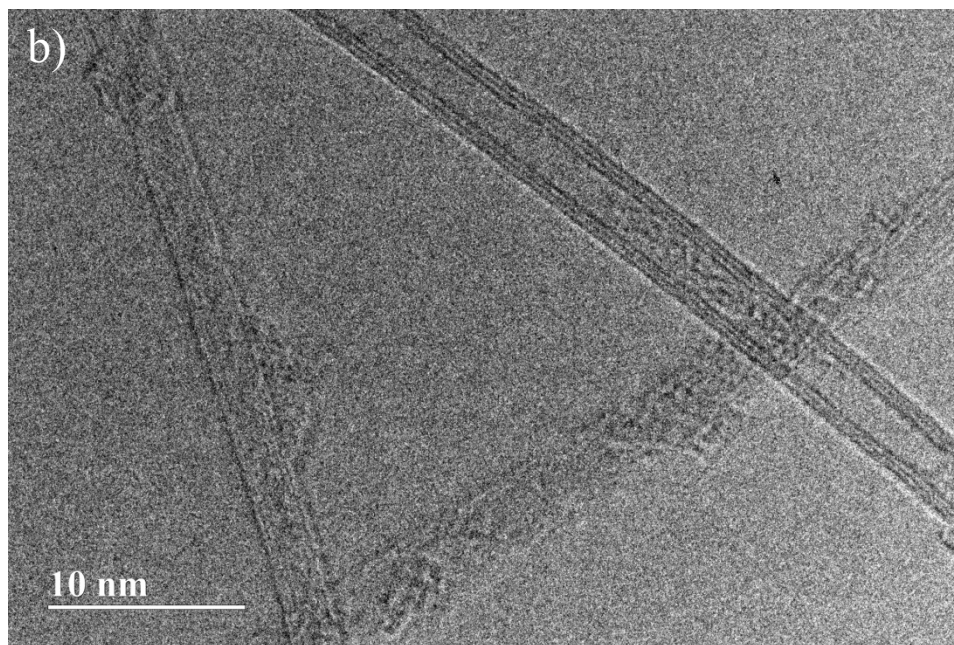


**Figure 3.9)** TEM images depicting the solution-injected CVD growth yield of BFWNTs with a lower growth temperature of 750 °C at various magnifications.

It is clear that the decreased growth temperature does not impede the fabrication of nanotubes during the CVD process. Furthermore, it is observable that the nanotubes have a high aspect ratio with wall numbers within the FWNT range. Another impact factor within the CVD growth process is the carbon content of the source solution. Reports on CVD growths of FWNTs indicate that a higher concentration of methanol in a methanol/ethanol carbon source solution reduces the amount of impurities in the growth yield.<sup>[58]</sup> A CVD growth of B-FWNTs was thus conducted with a carbon source solution consisting of a 3:1 methanol/ethanol ratio with a 2.0 atm% boron content. Figure 3.10 displays TEM images of this growth yield.

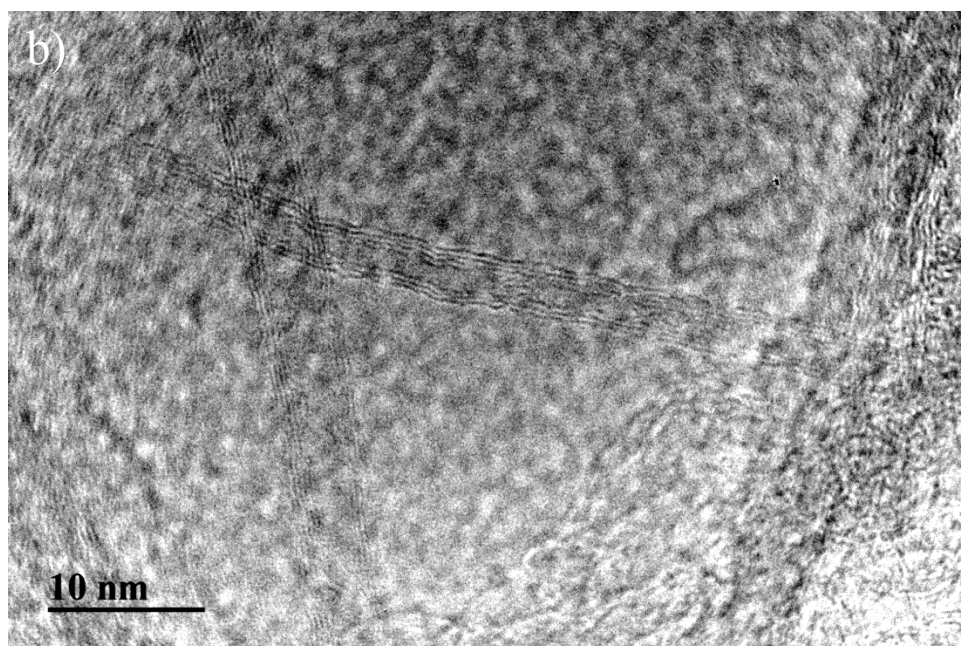
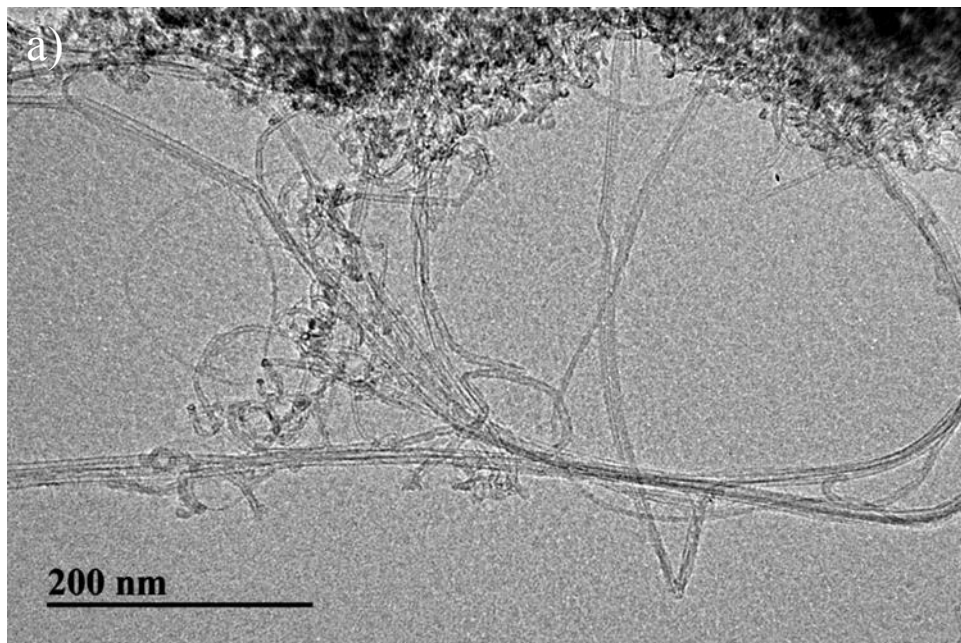
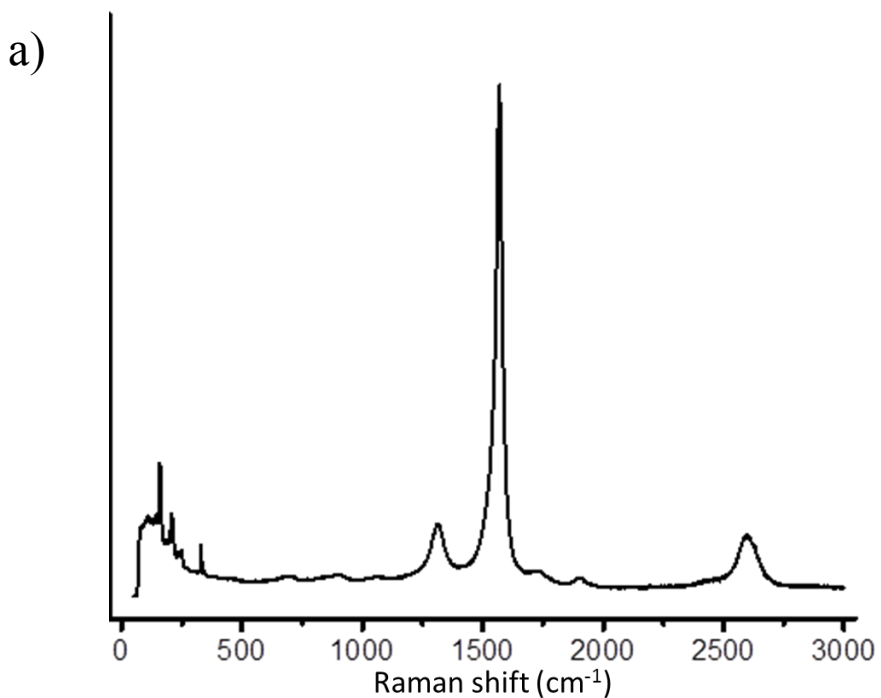


**Figure 3.10)** TEM images depicting the solution-injected CVD growth yield of BFWNTs with a higher methanol content in the source solution of 3:1 methanol to ethanol at various magnifications.

It is observable in Figure 3.10a that the altered source solution with a higher methanol content permits the growth of CNTs during the CVD process. It seems that the nanotubes

exhibit high aspect ratios, yet also demonstrate a significant number of kinks and bundles. Figure 3.10b demonstrates that the wall number of the doped CNTs grown with a 3:1 methanol/ethanol source solution is within the range for FWNTs, with CNTs possessing a wall number of 3 and 5 clearly visible in the TEM image. It is also observable that the B-FWNTs in Figure 3.10b possess structural deformations along the graphitic walls in the form of “wavy” with fluctuating inner and outer diameter. This behavior is investigated further later in this chapter.

A comparison of the structural characteristics of the B-FWNTs grown by CVD processes with various conditions may be drawn from their Raman spectra. Figure 3.11 illustrates the Raman spectra of B-FWNT growths with different combinations of the temperature and content of the source solution.



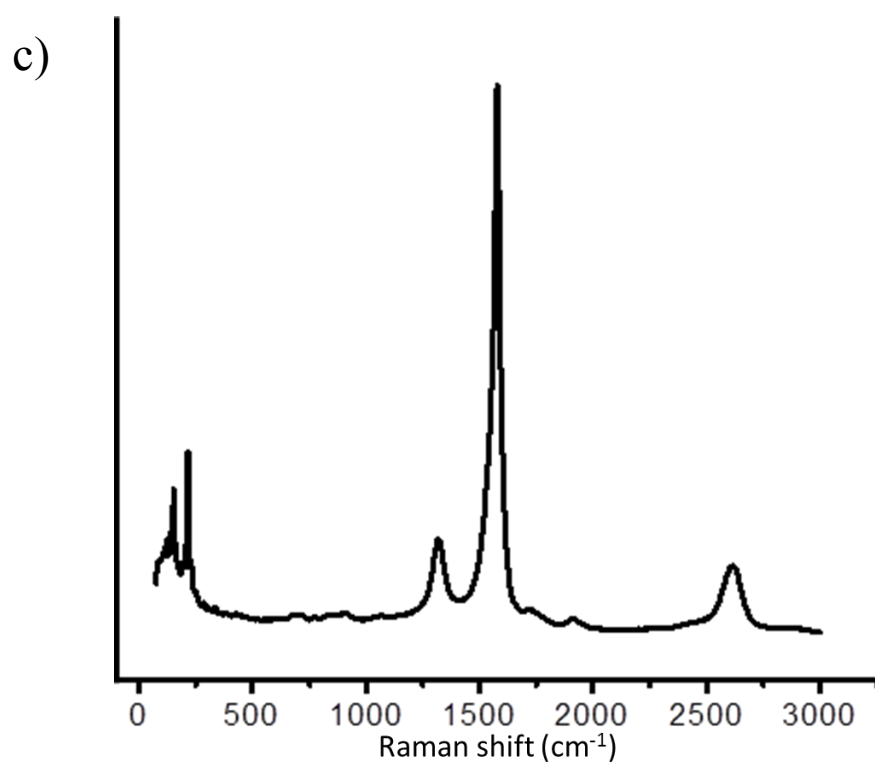
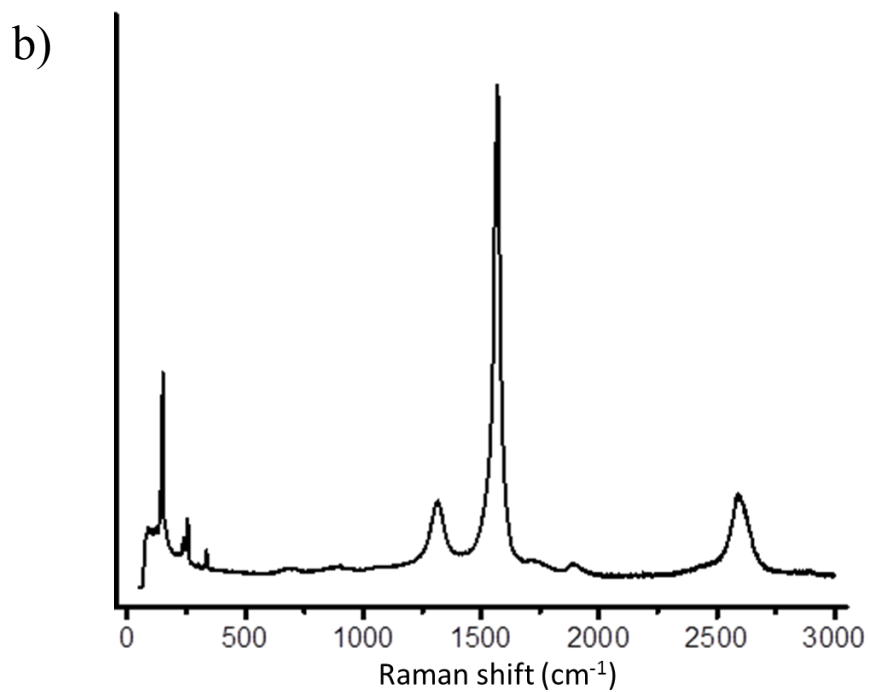


**Figure 3.11)** (a) Raman spectrum of as-grown B-FWNTs, grown at 850 °C with 1:1 methanol/ethanol, (b) Raman spectrum of as-grown B-FWNTs, grown at 750 °C with a 1:1 methanol/ethanol source solution, and (c) Raman spectrum of as-grown B-FWNTs, grown at 850 °C with 3:1 methanol/ethanol in the source solution.

The comparative metrics for these spectra are shifts in the wavelengths of the characteristic peaks (D-band, G-band, and G'-band) reported for undoped FWNTs and differences in the ratio of the D-band and G-band intensities (D/G).<sup>[83, 104-109]</sup> These characteristics are summarized for the spectra in Figure 3.11 in Table 3.3.

	Carbon source	Growth Temp. (°C)	D-band (cm <sup>-1</sup> )	G-band (cm <sup>-1</sup> )	D'-band (cm <sup>-1</sup> )	D/G
1	1:1 methanol/ethanol	850 °C	1313.5	1568.5	2600.5	0.1511
2	1:1 methanol/ethanol	750 °C	1314.1	1570.3	2594.5	0.1897
3	3:1 methanol/ethanol	850 °C	1318.2	1578.1	2615.7	0.1803
4	methane (undoped)	850 °C	1325.8	1575.1	2619.7	0.0986

**Table 3.3)** Characteristic features of Raman spectra for BFWNT samples synthesized under various source solutions and CVD growth temperatures, such as the wavenumber of the D-band, the wavenumber of the G-band, the wavenumber of the D'-band, and the ratio of the D-band peak intensity to the G-band peak intensity.

Previous studies demonstrate that p-doping the carbon lattice with boron will lead to shifts in the characteristic peaks of the Raman spectra of the B-FWNT; upshifts in the G-band occur due to alterations to the Fermi energy, and downshifts occur in the D-band and G\*-band due to a weaker C-B bond compared to C-C bonds. As we see in Table 3.3, there is a strong downshift of the D-band of undoped FWNTs by approximately 12.3 cm<sup>-1</sup> and a stronger downshift of the D'-band by approximately 19.2 cm<sup>-1</sup> for Growth 1. This infers weaker coupling of B-C bonds included in the carbon lattice due to boron substitution. In addition, there is a dramatic increase in the ratio of the D-band and G-band intensities (D/G = 0.1511) from that of undoped FWNTs (D/G = 0.0986). This

indicates that boron doping of carbon nanotubes disrupts the graphitization during the growth of carbon nanotubes, which is reported in previous studies.<sup>[83]</sup> The downshift of the G-band is uncharacteristic for a p-doped graphitic lattice; however, reports indicate that shifts in the G-band are insignificant at low boron concentrations substituted into the carbon lattice.<sup>[92]</sup>

Growth 2 demonstrates a downshift in the D-band of undoped FWNTs by approximately  $9.7 \text{ cm}^{-1}$  and in the D'-band by approximately  $24.2 \text{ cm}^{-1}$ , which also indicates shifts in the structure of the carbon lattice from undoped FWNTs. The ratio of the D-band and G-band intensities for Growth 2 is  $D/G=0.1897$ , which is also a significant increase than that for undoped FWNTs. The greater D/G ratio for Growth 2 than for Growth 1 suggests that a decrease in the growth temperature of the CVD method fabricates B-FWNTs with a higher defect density. Smaller downshifts from the wavelengths of the D-band and the D'-band in the Raman spectrum of undoped FWNTs occur for Growth 2 than for Growth 1. This suggests that the greater D/G ratio for Growth 2 is not due to higher concentrations of B-C bond formations in the carbon lattice than Growth 1. Thus lowering the temperature during the CVD growth may lead to B-FWNTs with greater morphological defects such as kinks and bends, or more carbonaceous impurities.

Growth 3 demonstrates a downshift in the D-band of undoped FWNTs by approximately  $7.6 \text{ cm}^{-1}$  and in the D'-band by approximately  $4.0 \text{ cm}^{-1}$ , which also indicates shifts in the structure of the carbon lattice from undoped FWNTs. The ratio of the D-band and G-band intensities for Growth 3 is  $D/G=0.1803$ , which is also a significant increase than for undoped FWNTs. The D/G ratio for Growth 3 is greater

than for Growth 1 but nearly equivalent to Growth 2; however, the downshift of the D-band and D'-band wavelengths from those of the undoped FWNTs is significantly lower in Growth 3 than in Growths 1 and 2. There is also an upshift in the G-band wavelength for Growth 3 from that of undoped FWNTs by  $3.0 \text{ cm}^{-1}$ , which is characteristic for a p-doped graphitic lattice. Evidence of boron substitution in Growth 3 may be drawn from the upshift in the G-band, the downshift of the D-band, and downshift of the D'-band from the undoped FWNTs; however, the increase in the D/G ratio from Growth 1 may not be caused from increased boron substitution since the shifts in the wavelengths of the characteristic peaks in Growth 3 from those of the undoped tubes are smaller than the shifts for Growth 1. Therefore, it may be concluded that increasing the methanol content of the source solution forms nanotubes with greater defect density or forms yields with greater quantities of carbonaceous impurities.

Thermal gravimetric analysis of the B-FWNT growth yields was conducted to determine their content and the thermal stability of the doped nanotubes. The blue line in the TGA measurement illustrates a comparative reference point of the nanotube yield thermal stability. Figure 13a depicts the TGA measurement of B-FWNT grown at  $850 \text{ }^\circ\text{C}$  with a 1:1 methanol to ethanol source solution. Figure 13.b depicts a TGA of B-FWNT grown at  $850 \text{ }^\circ\text{C}$  with a 3:1 methanol to ethanol source solution



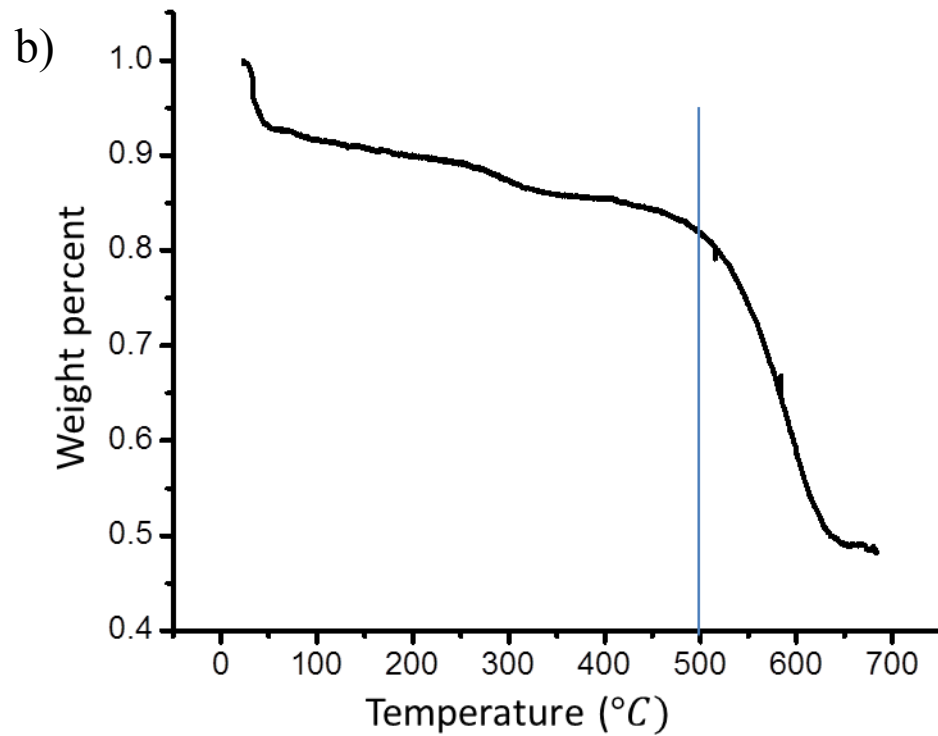
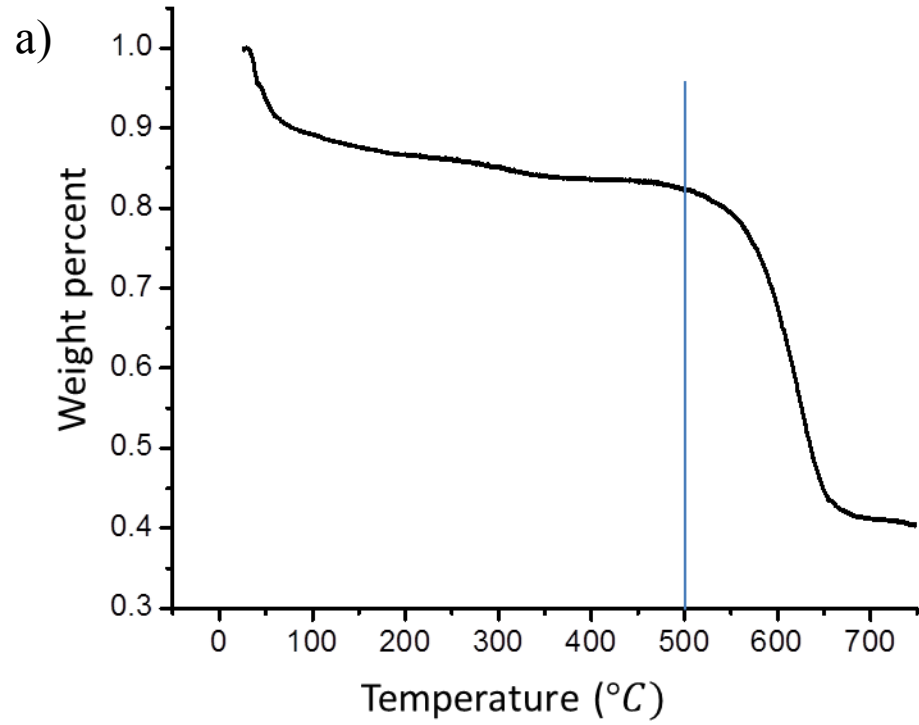


**Figure 3.12)** (a) TGA of B-FWNT grown at 850 °C with a 1:1 methanol to ethanol source solution, Growth 1 and (b) a TGA of B-FWNT grown at 850 °C with a 3:1 methanol to ethanol source solution, Growth 3.

For each regression the amorphous carbon oxidizes at approximately 300 °C, which agrees well with literature. It is clear by comparing the TGA regressions in Figure 3.12 that Growth 1 has a higher thermal stability than Growth 3. This is due to the larger area under the TGA curve past 500 °C for Growth 1 compared to Growth 3, which demarks a higher oxidation temperature of the doped nanotubes. Since the D/G ratio of Growth 3 is higher than Growth 1, the lower thermal stability of Growth 3 may be attributed to a higher defect density in the nanotubes. This indicates that the BFWNTs of Growth 1 possess a higher graphitic quality than Growth 3. Another observation is that the carbon content in Growth 1 contains 6.6 wt% amorphous carbon whereas there is 10.8 wt% amorphous carbon within the total carbon content of Growth 3. These quantities were evaluated by distinguishing the two carbon phases in the mass loss spectra from 200-700 °C and determining the relative mass loss within the total carbon oxidized during the thermal treatment. It may be concluded therefore that the CVD yield in Growth 3 produces less thermally stable nanotubes and a higher impurity content than Growth 1.

It was mentioned that morphological characteristics of B-FWNTs include wavy graphitic walls. Evidence of this behavior is illustrated in the TEM images in Figure 3.13.

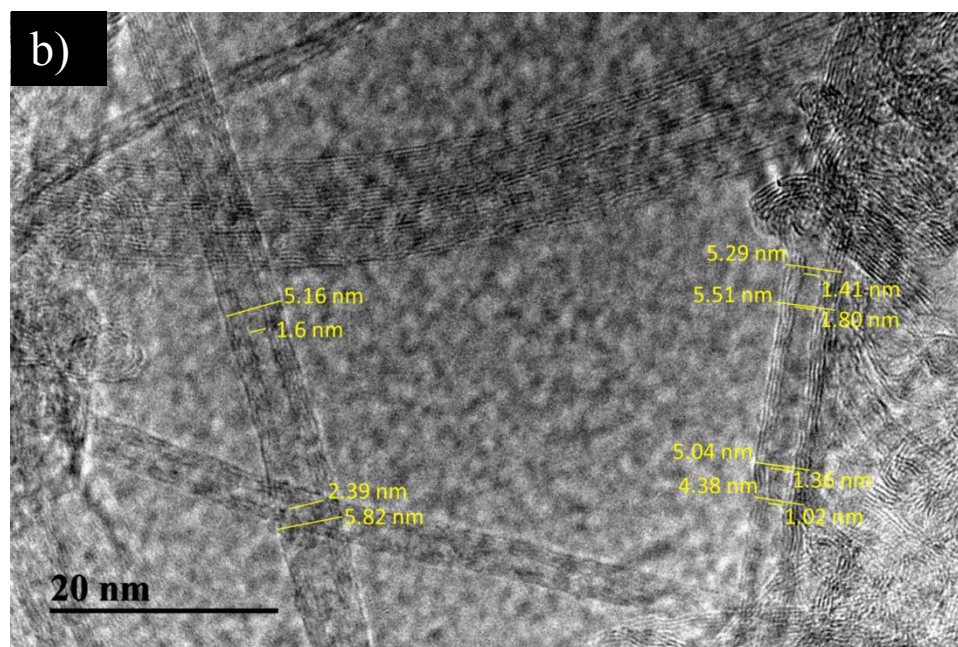
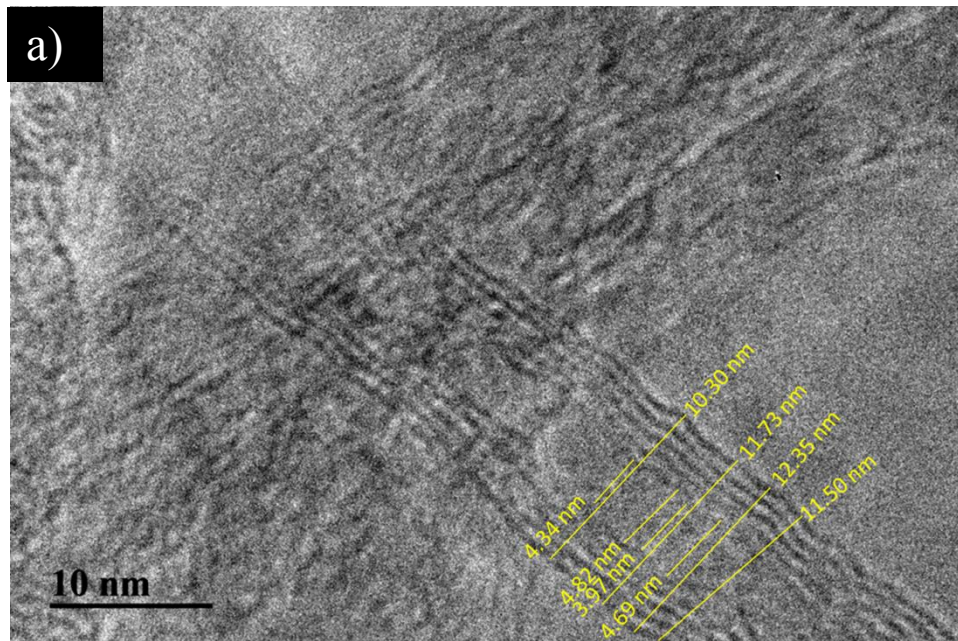


**Figure 3.13)** TEM with various magnifications of the morphology of wavy B-FWNTs, which clearly demonstrates fluctuations in the inner and outer diameters of the nanotubes.

According to Figure 3.13, inner and outer diameters are not uniform across the entire length of the nanotubes. This behavior persists for nanotubes with different wall

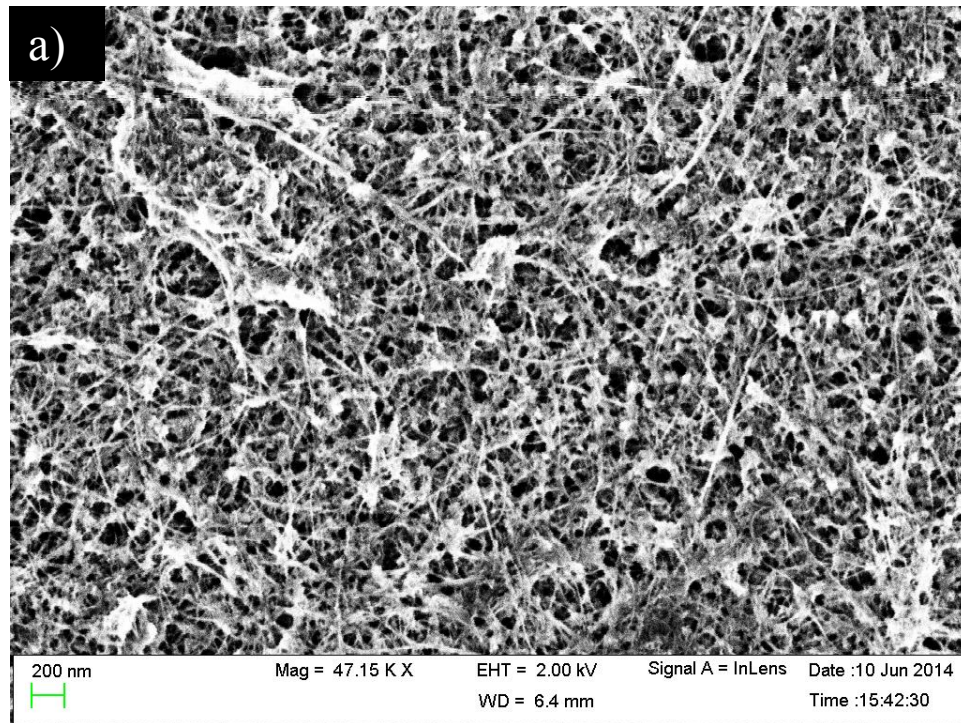
numbers, with the deformations propagating through all the graphitic walls at each occurrence. Figure 14a displays a FWNT with five walls, with a fluctuation of the inner wall reaching  $\Delta d \approx 0.85 \text{ nm}$  and a fluctuation of the outer wall reaching  $\Delta d \approx 2.0 \text{ nm}$ . It is observable in the high-resolution TEM (HRTEM) image that the change in the inner and outer wall diameters is not uniform at each deformation. Figure 14b displays a TEM image depicting inner and outer diameter fluctuations in FWNTs with four and five walls. Approximate changes in the inner diameters are  $\Delta d \approx 0.8 \text{ nm}$  for the five-walled nanotube and four-walled nanotube, while the changes in the outer diameters are  $\Delta d \approx 0.66$  for the five-walled nanotube and  $\Delta d \approx 1.13 \text{ nm}$  for the four-walled nanotube.

### 3.3.2 Impact of purification on BFWNT spray-coating properties

As mentioned in the previous section, Growth 1 of BFWNTs was conducted with a CVD growth at a temperature of  $850 \text{ }^\circ\text{C}$  with a 2.0% atm boron solution with a mixed solvent of ethanol/methanol at a ratio of 1:1. Since the TEM images of the nanotubes synthesized in each of the growths demonstrated significant degrees of bundling, an ink-making process described in Chapter 2 was utilized to disperse the BFWNTs in IPA. A thermal purification step to eliminate amorphous carbon from the growth yield without reducing the BFWNT content was conducted on the pristine nanotube yield at a temperature of  $500 \text{ }^\circ\text{C}$  for 1 hour in accordance with Figure 3.12(a). Approximately 30 mg of the purified BFWNTs were then refluxed in 80 mL of a 10 M  $\text{HNO}_3$  solution for approximately 2 hours, as described in Chapter 2. The refluxed BFWNTs were then washed with over 500mL of DI water via a vacuum filtration, and then redispersed in IPA at an approximate concentration of 0.6 mg/mL. The resulting inks were finally spray-

coated with an airbrush (A470M airbrush at 200 kPA of argon) onto 100mm<sup>2</sup> area on a cleaned glass substrate heated to 120 °C.

Although the expected sheet resistance of the spray-coated films was expected to be nominally lower than the undoped FWNT spray-coatings at the same thickness, it was quickly discovered that it was in fact at least an order of magnitude higher. An investigation into the spray-coated film characteristics reveals that a secondary phase exists in the random network that may impede the electronic transport, as seen in the SEM images of the coating surface in Figure 3.14.



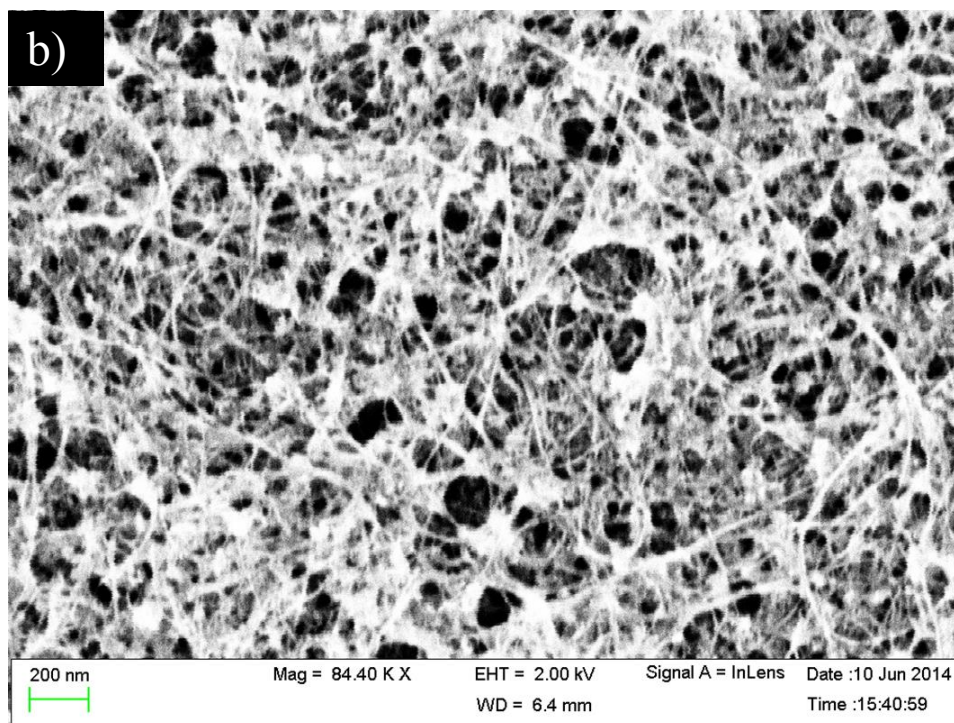


**Figure 3.14)** SEM images at various magnifications of spray-coated BFWNT films following a reflux of the nanotubes in 10 M HNO<sub>3</sub> for about 2 hours. Images were taken at high contrast in order to illuminate the BFWNTs along with the presence of a seemingly amorphous secondary phase.

The SEM images of the spray-coating surface clearly display BFWNTs with a high aspect ratio incorporated in a random network, along with a secondary phase that appears as an amorphous impurity. Energy Dispersive Spectroscopy (EDS) does not distinguish any unordinary element from the sample; only carbon, oxygen, and boron are most prevalent in the sample. This secondary phase is most logically supplied during the CVD synthesis of the BFWNTs, as evidenced by the additional grey powder visible on the surface of the CVD growth yield in Figure 3.3. The consistency of this grey phase is much lighter and separates easier than the powder of tangled nanotubes. After separating the grey “ash” from the CVD growth yield, ATR-FTIR measurements were performed better elucidate its molecular structure by comparing it to the primary phase believe to

possess primarily BFWNTs. Figure 3.15 presents the FTIR spectrum of Growth 1 with both phases present in the sample.

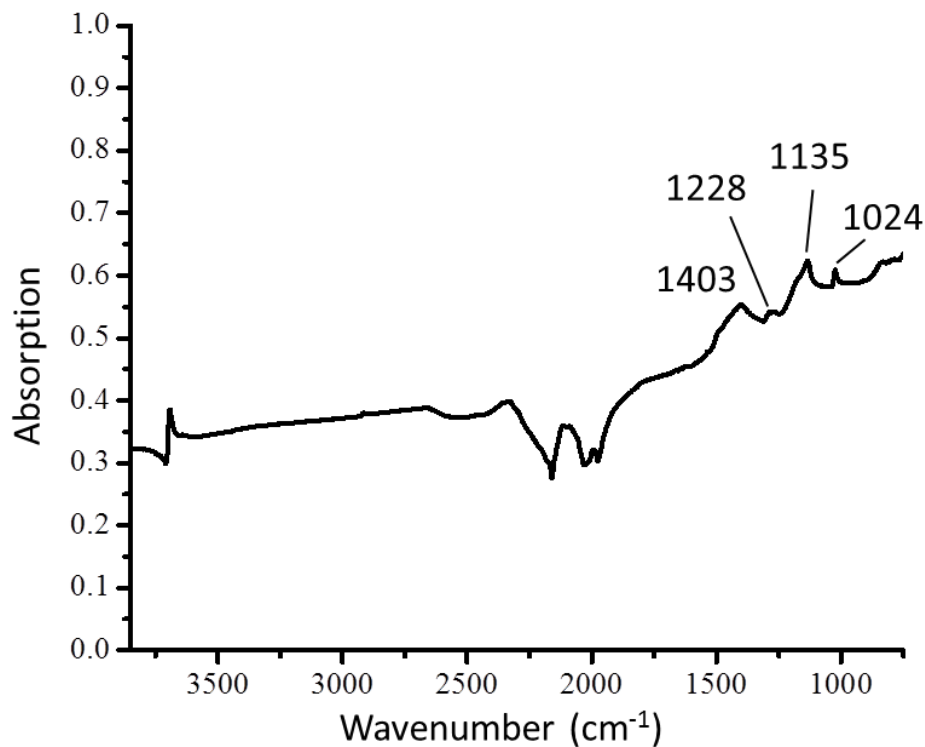


**Figure 3.15)** ATR-FTIR spectrum of Growth 1 BFWNTs with the wavenumber of prevalent peaks labeled.

The wavenumbers of the characteristic peaks in Figure 3.15 may be representative of multiple components, including oxygenated graphitic structures, boron oxide, and boric acid. These conclusions are formed based on evidence of the formation of a white powder on the window of the tube furnace during the CVD growth, which is reported as boron oxide and boric acid in the literature.<sup>[92]</sup> The prominent peaks at 1135 cm<sup>-1</sup> and 1403 cm<sup>-1</sup> may represent in-plane B-O-H bending and asymmetric B-O stretching respectively, with respect to a system consisting of boron oxide and boric acid;<sup>[93, 94]</sup>

however the faint peak at  $1024\text{ cm}^{-1}$  is characteristic of B-O-C stretching that attributes to boron-carbon bonding,<sup>[95,96]</sup> in which case the  $1135\text{ cm}^{-1}$  peak may represent B-C bond stretching.<sup>[89-91]</sup> Interestingly, there is no distinct peaks reflecting C=C bonds of graphitic carbon, wherein the  $1135\text{ cm}^{-1}$  may represent C-O groups.<sup>[97]</sup>

The grey “ash” was isolated from Growth 1 in order to distinguish the contributions of the secondary phase towards the FTIR spectrum of Growth 1. Fourier Transform IR spectra of the secondary phase in the initial growth yield reveal peaks at wavelengths characteristic of boron carbide and amorphous carbon, as seen in Figure 3.16.

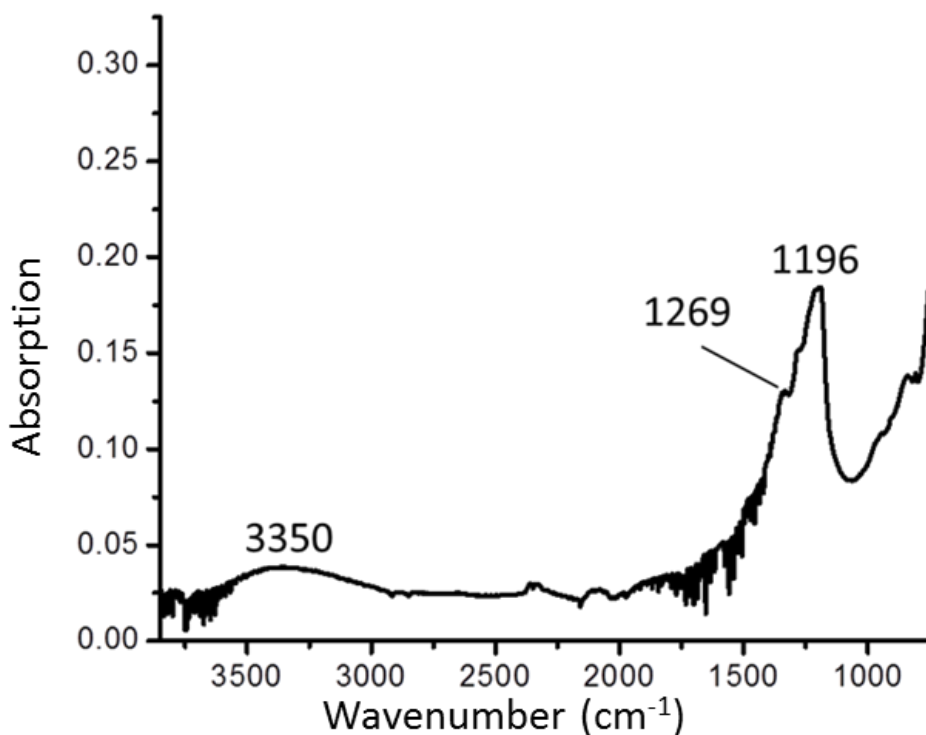


**Figure 3.16)** FTIR spectrum generated from an ATR measurement of grey “ash” from Growth 1 of the CVD synthesis of BFWNTs as depicted in Figure 3.3.

The characteristic wavelengths in Figure 3.4 are representative of bonds reported for boron oxide; a wide peak centered at about  $3350\text{ cm}^{-1}$  for stretching of O-H bonds and a



sharp asymmetric peak at about  $1196\text{ cm}^{-1}$  representative of B-O deformation. Boron carbide was eliminated as the prominent secondary phase since the broad shoulder around  $1050\text{ cm}^{-1}$  characteristic of boron carbide phonons is not present.<sup>[98,99]</sup> Another condition that is not met for the formation of prevalent boron carbide impurities during the CVD procedure is a high growth temperature ( $> 1000\text{ }^{\circ}\text{C}$ ).<sup>[89, 100]</sup>

After the secondary phase was oxidized at  $500\text{ }^{\circ}\text{C}$  we see additional peaks characteristic of oxygen groups appear in the FTIR spectrum, as seen in Figure 3.17.

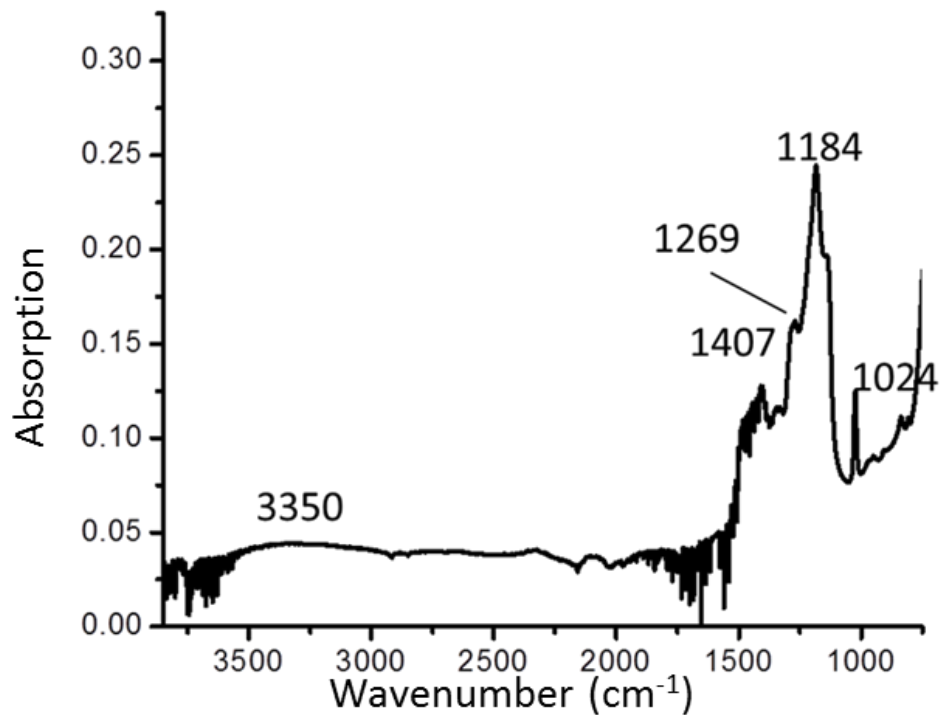
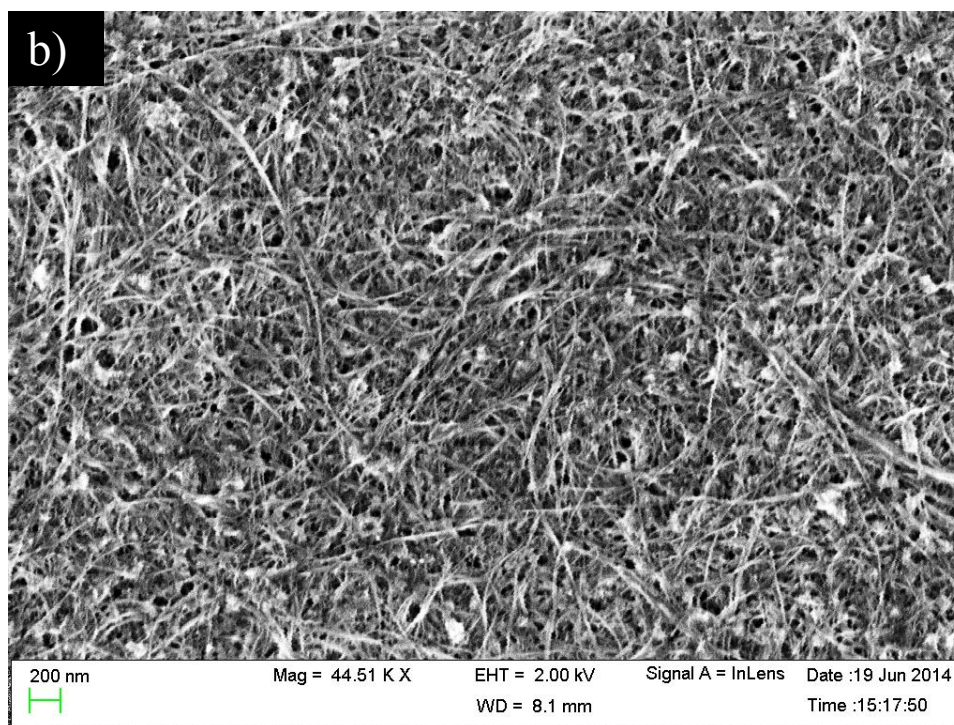
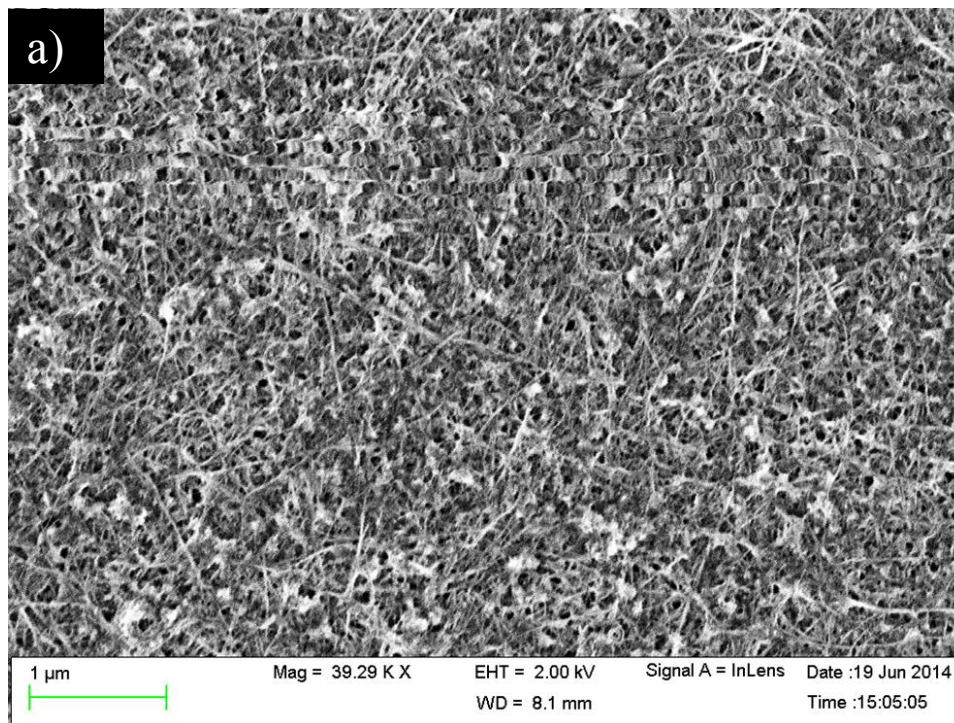


**Figure 3.17)** FTIR spectrum generated from an ATR measurement of grey “ash” from Growth 1 of the CVD synthesis of BFWNTs after an oxidation at  $500\text{ }^{\circ}\text{C}$  for 1 hour.

As illustrated in Figure 3.17, a peak emerges in the FTIR spectrum at about  $1407\text{ cm}^{-1}$  representing B-O bond stretching. Furthermore, a sharp peak at  $1024\text{ cm}^{-1}$  emerges after the oxidation, which is attributed to B-O-C bond stretching. It is also observable in Figure 3.17 that the peak representing O-H bonds flattens after the oxidation with regards

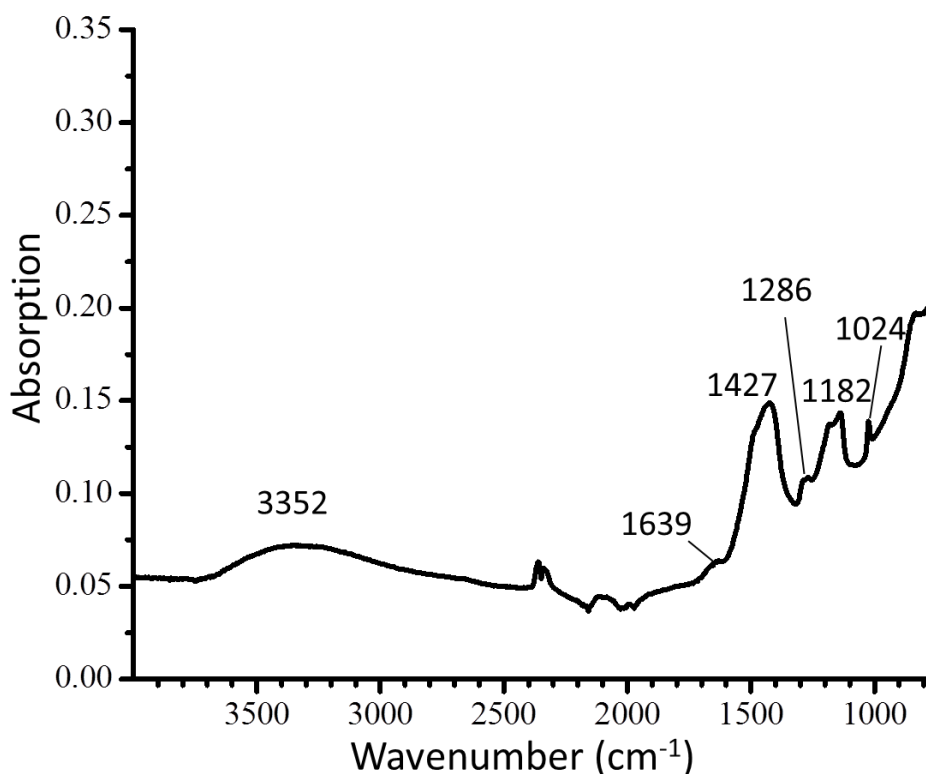
to the background baseline while the absorption peak intensity at  $1184\text{ cm}^{-1}$  attributed to B-O bond deformation increases. This illustrates that there is a decrease in amorphous carbon after oxidation, but not a removal of the secondary phase. Although these peaks infer that the secondary phase consists of boron oxide, the additional B-O-C peak muddles the explanation of the exact structural composition from the FTIR spectra.

Since it appears that the secondary phase of the CVD growth yield consists of bonds that attribute to boron oxide, an additional purification step was instituted to remove it from the BFWNT yield. After thermally treating the as-grown BFWNTs, the grey “ash” was carefully scraped off the primary phase. The primary phase BFWNTs were then dispersed in methanol and boiled via a heating mantle in order to dissolve any residual boron oxide remaining after scraping off the “ash.” After the BFWNTs were boiled in methanol for 1hr, an ink-making process was conducted to disperse the nanotubes in IPA following a reflux in 10 M  $\text{HNO}_3$  for 2 hours and then a rinse in DI water via a vacuum filtration. The resulting inks were finally spray-coated with an airbrush (A470M airbrush at 200 kPa of argon) onto  $100\text{mm}^2$  area on a cleaned glass substrate heated to  $120\text{ }^\circ\text{C}$ . Figure 3.18 demonstrates SEM images of the surface of the spray-coatings, which may be compared to Figure 3.14 to determine a difference in the composition of the random network.



**Figure 3.18)** SEM images of spray-coated surface of methanol-washed BFWNTs refluxed in 10 M  $\text{HNO}_3$  for 2 hours and dispersed in IPA at an approximate concentration of 0.6 mg/mL



The surface coating depicted in Figure 3.18 demonstrates a clear decrease in the amorphous phase material overwhelming present in the SEM images depicted in Figure 3.14; however, there is still a distinguishable impurity intermingled with the random network of BFWNTs. Since the methanol wash is expected to remove any residual boron oxide or boric acid that remain present in the BFWNT growth yield after a thermal purification, it may be concluded that an additional impurity phase is formed in the CVD synthesis. Since the elemental composition and molecular structure of the BFWNT sample does not distinguish any other unique phases that may be eliminated with additional purification steps, it is proven difficult to efficiently eliminate all the impurities that may exist in the CVD yield.



**Figure 3.18)** FTIR spectrum generated from an ATR measurement of Growth 1 of the CVD synthesis of BFWNTs after an oxidation at 500 °C for 1 hour.

Further contradictions in the composition of Growth 1 appear when considering its FTIR spectrum after a thermal purification at 500 °C for 1 hour and a methanol wash, as seen in Figure 3.19. The FTIR spectrum in Figure 3.19 displays the characteristic peaks of boron oxide ( $1427\text{ cm}^{-1}$  representing B-O bond stretching and  $1182\text{ cm}^{-1}$  attributed to B-O bond deformation), which are prevalent in the secondary phase grey “ash” spectrum in Figure 3.17 after thermal purification and in the spectrum for untreated CVD growth yield in Figure 3.15. Despite the similarities of these characteristic peaks for boron oxide in the spectra of pre- and post-purified Growth 1, there is a discernible upshift in the wavenumbers of the peak intensity; a  $47\text{ cm}^{-1}$  shift in the wavenumber attributed to the B-O bond deformation after thermal purification ( $1135 - 1182\text{ cm}^{-1}$ ) and a  $24\text{ cm}^{-1}$  shift in the wavenumber attributed to the B-O bond stretching after thermal purification ( $1403 - 1427\text{ cm}^{-1}$ ). This is noteworthy because there is smaller  $12\text{ cm}^{-1}$  downshift in the wavenumber attributed to the B-O bond deformation after thermal purification of the grey “ash” ( $1196 - 1184\text{ cm}^{-1}$ ) and no significant shift in the wavenumber attributed to the B-O bond stretching that appears after thermal purification of the grey “ash” in Figure 3.17 from the existing peak in Figure 3.15. This indicates that there is a structural shift in the primary phase of Growth 1 after a thermal treatment independent of the secondary phase, which may possibly be attributed to selective oxidation at sites in the BFWNTs where boron has substituted into the graphitic lattice. It is also noteworthy that the emergence of a small peak at a wavenumber representative of C=C phonon modes ( $1639\text{ cm}^{-1}$ ) appears after the oxidation of Growth 1, which is expected due to the clear presence of nanotube in the TEM images of the purified growth in Figure 3.5.

Although it is clear that the inadequate purification of the BFWNT yield prevents the formation of highly conductive spray-coatings, improving the ink dispersion through surface functionalization of the nanotube surface is still observed to impact the spray-coating uniformity and thus improve the electrical properties of the nanotube network. A comparison of spray-coated film properties formed from IPA-based inks containing BFWNTs that either have or have not been refluxed in acid is presented in Table 3.4.

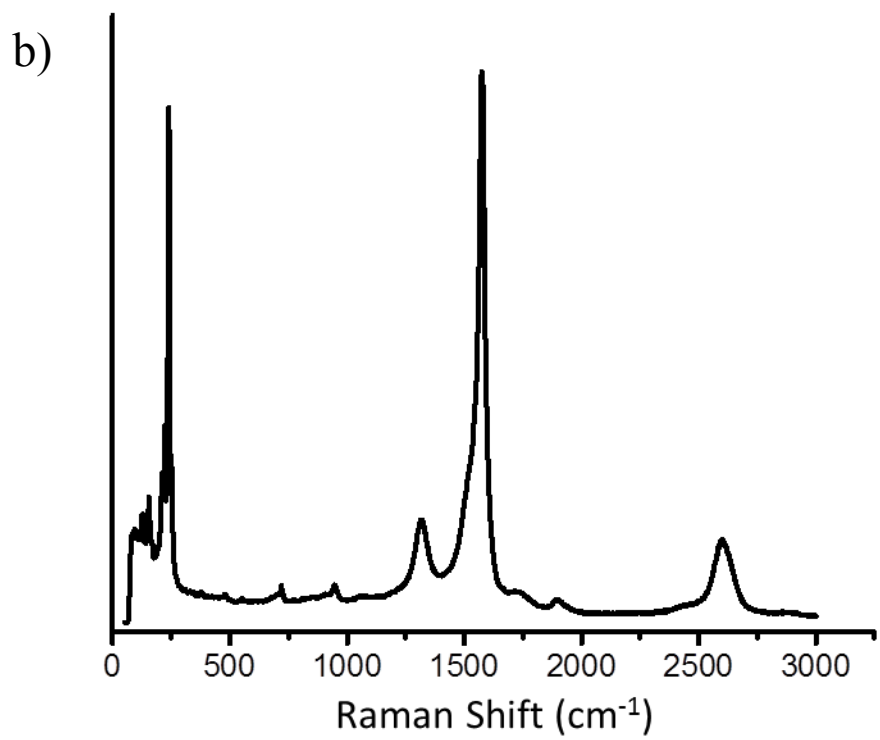
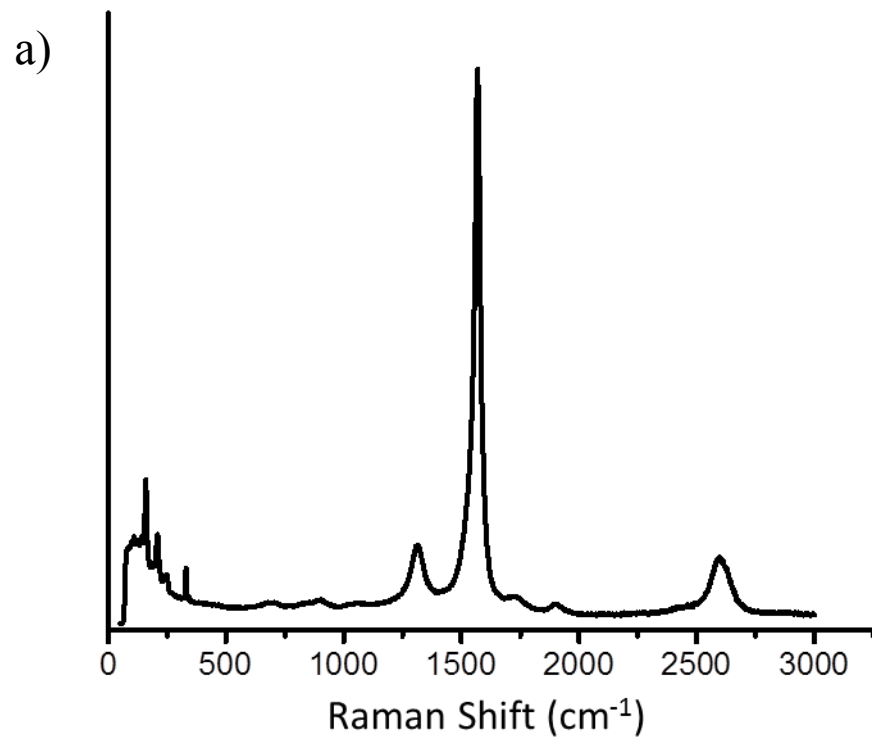
Sample	Zeta potential (mV)	Coating	Thickness ( $\times 10^{-5}$ cm)	Sheet resistance ( $\Omega/sq$ )	Conductivity (S/cm)
BFWNT (1)	-17.2		2.5 – 3	> 10K	< 5
BFWNT (2)	-29.5		6 – 7	138	103.5 – 120.8

**Table 3.4)** A comparison of spray-coated film properties formed from IPA-based inks containing BFWNTs that are synthesized via a CVD conducted at a 850 °C growth temperature with a 2.0 atm% boron source solution containing an ethanol/methanol mixture as a solvent with a 1:1 weight ratio. Each of the BFWNT growths were purified at 500 °C and washed in 100 mL of boiling methanol for 1 hour. Growth BFWNT(2) was dispersed in IPA after being refluxed in a 10 M HNO<sub>3</sub> solution for 2 hours while BFWNT(1) was suspended in IPA without being refluxed. The sheet resistance was measured with a four-point probe while the thickness was measured with a profilometer.

It is clear from the comparison of the zeta-potential of the IPA inks and the resulting surface coatings that the inks consisting of BFWNTs refluxed in 10 M HNO<sub>3</sub> for 2 hours (BFWNT(2)) possess a higher zeta-potential, which results in a higher spray-coating

uniformity. Although the conductivity of the BFWNT(2) spray-coating is higher than that for BFWNT(1), it is more than an order of magnitude lower than the conductivity reached by undoped FWNTs in Chapter 2. This relatively low conductivity may be due to a few reasons: 1) the presence of a disruptive impurity not eliminated by the thermal purification and methanol washing steps, 2) the destruction of BFWNTs in the acid reflux because of greater reactivity due to inherently greater strain from the boron substitution, or 3) higher intrinsic resistance of the BFWNTs due to a greater density of morphological defects than FWNTs.

In order to address the persistence of impurities in the growth yield, a higher oxidation temperature was investigated for the thermal purification. Although the TGA analysis of the sample in Figure 3.12 demonstrates that the elimination of amorphous carbon may be achieved at a sustained temperature of 500 °C, the FTIR analysis in Figure 3.18 demonstrates the presence of O-H bonds and B-O-C bonds at 3352  $\text{cm}^{-1}$  and 1024  $\text{cm}^{-1}$ , respectively. This indicates that there may be an inefficient removal of defective or amorphous material after a thermal purification at 500 °C that may contribute to the impurities that appear in the SEM images of the BFWNT random network in Figure 3.20 and thus lead to the low conductivity we see in Table 3.4. In order to investigate the impact of the oxidation temperature in the thermal purification of the BFWNTs, Raman spectroscopy measurements were performed on as-grown BFWNTs and BFWNTs oxidized at temperatures of 500 °C and 625 °C.





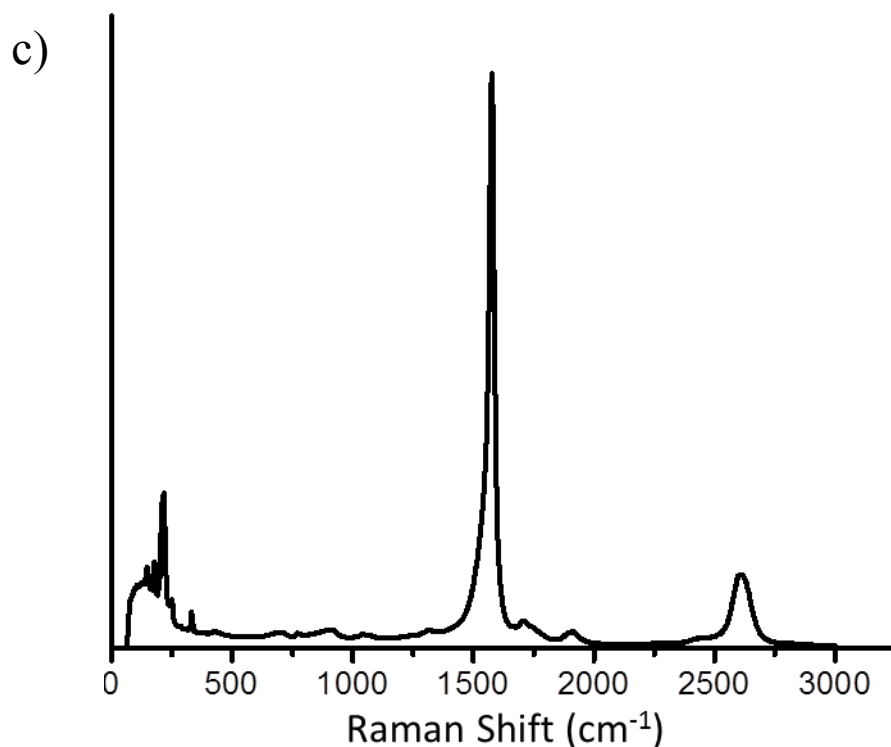


**Figure 3.20)** Raman spectra of BFWNTs that were synthesized via a CVD conducted at a 850 °C growth temperature with a 2.0 atm% boron source solution containing an ethanol/methanol mixture as a solvent with a 1:1 weight ratio (a) as grown, and that were purified at (b) 500 °C and (c) 625 °C.

Sample	D-band (cm <sup>-1</sup> )	G-band (cm <sup>-1</sup> )	G' -band (cm <sup>-1</sup> )	D/G
BFWNT (i)	1308	1569	2609	0.1503
BFWNT (ii)	1321	1576	2608	0.1996
BFWNT (iii)	1316	1578	2602	0.0327

**Table 3.5)** A comparison of the characteristic properties of the Raman spectra in Figure 3.20; BFWNT (i) representing the as grown BFWNTs (Figure 3.20a), BFWNT (ii) representing the BFWNTs that were purified at 500 °C (Figure 3.20b), and BFWNT (iii) representing the BFWNTs that were purified at 625 °C (Figure 3.20c).

Each spectra in Figure 3.20 was normalized by the peak intensity of the G-band; however, the comparisons between each spectra may be made between the wavenumbers of the characteristic bands in each spectra to distinguish any alterations to the intrinsic structure of the BFWNTs after oxidation at each temperature and between the intensity ratios of the D-band and G-band to determine the concentration of defective carbon in each sample. It is clear from the Raman spectra in Figure 3.20 that the presence of defective carbon is dramatically reduced at an oxidation temperature of 625 °C, reflected by the 78% reduction of the D/G ratio to 0.0327 from 0.1503. Interestingly, the D/G ratio of the BFWNT sample purified at 500 °C is about 33% larger than the D/G ratio of the as-grown BFWNTs. This indicates that there is an *increase* in the defective carbon in the BFWNT sample after a thermal purification at 500 °C, while there is a near elimination of the defective carbon after a thermal purification at 625 °C. A possible explanation for this behavior may be derived from the TGA data in Figure 3.12. It is observable in Figure 3.12a that the oxidation temperature of the BFWNTs synthesized in Growth 1 is close to 625 °C, while the oxidation of the BFWNTs begins to gradually intensify at 450 °C. If we connect the behavior of the thermal oxidation from what we observe in the Raman spectra in Figure 3.20, we may infer that a temperature of 500 °C is enough to deteriorate defective BFWNTs without fully oxidizing them. At greater temperatures, such as at 625 °C, amorphous carbon along with defective nanotubes may be oxidized and removed from the growth yield, which is reflected in a significant reduction in the D/G ratio of the oxidized BFWNT sample in Figure 3.20(b) from the as-grown BFWNTs in Figure 3.20(a). Since the lower oxidation temperature enhances the defect density of defective nanotubes without fully burning them away, we see an increase in the D/G ratio


of the oxidized BFWNT yield in Figure 3.20(c) from the as-grown BFWNTs in Figure 3.20(a). This explanation may be further supported by comparing TEM images of BFWNT sample oxidized at 625 °C, as we see in Figure 3.21, to the BFWNTs oxidized at 500 °C that are presented in Figure 3.5.

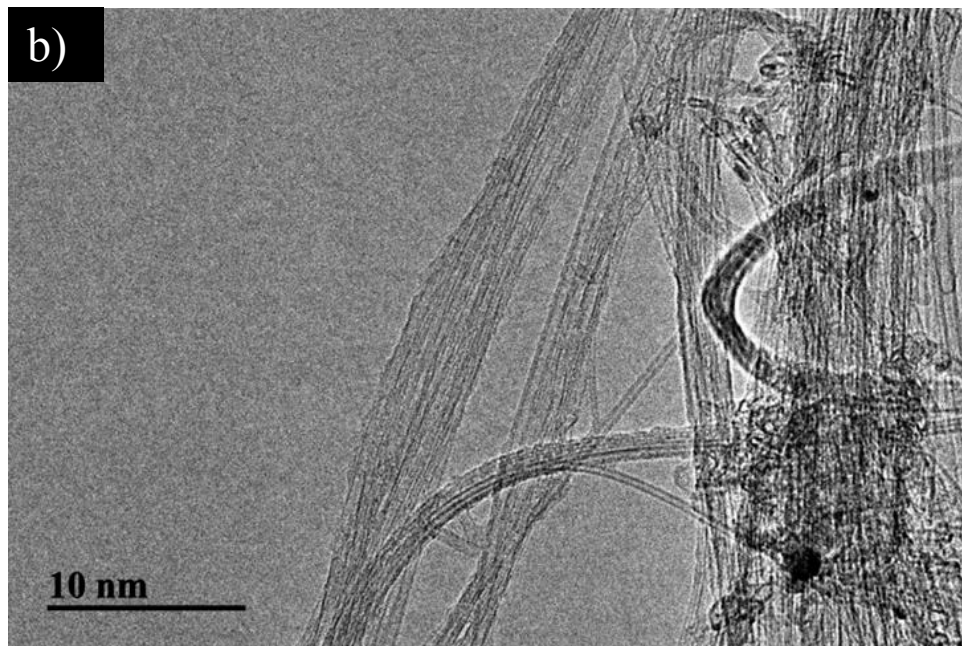
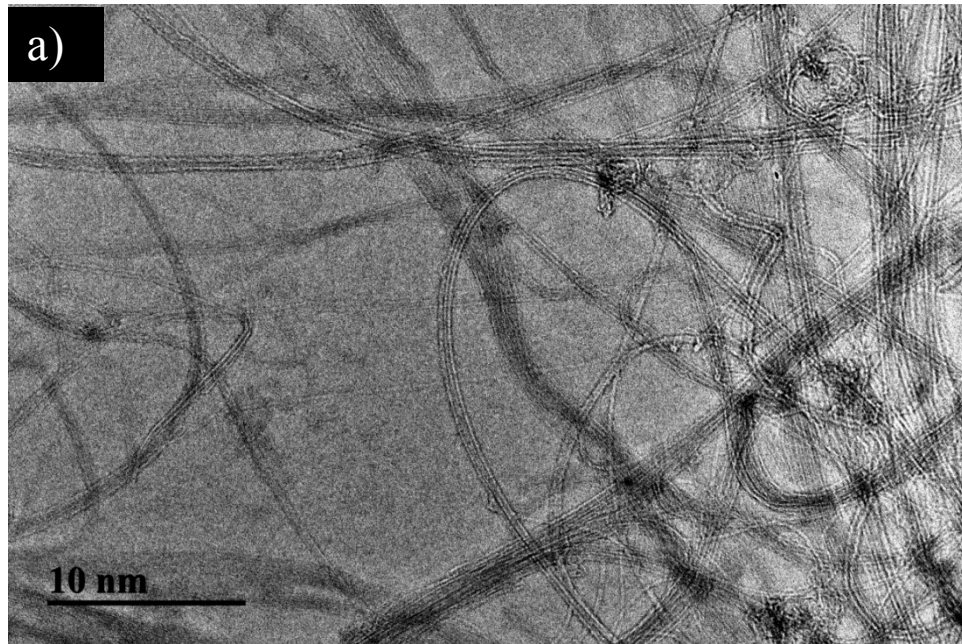


**Figure 3.21)** TEM images of BFWNTs synthesized via a CVD conducted at a 850 °C growth temperature with a 2.0 atm% boron source solution containing an ethanol/methanol mixture as a solvent with a 1:1 weight ratio.

Although the BFWNT samples depicted in the TEM images in Figure 3.5 and Figure 3.21 both demonstrate morphological defects such as kinks or bends, there is a distinguishably greater presence of defective graphitic carbon in Figure 3.5 than in Figure 3.21.

The effect of a higher purification temperature on the electrical properties of the spray-coated BFWNTs was evaluated by oxidizing Growth 1 BFWNTs at 625 °C for 1 hour, washing them in 100 mL of boiling methanol for 1 hour, and dispersing them in IPA following a reflux in a 10 M HNO<sub>3</sub> solution for 2 hours. Table 3.6 outlines the resulting spray-coating characteristics.

Sample	Coating	Thickness (cm)	Sheet resistance ( $\Omega/sq$ )	Conductivity (S/cm)
BFWNT (a)		$4 - 5 \times 10^{-5}$	116	172.4-215.5

**Table 3.6)** The spray-coated film properties formed from IPA-based inks containing BFWNTs that were synthesized via a CVD conducted at a 850 °C growth temperature with a 2.0 atm% boron source solution containing an ethanol/methanol mixture as a solvent with a 1:1 weight ratio. The BFWNT growth was purified at 625 °C, washed in 100 mL of boiling methanol for 1 hour, and dispersed in IPA following a reflux in a 10 M HNO<sub>3</sub> solution for 2 hours.

We see that a more effective elimination of the defective carbon impurities from the growth yield results in random networks of BFWNTs with greater conductivities than demonstrated for BFWNTs oxidized at 500 °C. Since the coating uniformity is good for

both BFWNT(a) and BFWNT(2), we may conclude that the greater conductivity of the random network in BFWNT(a) is achieved by better eradicating disruptive impurities from the film. It is noteworthy that although the conductivity of the BFWNT spray-coating increases after instituting a higher oxidation temperature during the thermal purification process, the conductivity is still much lower than what is achievable for the undoped FWNTs in Chapter 2. A distinct possibility that may explain this behavior is that a higher density of morphological defects causes the BFWNTs to have a higher intrinsic resistance than undoped FWNTs.

### 3.4 Summary

In conclusion, we introduce a new method to fabricate a novel boron-doped few walled carbon nanotube structure via a solution injected CVD synthesis method. Initial characterization of the B-FWNTs reveals that the graphitic lattice contains varying amounts of boron, which is reflected in EELS and Raman spectroscopy measurements. An investigation into the effect of the growth parameters on the B-FWNT structure revealed that a higher concentration of methanol in the source solution forms B-FWNTs with a lower thermal stability and a greater concentration of defective carbon. Additional studies on the impurity phases present in the growth yield and purification steps to eliminate them revealed the presence of boron oxide among the B-FWNTs, which was proven to be effectively removed from a methanol wash purification step. Although the conductivity of subsequent spray-coated B-FWNT inks were demonstrated to be lower than undoped FWNTs, the surface functionalization of the B-FWNTs similarly showed better film uniformity than for untreated B-FWNTs.

## Chapter 4: Haze of Transparent and Conductive Silver Nanowire Electrodes

### 4.1 Silver nanowire transparent electrodes

A solar cell generates power by absorbing light and exciting electrons from a semiconductor p-n junction layer. A critical component of solar cells is the top electrode facing the sun, which must be conductive to adequately collect and carry extracted charges and also transparent to permit the highest intensity of light to absorb into the solar conversion layers. Transparent conducting electrodes in solar cells are typically composed of indium tin oxide (ITO) due to its low sheet resistance and high transparency. Despite these preferred properties for TCEs, ITO is limited by poor mechanical properties, scarce indium resources, and expensive manufacturing methods.<sup>[111, 112]</sup> Recent efforts to develop an alternative TCE that is suitable for flexible and robust optoelectronic devices have rendered encouraging results for various materials such as carbon nanotubes, graphene, conductive polymers, metal oxides, and metallic nanowires.<sup>[113-119]</sup> Among these reports, TCEs formed from networks of silver nanowires have emerged as a competitive alternative to ITO.<sup>[120]</sup> The following subsections elucidate the optimal theoretical characteristics for TCEs formed from Ag NW networks.

#### 4.1.1 Optical properties of silver nanowires

We discussed in Section 2.2.2 that the structure of the conducting sticks in a percolation network and the uniformity of the coverage density affect the conductivity of the random network. The optical properties of a Ag NW electrode also depend on the physical characteristics of the individual Ag NWs and the density of Ag NWs that form

the conductive network. Due to the high reflectivity of Ag NWs in visible peaks, higher film porosity as determined by a lower Ag NW area fraction  $A_F$  permits networks with higher transparency.<sup>[23]</sup> Although reducing the diameter of the Ag NWs with a fixed length in a network with a fixed number density will decrease the area fraction  $A_F$ , decreasing the nanowire diameter in networks with a low  $A_F$  will still dramatically increase the transmittance of visible light through the electrode. The effect of the diameter on the transparency may be determined using a finite-difference time-domain simulation that calculates the dimensionless ratio of optical and geometrical cross-sections:

$$Q_{ext} = Q_{abs} + Q_{scat} \quad (4.1)$$

where  $C_{ext}$  represents the extinction coefficient, which is the sum of the absorption coefficient  $C_{abs}$  and the scattering coefficient  $C_{scat}$ . Further explanation of the FDTD simulation mechanism is given in Section 4.3.1. Bergin et al. reports that  $C_{scat}$  increases from 3% to 147% as the diameter of individual nanowires increases from 10 nm to 100 nm, indicating that larger diameters may reflect more light at greater distances from the nanowire surface. Thus decreasing the diameter of the Ag NWs reduces the reflected scattering phenomena by the conductive channels, which ensures high electrode transparency.<sup>[23, 27, 121, 122]</sup>

#### 4.1.2 Optoelectronic performance of Ag NW TCEs

A figure of merit for TCEs is used to combine the optical transparency and sheet resistance into a single quantitative performance metric used to compare experimental reports. The expression for the sheet resistance  $R_s$  of a bulk-like film is given by Equation 4.2:

$$R_s = (\sigma_{DC} t)^{-1} \quad (4.2)$$

with  $\sigma_{DC}$  representing the DC conductivity and  $t$  representing the thickness of the film.

The transmittance  $T$  of a nanostructured material is given by Equation 4.3:

$$T = \left(1 + \frac{Z_0}{2} \sigma_{op} t\right)^{-2} \quad (4.3)$$

with  $\sigma_{op}$  representing the optical conductivity and  $Z_0$  representing the impedance of free

space, which may be defined as  $Z_0 = \sqrt{\frac{\mu_0}{\epsilon_0}}$ . The boundary condition for Equation 4.3 is

that the TCE film is much thinner than the incoming peaks incident on its surface, which allows us to assume that the imaginary part of the absorption coefficient is negligible.

The final relation between the transmittance and sheet resistance is described by Equation

4.4:

$$T = \left(1 + \frac{1}{2R_s} \sqrt{\frac{\mu_0}{\epsilon_0}} \frac{\sigma_{op}}{\sigma_{DC}}\right)^{-2} = \left(1 + \frac{188(\Omega)}{R_s} \frac{\sigma_{op}}{\sigma_{DC}}\right)^{-2} \quad (4.4)$$

where  $\frac{\sigma_{DC}}{\sigma_{op}}$  is a dimensionless value defined as the figure of merit used to compare the

performance of various TCEs.<sup>[121, 122]</sup> Reports indicate that Ag NWs with a high aspect

ratio ( $l/D > 100$ ) due to small diameters ( $< 100$  nm) and large lengths ( $> 10$   $\mu$ m) are

important to achieve high performance TCEs, such as in Figure 4.1.<sup>[121]</sup>



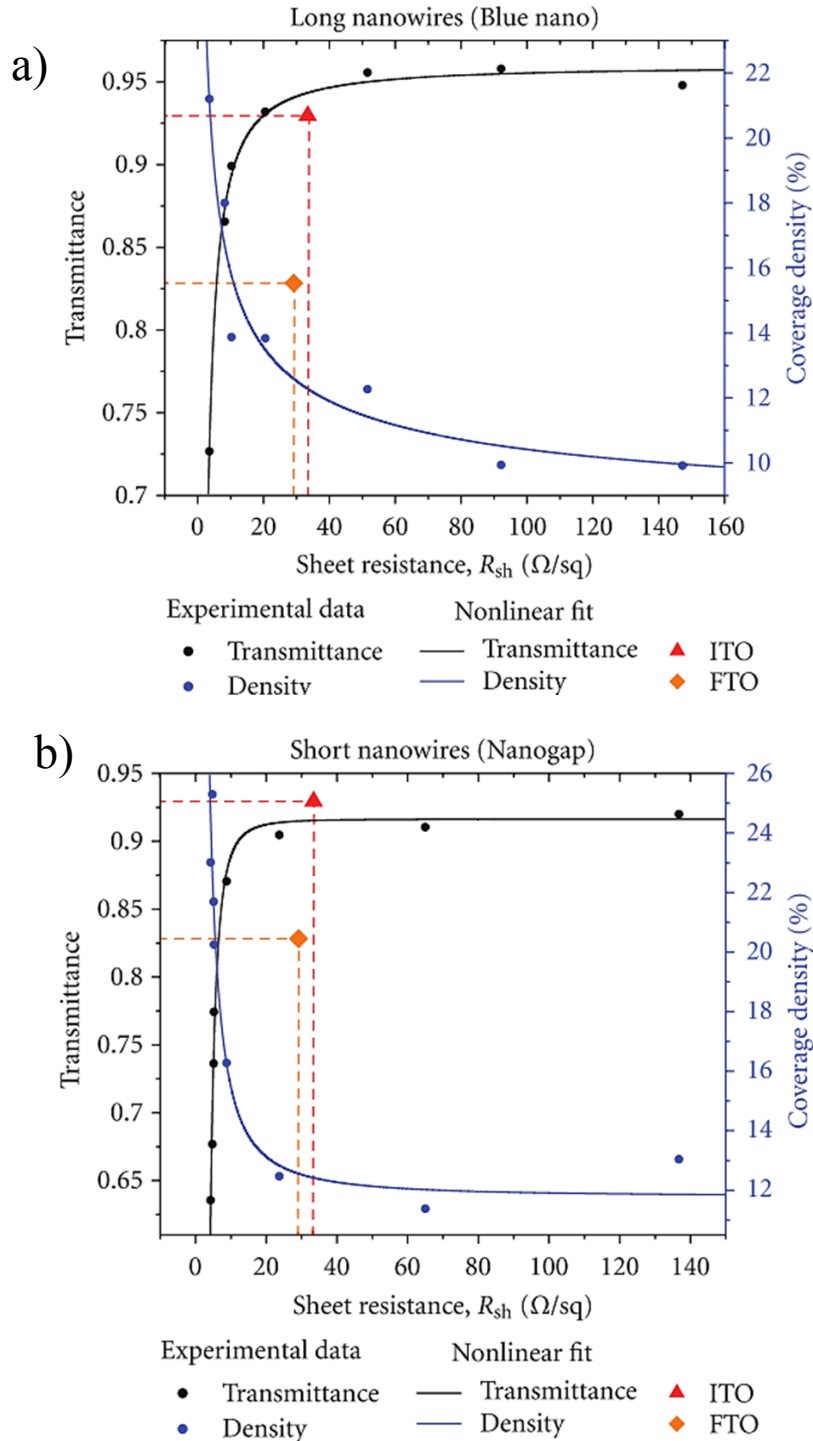


**Figure 4.1)** Plots of the transmittance and coverage density with respect to sheet resistance for networks of (a) long Ag NWs ( $19 \mu m$ ) purchased from Blue nano and (b) short Ag NWs ( $11 \mu m$ ) purchased from Nanogap compared to ITO and fluorine doped tin oxide (FTO). Non-linear curve fits of the experimental data for the transmittance and coverage density are also plotted for each of the short and long nanowire samples. This figure is printed from Sepulveda-Mora, et al., J. of Nanomaterials, 2012.<sup>[121]</sup>

Another conclusion from the comparison of literature reports on TCEs formed from Ag NW inks is that the fabrication process impacts the optoelectronic performance due to variations in surface coating properties and results from post-deposition treatments.

## 4.2 Silver nanowire transparent electrode fabrication

### 4.2.1 Silver nanowire synthesis

According to Sections 2.2.2 and 4.1.3, Ag NWs that are very long ( $> 100 \mu\text{m}$ ) with small diameters ( $< 100 \text{nm}$ ) project as the optimal geometry for both the percolation of current across the electrode and the transmittance of light through the electrode.<sup>[27, 122]</sup> Nanowires that exhibit these geometrical characteristics are referred to as having a high aspect ratio, which is the ratio of nanowire length to the diameter. The most common method to synthesize Ag NWs that may be dispersed in an ink solution begins with a seed mediated growth.<sup>[124-127]</sup> Silver nanoparticles are first formed by reducing a metallic salt (AgCl) into silver ions that condense into decahedral crystals three to five nanometers in diameter in a polyol solution (ethylene glycol), as seen in Figure 4.2.<sup>[125]</sup>

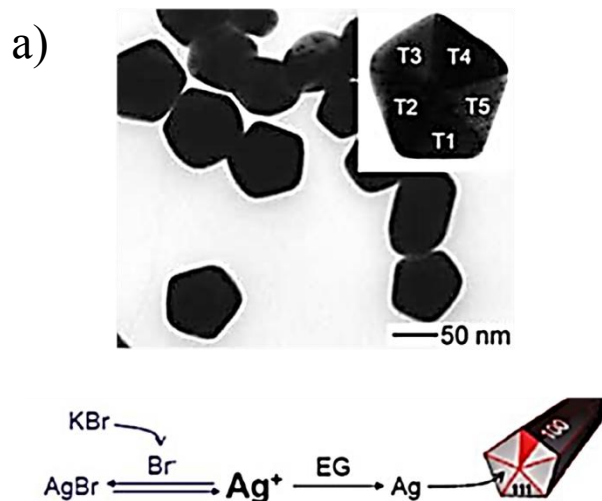


**Figure 4.2** (a) A TEM image of silver seeds for nanowire growth (inset demonstrating the crystal planes). This image was printed from Sun et al., *Nanoscale*, 2010.<sup>[19]</sup> (b) A schematic of a silver nanowire seed mediated growth reaction where the silver seed solution that act as nucleation sites for titrated silver ions ( $\text{Ag}^+$ ). The simultaneous formation of silver bromide ( $\text{AgBr}$ ) from the addition of a competing salt ( $\text{KBr}$ ) in the seed solution tapers the nucleation of silver ions on the seed particles in order to monitor the diameter. The presence of ethylene glycol ( $\text{EG}$ ) perpetuates the one-dimensional propagation of nanowire growth by bonding to the (100) planes of the nanowire.

The high surface energy of the [111] planes of the decahedral silver seed particles separated by twinned boundaries act as nucleation sites for additional silver ions to crystallize and grow into nanowires. The additional silver ions are supplied via a polyol reduction of silver nitrate ( $\text{AgNO}_3$ ) carefully titrated into the heated seed solution. The duration of this titration and the concentration of  $\text{AgNO}_3$  dissolved in the seed solution determine the length of the nanowires, while the drop rate of the titration impacts the nanowire diameter. In order to promote uniaxial propagation of the silver ions crystallizing on the seed particles, a polymer (CTAB, PVP, etc) is also included in the seed solution. Such polymers form a micelle around the [100] crystal planes that exist along the nanowire axis, which regulates the crystallization of the silver ions to the five-

fold multiple twinned [111] planes on the nanowire endcaps during the titration of  $\text{AgNO}_3$ . Reports also indicate that the addition of a small amount of a competing salt such as  $\text{KBr}$  or  $\text{CuCl}$  in the seed solution can taper the crystallization of silver ions onto the seeds and promote thinner diameters, as depicted in Figure 4.2b.<sup>[4, 124, 126]</sup>

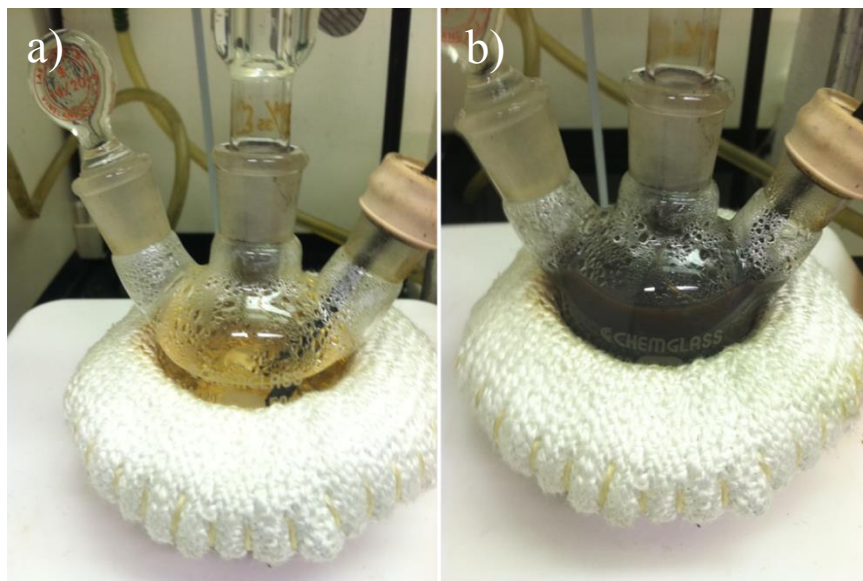


**Figure 4.3)** Images of the (a) seed solution before the titration of  $\text{AgNO}_3$  and (b) the solution after the titration of  $\text{AgNO}_3$ , where the translucent yellow seed solution has transformed into a brownish-grey opaque solution.

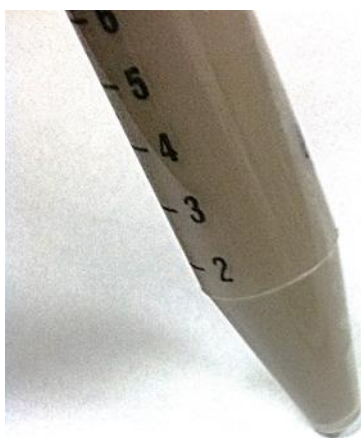


**Figure 4.4)** A silver nanowire ink solution in a centrifuge vial.

Figure 4.3 illustrates the color change of the growth solution after the  $\text{AgNO}_3$  titration to the seed solution, indicating the growth of Ag NWs. After the silver nanowire growth is terminated by cooling the solution and removing the polymer and salt impurities from solution via centrifugation in methanol, the nanowires may be evenly dispersed in a water or alcohol-based ink as seen in Figure 4.4.

#### 4.2.2 Silver nanowire electrode formation

In addition to maximizing the aspect ratio of the Ag NWs, networks of uniformly dispersed conducting channels promote the highest transmittance at the lowest sheet resistance. A uniform network ensures even percolation across the electrode and prevents areas with greater reflective losses than individual Ag NWs due to a localized high number density. Silver nanowires that are suspended in solution may be deposited through various methods to form random networks of Ag NWs that serve as transparent electrodes; these methods include spray-coating,<sup>[131]</sup> electrospinning,<sup>[117]</sup> electrostatic spray-deposition,<sup>[132]</sup> chemical etching,<sup>[134]</sup> Meyer rod coating,<sup>[124]</sup> and dip-coating.<sup>[121]</sup> Each method has its own challenges to efficiently preserve the dispersion achieved in the ink suspension during the deposition process. A simple drop-cast can deposit Ag NW inks onto a substrate, but the coatings often form nanowire agglomerations within the network.<sup>[130]</sup> This is due to uneven evaporation rates of droplets with large wetting thicknesses, which may be prevented with more precise coating techniques such as Meyer rod coating or spray-coating.<sup>[131-134]</sup>

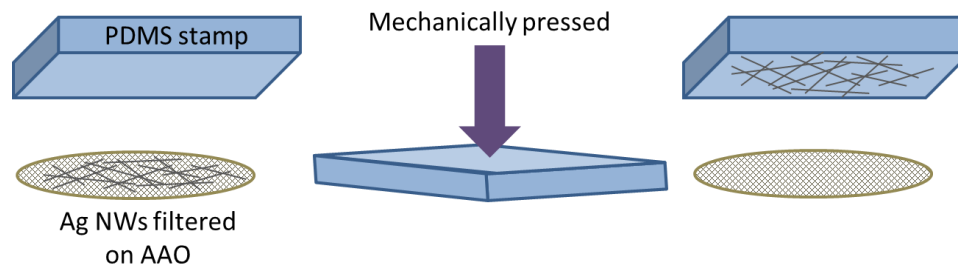


**Figure 4.5)** A schematic illustrating the dry-transfer process for fabricating TCEs on a PDMS stamp that delaminates a uniform filtered random network of Ag NWs off its AAO filter.

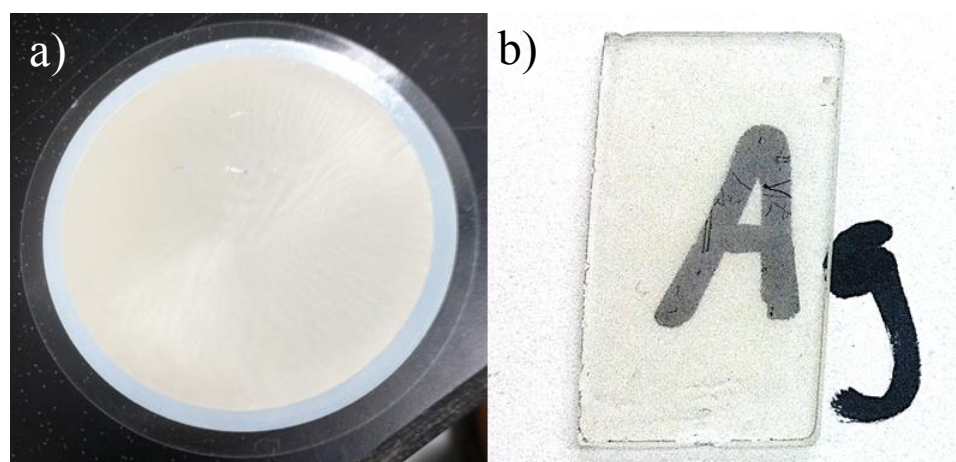


**Figure 4.6)** Images that illustrate (a) a vacuum filtered Ag NW network derived from an ink suspension and (b) an example of a dry-transferred electrode random network of Ag NWs on a PDMS substrate.

Filtrations of dilute Ag NW inks onto microporous filters exhibit very high uniformity of the Ag NW network since the stable suspension remains intact for the duration of the solvent removal. Madaria et al. demonstrates a dry-transfer method to form a TCE from a Ag NW network formed via a filtration; a Ag NW network is peeled off an anodic aluminum oxide (AAO) microporous filter with a transparent flexible polydimethylsiloxane (PDMS) “stamp,” which is illustrated in Figure 4.5. The dry-transfer method is advantageous because it may be conducted at room temperature without the need to adjust various deposition parameters such as with spray-coating or

electrostatic spray deposition. The dry-transfer method is utilized to find the transparent electrodes studied in this chapter, as diagrammed in Figure 4.6.

### 4.3 Transmission haze in TCEs

Transmission haze or transmission haze is an important characteristic of transparent electrodes in solar cells because it offers a unique advantage for light trapping in thin-films. Thin-film modules offer a host of benefits in commercial photovoltaic devices; such as flexibility, lower costs, lighter weight, and smaller modular size for handheld devices. The primary limitation in thin-film solar cells is a low absorbance of wavelengths near the bandgap of the semiconductor, especially in cases of indirect semiconductors like silicon as seen in Figure 4.7. Significant efforts are being made, therefore, to introduce light trapping mechanisms that improve the light absorption in the thin solar conversion layers.<sup>[135-137]</sup> Since diffuse light scattering causes transmitted light to propagate at an angle from the incident axis, the path length of diffuse transmitted light is longer than the path length of specular transmitted light, as seen in Figure 4.8. This enables more light to be absorbed in the conversion layers of thin-film solar cells, and thus enhances the current density of those solar cells.<sup>[138-140]</sup> While most reports indicate that large aspect ratios achieved by small diameters and long lengths best optimize the performance of Ag NW TCEs, larger diameters are conversely attributed to larger scattering cross-sections. The study in this chapter elucidates the significance of haze in evaluating nanostructured TCE performance in solar cells, and calls in to question the contemporary figure of merit for such TCEs.

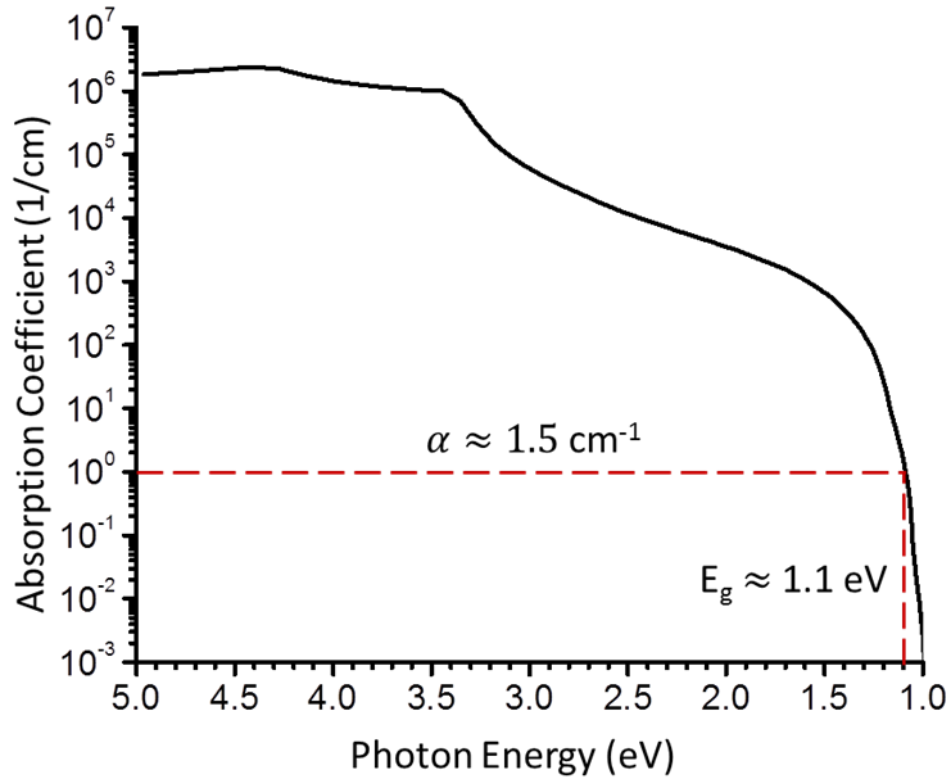
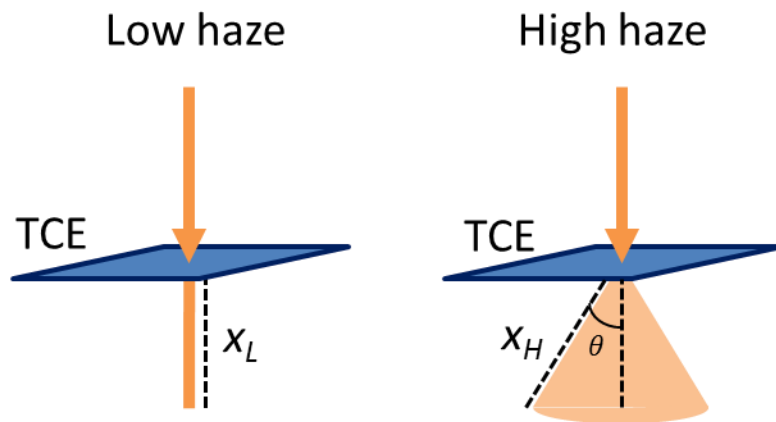


**Figure 4.7)** A plot of the photon energy of incident light waves versus the absorption coefficient of silicon that demonstrates thin films of silicon ( $< 1 \mu m$ ) are inadequate absorbers of light at their band gap energy.



$$A = \log (e^{\alpha x})$$

**Figure 4.8)** A schematic that demonstrates path length of light propagating through a TCE with high optical haze is longer than for low optical haze, which enables greater light absorption in the conversion layer beneath the TCE in the solar cell stack.



#### 4.3.1 Mie theory of diffuse light scattering

The Mie scattering theory describes the interaction of spherical particles in the presence of external electromagnetic waves.<sup>[141]</sup> The balance of energy during these interactions and the propagation of scattered waves are deduced through a discussion involving the Poynting theorem. The Poynting theorem states that the rate of electromagnetic energy  $W$  that propagates out normal to a surface  $A$  may be described by:

$$W = - \oint \mathbf{S} \cdot \hat{n} dA \quad (4.5)$$

where  $\mathbf{S} \equiv \frac{1}{\mu_0} (\mathbf{E} \times \mathbf{B})$  is the Poynting vector that describes the energy per unit time per unit area, or the energy flux density. This is more conveniently utilized as the time averaged energy flux crossing a unit area, or power flow per unit area:

$$\langle \mathbf{S} \rangle = \frac{1}{2\mu_0} \text{Re}\{\mathbf{E} \times \mathbf{H}^*\} \quad (4.6)$$

If we consider an imaginary sphere of radius  $a$  and surface  $A$  around a finite particle, we find that the rate of energy removed from the incident waves is expressed as a sum of the energy scattering rate and energy absorbing rate of the particle.

$$W_{abs} = W_0 - W_{sca} + W_{ext}$$

$$W_0 = - \oint \mathbf{S}_0 \cdot \hat{e}_a dA$$

$$W_{sca} = \oint \mathbf{S}_{sca} \cdot \hat{e}_a dA$$

$$W_{ext} = - \oint \mathbf{S}_{ext} \cdot \hat{e}_a dA$$

where  $\hat{e}_a$  represents a unit vector normal to the spherical surface.

In a non-absorbing medium:

$$W_{ext} = W_{abs} + W_{sca} \quad (4.7)$$

These rates may be normalized into optical cross-sections  $C$  that are relative to the intensity of the incident waves  $I_0$  and then further normalized by the geometrical cross-section of the particle  $G$  to arrive at dimensionless efficiency factors  $Q$ .

$$C = \frac{W}{I_0} \left\{ \begin{array}{l} C_{sca} = \frac{W_{sca}}{I_0} , C_{abs} = \frac{W_{abs}}{I_0} , C_{ext} = \frac{W}{I_0} \end{array} \right. \quad (4.8)$$

$$Q = \frac{C}{G} \left\{ \begin{array}{l} Q_{sca} = \frac{C_{sca}}{G} , Q_{abs} = \frac{C_{abs}}{G} , Q_{ext} = \frac{C_{ext}}{G} \end{array} \right. \quad (4.9)$$

These efficiency factors describe the penetration of scattering and absorbing interactions beyond the geometrical boundaries of the particle. Bohren and Huffman extrapolate efficiency factors for infinite non-absorbing cylinders, and demonstrate that the scattering efficiency normal to the cylinder axis heavily depends on the cylinder radius and incident angle.<sup>[141]</sup> The diffuse scattering efficiency of waves with incident angles normal to the tube axis theoretically increases for larger cylinder radii.<sup>[142]</sup>

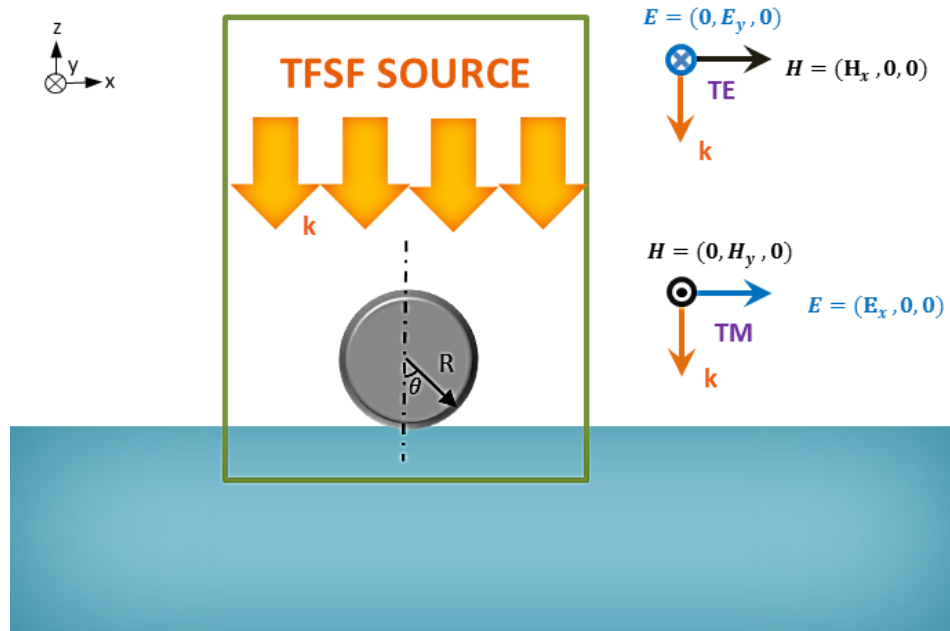


**Figure 4.9)** Schematic of the 2D simulation setup used to calculate the light scattering behavior at normal incidence from a single silver nanowire with a radius of  $R$ . The center of the nanowire is the origin of the axes. The green box represents a Total Field Scattered Field (TFSF) source with a length of 500 nm in the  $x$ -direction. The length is chosen according to the average spacing between Ag NW as calculated from SEM images.

Investigations into the scattering cross-sections of nanowires depicted by elliptical cylinders<sup>[143]</sup> and arbitrary cross-sections<sup>[144]</sup> have also been investigated. Regardless of the symmetry of the nanowire cross-section, Bessel and Hankel functions are the fundamental components to describe the scattered external and internal field. These fields are quantized in a FDTD simulation by measuring the power flux (Poynting vector) through monitored planes in a scattering model, as exemplified in Figure 4.9. A cylindrical Ag NW with a large aspect ratio rests on a semi-infinite dielectric plane. A plane wave with either a TE or TM polarization (as defined in the inset) is incident on the nanowire from above and is perpendicular to the plane of the substrate. Monitors are put outside the Total Field Scattered Field source (green box in Fig. 4.9) to detect the scattered power flow (time-averaged Poynting vector) in order to get the forward scattered power (i.e. power that resides within an angle of 90° from the z-axis). The ratio of these measured quantities introduces a term  $f$ , which represents the fraction of forward scattering of the total scattering of an incident plane wave on the nanowire:<sup>[123, 145]</sup>

$$f = \frac{P_{forward}}{P_{total}} = \frac{C_{forward}}{C_{total}} \quad (4.10)$$

Since the Poynting vector and the resulting scattering mechanism are different between TE and TM modes, each mode must be simulated separately in order to monitor the different forward scattering fractions and then averaged to get the total averaged forward scattering fraction for the incident radiation.

#### 4.3.2 Measuring transmission haze of TCEs

The large diffuse scattering efficiency theorized by Mie scattering models of infinite cylinders is supported by reports on the optical properties of Ag NW networks.

Typical transparency measurements report the total transmittance of light through the sample; however, this measurement fails to distinguish specular transmittance from diffuse transmittance. Light waves that pass through the pores in the Ag NW network without interacting with the nanowires transmit along the same axis as the incident light source, and are categorized by specular transmittance. Light waves that Ag NWs diffusely scatter through the network at angles from the incident source axis are categorized by diffuse transmittance. The ratio of diffuse transmittance to the total transmittance of a transparent electrode is referred to as transmission haze.

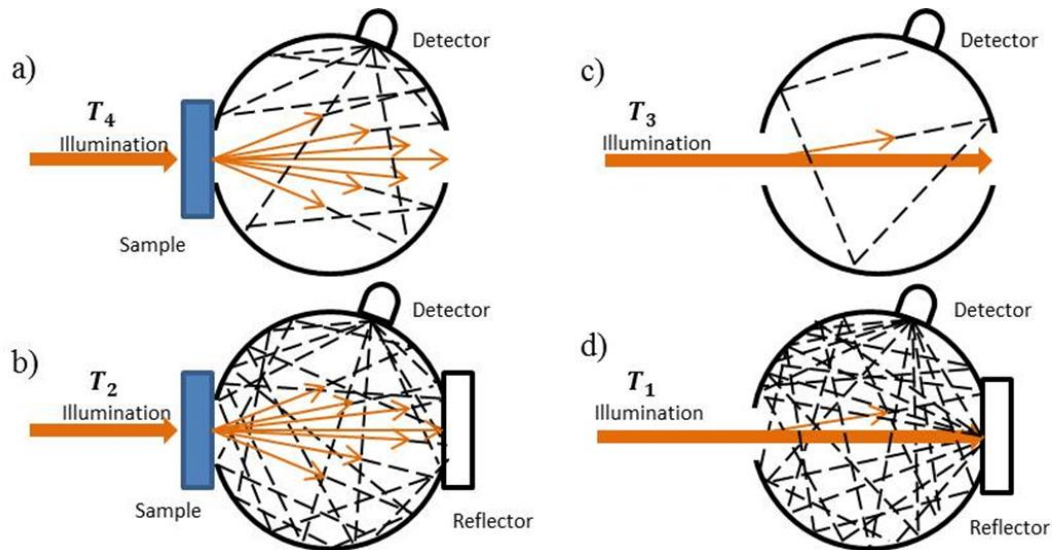


**Figure 4.10)** A schematic illustrating the experimental mechanism used to measure the transmission haze of a substrate with an integrating sphere and a back reflector; (a) the total diffuse scattering through the substrate is measured by detecting the light that does not transmit through the open window at a  $0^\circ$  angle from the perpendicular axis to the surface of the substrate, (b) the total transmittance through the substrate is measured by placing a white reflecting surface at the back window so as to detect all the light transmitted through the substrate, (c-d) and the experimental error of the system is measured to be subtracted from the data taken.

The diffuse transmittance and total transmittance may be individually measured with an integrating sphere in conjunction with a UV-Vis spectrometer in order to determine the transmission haze of a Ag NW transparent electrode. A schematic that

distinguishes each measurement is given by Figure 4.10. The transmission haze is thus calculated through the ratio of the diffuse transmittance and the total transmittance upon correcting for the experimental error caused by beam alignment and reflection losses through the open sample window:

$$H\% = \frac{T_4}{T_2} - \frac{T_3}{T_1} \quad (4.11)$$

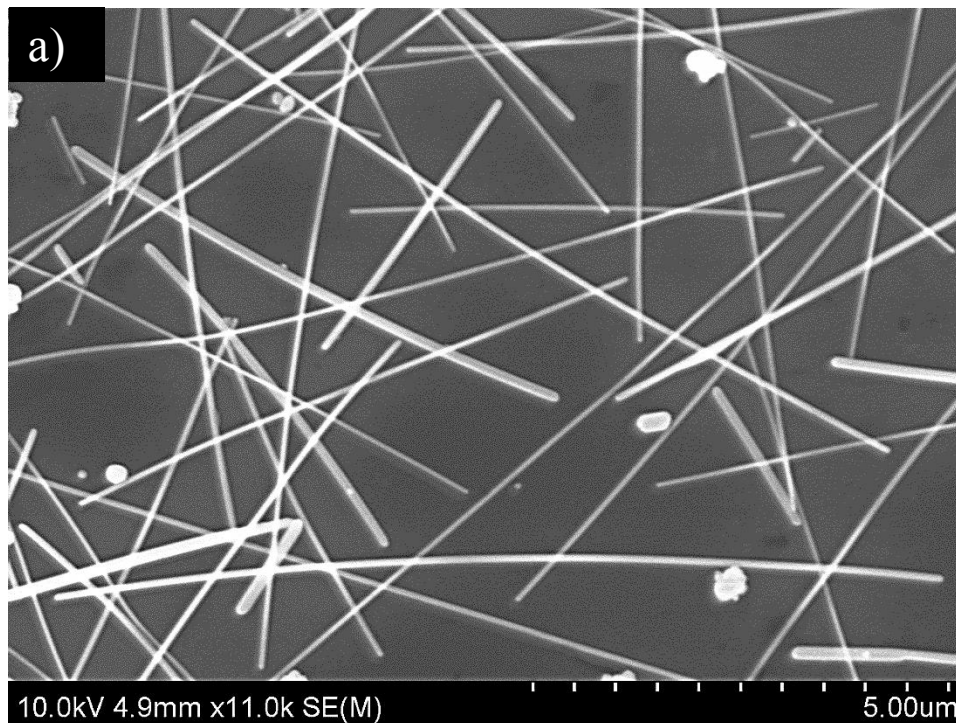
In this chapter, (1) the haze factor of small and large diameter individual Ag NWs is calculated and compared using Finite Difference Time Domain simulations, (2) the contemporary TCE figures of merit were compared for small and large diameter Ag NW TCE films, and (3) the haze factor of small and large diameter Ag NW TCE films with comparable sheet resistance and transparencies was experimentally measured and compared.

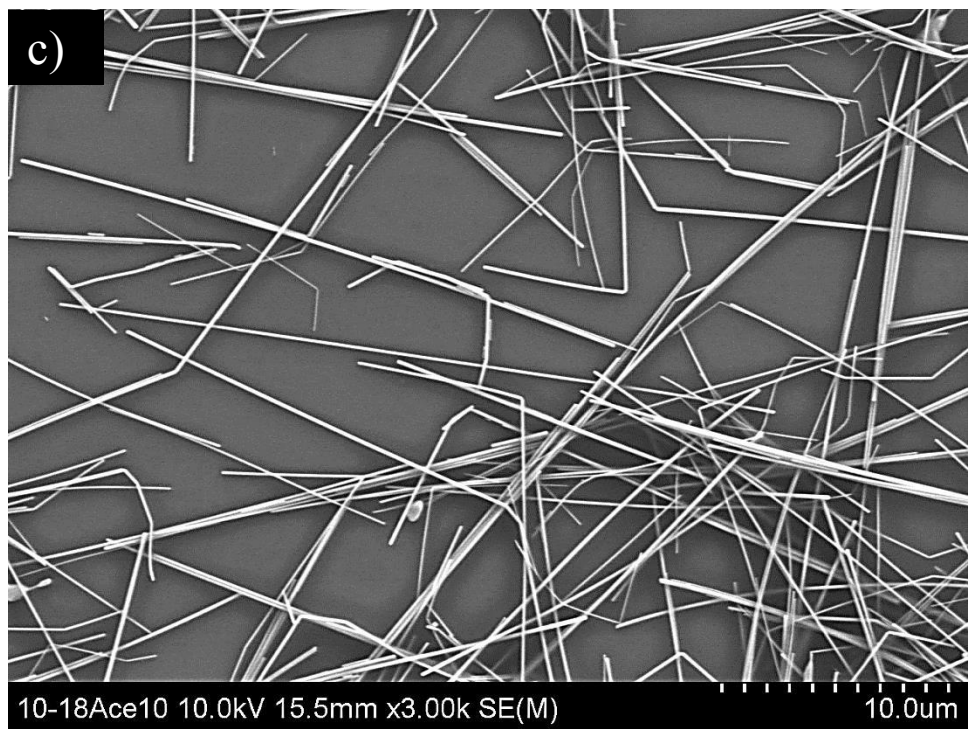
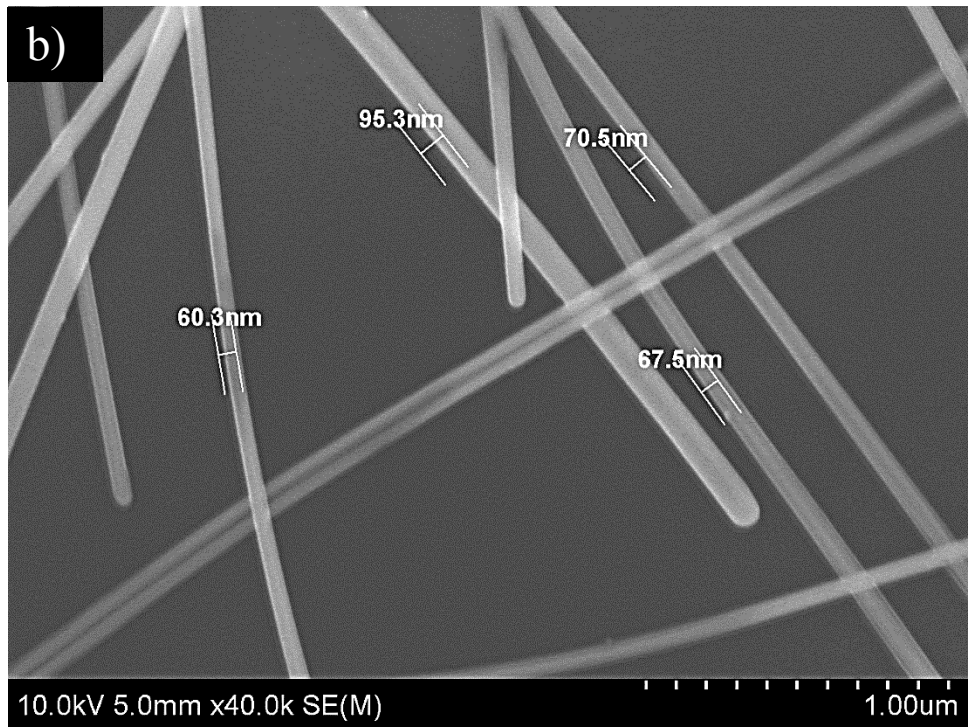
#### 4.4 Experimental Method

A seed mediated growth process with a slow titration method was used to fabricate Ag NWs with small diameters.<sup>[130, 146]</sup> The synthesis begins with a mixture of 0.668 g of polyvinylpropylene (PVP) and 0.022 g of KBr in 20 mL of ethylene glycol being heated to 170°C for 20-30 min. The silver seeds are then introduced to the solution by adding 0.050 g of silver chloride (AgCl) into the solution. This is followed by a slow titration of the growth solution, 0.220 g silver nitrate (AgNO<sub>3</sub>) in 10 mL of ethylene glycol, for 12-15 min. The titration of the AgNO<sub>3</sub> progressively stacks Ag<sup>+</sup> ions onto the silver seeds, while the PVP restricts this stacking to anisotropic growth of a 1D nanowire, and the KBr salt precursor moderates the wire diameter to ensure long thin nanowires. The solution remains at 170°C for 30 additional minutes to complete the nanowire

growth. The dispersion is then centrifuged three times with methanol at 6000 rpm for 30 min. each time to extract the nanowires from the dispersion. Silver nanowires with an average diameter of 150 nm dispersed in ethanol were also purchased from Blue Nano.

Figure 4.11 displays SEM images taken by a Hitachi SU-70 SEM of Ag NWs synthesized with the seed mediated growth with an average radius of 60-70 nm and length of about 25  $\mu\text{m}$  and the purchased Ag NWs with an average diameter of about 150 nm and length of about 20  $\mu\text{m}$ . It is observable from these images that there is high uniformity in length and diameter for both Ag NW yields, and there is a negligible presence of nanoparticles impurities. Ag NW films were transferred onto PDMS substrates via a dry-transfer method from a vacuum filtration onto Anopore aluminum oxide (AAO) substrates purchased from Anodisc.





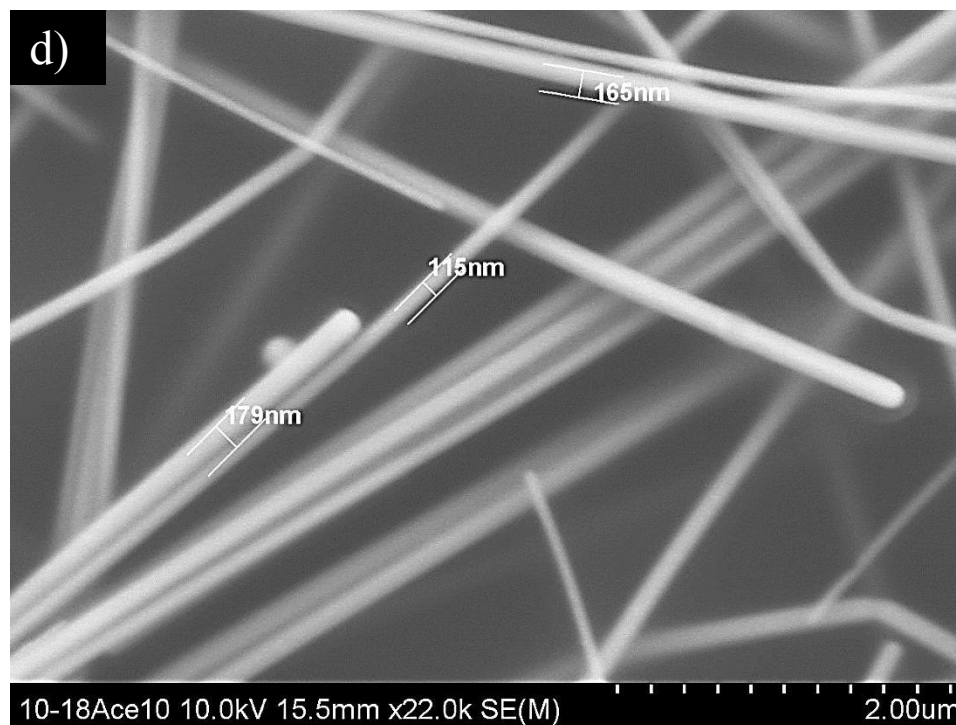
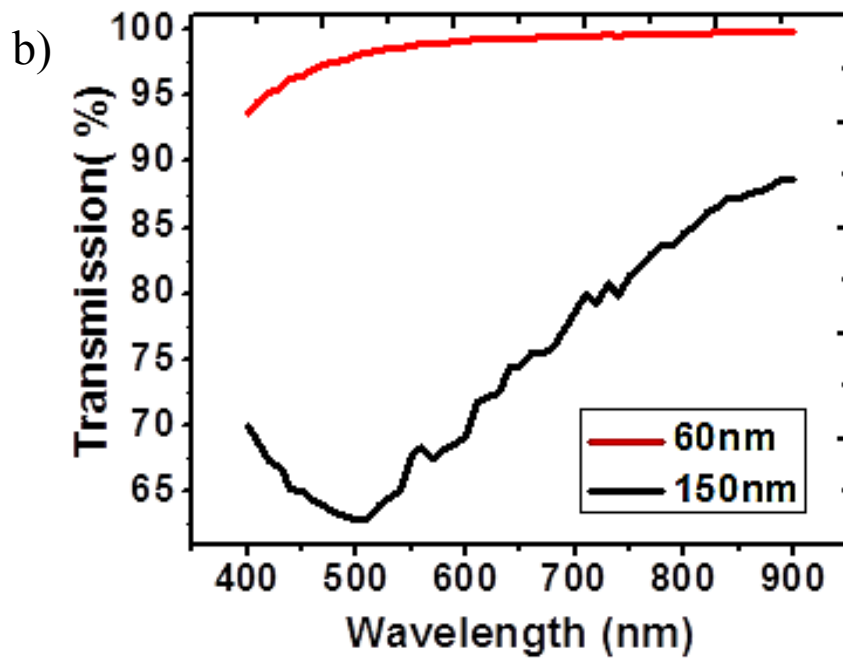
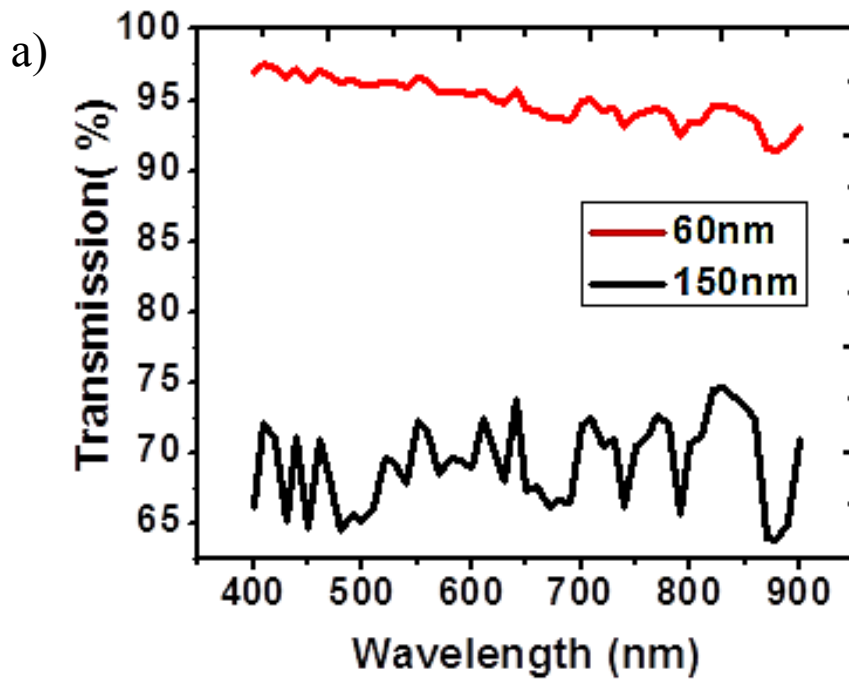


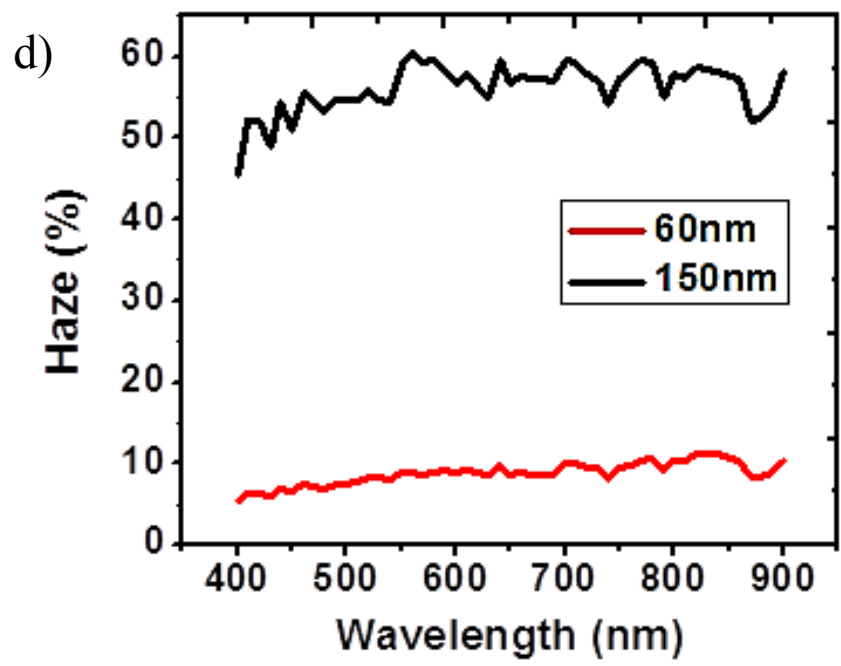
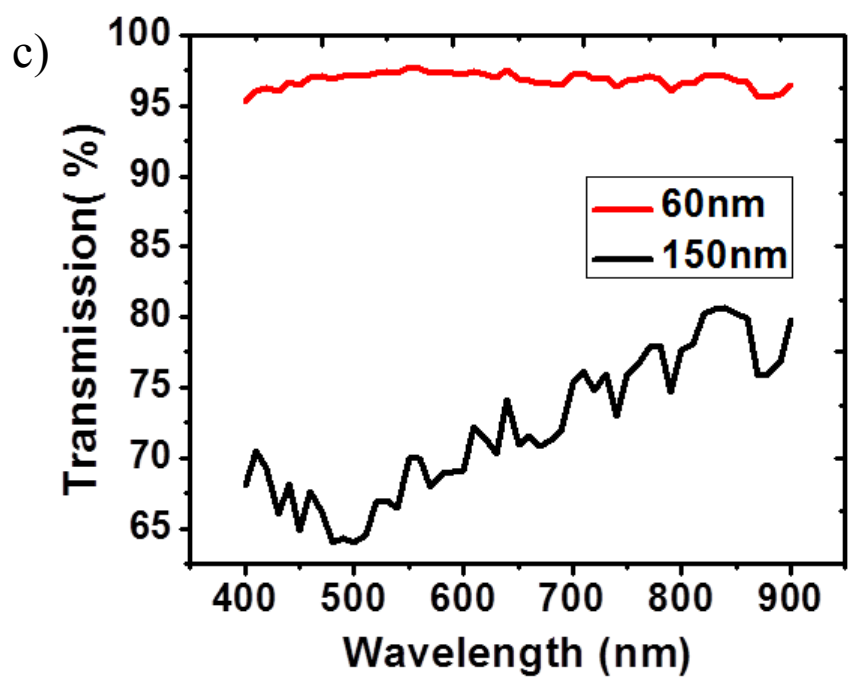
**Figure 4.11)** The SEM images of Ag NW; a) percolation network of the film with small diameters, b) display of small Ag NW diameters with little deviation, the diameters are as small as  $\sim 60$  nm, c) percolation network of film with large diameters, d) display of large Ag NW diameters with little deviation, averaged to be  $\sim 150$  nm.

#### 4.5 Results and Discussion

Finite Difference Time Domain (FDTD) simulations with Lumerical software were used to theoretically investigate the haze factor of Ag NWs with relative large and small diameters, as depicted in Figure 4.9. The diameters of the nanowires used in the simulations were picked based on SEM images of the two separate Ag NW yields with varying diameters. The simulated percent of incident light transmitted into the substrate and the simulated haze factor for different Ag NWs diameters with equal lengths are compared in Figure 4.12.







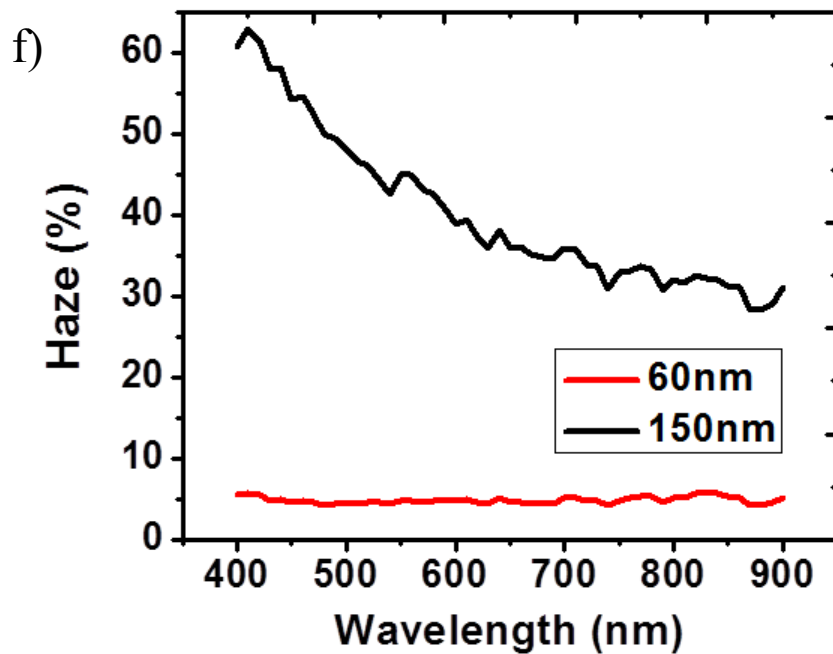
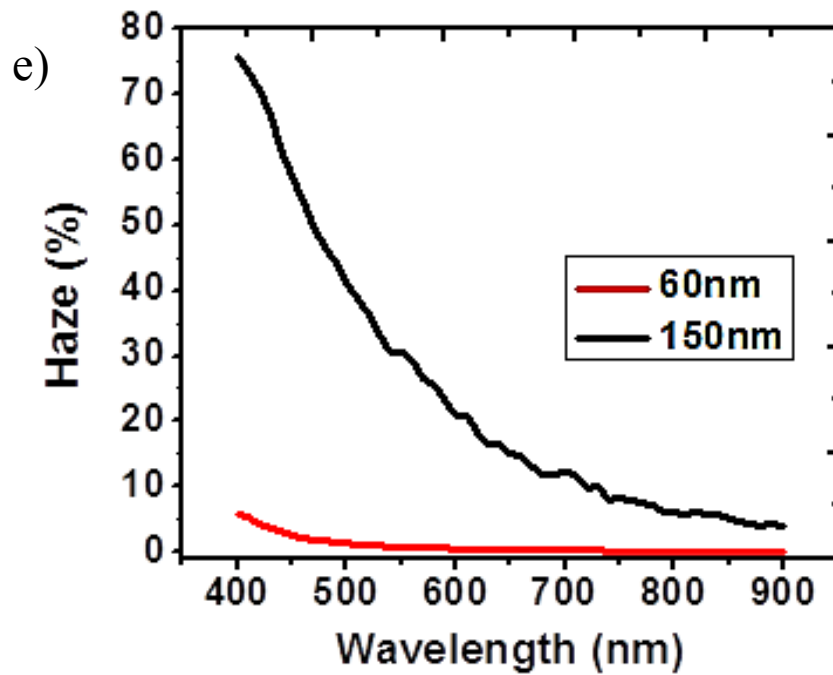
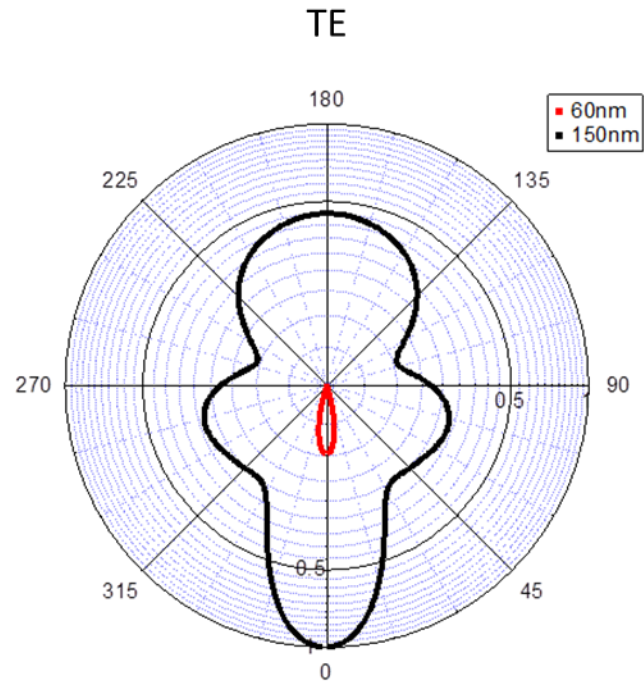


**Figure 4.12)** Simulation of the transmittance for a large (150nm) and small (60nm) diameter nanowire with (a) TE polarization, (b) TM polarization, and (c) averaged transmission; and the transmission haze simulation for a large (150nm) and small (60nm) diameter nanowire with (d) TE polarization, (e) TM polarization, and (f) averaged haze factor of Ag NW's with different diameters (60nm and 150nm).

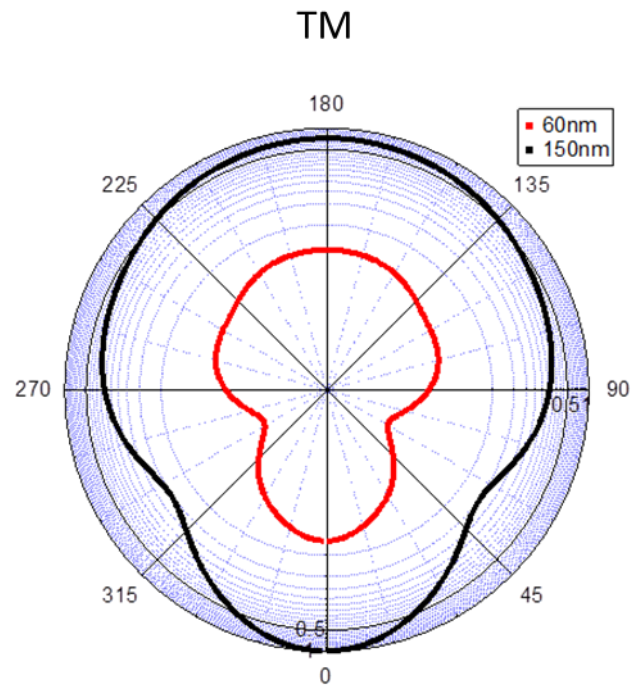
The transmittance of the larger diameter nanowires is less than the smaller diameter nanowires by  $\leq 30\%$  according to the average of the TM and TE polarization modes; however both large and small diameter transparencies are suitable for TCE utilization. Referring to past studies on the resistivity of individual silver nanowires,<sup>[147]</sup> the intrinsic conductivity of silver nanowires does not vary significantly between these two diameters. According to the current figure of merit, nanomesh films composed of the smaller diameter nanowires with the higher aspect ratio are more suitable for TCEs.

Figure 4.13 displays the simulated scattered field intensity with regards to the scattering angle of the silver nanowires with different diameters. This demonstrates that for both TE and TM polarizations the field intensities that propagate forward are higher than the reflected fields. It is also observable that highest intensities are measured for a range of forward angles (0-90°). Because the forward scattered fields are not restricted to negligibly small angles, but expand to larger forward angles as well, the impact of diffuse scattered light must be addressed when describing optoelectronic performance of Ag NW electrodes.

a)



b)



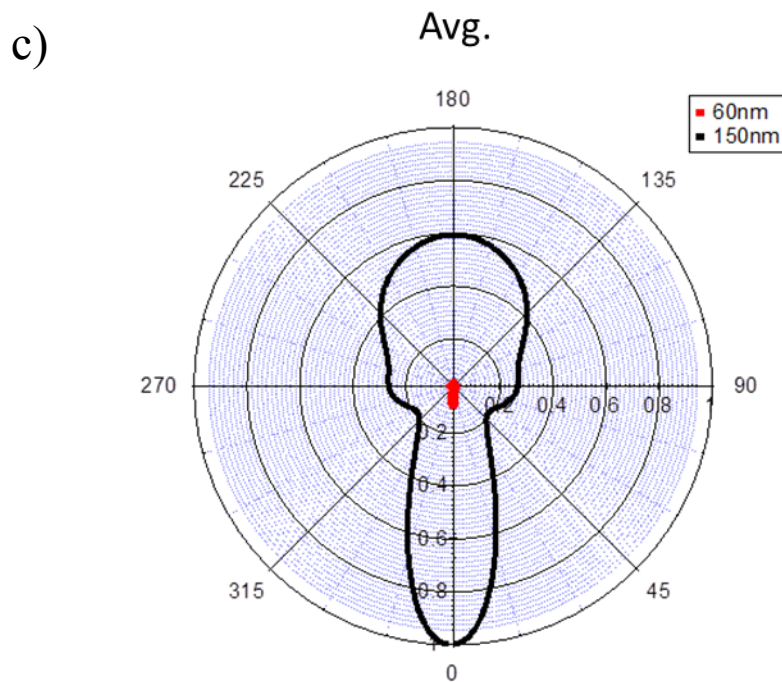


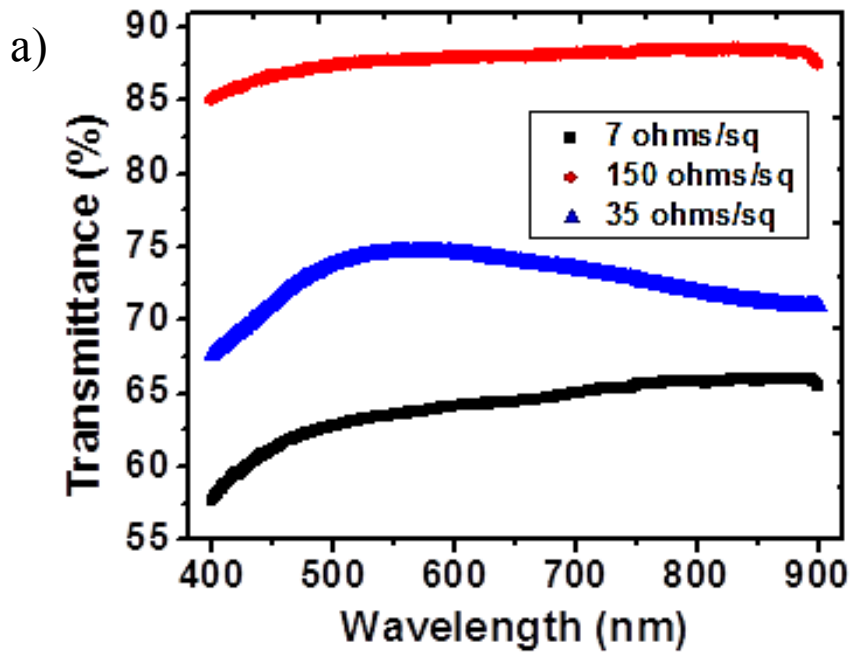
**Figure 4.13)** Simulation of the normalized scattered field intensity versus scattering angle from the axis normal to the silver nanowire with diffuse scattering represented by acute angles (0-90° and 270°-360°) and backscattering represented by obtuse angles (90-270°) for (a) TE polarization and (b) TM polarization and (c) average of TE and TM for 60 nm and 150 nm diameter silver nanowires. (a) and (b) are in log scale and (c) is in linear scale for clarity.

It is also clear from the simulations in Figure 4.13 that the fraction of light scattered forward increases as the nanowire diameter increases. At a wavelength of 500 nm, the haze factor is 40% higher for the larger diameter (150 nm) Ag NWs than small diameter (60 nm) Ag NWs, with the haze factor almost entirely disappearing just beyond the visible spectra for small diameter Ag NWs. The higher intrinsic diffuse light scattering for Ag NWs with larger diameters suggests that even if the transparency and sheet resistance of separate nanomesh films comprised of small and large diameter Ag NW networks were the same after separately tuning the density of Ag NWs for each network,

the larger diameter Ag NWs would promote a longer average path length in the conversion layer than Ag NWs with smaller diameters.

#### 4.5.1. Comparing the figure of merit of Ag NW TCEs.

Films were formed with various number densities comprised of either small or large Ag NW diameters by controlling the concentrations of the nanowire dispersions before the vacuum filtration. Figure 4.14 displays the transmittance of the various films plotted against their respective sheet resistance. The sheet resistance of the Ag NW films was measured with an inline four-point probe, and the transmittance data was measured with a LAMBDA 35 UV/Vis spectrometer.



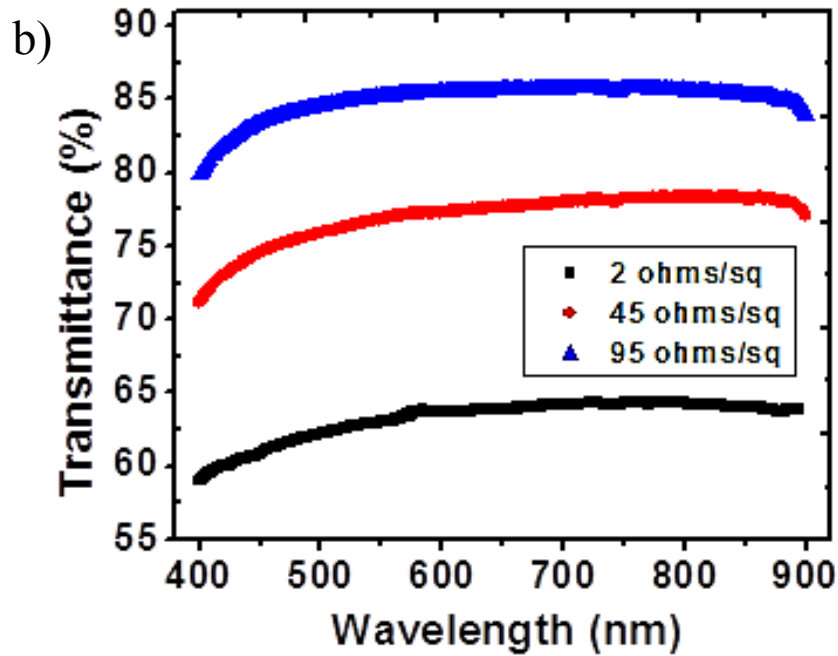


**Figure 4.14)** (a) The transmittance spectrum for the various films formed from vacuum filtration of Ag NW dispersions with large diameters (~150 nm), and b) the transmittance spectrum for the various films formed from vacuum filtration of Ag NW dispersions with small diameters (~60 nm).

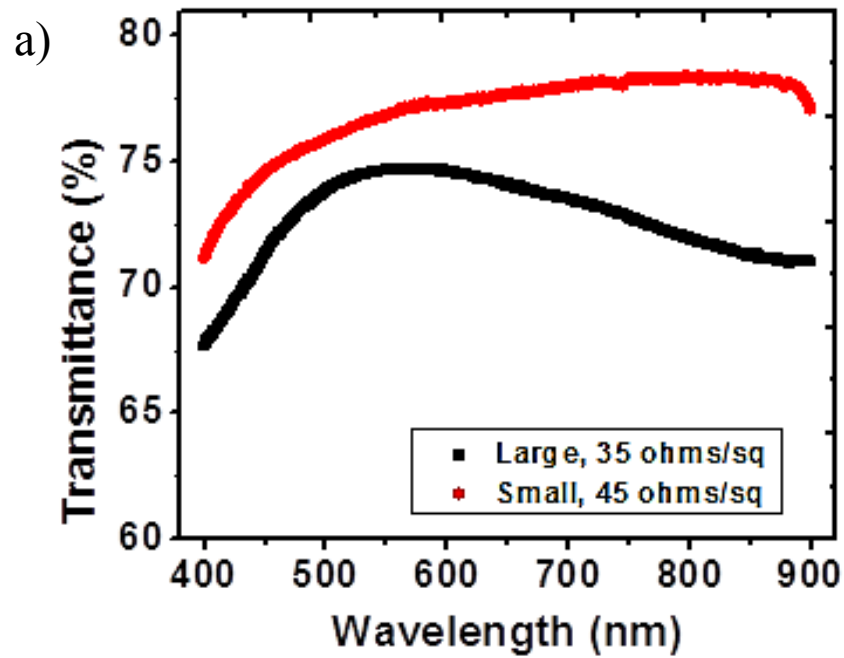
Various number densities of nanowires yield Ag NW films with a distribution of optoelectronic properties, as demonstrated by Figure 4.14. According to the figure of merit model in Equation 4.4, the films with small diameters exhibit a better performance (larger  $\sigma_{DC}$  values) than those with the larger diameters due to the higher film transparencies.

#### 4.5.2. Comparing the Ag NW TCE haze factor to the figure of merit

In order to isolate the difference of the haze factor in TCE films comprised of small and large diameter Ag NWs, two Ag NW samples with similar the transparency and sheet resistance values as illustrated by Figure 4.14 were chosen for comparison. The haze



factor of these films was measured by an integrating sphere setup as depicted in Figure 4.10, and is calculated by Equation 4.11. The haze was calculated and compared for films of each diameter size in order to confirm what nanowire size best enhances forward scattering. The diameter of the wires is the primary contributor to the transmission haze measurements because the average nanowire length is approximately the same for both Ag NW dispersions. The comparison of the transmittance and sheet resistance for films comprised of relative small and large diameters is given in Figure 4.15.



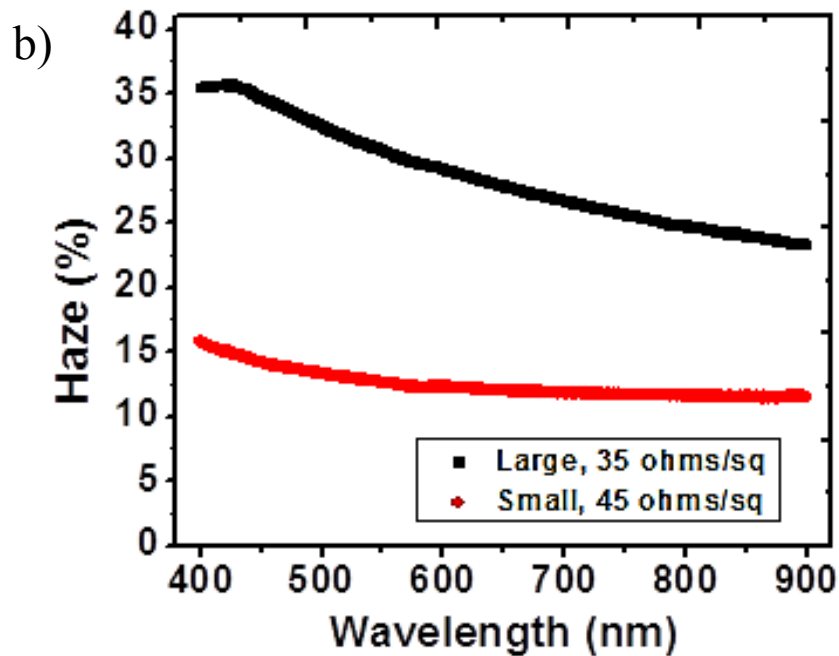


**Figure 4.15)** (a) Comparison of experimental transmittance data for a small diameter (~60 nm) Ag NW TCE film with  $R_s = 45 \Omega/\text{sq}$  and a large diameter (~150 nm) Ag NW TCE film with  $R_s = 35 \Omega/\text{sq}$ , and b) haze factor comparison between the same small diameter and large diameter Ag NW TCE films.

The transmittance curves of small diameter and large diameter Ag NW TCE films are nearly identical (average deviation is 5.5%) as are the sheet resistances. According to current figure of merit models for TCE performance, these two Ag NW TCE films share near equal performances due to the similar transparency and conductivity characteristics. The transmission haze values for the large diameter Ag NW TCE films are twice as large as the small diameter films. Despite similar transparency and conductivity of the two film types, the TCE films consisting of Ag NWs with larger diameters prove to be better for solar cells due to the larger haze values. This observation opposes the generally accepted idea that increasing the aspect ratio by shrinking the nanowire diameters will produce a higher performing TCE in applications where a larger haze factor is preferred.

### 4.5.3. Thin-film CZTS solar cells

Thin-film solar cells are an emerging solution for flexible, modular, and cost-effective photovoltaic technology. A typical thin-film solar cell stack is given in Figure 4.16.

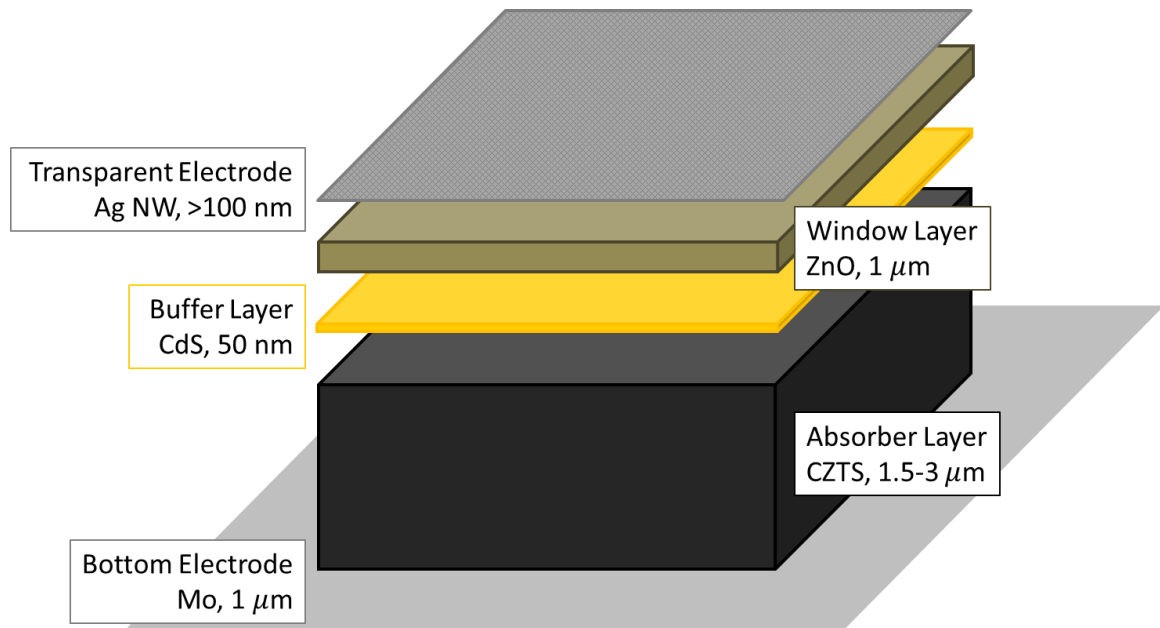


Figure 4.16) A schematic of a typical thin-film solar cell stack.

In the assembly of the thin-film solar cell, first a molybdenum layer is sputtered onto the substrate to provide the bottom electrode. The p-type absorber layer is then coated onto the substrate via a solution-based coating method such as Meyer rod coating, and then annealed to fuse the film into larger grains. A thin n-type buffer layer of CdS is deposited on the absorber layer via chemical bath deposition in order to protect the p-n junction interface. The n-type ZnO window layer is then sputtered onto the absorber layer to complete the p-n junction; however, the buffer layer (50 nm) and window layers (1 μm) are thin to prevent the carrier mobility from being inhibited. The final TCE is applied on the window layer to complete the solar cell stack.

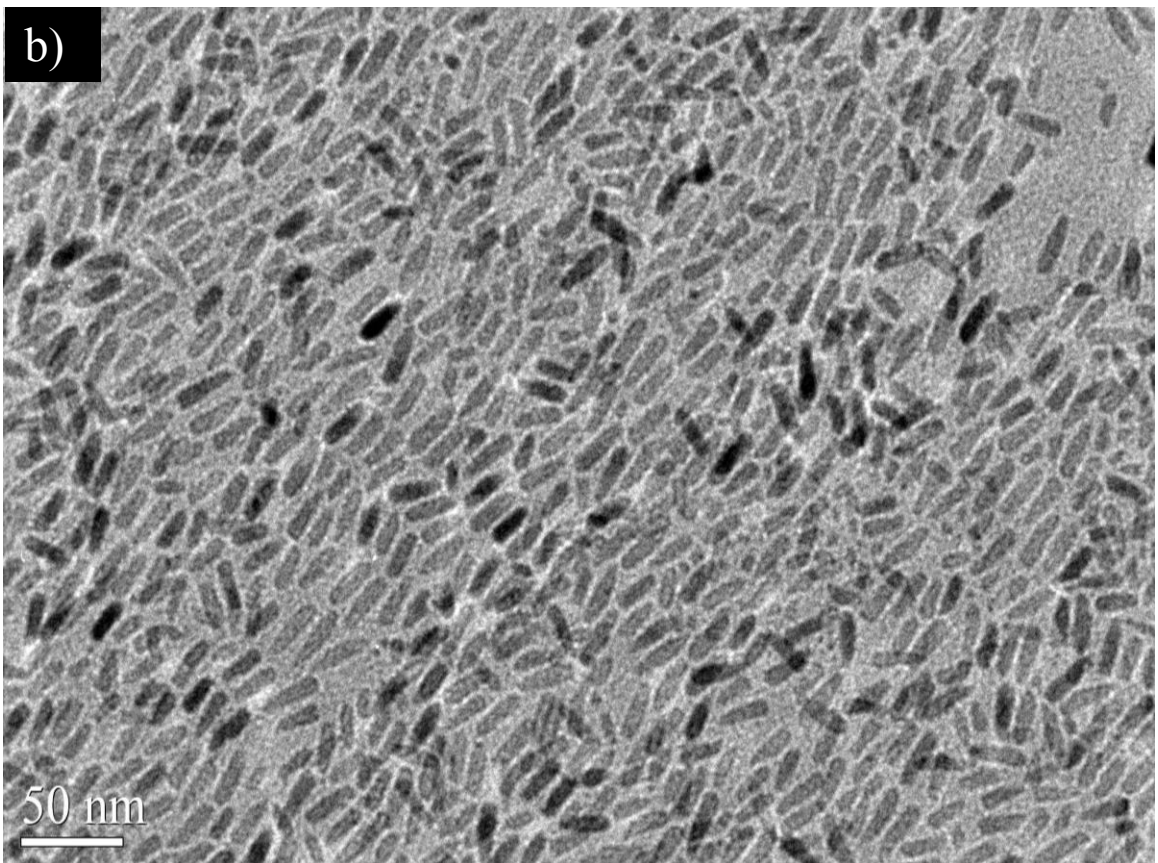
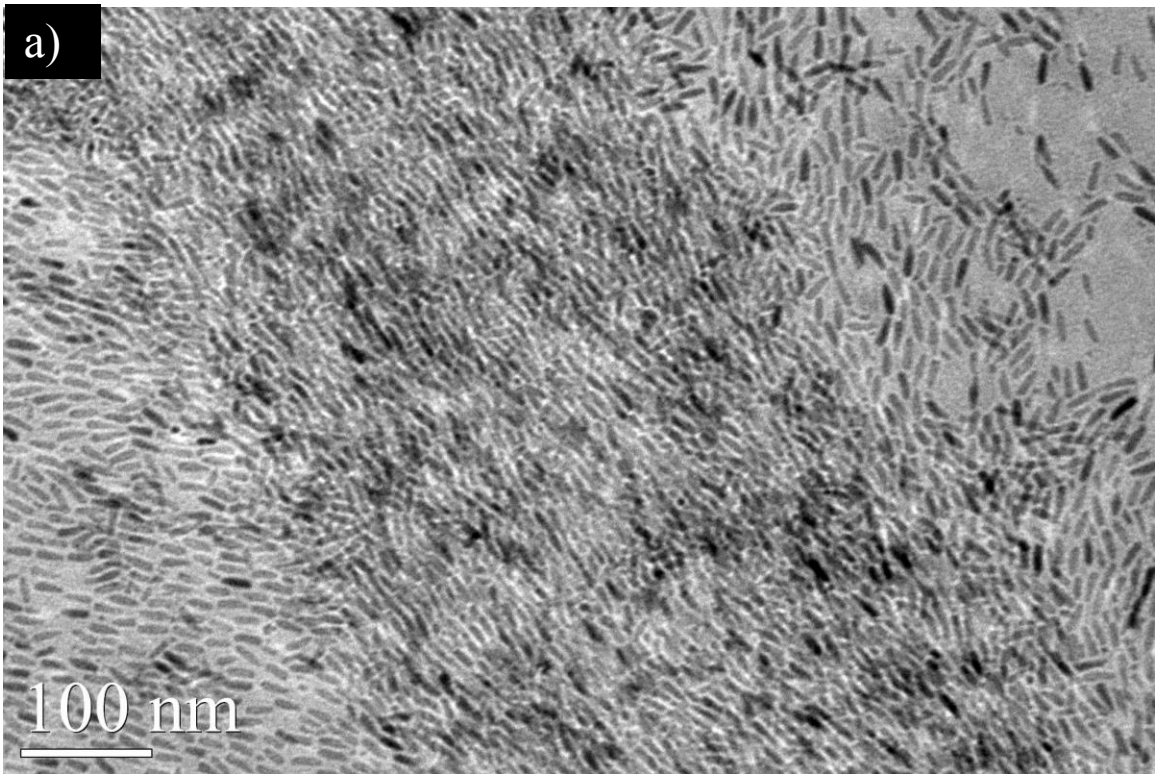
Solar cell modules that incorporate  $\text{Cu(In,Ga)Se}_2$  (CIGS) layers as the conversion layer are reported to exhibit efficiencies above 20.0%. Further research dedicated to reducing the fabrication costs of thin-film solar cells demonstrates that an isoelectronic replacement of indium and gallium with zinc and tin respectively forms a  $\text{Cu}_2\text{ZnSn(S,Se)}_4$  (CZTS) absorber layer with a reported band-gap between 1.32-1.85 eV, which provides a suitable photovoltaic (PV) conversion layer from safe and cost-efficient materials.<sup>[168-171]</sup> Reports demonstrate that CZTS kesterite crystals may form absorber layers through various solution-based coating techniques and subsequent high temperature annealing, which enables solar cell efficiencies higher than 10%.<sup>[172-174,182]</sup>

Additional reports introduce a CZTS wurtzite crystalline structure that forms nanorods.<sup>[174-178]</sup> These nanorods may be coated via solution-based methods into a highly packed thin-film that enables an annealed absorber layer with large grains.<sup>[175, 179-181]</sup> Singh et al. demonstrates a method to fabricate CZTS nanorods by injecting a liquid sulfur source into a heated precursor solution containing a ratio copper, zinc, and tin that achieves a desired band gap of 1.43 eV.<sup>[179]</sup> Figure 4.17 illustrates a setup reproduced from this study to synthesize CZTS nanorods.



**Figure 4.17)** The synthesis setup for a fabrication of CZTS nanorods. In a typical synthesis, copper(II) acetylacetonate (0.261g, 1mmol), Zinc acetate (0.091g, 0.5mmol), Tin(IV) acetate (0.177g, 0.5mmol) and TOPO (1.353g, 3.5mmol) were mixed with 10mL of 1-octadecene in a three-neck round-bottom flask and evacuated at room temperature for 30-45mins. The solution was then heated to 240-260°C under an argon atmosphere. At 150- 160°C, a mixture of 0.25mL 1-dodecanethiol and 1.75mL t-dodecanethiol was quickly injected into the flask which resulted in an immediate color change from dark green to wine red and then finally to brown. After injection, the reaction was allowed to proceed for 15-30 minutes with continuous stirring. The nanorod growth was terminated by a removal of the heating mantle and at 80°C, 2-4 ml anhydrous toluene were added to the mixture to quench the reaction.

Figure 4.18 illustrates the CZTS nanorods fabricated by the synthesis method depicted in Figure 4.17, with varying degrees of self-alignment clearly visible in the TEM images. The CZTS nanorods appear as bullet-shaped nanocrystals with a diameter reaching approximately 8 nm, as seen in Figure 4.18c.



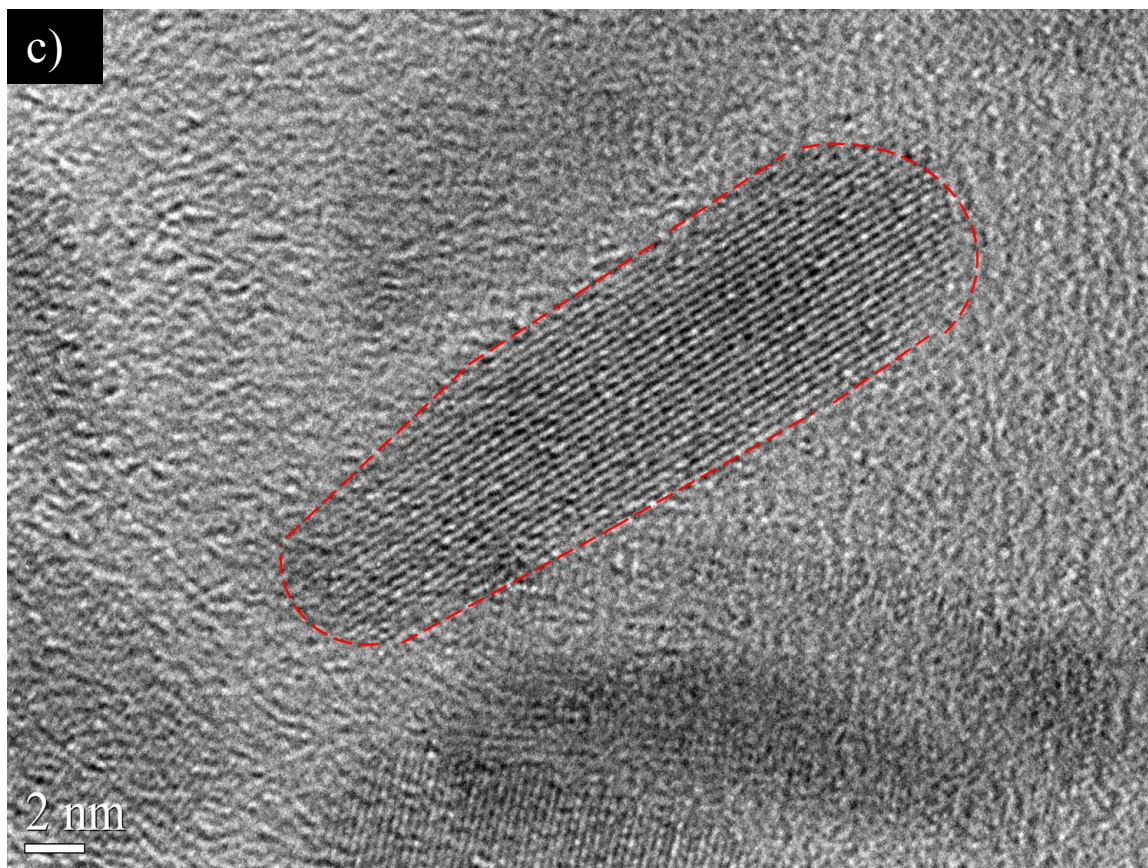


**Figure 4.18)** TEM images of CZTS nanorods at different magnifications demonstrating varying degrees of self-alignment (a, b), and a HRTEM image of a CZTS nanorod demonstrating the atomic crystalline structure.

In order to ascertain the band gap of the CZTS nanorods, the absorbance of CZTS solutions at varying concentrations was measured at 500 nm with a PerkinElmer Lambda 35 UV–Vis Spectrometer. The concentrations of the CZTS solutions were varied by increasing the number of drops of CZTS solution in a fixed 10 mL volume of solvent. Table 4.1 demonstrates the absorbance measurements of each CZTS sample and Figure 4.19 demonstrates the linear fit of the absorbance versus concentration. The absorption coefficient of the CZTS nanorods may be extrapolated from the slope of the linear fit in Figure 4.19.

Concentration (# CZTS drops/ 10 mL solvent)	Absorbance
4	.3039
5	.3169
6	.3345
7	.3514
8	.3724
9	.3924
10.5	.4237
12	.4643

**Table 4.1)** The tabulated data of the CZTS concentration in solution versus the absorbance of that solution at 500 nm.

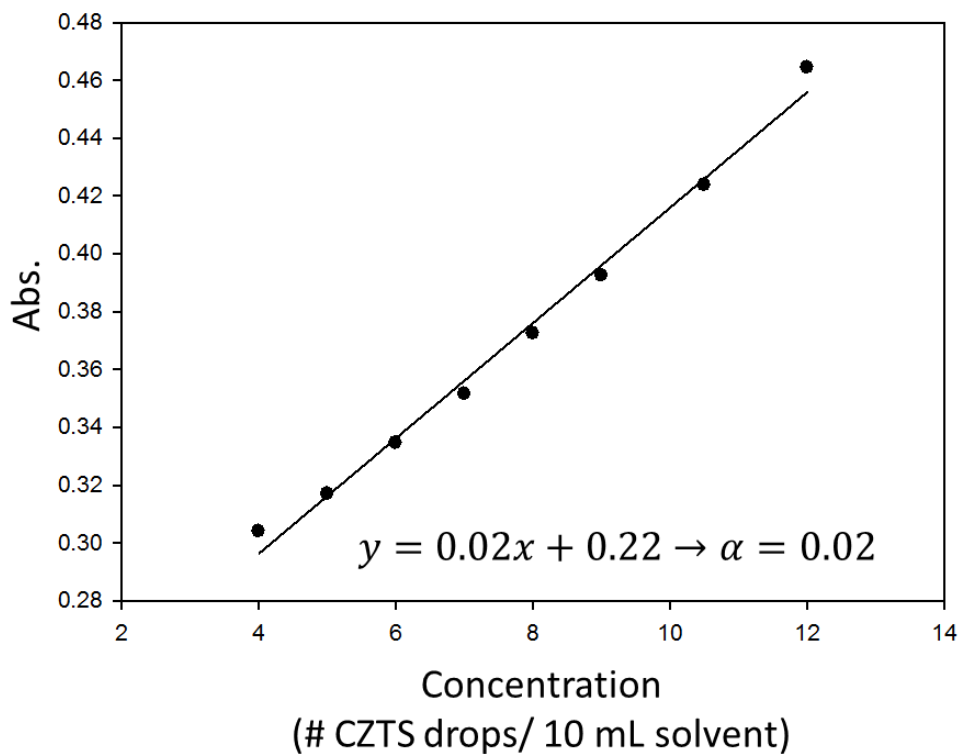


**Figure 4.19)** A plot of the CZTS concentration in solution versus the absorbance of that solution at 500 nm, and a linear fit of the regression. The slope of the linear regression is calculated to be  $\alpha = 0.02$ , which is the absorption coefficient as calculated by this plot.



The Tauc's relation in Equation 4.12 may be used to determine the band gap of the CZTS nanoparticles given the absorbance measurements and absorption coefficient:<sup>[183-185]</sup>

$$\alpha h\nu = A(h\nu - E_g)^{\frac{1}{2}} \quad (4.12)$$

A plot of  $(\alpha h\nu)^2$  versus  $h\nu$  illustrates a curve that may generate a linear fit with an x-intercept at the band gap ( $E_g$ ). This plot is demonstrated in Figure 4.20, with a band gap approximated at  $E_g = 1.43$  eV

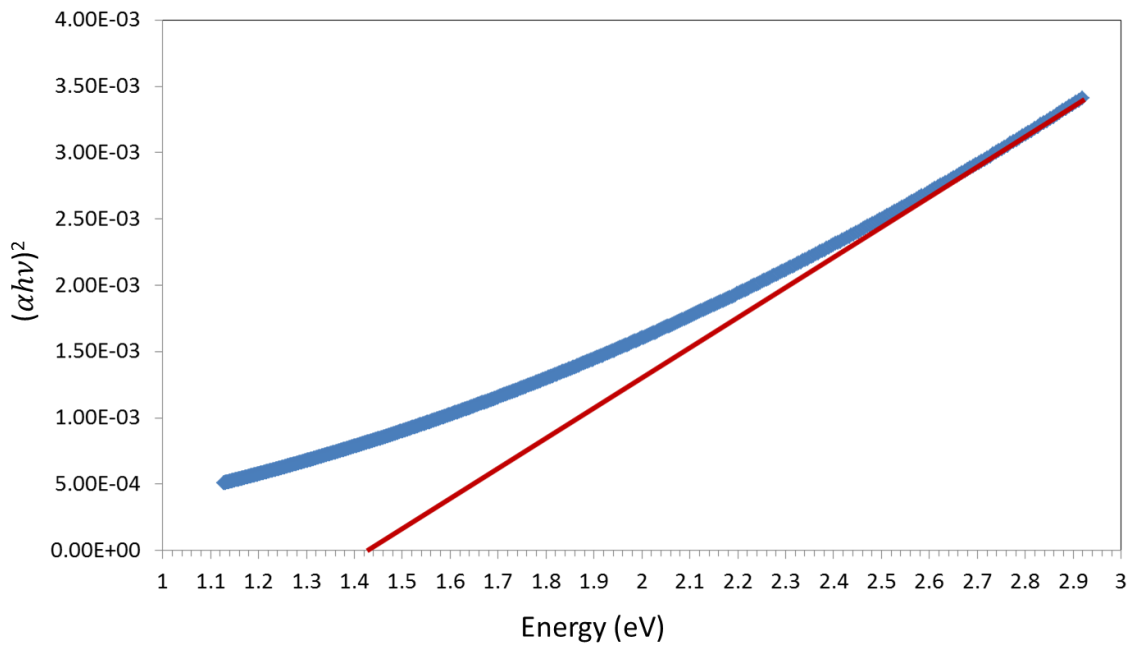


**Figure 4.20)** A plot of the  $(\alpha h\nu)^2$  versus  $h\nu$  that demonstrates a linear fit intercepting the x-axis at approximately 1.43 eV.

Despite the useful band gap and high packing order of the CZTS nanocrystals, a high temperature annealing stage is required to fuse the individual crystals into larger sized grains that enable a higher current density with less recombination in the absorber layer. The annealing stage of the CZTS layer often dictates the grain size as well as its band gap with selenization or sulfurization.<sup>[186-188]</sup> The SEM images in Figure 4.21 demonstrate the annealed grains of CZTS nanocrystals at 500 °C in a selenium environment.

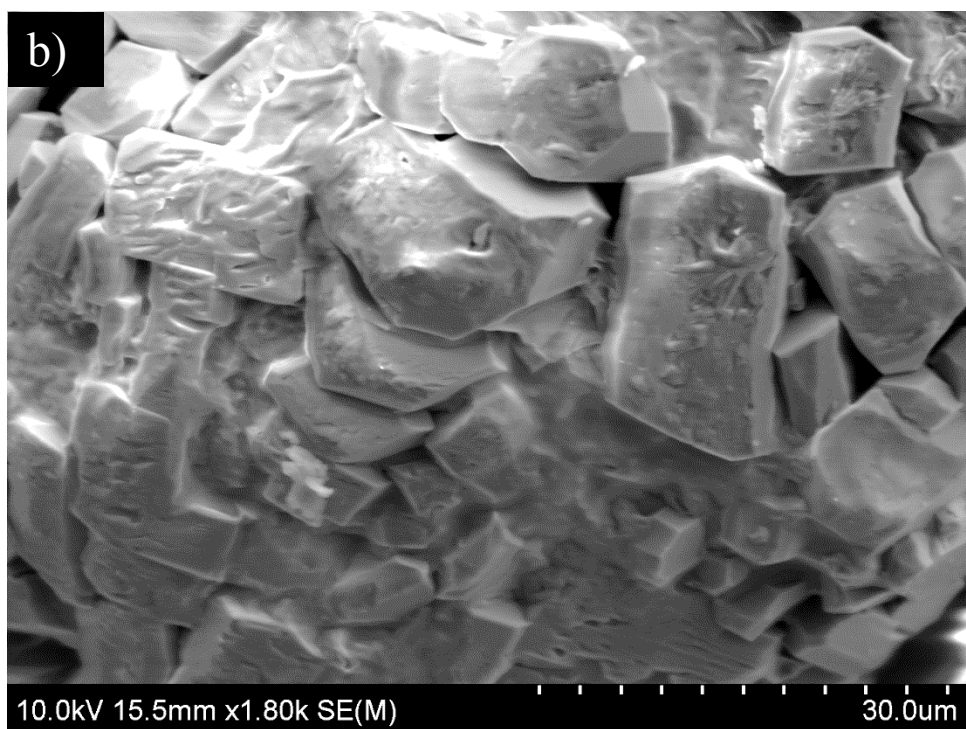
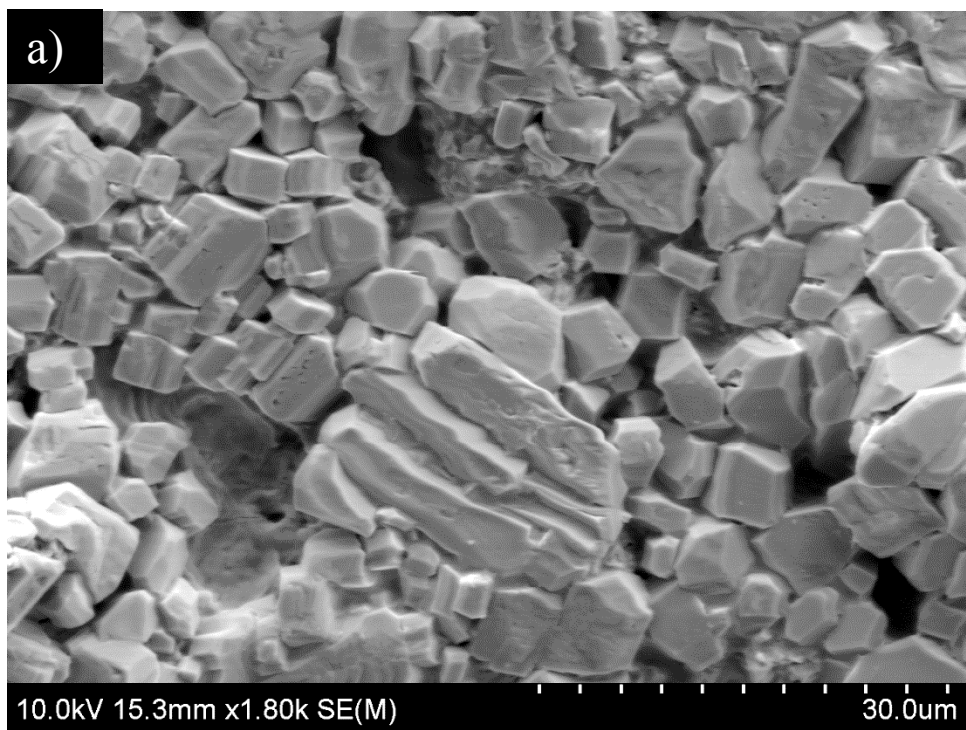
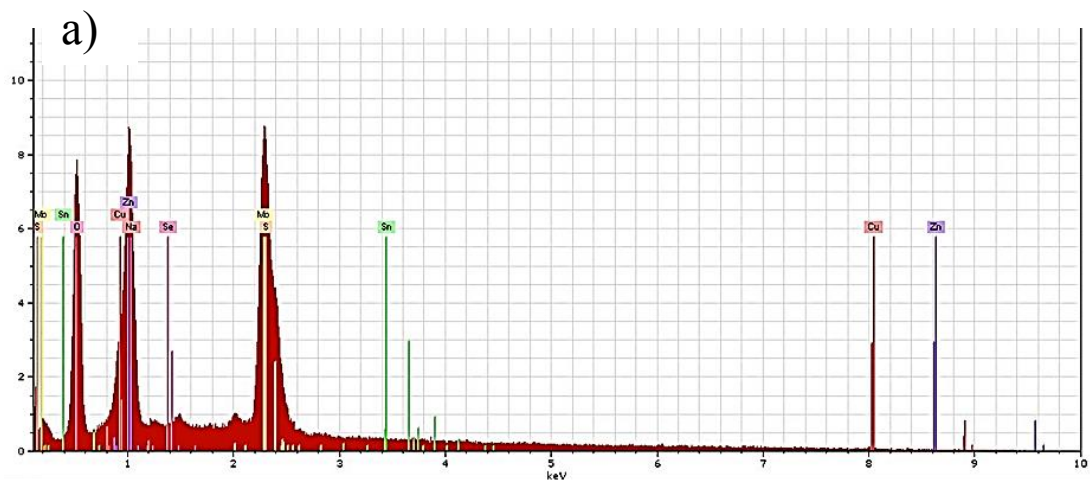
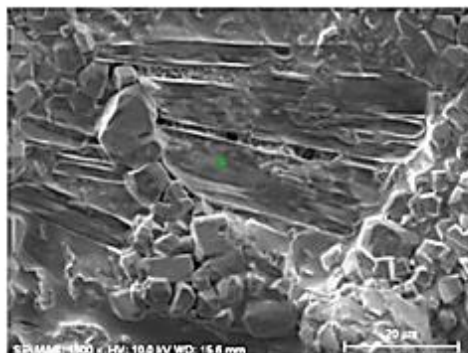
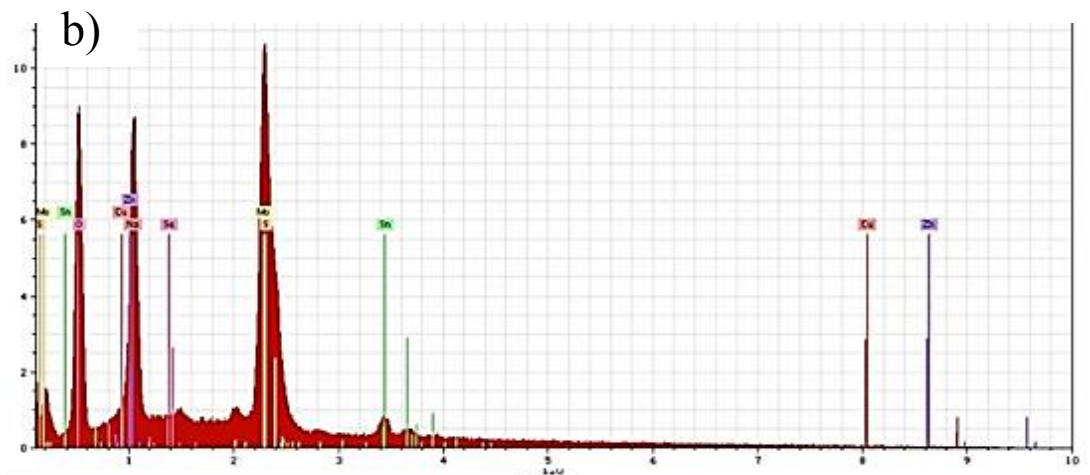


**Figure 4.21)** TEM images of a thin-film composed of CZTS nanorods coated onto a molybdenum sputtered soda lime glass substrate, which is then annealed at 500 °C for 10-15 min in a selenium environment.



El	AN	Series	unn. [wt.%]	C norm. [wt.%]	C Atom. [at.%]	C Error [%]
Mo	42	L-series	32.50	39.77	16.78	1.8
O	8	K-series	15.64	19.14	48.44	1.9
Zn	30	L-series	14.63	17.91	11.09	5.1
Cu	29	L-series	8.63	10.56	6.73	1.4
Na	11	K-series	5.55	6.79	11.97	3.1
S	16	K-series	2.45	3.00	3.79	0.8
Sn	50	L-series	1.21	1.49	0.51	0.1
Se	34	L-series	1.10	1.34	0.69	0.1
Total:			81.73	100.00	100.00	



El	AN	Series	unn. [wt.%]	C norm. [wt.%]	C Atom. [at.%]	C Error [%]
Mo	42	L-series	45.86	52.28	20.04	2.2
O	8	K-series	19.42	22.14	50.89	2.3
Na	11	K-series	12.63	14.40	23.03	2.3
Sn	50	L-series	5.44	6.21	1.92	0.2
S	16	K-series	2.12	2.41	2.77	0.9
Cu	29	L-series	1.26	1.43	0.83	0.3
Se	34	L-series	0.99	1.12	0.52	0.1
Zn	30	L-series	0.00	0.00	0.00	0.0
Total:			87.71	100.00	100.00	

**Figure 4.22)** SEM-EDS spectra at different locations on annealed CZTS thin-film layers, with corresponding SEM images with the scan location marked and tables of the atomic compositions at each scan.

It is clear from the TEM images in Figure 4.21 that the annealed grains are discontinuous with a large dispersion of sizes. This may be due to the inhomogeneous packing density of the CZTS nanocrystals, and the high mobility of the nanorods in the thin-film during the high temperature annealing. It is clear from the Energy Dispersive Spectroscopy (SEM-EDS) that there are varying levels of each characteristic element in the annealed CZTS film; however, there is a consistently low level of copper and high level of oxygen, which is uncharacteristic for CZTS absorber layers. It may be concluded from the SEM-EDS data in Figure 4.22 and the SEM images in Figure 4.21 that further study is required to successfully fabricate a CZTS absorber layer with the correct stoichiometry and void of any secondary phases, which is beyond the scope of this thesis work.

#### 4.6 Conclusion

This study provides a theoretical and experimental study of haze properties for Ag NWs, and evidence that the current figure of merit for TCEs is insufficient to project the performance of TCEs used in solar cell applications. According to the current models, transparency and conductivity are the only properties significant to the TCE performance. Although these properties are certainly important, haze factor is a critical property in TCEs for solar cells. This study demonstrates that the impact of haze factor is overlooked in films that contemporary figure of merit models would deem identical and that the haze factor must be an independent variable to include in new figure of merit formulas.

## Chapter 5: Silver Nanowire Transparent Paper-based Electrode with High Transmission Haze

Although there are a variety of alternatives to ITO for high performance and flexible TCEs, the Ag NWs exhibit a superior transparency, conductivity, and flexibility collectively. Combining Ag NWs with other conductive or flexible components is demonstrated to boost the optoelectronic properties and the mechanical properties of the composite Ag NW TCE. Embedding AgNWs in conductive polymers such as poly(3,4-ethylenedioxythiophene) polystyrene sulfonate (PEDOT:PSS) or polydiacetylene (PDA) are reported to form highly flexible TCEs with high transmittance; however, the insulating polymer matrix hinders the connectivity of the conductive network and thus increases the sheet resistance.<sup>[148, 149]</sup> Studies also show that embedding a conductive Ag NW network onto the surface of a flexible substrate similarly stabilizes it to mechanical strain without compromising the low sheet resistance.<sup>[5, 150]</sup>

The most common substrate to host flexible electronics is plastic; however recent studies report paper substrates with high transparency that are amenable to hosting printed electronics.<sup>[151]</sup> Printing flexible electronics on paper rather than plastic substrates further bolsters economical production due to the renewable, environmentally friendly, light-weight, mechanically flexible, and disposable properties of paper.

### 5.1 Paper Substrates for Transparent Electrodes

Common paper substrates are composed of large cellulose fibers (20-50  $\mu\text{m}$  diameter) that instill a high surface roughness, high porosity, and high opacity that prevent their ability to host thin-film optoelectronic devices. Recent research efforts

demonstrate paper substrates reengineered with cellulose structures derived from the hierarchical composition of wood fibers can exhibit new properties such as high transparency, greater toughness, greater elasticity, greater strength, and greater surface smoothness. These paper substrates not only possess optical and mechanical properties that match or exceed those of common plastic substrates such as PET, but offer a renewable and environmentally friendly alternative to plastics for optoelectronics.

The wood fibers extracting from trees that are used to fabricate common paper materials ubiquitously used in numerous industries actually possess a cell wall with a three-dimensional hierarchical structure, as depicted in Figure 5.1.

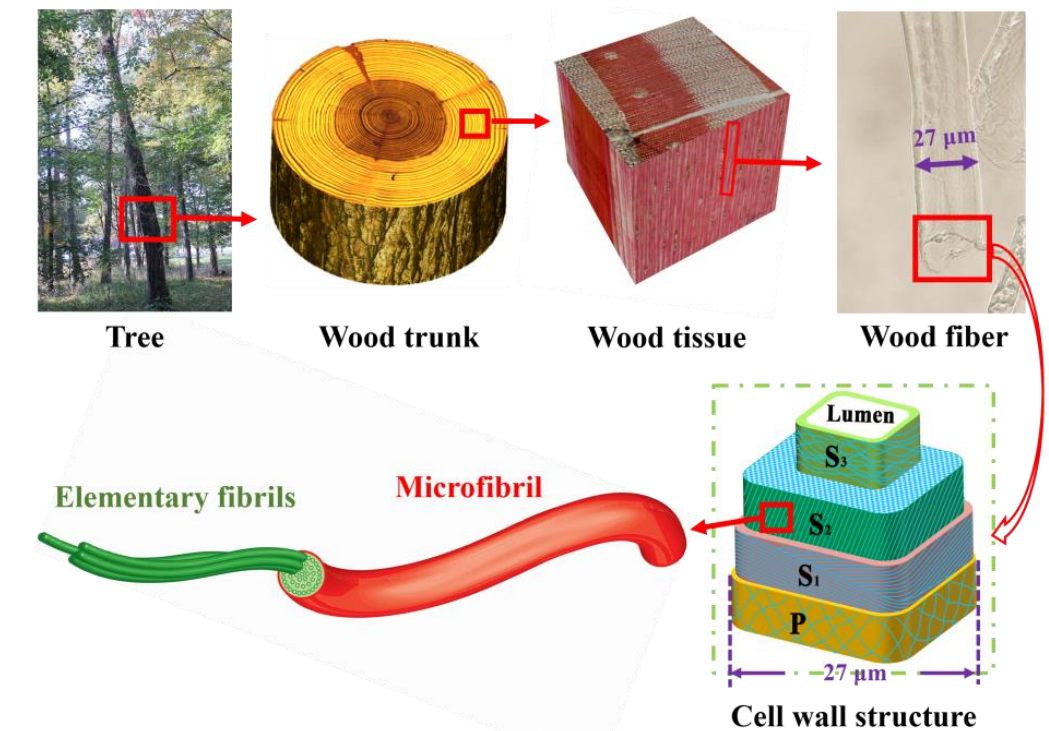


**Figure 5.1)** A schematic detailing the derivation of wood fibers from trees as well as the hierarchical structure of these wood fibers, which enables cellulose nanofibers and microfibrils to be extracted from the cell wall of the wood fibers.<sup>[6]</sup>

As seen in Figure 5.1, the cell wall of the wood fibers is composed of multiple layers. Bundles of cellulose microfibrils form each layer of the cell wall and provide unique

structural stability to the cell wall. Since the  $S_2$  layer comprises 75% of the cell wall volume, the majority of the cellulose microfibril bundles are extracted from this layer. Each of these microfibrils is composed of smaller elementary fibrils less than a micron in length with diameters of 1.5 – 3.5 nm aggregated into a distribution of diameters (5-50 nm) with lengths of several microns. The assembly of the elementary fibrils into a hierarchical structure enables fibers with a diameter from microscale to several nanoscale to be extracted from the cellulose fibers by chemical and/or mechanical treatments.

Nanofibrillated cellulose (NFC) are nanoscale diameter fibers disintegrated from wood fibers, and enable the formation of transparent paper with stable mechanical properties. The schematic in Figure 5.2 illustrates a random network assembled from NFC to form a nanopaper substrate, which represents Generation 1 of transparent paper technology.

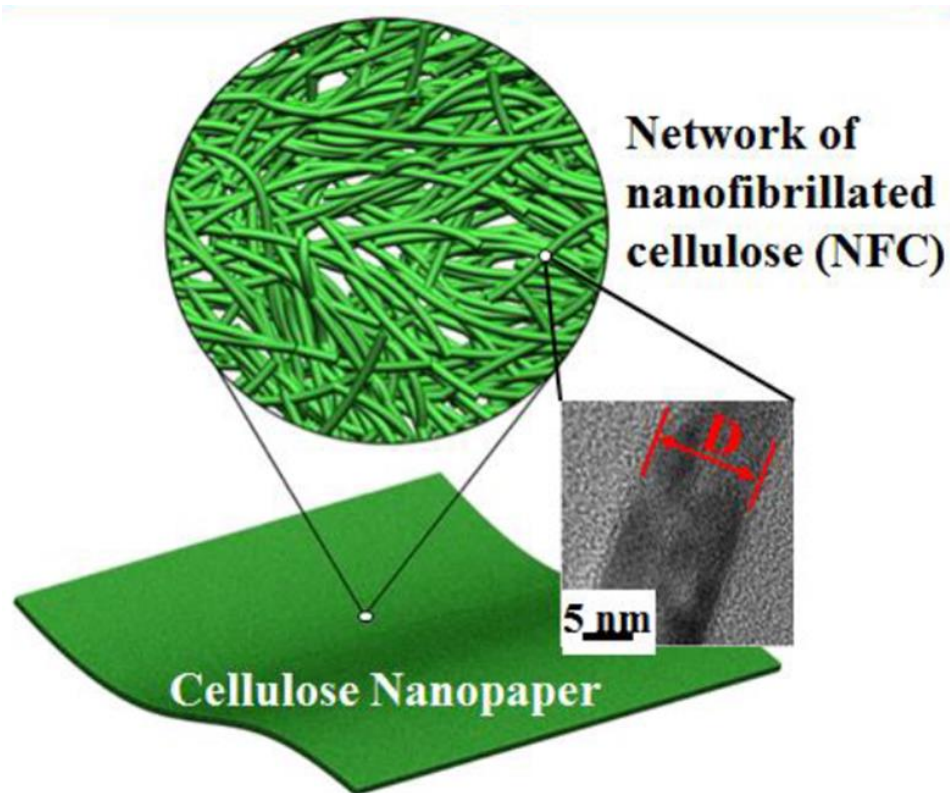


**Figure 5.2)** A schematic depicting the random network of nanofibrillated cellulose (NFC) with approximate diameters less than 15 nm as illustrated in the inset TEM image.<sup>[7]</sup>

Transparent paper consisting solely of NFC is reported to reach a transmittance above 80% and exhibits a surface roughness below 5 nm. Common paper substrates are composed of a network of micro-sized wood fibers (20 – 50  $\mu\text{m}$  diameter) permeated by numerous micro-sized air cavities. The different refractive indices of the cellulose and air (1.5 and 1.0, respectively) causes light scattering at the fiber surfaces that renders the entire substrate opaque. The improved transmittance of NFC paper substrates attributes to a higher density fibrous network that diminishes the pore size of the air cavities, and thus reduces the reflective loss.

Although the NFC paper may exhibit an optical transmittance and surface smoothness suitable for optoelectronic device integration, the procedures to extract NFC from wood fibers is very time and energy consuming. The energy consumption of NFC manufacturing has progressed from high pressure homogenization of wood fibers with an energy consumption of 25,000  $\text{kW} \cdot \text{h}/\text{ton}$  to the formation of a cellulose “nanopulp” with an energy consumption of 443  $\text{kW} \cdot \text{h}/\text{ton}$ . Low concentrations of NFC ( $\leq 2 \text{ wt}\%$ ) in water may be vacuum filtered and dry-pressed to form nanopaper substrate; however, the filtration process is extremely slow due to the gel-like viscosity of the NFC suspension. In addition to the limitations of the manufacturing process, paper substrates formed exclusively with NFC exhibit very low transmission haze due to the small scattering cross-section of the NFC.



A hybrid network of microscopic wood fibers and NFC may be fabricated to form transparent paper with higher transmission haze. A schematic of this hybrid network is illustrated in Figure 5.3, and represents Generation 2 of transparent paper.

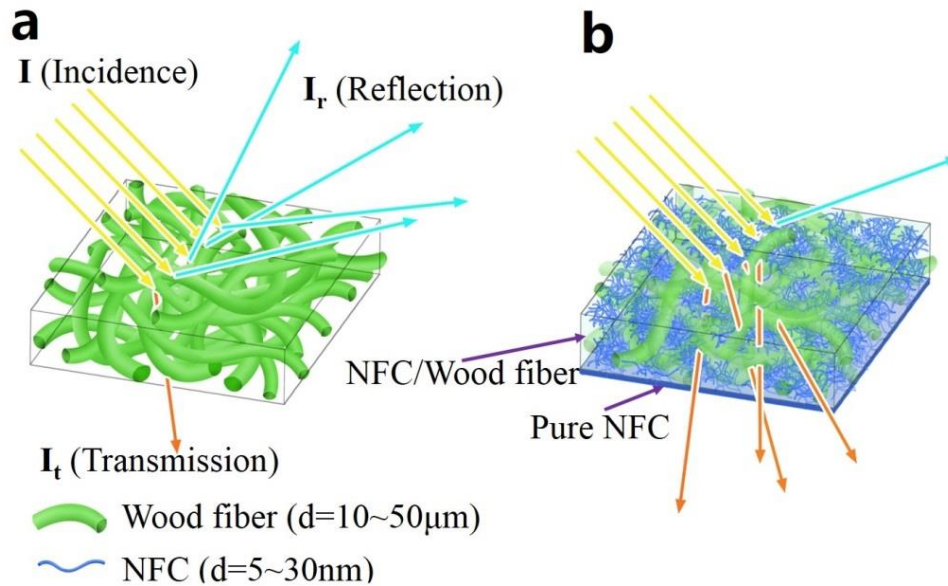


**Figure 5.3)** A schematic of how an opaque porous network of wood fibers with diameters between 10-50  $\mu\text{m}$  is transformed into a transparent substrate with significant diffuse scattering. NFC with diameters between 5-30 nm fill the space within the wood fiber network to create a denser hybrid network from the two cellulose structures that reduces the surface reflection and enhances the transmission through the paper substrate.<sup>[8]</sup>

The manufacture of Generation 2 hybrid paper is more energy efficient than that for Generation 1 nanopaper since the fibrous network consists of lower concentrations of NFC. The NFC fills the microsized pores in the network of wood fibers, which decreases the reflectance off the surface of the substrate. The transmittance of Generation 2 transparent paper is reported to exceed 90%. The transparent hybrid paper substrate demonstrates high transmission haze due to the large scattering cross-section of the larger wood fibers. Fang et. al demonstrates that the transmission haze and transmittance of the

hybrid paper substrate is directly related to the concentration of NFC in the fibrous network;<sup>[154]</sup> greater concentrations of NFC result in increased transmittance, but decreased transmission haze.

The nature of increasing the transmission haze of transparent substrates at the cost of increasing the reflectance and thus decreasing the transmittance is a well reported behavior in transparent paper and other transparent substrates, and presents a conundrum for designing substrates suitable for thin-film solar cells. As we discussed in Chapter 4, transparent electrodes for solar cells exhibit the best performance with high optical transmittance in conjunction with high transmission haze.

## 5.2 Synthesis of Transparent Paper with High Haze

A transparent paper with simultaneously high transmission haze may be fabricated by creating a dense network of microscopic cellulose fibers, which offers an optimal substrate for the transparent conducting electrode of thin-films solar cells. A schematic of the transformation of a porous network of microscopic fibers into a denser network after chemical treatments is depicted in Figure 5.4, and represents Generation 3 of transparent paper technology.

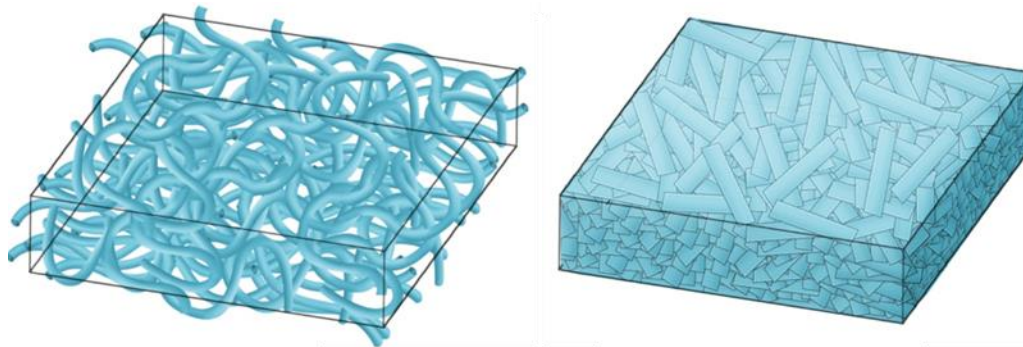


**Figure 5.4)** A schematic illustrating the transformation of a network of microscopic cellulose fibers into a densely packed cellulose network by altering the fiber structure.<sup>[152]</sup>

As seen in Figure 5.4, the chemical pretreatment of the wood fibers alters their morphology to allow them to stack into a dense network. The collapse of the pores in the fibrous network while preserving the large scattering cross-section enables paper substrates with high diffuse transmittance. This structural design overcomes the prevalent pattern of a higher transmission haze adjoining lower optical transmittance.

The alteration of the cellulose fiber morphology occurs during an oxidation of the fibers with (2,2,6,6-Tetramethylpiperidin-1-yl)oxy, or TEMPO. As described in the report by Fang et al., five grams of bleached sulfate softwood pulp extracted from southern yellow pine was dispersed in water to form a 1% pulp solution. The wood pulp solution was reacted with 10% wt TEMPO with constant stirring to oxidize the cellulose fibers, while a small concentration of NaBr and a continuous titration of NaClO stabilized the pH of the aqueous solution at 10.5 to prevent it from becoming acidic. The TEMPO-treated wood pulp was diluted to approximately 0.2 wt % in solution with deionized water.

The TEMPO treatment introduces carboxyl bonds to the cellulose molecules. These carboxyl bonds provide repulsive electrostatic forces that oppose the hydrogen bonds that aggregate the microfibril bundles in the cell wall of the wood fibers, which results in the fibers opening, compacting, and disintegrating into shorter lengths. The energetically favorable oxidation sites across the wood fibers are at locations where the typically crystalline cellulose structure is disordered; therefore, the resulting TEMPO-treated fibrous network has a higher packing order and is composed of cellulose

microstructures with higher crystallinity. These effects to the fiber structure after the TEMPO-treatment process is demonstrated in Figure 5.5.

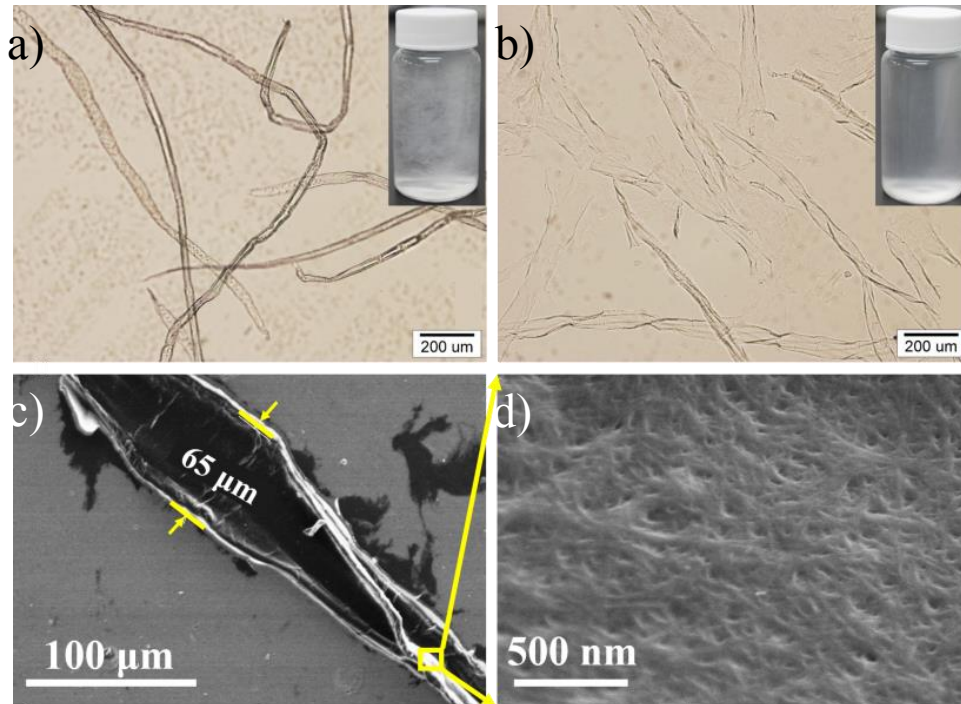


**Figure 5.5** (a) The morphology of original bleached sulfate wood fibers under an optical microscope. Inset is a 0.25 wt% original bleached sulfate wood pulp suspension. (b) The morphology of TEMPO-oxidized wood fibers under an optical microscope. Inset is a 0.25 wt% TEMPO-oxidized wood fiber suspension. SEM images of unzipped TEMPO-oxidized wood fibers (c) and (d) nanofibers on the cell wall of TEMPO-oxidized wood fiber.<sup>[152]</sup>

It is clearly observable in the comparison of the optical microscope images of the wood pulp solution in Figure 5.5(a) and the diluted TEMPO-treated wood pulp solution in Figure 5.5(b) that the tubular fibers are disintegrated and flattened into microstructures that are more visibly transparent than their previous form. Figure 5.5(c) better elucidates this structural transformation with an SEM image of a TEMPO-treated wood fiber cleaved along its axis. This weakening of the interfibrillar hydrogen bonds that result in

the fibers opening, with the width expanding and the length segmented into smaller microstructures. This disintegration of the fibrils is also observable on the surface of the cell wall in Figure 5.5(d), where chinks in the surface appear from the removal of cellulose nanofibers during the TEMPO-treatment.

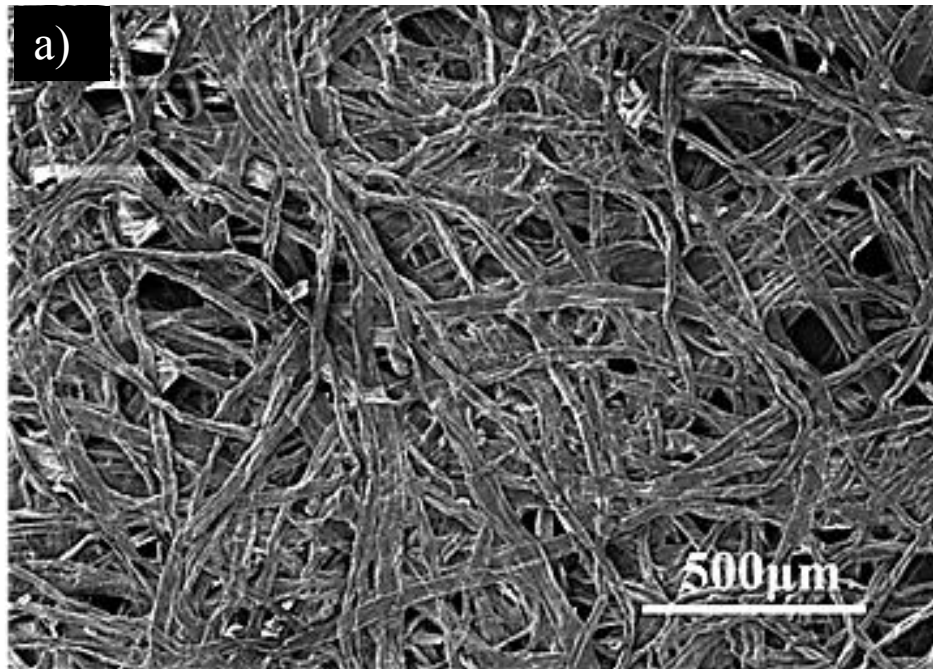
This diluted TEMPO-treated wood pulp was used to fabricate transparent paper with a vacuum filtration method using a 20 cm filter membrane (0.65  $\mu\text{m}$  pore size polyvinylidene difluoride (PVDF) membrane). The resulting wet film was placed between two stacks of regular filter paper and dried at room temperature under pressure. The resulting paper substrate is depicted in Figure 5.6.



**Figure 5.6)** An image of transparent paper produced from TEMPO-oxidized wood fibers with a diameter of 20 cm.<sup>[152]</sup>

The unzipped, cleaved, and flattened TEMPO-treated fibers form a dense network with high optical transmittance while still inducing considerable diffuse light scattering. This

is demonstrated in Figure 5.6 with the clearly visible lettering when the transparent paper is held close, while the lettering becomes increasingly hazy farther away from the transparent paper due to the light scattering. The impact of the altered fiber morphology on the network density may be demonstrated by comparing the SEM images of the surface of an untreated paper substrate and a TEMPO-treated paper substrate in Figure 5.7.



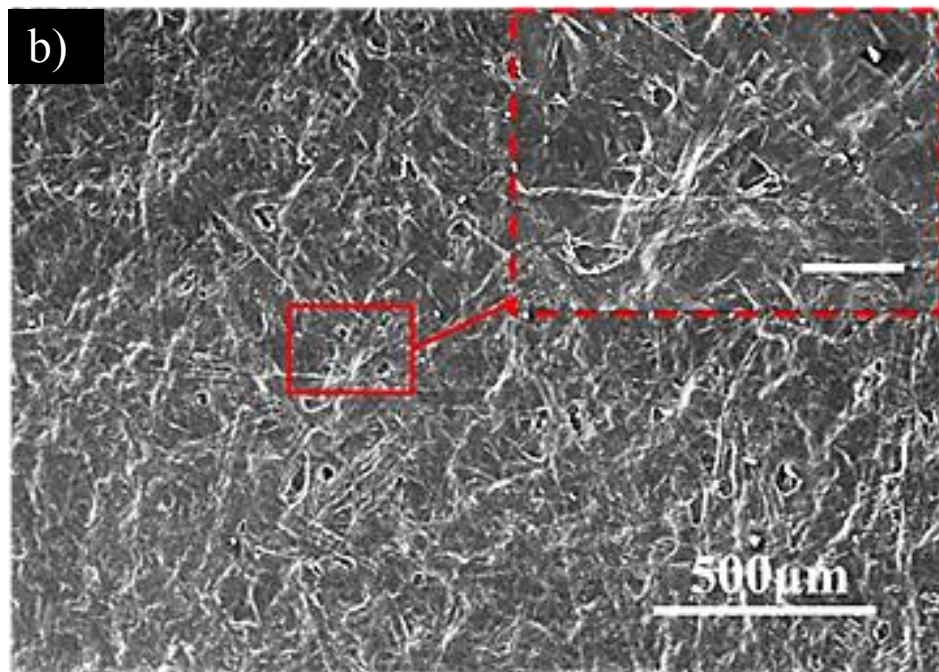


**Figure 5.7)** SEM images of the surface of (a) an untreated regular paper substrate and (b) the transparent paper substrate, with the inset magnifying the scale bar to 100  $\mu\text{m}$ .<sup>[152]</sup>

The SEM image in Figure 5.7(a) depicts the surface of an untreated paper substrate, which demonstrates the highly porous network of wood fibers. The SEM image of the transparent paper in Figure 5.7(b) clearly demonstrates that the TEMPO-treated fibers form a much denser network that conform into a homogenous surface morphology. The insert in Figure 3.7b further illustrates the diminished porosity of the TEMPO-treated fibrous network, with scale bar representing 100  $\mu\text{m}$ . The dual nature of high transmission haze and high transmittance as well as the mechanical properties exhibited by this transparent paper are explored and compared to other substrates in the following section.

### 5.3 Transparent Paper Properties

#### 5.3.1 Optical properties of transparent paper

The optical transmittance and total transmission haze were measured using a PerkinElmer Lambda 35 UV–Vis Spectrometer with an integrating sphere. The optical transmittance of transparent paper is depicted in Figure 5.8, and compared to the optical transmittance of a polyethylene terephthalate (PET) plastic substrate and nanopaper composed of NFC fabricated by pumping the TEMPO-treated pulp solution once through a 200  $\mu\text{m}$  diameter chamber in a Microfluidizer under a pressure of 20,000 psi.

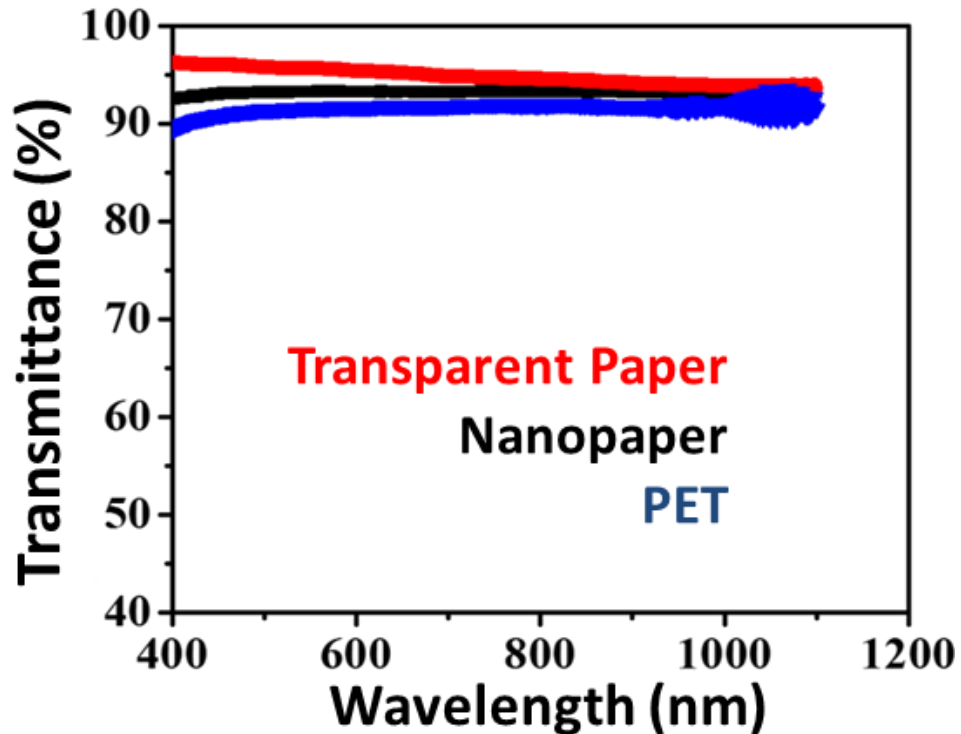


**Figure 5.8)** The total transmittance of the transparent paper, nanopaper, and PET substrates.<sup>[152]</sup>

As we see in Figure 5.8, the optical transmittance of transparent paper is above 90% for all visible wavelengths. The approximate 96% transmittance at 550nm is also



distinguishably higher than nanopaper and PET, which demonstrates transparent paper is more favorable as the transparent electrode substrate for solar cells since that wavelength represents the peak intensity of the solar spectrum.

Figure 5.9 illustrates the transmission haze spectra for the transparent paper, nanopaper, and PET substrates measured in Figure 5.8. Comparing these spectra provides more substantial evidence that transparent paper is a more suitable substrate for the transparent electrode in solar cells.

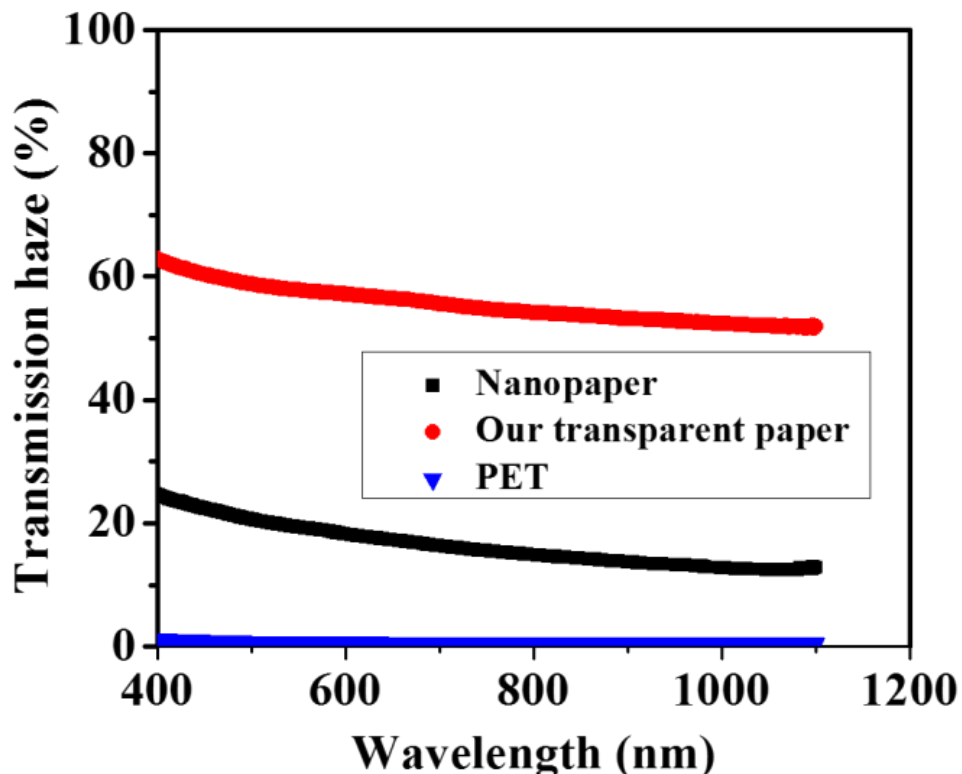
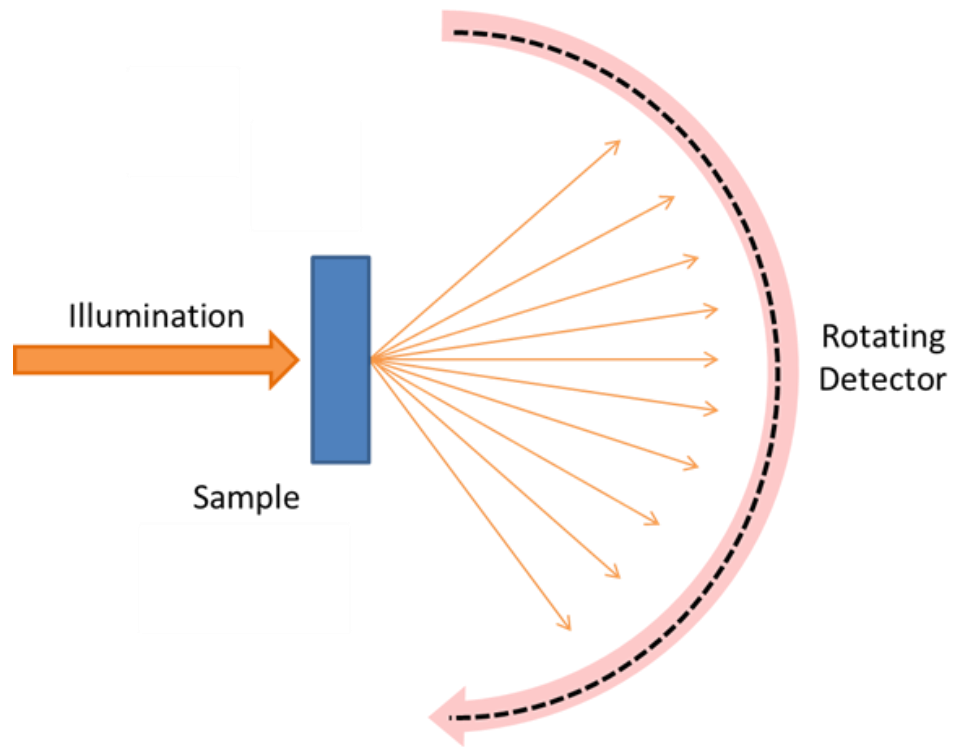


**Figure 5.9)** The total diffuse scattering of the transparent paper, nanopaper, and PET substrates measured in Figure 5.9.<sup>[152]</sup>

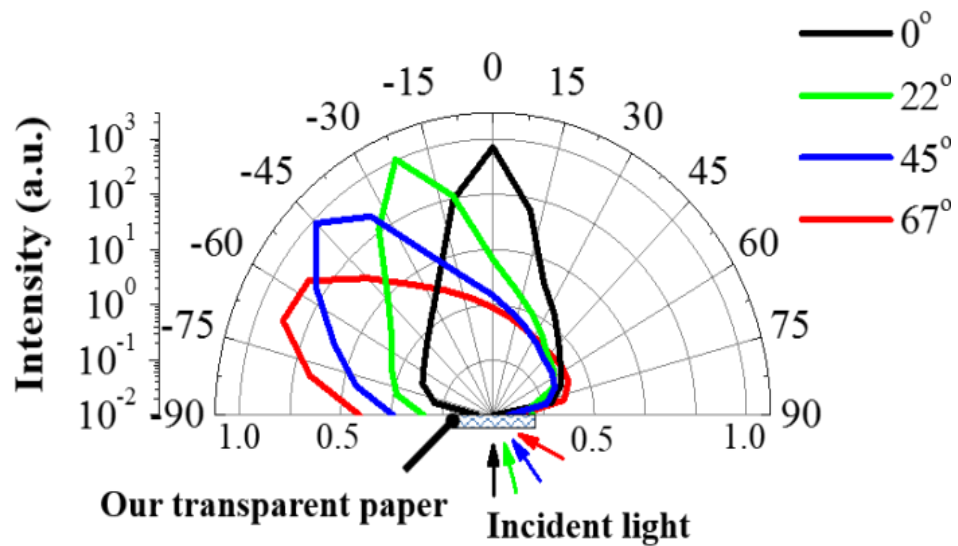
Although the optical transmittance of PET is approximately 90% at 550 nm, the transmission haze at that wavelength is negligible. This demonstrates that light incident on the PET substrate is not affected by any distinguishable scattering phenomena as it

propagates through it. The optical transmittance of nanopaper at 550 nm is approximately 92%, while the total transmission haze is 20%. This indicates that 20% of light propagating through the nanopaper is diffusely scattered at angles to the incident beam larger than approximately  $5^\circ$ . Another way to describe this measurement is that the transmission haze of nanopaper may contribute to distinct increases in the path length of 20% of light propagating through the thin-film conversion layers in solar cells if it is applied as the substrate for a transparent electrode in that device. Despite the high optical transmittance of transparent paper, the transmission haze at 550 nm is 60%. This indicates that the percent of light that is diffusely scattered through the transparent paper is 3 times that of nanopaper and 60 times that of PET, indicating significantly higher light trapping in solar cells that incorporate transparent paper in the transparent electrode as opposed to PET or nanopaper.

The angular distribution of the diffusely scattered light through the transparent paper is measured by a light detector rotated behind the substrate, which quantifies the transmitted light intensity at all diffuse angles. This measurement was repeated for multiple incident angles with a 532 nm wavelength laser. Figure 5.10 illustrates a schematic of the setup and Figure 5.11 presents the angular distribution spectrum of the diffusely scattered light through the transparent paper with multiple incident angles.



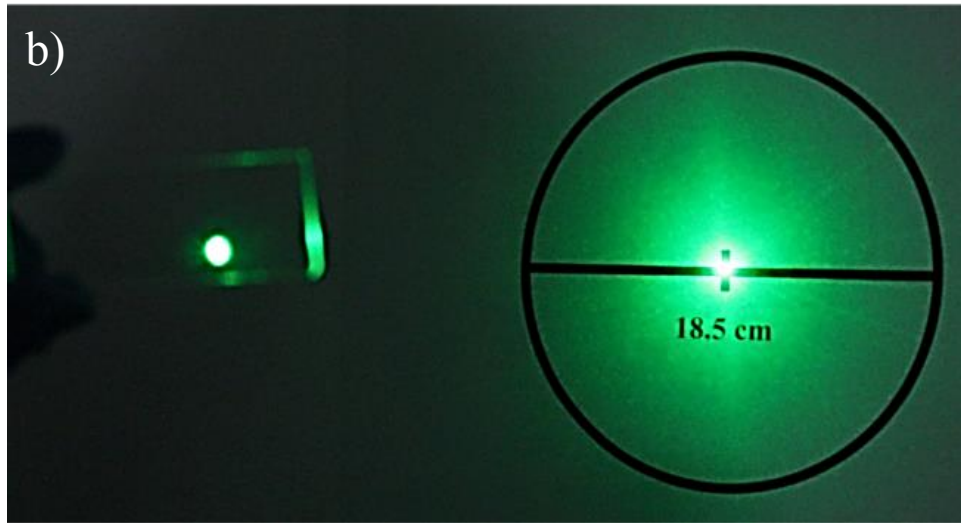
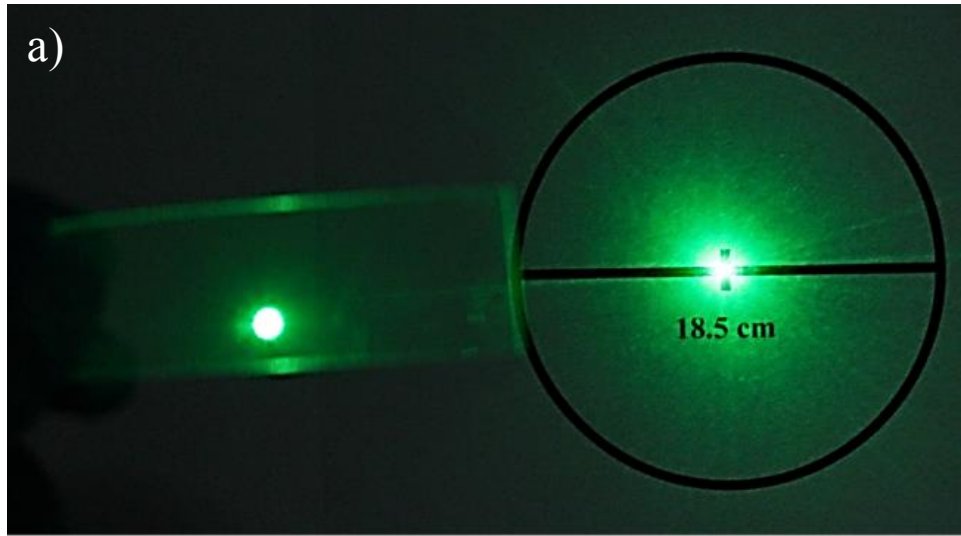
**Figure 5.10)** A schematic illustrating how the angular distribution of the diffusely scattered light is measured, with a rotating detector measuring the intensity of light every two degrees from  $-90 \leq \theta \leq 90^\circ$  to the perpendicular axis of the substrate surface.



**Figure 5.11)** A polar plot demonstrating the angular distribution of light diffusely scattered by transparent paper for multiple incident angles on the substrate surface by the illumination source.<sup>[152]</sup>

The spectra in Figure 5.11 compose a polar plot of the diffusely scattered light intensity normalized by the incident light intensity across at angles  $-90^\circ \leq \theta \leq 90^\circ$  from the perpendicular axis of the transparent paper. The normalized diffusely scattered light intensity is also scaled logarithmically for comparative purposes. The different color spectra are each representative of unique incident angles of the 532 nm wavelength light source. It is observable from this plot that although the highest intensity of light is measured along the angle of incidence relative to the light source; however, the transmission haze of the transparent paper diffusely scatters light at angles  $\theta \leq 75^\circ$  for each spectrum. It is further observable that light incident on the transparent paper at increasing angles to its perpendicular axis diffusely scatter at angles increasingly greater than  $75^\circ$ . This data illustrates that regardless of the angle of incidence on the transparent paper by a light source, there is a large distribution of path lengths that the diffusely scattered light propagates across with respect to a finite distance from the substrate surface along its perpendicular axis.

The distribution of the incident light on a transparent substrate is effectively visualized by illuminating a target behind each sample. Figure 5.12 depicts targets illuminated behind a PET, glass, and transparent paper substrate by a 532 nm wavelength light source.



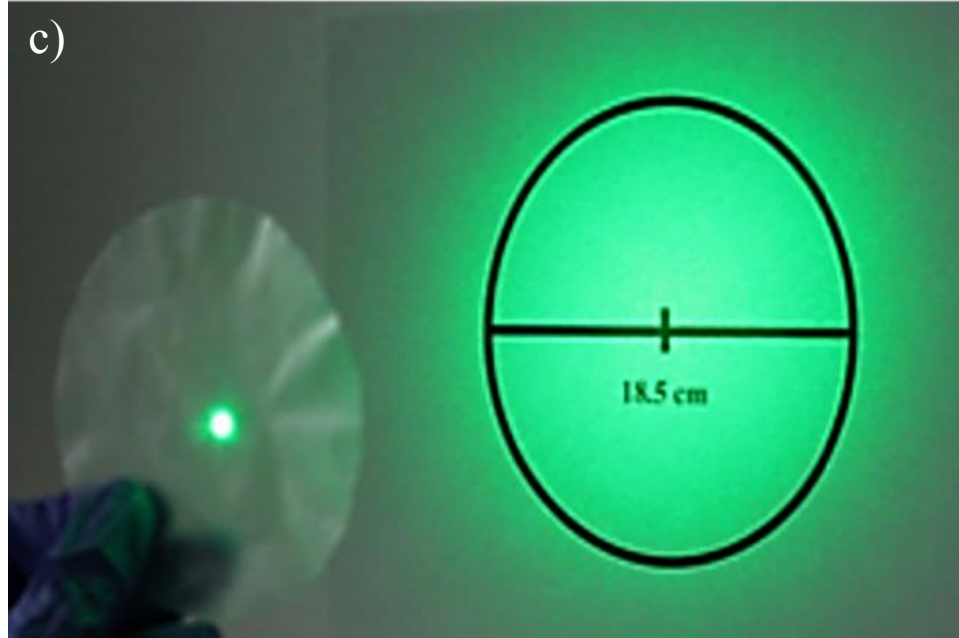


**Figure 5.12)** Images of the transmission haze effect on 532 nm light transmitted through (a) PET, (b) glass, and (c) transparent paper onto a target held at a fixed distance from the substrate surface.<sup>[152]</sup>

The target behind the transparent substrates displays a circle with a 18.5 cm diameter held approximately 30 cm away. The transmitted beam through the PET in Figure 5.12(a) and through the glass in Figure 5.12(b) remains brightest in the middle of the target, with a negligible light intensity distributed at any large distances from the center cross-hair. This indicates that no distinct diffuse scattering phenomena occur as the incident beam propagates through the PET and glass samples. Figure 5.12(c) demonstrates that the high transmission haze of the transparent paper distributes the transmitted light across a large area on the target, with a distinguishable intensity of diffusely scattered light existing outside the target circumference. This is a clear indication that the transmission haze of transparent paper elongates the path length of light diffusely scattered through the substrate at finite distances from the surface.

Another unique behavior of the transparent paper is the effect of substrate thickness on the optical properties. Figure 5.13 displays the transmission haze of transparent paper at a thickness from 20 – 69 mm.

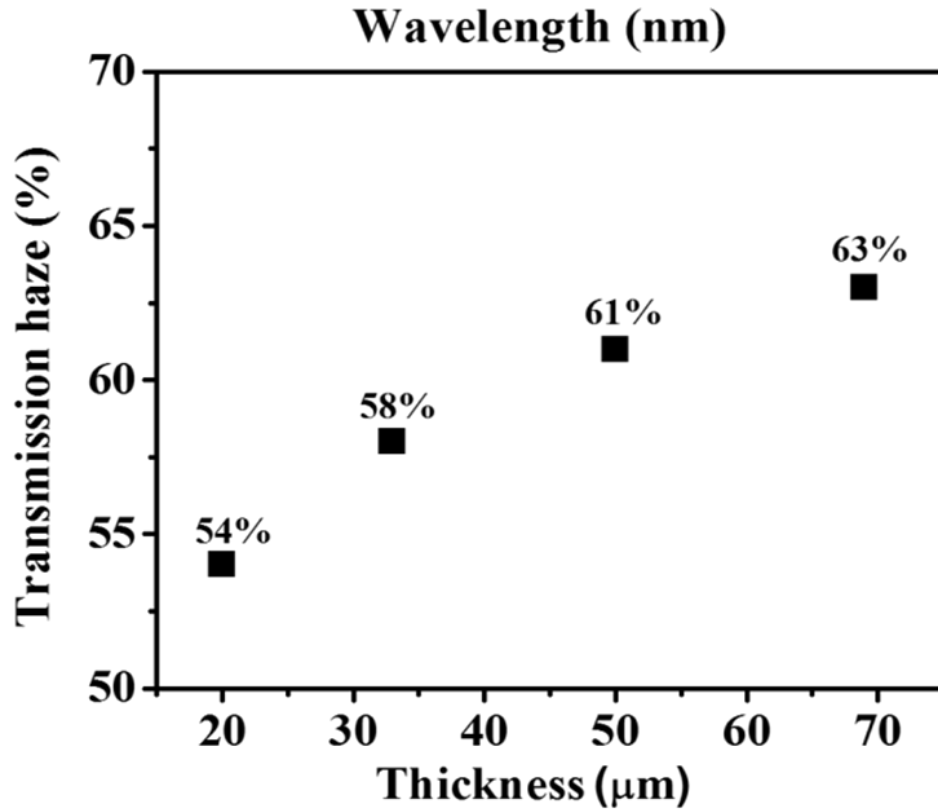


**Figure 5.13)** A plot demonstrating the total diffuse light scattering through transparent paper substrates with varying thicknesses.<sup>[152]</sup>

An expected increase in the total diffuse scattering by the transparent paper occurs with an increase in thickness, which coincides with an increase in scattering phenomena. An approximate 50 mm increase in thickness causes a 9% increase in the transmission haze. The corresponding change in the optical transmittance of the transparent paper with changes in the substrate thickness is depicted in Figure 5.14.

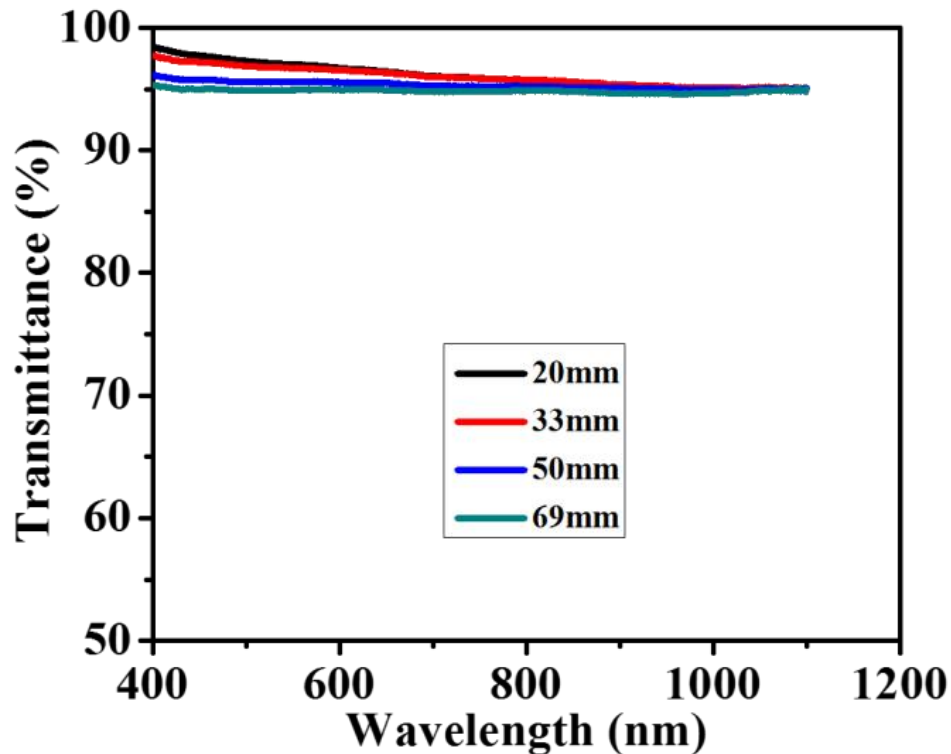


**Figure 5.14)** A plot demonstrating the total transmittance of light through transparent paper substrates with thicknesses correlating with Figure 5.14.<sup>[152]</sup>

The highest optical transmittance of approximately 97% at a wavelength of 550 nm is measured for the thinnest transparent paper substrate in Figure 5.14 of 20 mm. The lowest optical transmittance of approximately 95% at a wavelength of 550 nm is measured for the thickest transparent paper in Figure 5.14 of 69 mm. The change in optical transmittance of the transparent paper by increasing its thickness by approximately 50 mm is a decrease of approximately 2%; however, the lowest measured transmittance of approximately 95% in Figure 5.14 is still very high compared to other transparent substrates with high transmission haze. This change in optical transmittance is also significantly less than the approximate 9% increase in transmission haze



corresponding to the same increase in the transparent paper thickness. It may be concluded, therefore, that increases to the substrate thickness of the transparent paper provokes a more significant increase in the transmission haze than the decrease of the optical transmittance.

### 5.3.2 Mechanical properties of transparent paper

The alterations to the morphology of the wood fibers after a TEMPO-treatment impact the mechanical properties of the resulting microstructure network. An initial comparison of the mechanical properties of a common opaque paper substrate and the transparent paper was conducted via a tensile test, which generates stress versus strain curves for each sample in Figure 5.15.

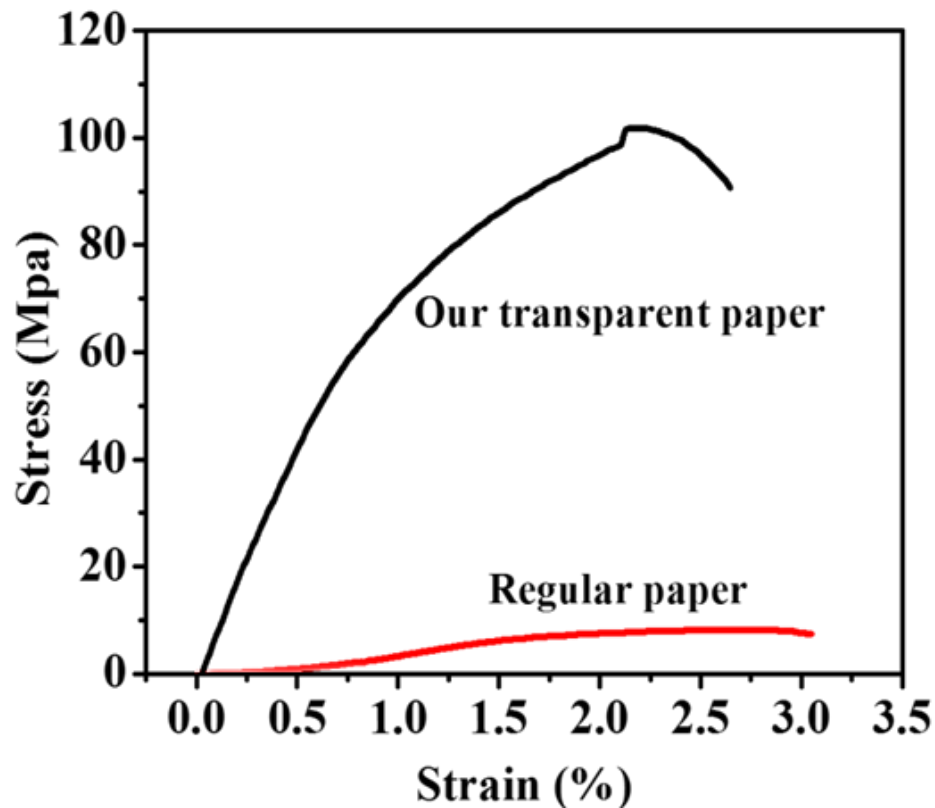


**Figure 5.15)** A stress versus strain curve for transparent paper and a regular paper substrate.<sup>[152]</sup>

It is common knowledge that common paper substrates tear under low levels of tensile stress, which is reflected in Figure 5.15 with the tensile strength reaching 8 MPa. This imparts a very low toughness of  $0.15 \text{ J/m}^3$  to conventional paper substrates. The transparent paper consisting of TEMPO-treated cellulose fibers displays a toughness of  $1.88 \text{ J/m}^3$  that is more than 10 times the toughness of untreated paper substrates. This higher toughness of transparent paper is the product of a dramatically improved mechanical stability of the fibrous network after a TEMPO-treatment of the cellulose, reflected in a Young's modulus of approximately 90 MPa and a tensile strength of 105 MPa that are both an order of magnitude greater than those of regular untreated paper substrates. Table 3.1 reports these mechanical characteristics of the transparent paper, regular paper, and also for a flexible PET substrate. It is clear from these values that although the flexible PET may endure much higher degrees of strain that imparts a higher toughness than transparent paper, the transparent paper has a much higher Young's modulus and tensile strength than PET. This indicates that the transparent paper can withstand much higher tensile stress without significantly deforming or failing than both common paper and PET.

	Young's Modulus (MPa)	Tensile Strength (MPa)	Toughness ( $\text{J/m}^3$ )
Transparent Paper	~ 90	105	1.88
Regular Paper	~ 0.7	8	0.15
PET	2-2.7	55-75	~ 5

**Table 5.1)** Mechanical properties of transparent paper, regular paper, and PET measured by the tensile strength test in Figure 5.16.<sup>[152]</sup>

The improved mechanical stability of the transparent paper may be explained through an investigation of the interactions between the TEMPO-treated cellulose fibers. The morphological transformation of the untreated hollow cellulose fibers due to the TEMPO-treatment increases the surface area of the cellulose microstructures by exposing the inner surface area of the fibers after they are unzipped and improves the packing density of the network by rendering flattened cellulose flakes with various sizes. There are consequently many more hydrogen bonds between the cellulose microstructures after the TEMPO-treatment of the wooden fibers that stabilize the dense fibrous network, which is illustrated in Figure 5.16.

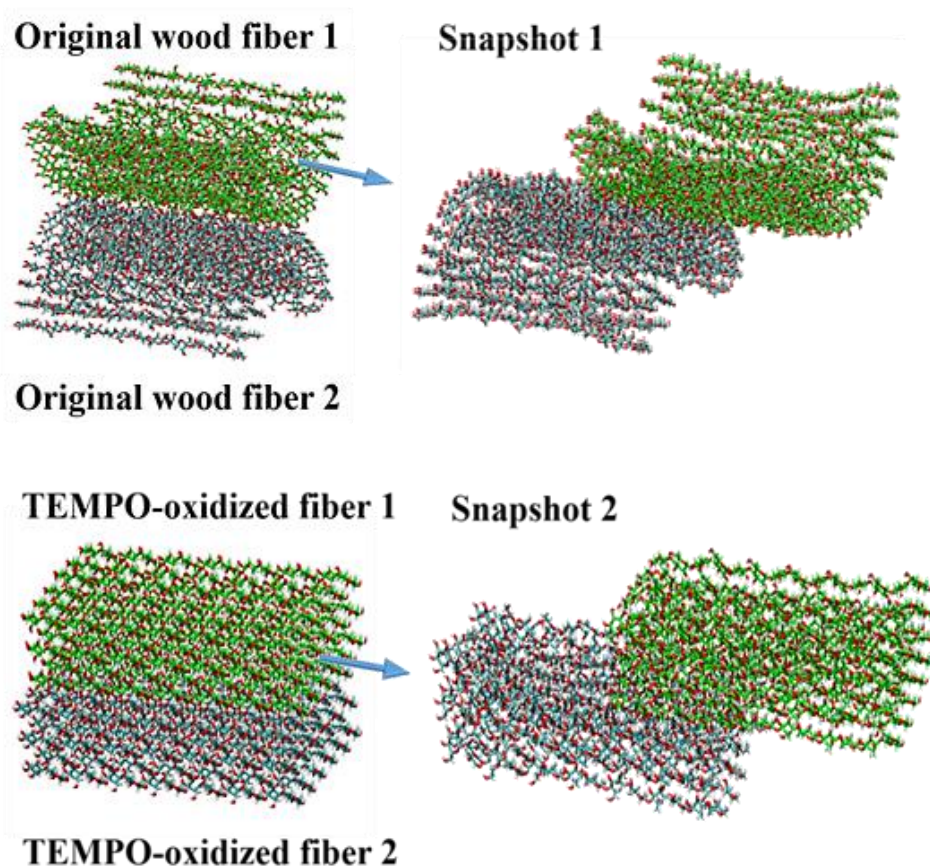


**Figure 5.16)** A schematic demonstrating the change in the number of interfacial bonds between a curved wood fiber and a TEMPO-oxidized flattened cellulose fiber.<sup>[152]</sup>

#### 5.4 Smooth Transparent Paper for Conductive Electrode

Paper substrates offer an environmentally friendly alternative to plastic while exhibiting nominal optical properties and mechanical stability. Transparent paper that exhibits both high optical transmittance and high transmission haze is realized with a densely packed network of cellulose microstructures produced by a TEMPO oxidation process of wood fibers. The optical transmittance of the transparent paper at a 550 nm wavelength is measured at approximately 96% for a 50  $\mu\text{m}$  thick substrate with a corresponding total transmission haze of approximately 60%. Quantitative and qualitative experiments demonstrate that the diffusely scattered light extends the path length of light through the transparent paper without compromising the optical transmittance, which is beneficial for thin-film solar cells. The transparent paper was also revealed to exhibit good mechanical stability, with a Young's modulus and tensile strength significantly greater than common opaque paper and flexible PET.

In addition to these compelling attributes, transparent paper with a conductive Ag NW network hosted on its surface may exhibit high conductivity, which makes it the most suitable alternative to ITO TCEs in flexible thin film photovoltaic modules. Ag NW films are also reported to exhibit significant diffuse light scattering properties that depend on the density of the wires in the network and their diameter.<sup>[23, 27]</sup> Investigations into the total diffuse scattering is previously reported for Ag NW films and paper individually, but there are no reports of the angular distribution of light scattered through

these respective layers, nor are there any reports of the optical properties for a composite TCE of a Ag NW embedded on a transparent paper substrate.

In this study we introduce a novel TCE structure that consists of an Ag NW network embedded onto the surface of a transparent paper substrate through a simple, novel lamination process without the need for any pre-treatments. By embedding the Ag NW network onto the surface of the transparent paper substrate through a wet-lamination process, the TCE possesses a high mechanical stability while retaining its conductivity.

Figure 5.17 schematically illustrates the design for this new structure.

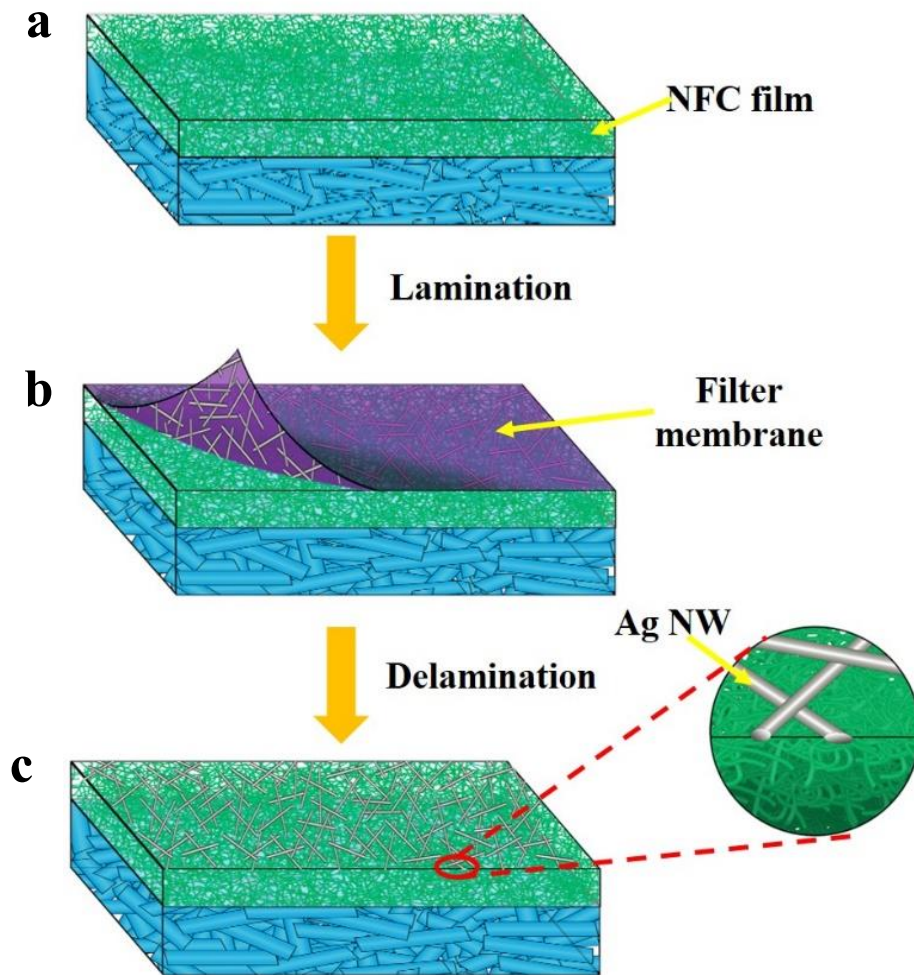
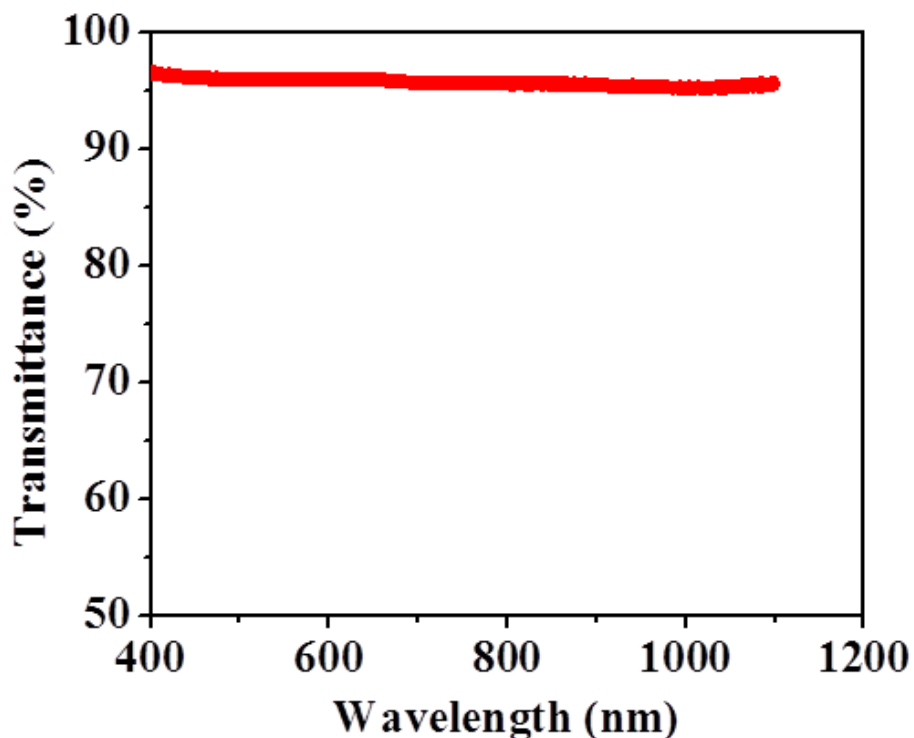


**Figure 5.17)** Schematic of Ag NW network embedded in a nanopaper surface on the transparent paper. (a) Nanofibrillated cellulose was filtered through TEMPO-treated paper to form a smooth surface, (b) with a novel lamination process, a filtered Ag NW network is embedded in the smooth NFC surface, and (c) the final structure is a uniform Ag NW network embedded onto the surface of transparent paper.

This Ag NW paper electrode is low cost, renewable, durable, and demonstrates high optoelectronic performance. Along with introducing a novel TCE structure with nominal optoelectronic properties, this study also investigates the unique transmission haze properties of the Ag NW transparent paper, and directly correlates these optical properties to better light absorption in thin film solar conversion layers as compared to similar devices consisting of ITO.

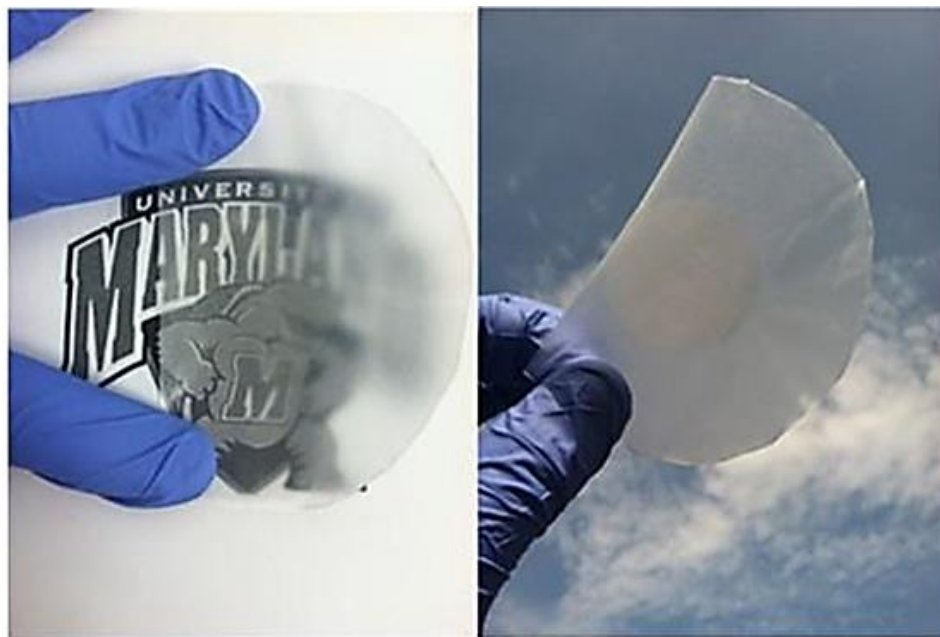
### 5.5 Experimental Method

A method outlined in Section 5.2 was used to fabricate transparent paper by vacuum filtering a 1 wt % solution of TEMPO-treated wood pulp. Bleached sulfate softwood pulp extracted from southern yellow pine was dispersed in distilled water containing sodium bromide and TEMPO, and then disintegrated in the solution with a Turrax mixer. A portion of the TEMPO-treated pulp was passed through a Microfluidizer to produce nanofibrillated cellulose. The NFC was then filtered into a thin wet NFC film for the purpose of getting high smoothness to host the Ag NW conductive network on the transparent paper. TEMPO-treated pulp was then filtered through the NFC film to form a wet transparent paper substrate with a smooth surface layer. The transparency of this substrate reaches 96% at a wavelength of 550nm, as illustrated in Figure 5.18.

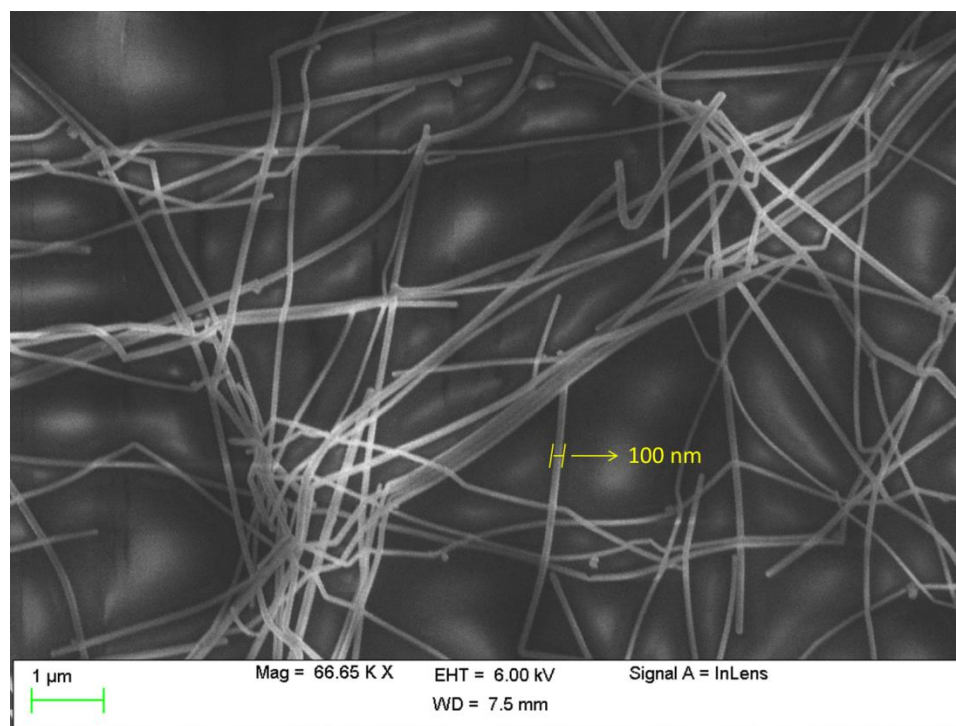


**Figure 5.18)** The transmittance curve for the paper substrate before a Ag NW network is embedded into the surface.

A 10 mg/ml Ag NW suspension was diluted into 0.1mg/ml with ethanol and filtered onto the transparent paper to form a uniform Ag NW film. Finally, the Ag NW film was laminated with the pure NFC layer of the abovementioned transparent paper, and the laminated paper was placed between regular filter papers to absorb residue water within the wet sheet and dried at room temperature under pressure. Figure 5.19 depicts the Ag NW transparent paper electrode sample. Figure 5.19 demonstrates a visibly homogenous Ag NW network on the transparent paper with good transparency. It is also clear that the light scattering through this electrode is very high; the transparency through the electrode diminishes rapidly and images farther from the surface appear very cloudy.



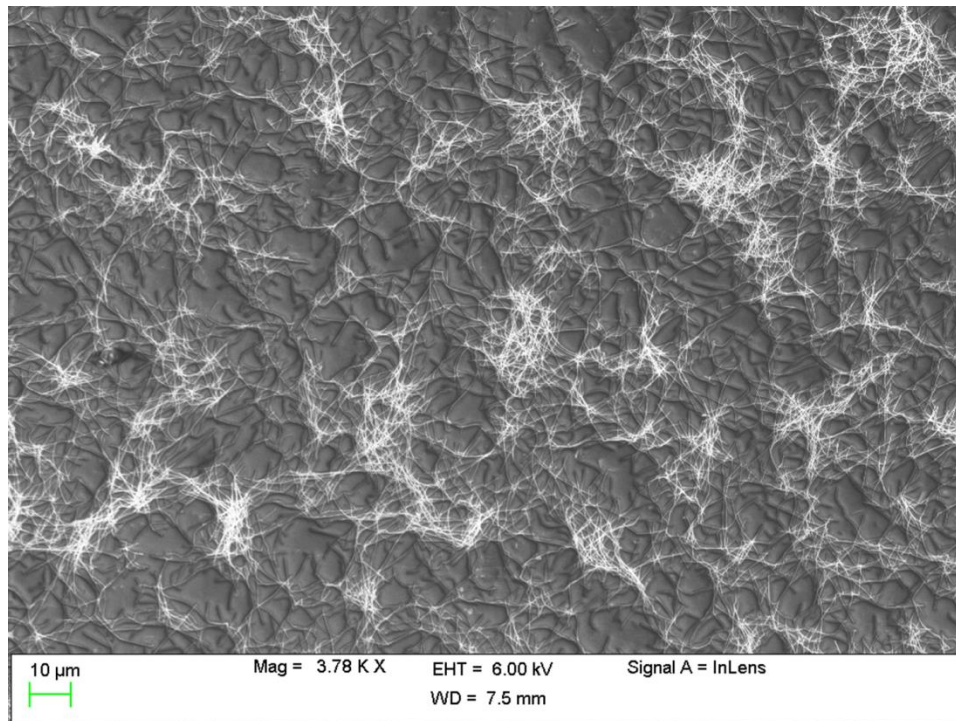
**Figure 5.19)** Optical image of Ag NW transparent paper.



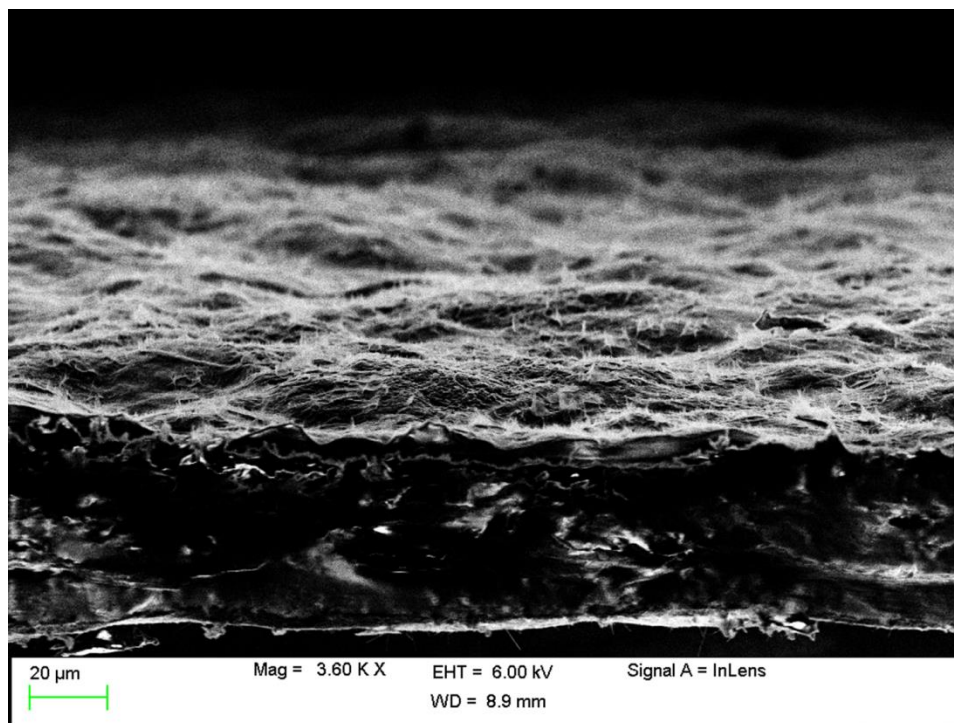
**Figure 5.20)** An SEM image of Ag NWs with a diameter of 100 nm.



Figure 5.20 is an SEM image taken with a ZEISS (LEO) 1550VP SEM that demonstrates the Ag NW consists of long wires with a diameter of 100nm. As previously reported in Chapter 4, this larger diameter for the Ag NWs enables greater light scattering. The long Ag NW length enables a large percolation network while still enabling a high transparency for the Ag NW network, and is depicted in the SEM image of the electrode surface in Figure 5.21.<sup>[3, 133, 155]</sup> It is important to note the obvious embedding of the Ag NWs into the transparent paper surface, which stabilizes the mechanical properties of the conducting layer and prevent delamination.



**Figure 5.21)** Top view of Ag NW transparent paper demonstrating embedded Ag NW network.



**Figure 5.22)** An SEM image of the cross-section of Ag NW transparent paper.

Figure 5.22 further demonstrates this embedded nature of the Ag NW into the surface of the transparent paper, with a clear depiction of the larger transparent paper substrate thickness compared to the Ag NW network.

## 5.6 Results and Discussion

### 5.6.1 Optoelectronic performance

To verify the initial observations of the high transparency of the Ag NW transparent paper electrode, a UV-Vis spectrometer with an integrating sphere was used to measure the total transmittance of the entire TCE. The total electrode transmittance with respect to the wavelength is depicted in Figure 5.23. At a wavelength of 550 nm the total transmittance of the TCE is about 91%. This transparency is among the highest reported for TCEs. This value depends on both the optical properties of the substrate as

well as the Ag NW network; the nanowires have minimal impact on the transmittance of the composite structure, yet change the paper from insulating to highly conductive. The sheet resistance of this Ag NW transparent conducting paper electrode was measured as  $13 \Omega/\text{sq}_{\text{cm}}$ . The total transmittance was measured with a PerkinElmer Lambda 35 UV-Vis Spectrometer with a Labsphere RSA-ES-20 integrating sphere. The sheet resistance was measured with an in-line four-point probe.

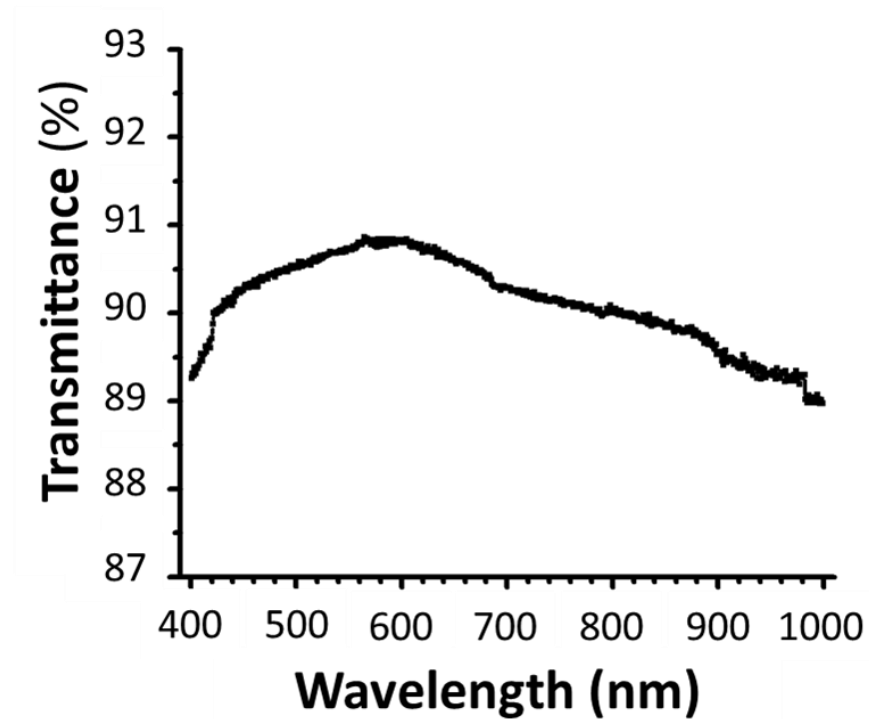


**Figure 5.23)** Total transmittance versus wavelength of Ag NW paper.

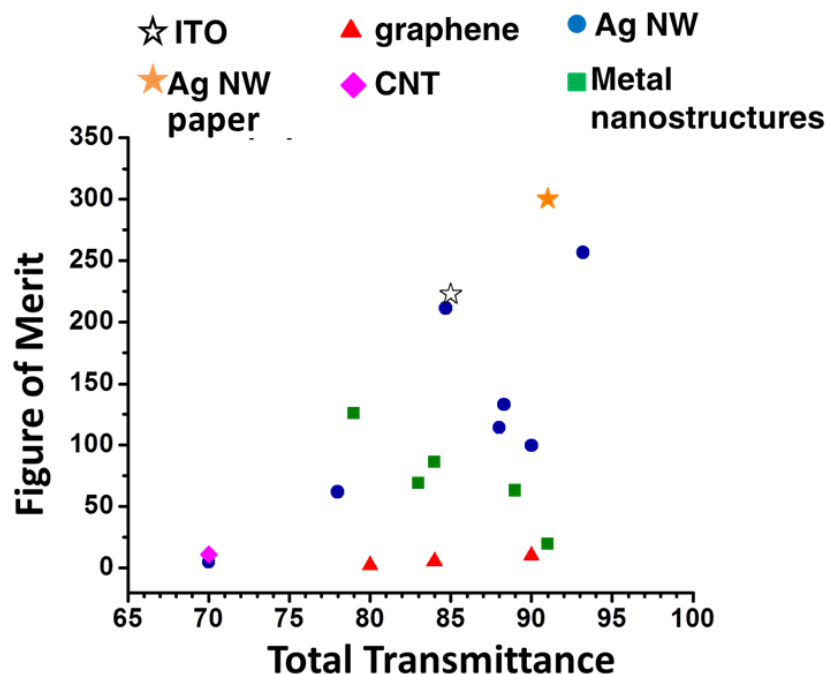


**Figure 5.24)** Figure of merit versus total transmittance for previous TCE reports, ITO, and our Ag NW transparent paper [54, 113, 121, 133, 150, 156-158]

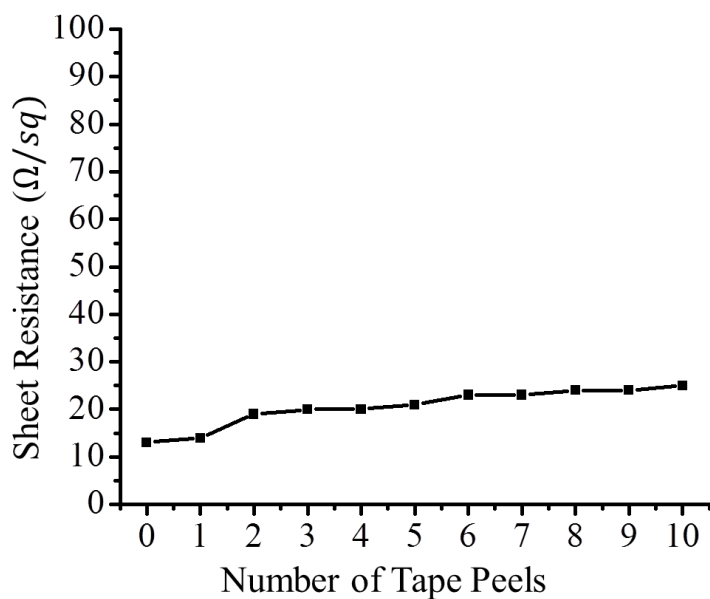
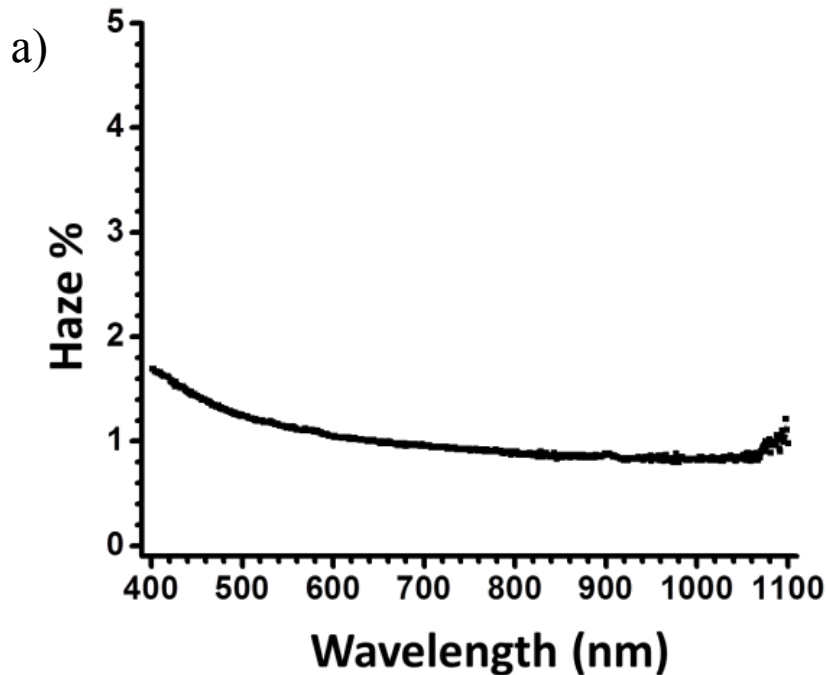


**Figure 5.25)** The tabulated results for the tape test measurement on the Ag NW paper TCE sample. The initial sheet resistance of the sample was measured at 13  $\Omega/sq$ , which increased to 25  $\Omega/sq$  after manually pressing scotch tape down on the sample and peeling it off a total of ten times.

To evaluate the performance for this TCE, the contemporary figure of merit for transparent electrodes composed of nanostructured films with a thickness below the percolation limit was used to relate the total transmittance at 550 nm and the sheet resistance in Equation 4.4. Figure 5.24 displays a comparative review of previously reported figures of merit for various TCEs of various compositions including CNTs;<sup>[54]</sup> graphene;<sup>[113]</sup> and ink based metallic networks composed of copper nanowires<sup>[156]</sup>, gold nanowires<sup>[156]</sup>, and silver nanowires.<sup>[121, 133, 150, 156-158]</sup> According to this comparison, our Ag NW transparent conducting paper electrode has a much greater figure of merit than ITO and has the highest figure of merit for solution based TCEs. It is important to note that the previously reported Ag NW TCEs from ink based solutions normalize their optical properties to eliminate the impact of the substrate the networks are deposited on. The figure of merit for our Ag NW transparent conducting electrode includes the substrate within the evaluation of the TCE performance; therefore, it is an accurate performance metric within a device rather than as an isolated Ag NW film. Despite the possible reduction in optoelectronic performance that may occur when evaluating the Ag NW in conjunction with the substrate, our Ag NW transparent conducting paper still possesses the highest reported figure of merit TCEs fabricated with a conventional solution based process. This result is due to the uniform Ag NW network enabled by a filtration onto the transparent paper substrate and the subsequent mechanically pressed NW junctions during the lamination process. In addition the performance was maintained even after several peeling tests with scotch tape, as seen in Figure 5.25. This demonstrates the high resistance to delamination of the Ag NW transparent paper due to the embedded nanomaterials.<sup>[148, 155, 159]</sup>

### 5.6.2 Haze properties

The total diffuse scattering, or diffuse transmission haze, of an ITO sample sputtered on soda-lime glass, a transparent paper substrate, and the Ag NW paper was measured with a UV-Vis spectrometer with an integrating sphere. The mechanism for haze measurements with an integrating sphere is depicted in Figure 4.8. The transmission haze for the ITO film on soda lime glass is very small (1% at 550 nm), as depicted in Figure 5.26(a). The transmission haze for the transparent paper reaches 59% at 550 nm (Figure 5.26(b)), and the transmission haze for the Ag NW transparent paper slightly surpasses 65% at 550 nm (Figure 5.26(c)). These values are accurate determinations of the total transmission haze through each sample but do not detail the exact behavior of the diffuse scattered light.



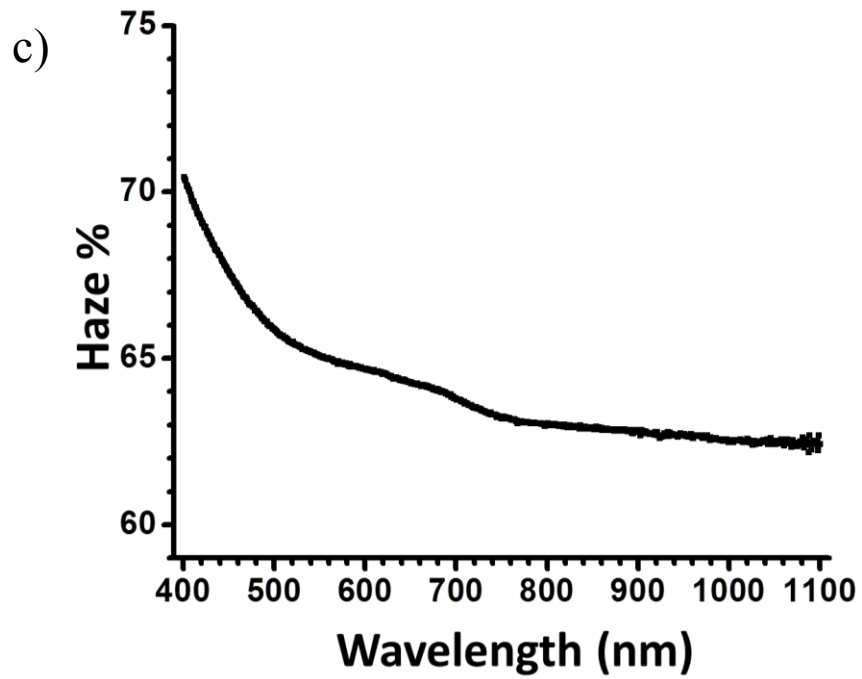
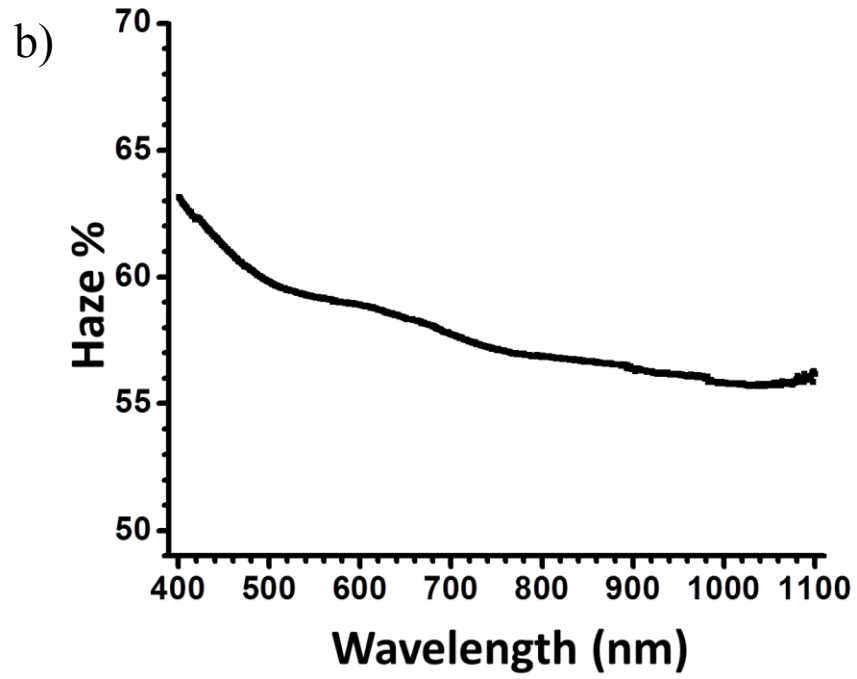


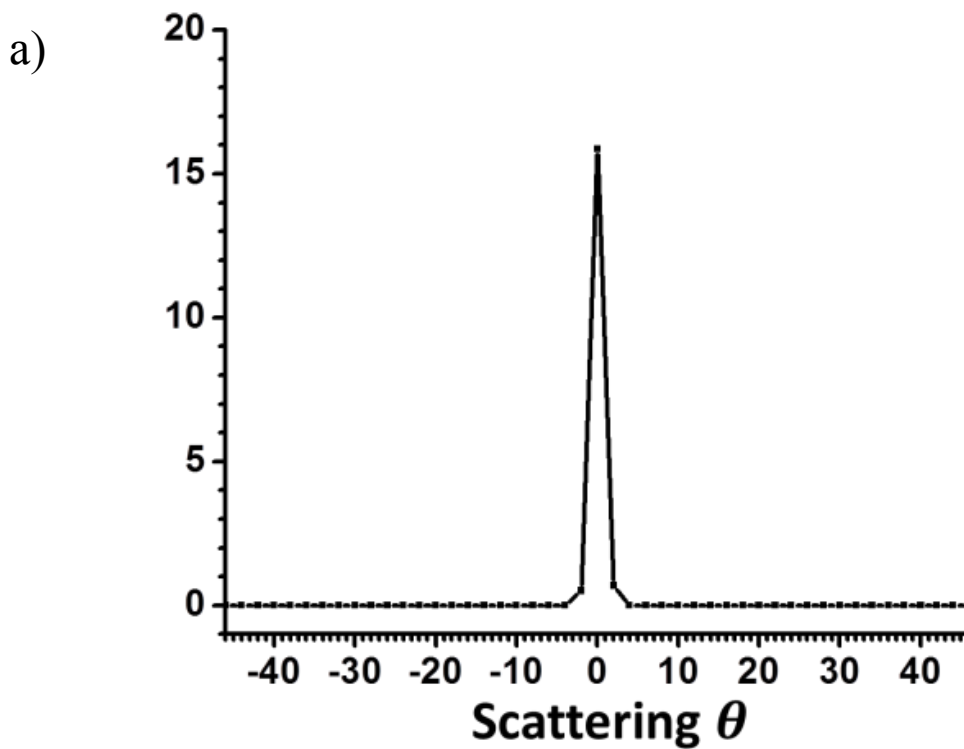
**Figure 5.26** The total diffuse transmission haze for (a) ITO on glass, (b) transparent paper, and (c) Ag NW paper.

An additional experiment to determine the angular distribution of the diffusely scattered light through a surface was conducted to expound upon the transmission haze values measured by the UV-Vis spectrometer. The angular distribution of the transmitted light emitted from a source normal to the surface is separated into a non-deflected component and a diffuse component that extends over all transmitted scattering angles.<sup>[159]</sup> For surfaces like ITO on optically smooth glass, the specular coherent component dominates the angular distribution and displays an extremely narrow curve with a width that depends on the spot size of the incident beam and the detector area. An ideal specular curve with no haze resembles a dirac-delta function. Surfaces like transparent paper or Ag NW networks possess a dense fibrous network that have large scattering cross-sections emanating from each nanomaterial, where the diffuse component dominates resulting in broadened angular distribution.

The scattering angle distributions were measured with a detector rotating behind sample surfaces illuminated with a 532 nm semiconductor laser, as depicted in Figure 5.10. Measurements for an ITO sample sputtered on soda-lime glass (Figure 5.27(a)), a transparent paper substrate (Figure 5.27(b)), and the Ag NW transparent conducting paper sample evaluated in the previous section (Figure 5.27(c)) were taken with this optical setup to show the angular distribution of diffusely scattered light through each sample. As expected, for ITO the angular distribution of the transmitted light is concentrated in the incident direction, demonstrating almost entirely specular transmittance. A slight deviation from an ideal dirac-delta regression in Figure 5.27(a) is due to the detector area and spot size of the incident beam, making perfect point measurements impossible for this setup. The transmission through the transparent paper



substrate in Figure 5.27(b) produces high diffuse scattering in a Gaussian-like pattern. The diffuse scattering angle range is defined in this paper as the scattered angles that demonstrate a light intensity greater than 5% of the peak intensity at  $0^\circ$ . The scattering distribution extends radially up to  $16^\circ$  from the axis of symmetry for the transparent paper substrate, which delivers a maximum scattering solid angle of  $32^\circ$ . Once the Ag NW network is embedded into the paper substrate to form the Ag NW transparent conducting paper electrode the scattering distribution extends to  $17^\circ$  in the radial direction from the axis of symmetry, which delivers a maximum scattering angle range of  $34^\circ$  as seen in Figure 5.27(c).



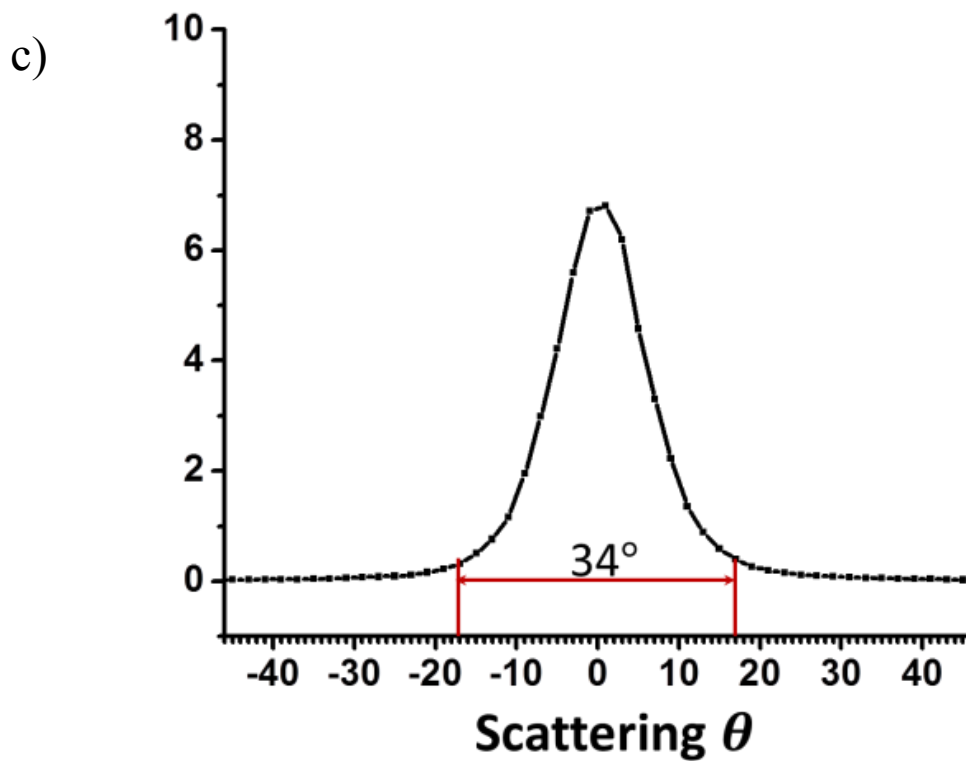
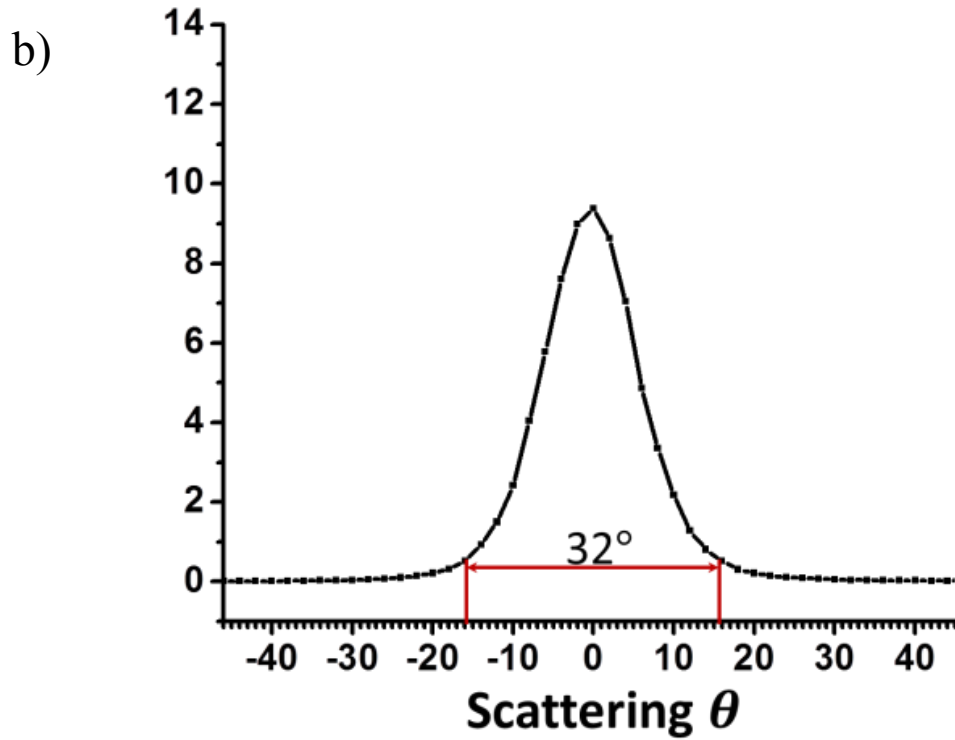


**Figure 5.27)** Diffuse scattering angular distribution with arbitrary y-axis units for (a) ITO on glass, (b) transparent paper, and (c) Ag NW paper.

In order to verify the total diffuse scattering of Figure 5.26(c) with Figure 5.27(c) the integral of the total angular distribution of the light intensity minus solid angle of the incident opening in the integrating sphere of the UV-Vis Spectrometer was taken in polar coordinates with respect to  $\theta$  and rotated around the incident axis for all  $\phi$  angles. It is obvious from these measurements that ITO exhibits specular transmission with no significant diffuse scattering phenomena measured, while the Ag NW transparent conducting paper electrode exhibits high diffuse scattering across a wide angular range. It is also clear from these measurements that diffuse scattering properties are not restricted to the paper substrate, or just the Ag NW embedded network, but that there is a nominal contribution from each component of the hybrid structure to the transmission haze as well as the maximum scattering angle range of the TCE. The large scattering coefficient of the Ag NWs in the conductive network further enhances the diffuse light scattering through the transparent paper. The enhancement of the angular distribution by the addition of the Ag NW can be attributed to the compounding scattering mechanisms of the paper substrate and the Ag NW network.

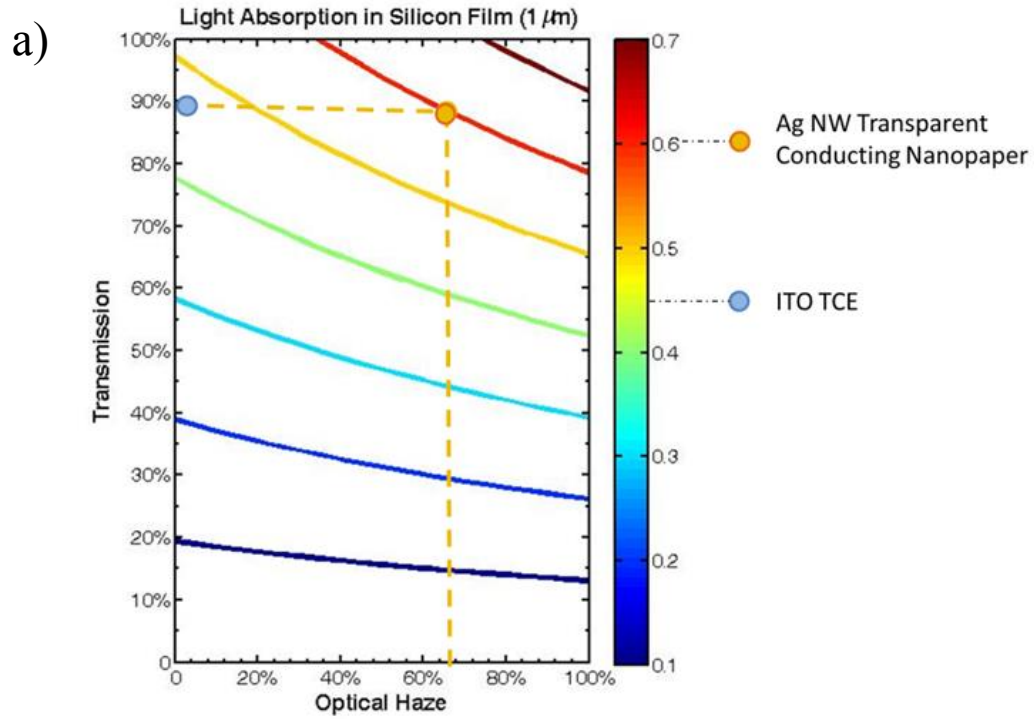
### 5.6.3 Photovoltaic light absorption simulation

The transmission haze of a TCE will contribute light trapping that can greatly increase absorption and/or reduce required material in photovoltaic devices. Despite this, haze is generally not considered when evaluating and comparing TCE's. In order to compare the above films and other standard films in terms of potential photovoltaic performance, a ray-optics simulation was created in collaboration with the Jeremy Munday group in the Electrical Engineering Department of the University of Maryland.<sup>[160]</sup> The simulation was performed with several generalizing assumptions.

While these assumptions don't describe a real device, they do capture all of the important physics and give a non-arbitrary comparison of different TCE's without requiring a large number of inputs. Here we assume: 1) light is incident on the TCE as part of a TCE/Absorber/Mirror stack; 2) a fraction of light ( $T$ ) is transmitted through the TCE on the first pass; 3) the angular distribution of light is then split into a diffuse component with fractional power  $H$  with cosine (Lambertian) angular dependence and a specular component with fractional power  $(1 - H)$ ,<sup>[161]</sup> 4) the reflection at the absorber/TCE interface is then determined by Fresnel coefficients,<sup>[162]</sup> and 5) the diffuse component undergoes Lambertian scattering at the absorber/TCE and the specular component experiences no scattering but loses coherence at the interface. The calculated absorption values are then weighted by the solar spectrum and averaged.

Figure 5.28 shows contour plots for the fraction of light absorbed in the absorbing layer of several simulated thin film photovoltaic structures with varied transmission haze and initial transmission for the TCE. As shown, in the region of high transmission large gains in absorption can be attained by increasing the transmission haze. In addition, Figure 5.28 compares a high performance ITO TCE having no transmission haze but 90% transmittance, and the Ag NW transparent conducting paper with our demonstrated 65% transmission haze at roughly the same transmittance as ITO. Silicon thin films demonstrate over 25% greater light absorption for structures using Ag NW transparent conducting paper rather than ITO, as illustrated in Figure 5.28a. Similarly gallium arsenide (GaAs) thin films demonstrate over 45% greater light absorption for structures using Ag NW transparent conducting paper rather than ITO (Figure 5.28b) and cadmium telluride (CdTe) thin films demonstrate over 35% greater

light absorption for structures using Ag NW paper TCE rather than ITO (Figure 5.28c). It is clear that Ag NW transparent conducting paper induce significantly more light absorption in thin film photovoltaic absorbers than ITO TCEs.



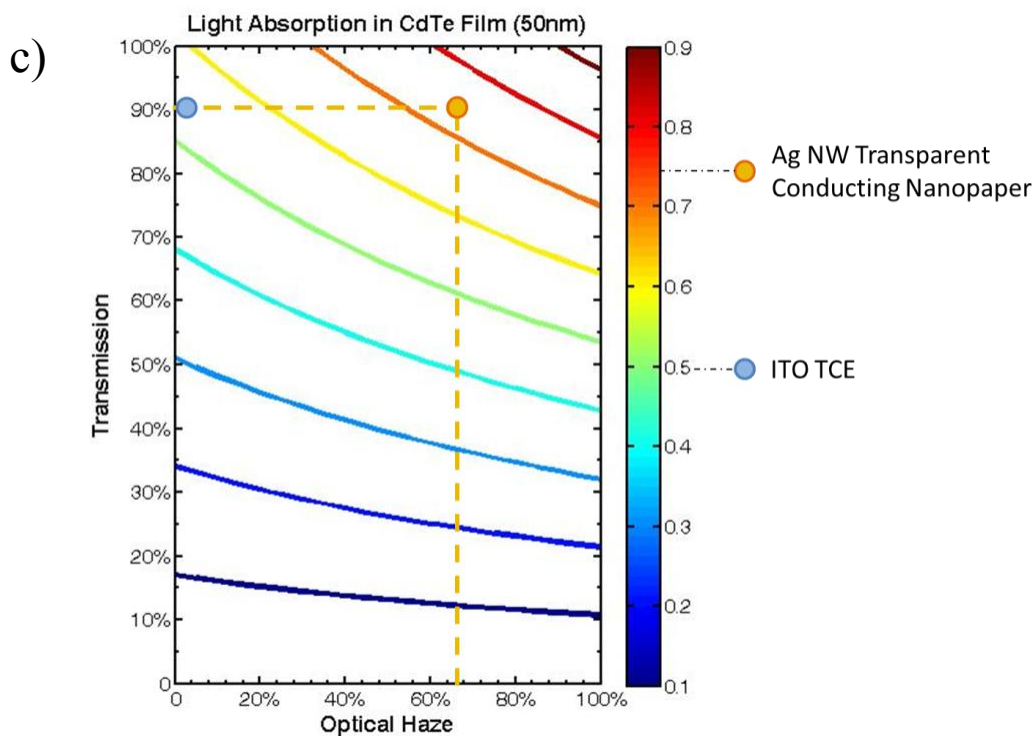
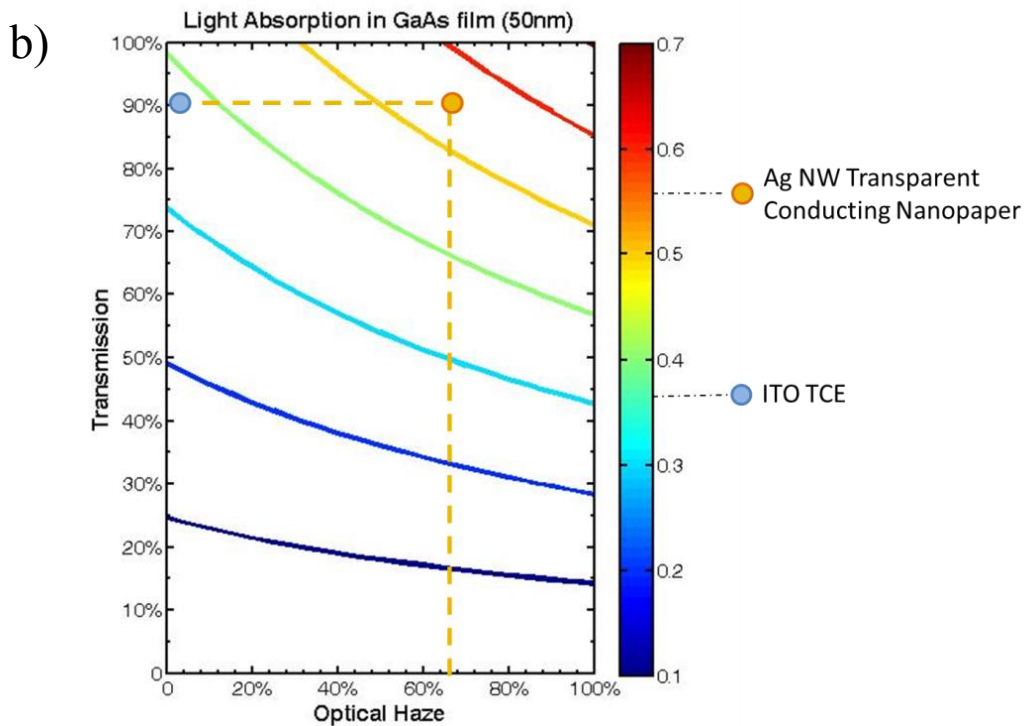


**Figure 5.28)** Light absorption dependence of a structure including either a TCE with varying optical properties and an absorber layer (a) a 1  $\mu\text{m}$  thick Si film, (b) a 50 nm thick GaAs film, and a 50 nm thick CdTe film. Light absorption in these absorbers for a highly transparent ITO TCE and our Ag NW paper TCE are compared as well.

### 5.7 Conclusion

A new highly stable TCE structure composed of an Ag NW network embedded into the surface of transparent paper was achieved and its optoelectronic properties were investigated. Compared to ITO TCEs, the materials and manufacturing methods of the TCE reported in this study is cheaper, more flexible, and more amenable to large scale manufacturing. It was demonstrated that the Ag NW transparent conducting electrode exhibits better optoelectronic properties according to conventional TCE performance models, and is projected to induce greater light absorption in thin film photovoltaic absorbers than ITO TCEs due to its greater transmission haze. There is conclusive evidence from the data in this investigation that Ag NW transparent conducting electrodes are an optimal replacement for ITO TCEs in thin film photovoltaics based on their superior individual performance and projected enhancement of solar device performance.

## Chapter 6: Conclusion and Outlook

### 6.1 Thesis Summary

In this work we explore random networks of carbon nanotubes and seek ways to maximize the conductivity of these networks by manipulating the intrinsic properties of the nanotubes and their interactions between each other in solution. In order to minimize inter-tube bundling in solution while maintaining the structural stability of each nanotube, a unique ink engineering process to stabilize FWNTs in an IPA-based solution via surface functionalization was developed. The stabilization of the inks was directly related to higher uniformity of the spray-coated random network of FWNTs. Through this investigation, we demonstrate a spray-coated FWNT film with conductivity above 2100 S/cm, which is the highest for CNT spray-coatings derived from surfactant-free IPA-based inks.

A novel boron doped FWNT structure intended to lower the resistivity of the nanotubes and thus increase the conductivity of subsequent spray-coatings was also introduced and investigated. A unique solution injected CVD process to grow FWNTs that are substitutionally doped with boron during their growth was developed and optimized. The structural, morphological, and electrical properties of the boron-doped FWNTs were analyzed and compared to the characteristics of the pristine FWNTs. An investigation into the purification of the growth yield revealed a boron oxide impurity that may be partially removed with a methanol wash; however, not all impurity phases were conclusively identified or removed. The effect of the ink fabrication process on the



properties of the boron-doped FWNTs elucidated the effect of dispersion forces in solution on the film uniformity.

Random networks of silver nanowires were also investigated in this work, with a primary focus on their diffuse light scattering behavior. A theoretical and experimental study of the optoelectronic properties of individual Ag NWs and transparent random networks Ag NWs examined the difference between their diffuse transmittance from their specular transmittance. This analysis provided evidence that the current figure of merit for Ag NW TCEs is insufficient to evaluate their use in thin film solar cells due to the omission of transmission haze in the performance metric.

A new transparent electrode composite structure of an Ag NW network embedded into the surface of novel transparent paper with high diffuse transmittance fabricated and investigated. It was demonstrated that the Ag NW transparent conducting electrode exhibits better optoelectronic properties according to conventional TCE performance models, and is projected to induce greater light absorption in thin film photovoltaic absorbers than ITO TCEs due to its greater transmission haze.

## 6.2 Impact and Future Works

The research detailed in this thesis work has gained recognition through various scientific forums and has the potential to make a significant impact on future device technologies and functionalities. The following subsections outline the As discussed in Chapter 2, FWNTs were fabricated and spray-coated to form nanotube networks that exhibit among the highest conductivity ( $\sim 2100$  S/cm) for spray-coated CNT films from surfactant-free inks. These films with high electrical performance from scalable and printable fabrication methods have unique applications in lightweight or flexible

electronics where surfactant removal from an electrode is a primary issue, such as flexible batteries, thermal conductors, or circuits. The results demonstrate the impact of nanostructure dispersion forces in an ink solution on the spray-coated film uniformity and consequential conductivity, which will improve future ink-processing parameterization for surfactant-free FWNT inks. The content in Chapter 2 was presented at the Materials Research Society Spring Meeting 2014 as an oral presentation, and was submitted to Nano Research in a manuscript that is currently under revision.

In Chapter 3 we introduced a new carbon nanostructure that was fabricated through an original solution-injected CVD process as described in this thesis work. The reported study of the structure and composition of the B-FWNTs, the impact of the growth parameterization on the subsequent structural properties of the B-FWNTs, and the purification of the growth yield are the first ever for this specific nanostructure fabricated by this growth method. The content of this chapter was presented at the Materials Research Society Fall Meeting 2014 as an oral presentation, in which I was asked to attend a dinner for the invited speakers of the symposium. Although the investigation on the structure, morphology, and purification steps yield compelling results, additional studies are needed to explain the disparity between the conductivity of the undoped FWNT spray-coatings and of these B-FWNTs. Two studies that may illuminate an explanation to the relatively low conductivity of the B-FWNT spray coatings are 1) an investigation into the intrinsic electrical properties of the individual B-FWNTs as compared to the undoped FWNTs, and 2) an attempt to properly optimize the growth parameters to eliminate the disruptive impurities that form during the CVD of the B-FWNTs. The investigation into the electrical properties of the B-FWNTs as compared to

the undoped FWNTs may ascertain the impact of the substitutional boron doping on the band structure of the FWNTs and their intrinsic resistivity. Scanning tunneling microscopy (STM) has been reported to experimentally confirm the band structure of doped nanotubes, which may more conclusively determine whether the mechanism of boron substitution into the graphitic lattice is random or forms  $BC_3$  nanodomains.<sup>[85]</sup> A direct comparison of the electrical resistivity across individual FWNTs and B-FWNTs may be measured by drop-casting a dilute nanotube solution on silicon dioxide ( $SiO_2$ ), applying a patterned electrode on the isolated nanotubes via a shadow mask, and measuring the resistivity across individual nanotubes for set temperatures. These measurements will determine if the doping mechanism successfully quenched the band gap of semiconducting nanotubes and if the conductance across each individual nanotube is improved. Determining the effect of the boron substitution on the band structure and the intrinsic resistivity of the B-FWNTs as compared to the undoped FWNTs will determine if structural or morphological defects limit the spray-coating conductivity, or if the primary limitation draws from the purification of the CVD growth yield. A combination of several CVD fabrication processes with various growth temperatures, boron and carbon sources, and solution/gas flow rates may yield a distribution of impurity phases that may better illuminate the CVD growth kinetics, which is useful for controlling the B-FWNT properties and total contents of the CVD yield. Additional investigations into the secondary phase with combined Raman spectroscopy, TGA, FTIR, and TEM may improve the understanding of how to eliminate the impurities from the growth yield that may disrupt the charge transport in the random network of B-FWNTs.

In Chapter 4 we revealed an inconsistency in the current performance evaluation of TCEs for thin-film solar cells based on a discussion about the impact of transmission haze on light absorption and its dependence on the diameter of Ag NWs that form a random network. The results in this chapter promote a reconsideration of the performance metric for TCEs in thin-film solar cells that highlights the impact of transmission haze, which can alter future designs and research efforts for these devices. The content of this chapter was published in Nano Research, which has currently garnered 12 citations from other publications.<sup>[166]</sup> Based on this work, I was invited to contribute a chapter that reviews current research and technological progress on Ag NW TCEs by the Springer Publishing Company for the “Handbook of Visual Display Technology, 2<sup>nd</sup> edition” expected to be published in 2015.

In Chapter 5 we introduced a new TCE for thin-film solar cells formed from a Ag NW network embedded on transparent paper with high transmission haze. The optoelectronic properties of 91% total transmittance and 13  $\Omega$ /sq is the highest reported performance for solution-based TCEs. In addition to the high total transmittance and low sheet resistance, the Ag NW paper TCE demonstrates high transmission haze that contributes to higher light absorption in thin-film absorber layers than ITO. There is conclusive evidence from the data in this chapter that Ag NW paper TCEs are an optimal replacement for ITO in thin-film photovoltaics based on their superior individual performance and projected enhancement of solar device performance. The contents of this chapter were published in the Journal of Materials Chemistry C, which has garnered 7 citations from other publications.<sup>[167]</sup> In addition, the contents of this chapter were presented at the Materials Research Society Fall Meeting 2013, which was highlighted as

one of the top oral presentations of the day by the MRS Meeting Scene. Although the simulated light absorption promoted by the Ag NW paper TCE is an encouraging indicator for its use in thin-film solar cells, additional work is required to actually integrate this material in thin-film photovoltaic devices. Another important study that may better determine its device functionality is an investigation into the environmental stability of the Ag NW paper TCE under humid or harsh environments.

## Bibliography

- 1) D. Jariwala, V. K. Sangwan, L. J. Lauhon, T. J. Marks, and M. C. Hersam, "Carbon nanomaterials for electronics, optoelectronics, photovoltaics, and sensing.," *Chem. Soc. Rev.*, vol. 42, no. 7, pp. 2824–60, Apr. 2013.
- 2) M. F. L. De Volder, S. H. Tawfick, R. H. Baughman, and a J. Hart, "Carbon nanotubes: present and future commercial applications.," *Science*, vol. 339, no. 6119, pp. 535–9, Feb. 2013.
- 3) D. S. Hecht, L. Hu, and G. Irvin, "Emerging transparent electrodes based on thin films of carbon nanotubes, graphene, and metallic nanostructures.," *Adv. Mater.*, vol. 23, no. 13, pp. 1482–513, Apr. 2011.
- 4) P. Lee, J. Lee, H. Lee, J. Yeo, S. Hong, K. H. Nam, D. Lee, S. S. Lee, and S. H. Ko, "Highly stretchable and highly conductive metal electrode by very long metal nanowire percolation network.," *Adv. Mater.*, vol. 24, no. 25, pp. 3326–32, Jul. 2012.
- 5) F. Xu and Y. Zhu, "Highly conductive and stretchable silver nanowire conductors.," *Adv. Mater.*, vol. 24, no. 37, pp. 5117–22, Sep. 2012.
- 6) M. W. Rowell and M. D. McGehee, "Transparent electrode requirements for thin film solar cell modules," *Energy Environ. Sci.*, vol. 4, no. 1, p. 131, 2011.
- 7) S. Iijima, "Helical Microtubules of Graphitic Carbon" *Nature*, 354, pp. 56-58, 1991.
- 8) L. Hu, D. S. Hecht, and G. Grüner, "Carbon nanotube thin films: fabrication, properties, and applications.," *Chem. Rev.*, vol. 110, no. 10, pp. 5790–844, Oct. 2010.
- 9) S. Y. Kim, J. Hong, R. Kaviani, S. W. Lee, M. N. Hyder, Y. Shao-Horn, and P. T. Hammond, "Rapid fabrication of thick spray-layer-by-layer carbon nanotube electrodes for high power and energy devices," *Energy Environ. Sci.*, vol. 6, no. 3, p. 888, 2013.
- 10) O. Brand, G. Fedder, C. Hierold, J. Korvink, O. Tabata, "Carbon Nanotube Devices: Properties, Modeling, Integration and Applications. Advanced Micro & Nanosystems," vol. 8, Wiley-VCH, 2008.
- 11) Z.W. Pan, S.S. Xie, B.H. Chang, C.Y. Wang, L. Lu, W. Liu, W.Y. Zhou, W.Z. Li, L.X. Qian, "Very long carbon nanotubes," *Nature (London)*, vol. 394 no. 6694, pp. 631–632, 1998.

- 12) Q. Cao and J. a. Rogers, "Ultrathin Films of Single-Walled Carbon Nanotubes for Electronics and Sensors: A Review of Fundamental and Applied Aspects," *Adv. Mater.*, vol. 21, no. 1, pp. 29–53, Jan. 2009.
- 13) S. Reich, C. Thomsen, J. Maultzsch, "Carbon Nanotubes: Basic Properties and Physical Concepts," Wiley-VCH, 2004.
- 14) A. Rubio, "Spectroscopic Properties and STM Images of Carbon Nanotubes," *Appl. Phys. A*, vol. 68, no. 275, 1999.
- 15) C.T. White, T.N. Todorov, T. N., "Carbon nanotubes as long ballistic conductors," *Nature*, vol. 393, no. 240, 1998.
- 16) A. M. Rao, E. Richter, S. Bandow, B. Chase, P. C. Eklund, K. A. Williams, S. Fang, K. R. Subbaswamy, M. Menon, A. Thess, R. E. Smalley, G. Dresselhaus, and M. S. Dresselhaus, "Diameter-Selective Raman Scattering from Vibrational Modes in Carbon Nanotubes," *Science*, vol. 275, pp. 187–191, 1997.
- 17) M. S. Dresselhaus, G. Dresselhaus, R. Saito, and a. Jorio, "Raman spectroscopy of carbon nanotubes," *Phys. Rep.*, vol. 409, no. 2, pp. 47–99, Mar. 2005.
- 18) M. S. Dresselhaus, G. Dresselhaus, A. Jorio, A. G. S. Filho, and R. Saito, "Raman spectroscopy on isolated single wall carbon nanotubes q," vol. 40, pp. 2043–2061, 2002.
- 19) M. Kumar and Y. Ando, "Chemical Vapor Deposition of Carbon Nanotubes: A Review on Growth Mechanism and Mass Production," *J. Nanosci. Nanotechnol.*, vol. 10, no. 6, pp. 3739–3758, Jun. 2010.
- 20) M. Pérez-Mendoza, C. Vallés, W. K. Maser, M. T. Martínez, and a M. Benito, "Influence of molybdenum on the chemical vapour deposition production of carbon nanotubes," *Nanotechnology*, vol. 16, no. 5, pp. S224–S229, May 2005.
- 21) G. Y. Xiong, Y. Suda, D. Z. Wang, J. Y. Huang, and Z. F. Ren, "Effect of temperature, pressure, and gas ratio of methane to hydrogen on the synthesis of double-walled carbon nanotubes by chemical vapour deposition," *Nanotechnology*, vol. 16, no. 4, pp. 532–535, Apr. 2005.
- 22) L. Hu, D.S. Hecht, G. Gruner, "Percolation in Transparent and Conducting Carbon Nanotube Networks, *Nano Letters*," vol. 4, no. 12, pp. 2513-2517, 2004.
- 23) S. M. Bergin, Y.-H. Chen, A. R. Rathmell, P. Charbonneau, Z.-Y. Li, and B. J. Wiley, "The effect of nanowire length and diameter on the properties of transparent, conducting nanowire films.," *Nanoscale*, vol. 4, no. 6, pp. 1996–2004, Mar. 2012.

- 24) J. Li and S.-L. Zhang, "Conductivity exponents in stick percolation," *Phys. Rev. E*, vol. 81, no. 2, p. 021120, Feb. 2010.
- 25) P. Keblinski and F. Cleri, "Contact resistance in percolating networks," *Phys. Rev. B*, vol. 69, no. 18, p. 184201, May 2004.
- 26) M. Žeželj and I. Stanković, "From percolating to dense random stick networks: Conductivity model investigation," *Phys. Rev. B*, vol. 86, no. 13, p. 134202, Oct. 2012.
- 27) R. M. Mutiso, M. C. Sherrott, A. R. Rathmell, B. J. Wiley, and K. I. Winey, "Integrating simulations and experiments to predict sheet resistance and optical transmittance in nanowire films for transparent conductors.," *ACS Nano*, vol. 7, no. 9, pp. 7654–63, Sep. 2013.
- 28) D. Hecht, L. Hu, and G. Grüner, "Conductivity scaling with bundle length and diameter in single walled carbon nanotube networks," *Appl. Phys. Lett.*, vol. 89, no. 13, p. 133112, 2006.
- 29) P. E. Lyons, S. De, F. Blighe, V. Nicolosi, L. F. C. Pereira, M. S. Ferreira, and J. N. Coleman, "The relationship between network morphology and conductivity in nanotube films," *J. Appl. Phys.*, vol. 104, no. 4, p. 044302, 2008.
- 30) L. Dumée, K. Sears, J. Schütz, N. Finn, M. Duke, and S. Gray, "Influence of the Sonication Temperature on the Debundling Kinetics of Carbon Nanotubes in Propan-2-ol," *Nanomaterials*, vol. 3, no. 1, pp. 70–85, Jan. 2013.
- 31) Q. Cheng, E. Gregan, and H. Byrne, "Ultrasound-Assisted SWNTs Dispersion: Effects of Sonication Parameters and Solvent Properties Ultrasound-assisted SWNTs dispersion : effects of sonication parameters and solvent properties," vol. 114, no. 19, pp. 8821–8827, 2010.
- 32) Y. Y. Huang and E. M. Terentjev, "Dispersion of Carbon Nanotubes: Mixing, Sonication, Stabilization, and Composite Properties," *Polymers (Basel)*, vol. 4, no. 4, pp. 275–295, Jan. 2012.
- 33) J. Hilding, E. a. Grulke, Z. George Zhang, and F. Lockwood, "Dispersion of Carbon Nanotubes in Liquids," *J. Dispers. Sci. Technol.*, vol. 24, no. 1, pp. 1–41, Jan. 2003.
- 34) V. Moore, M. Strano, E. Haroz, R. Hauge, R. Smalley, "Individually Suspended Single-Walled Carbon Nanotubes in Various Surfactants," *Nano Letters*, vol. 3 no. 10, pp. 1379-1382, 2003.
- 35) S. Banerjee, T. Hemraj-Benny, S. Wong, "Covalent Surface Chemistry of Single-Walled Carbon Nanotubes," *Advanced Materials*, 17 (1), 17-29, 2005.



- 36) J. L. Bahr and J. M. Tour, "Covalent chemistry of single-wall carbon nanotubes," *J. Mater. Chem.*, vol. 12, no. 7, pp. 1952–1958, Jun. 2002.
- 37) M. Martinez, M. Callejas, A. Benito, M. Cochet, T. Seeger, A. Anson, J. Schreiber, C. Gordon, C. Marhic, O. Chauvet, J. Fierro, W. Maser, "Sensitivity of single wall carbon nanotubes to oxidative processing: structural modification, intercalation, and functionalization," *Carbon*, vol. 4, pp. 2247-2256, 2003.
- 38) R. Yudianti, H. Onggo, Y. Saito, T. Iwata, and J. Azuma, "Analysis of Functional Group Sited on Multi-Wall Carbon Nanotube Surface," *The Open Materials Science Journal*, vol. 5, pp. 242–247, 2011.
- 39) N. Kumar, I. Jeon, G. Sohn, R. Jai, S. Kumar, J. Baek, "Highly Conducting and Flexible Few-Walled Carbon Nanotube Thin Film," *ACS Nano*, vol. 5, no. 3, pp. 2324-2331, 2011.
- 40) L. Q. Hoa, M. C. Vestergaard, H. Yoshikawa, M. Saito, and E. Tamiya, "Enhancing catalytic performance of Pt-based electrodes with a noncovalent interaction-induced functionalized carbon nanotube-grafted matrix," *J. Mater. Chem.*, vol. 22, no. 29, p. 14705, 2012.
- 41) R. Tenent, T. Barnes, J. Bergson, A. Ferguson, B. To, L. Gedvilas, M. Heben, J. Blackburn, "Ultrasoft, Large-Area, High-Uniformity, Conductive Transparent Single-Walled-Carbon-Nanotube Films for Photovoltaics Produced by Ultrasonic Spraying," *Advanced Materials*, vol. 21, pp. 3210-3216, 2009.
- 42) M. Majumder, C. Rendall, M. Li, N. Behabtu, J. Eukel, R. Hauge, H. Schmidt, M. Pasquali, "Insights into the physics of spray coating of SWNT films," *Chemical Engineering Science*, vol. 65, pp. 2000-2008, 2010.
- 43) R. Deegan, O. Bakajin, T. Dupont, G. Huber, S. Nagel, T. Witten, "Capillary flow as the cause of rings stains from dried liquid drops," *Nature*, vol. 389, pp. 827-829, 1997.
- 44) C. Su, A. Lu, Y. Chen, C. Wei, C. Weng, P. Wang, F. Chen, K. Leou, C. Tsai, "Scalable and Surfactant-Free Process for Single-Walled Carbon Nanotube Based Transparent Conductive Thin Films via Layer-by-Layer Assembly," *Journal of Physical Chemistry*, vol. 114, pp. 11588-11594, 2010.
- 45) G. Sassine, F. Martinez, M. El Khoury, F. Pascal, A. Hoffmann, "Measurements and Simulations of Surfactant's Impact on the Conductivity and the 1/f Noise in Percolation Carbon Nanotube Networks," *IEEE Transactions on Electron Devices*, vol. 59, no. 10, pp. 2803-2808, 2012.

- 46) J. Wang, J. Sun, L. Gao, Y. Wang, J. Zhang, H. Kajiura, Y. Li, K. Noda, "Removal of the Residual Surfactants in Transparent and Conductive Single-Walled Carbon Nanotube Films," *Journal of Physical Chemistry C*, vol 113, pp. 17685-17690, 2009.
- 47) S. Giordani, S. Bergin, V. Nicolosi, S. Lebedkin, M. Kappes, W. Blau, J. Coleman, "Debundling of Single-Walled Nanotubes by Dilution: Observation of Large Populations of Individual Nanotubes in Amide Solvent Dispersions," *Journal of Physical Chemistry B*, vol. 110, pp. 15708-15718, 2006.
- 48) C. Bower, a. Kleinhammes, Y. Wu, and O. Zhou, "Intercalation and partial exfoliation of single-walled carbon nanotubes by nitric acid," *Chem. Phys. Lett.*, vol. 288, no. 2-4, pp. 481-486, May 1998.
- 49) V. Datsyuk, M. Kalyva, K. Papagelis, J. Parthenios, D. Tasis, A. Siokou, I. Kallitsis, C. Galiotis, "Chemical oxidation of multiwalled carbon nanotubes. Carbon," *Carbon*, vol. 46, pp. 833-840, 2008
- 50) H. Geng, K. Kim, K. So, Y. Lee, Y. Chang, Y. Lee, "Effect of Acid Treatment on Carbon Nanotube-Based Flexible Transparent Conducting Films," *J. Am. Chem. Soc.*, vol. 129, pp. 7758-7759, 2007.
- 51) M. C. Hersam, "Progress towards monodisperse single-walled carbon nanotubes.," *Nat. Nanotechnol.*, vol. 3, no. 7, pp. 387-94, Jul. 2008.
- 52) A. Yu, C.-C. L. Su, I. Roes, B. Fan, and R. C. Haddon, "Gram-scale preparation of surfactant-free, carboxylic acid groups functionalized, individual single-walled carbon nanotubes in aqueous solution.," *Langmuir*, vol. 26, no. 2, pp. 1221-5, Jan. 2010.
- 53) S. W. Lee, B. M. Gallant, Y. Lee, N. Yoshida, D. Y. Kim, Y. Yamada, S. Noda, A. Yamada, and Y. Shao-Horn, "Self-standing positive electrodes of oxidized few-walled carbon nanotubes for light-weight and high-power lithium batteries," *Energy Environ. Sci.*, vol. 5, no. 1, p. 5437, 2012.
- 54) Y. Feng, X. Ju, W. Feng, H. Zhang, Y. Cheng, J. Liu, A. Fujii, M. Ozaki, and K. Yoshino, "Organic solar cells using few-walled carbon nanotubes electrode controlled by the balance between sheet resistance and the transparency," *Appl. Phys. Lett.*, vol. 94, no. 12, p. 123302, 2009.
- 55) B. Zhao, L. Zhang, Y. Liang, H. Qiu, J. Yang, "Efficient growth of millimeter-long few-walled carbon nanotube forests and their oil sorption," *Applied Physics A*, **2012**, vol. 108, pp. 351-355, 2012.

- 56) C. Qian, H. Qi, B. Gao, Y. Cheng, Q. Qiu, L.-C. Qin, O. Zhou, and J. Liu, "Fabrication of Small Diameter Few-Walled Carbon Nanotubes with Enhanced Field Emission Property," *J. Nanosci. Nanotechnol.*, vol. 6, no. 5, pp. 1346–1349, May 2006.
- 57) J. Di, D. Hu, H. Chen, Z. Yong, M. Chen, Z. Feng, Y. Zhu, and Q. Li, "Ultrastrong, foldable, and highly conductive carbon nanotube film.," *ACS Nano*, vol. 6, no. 6, pp. 5457–64, Jun. 2012.
- 58) H. Qi, C. Qian, and J. Liu, "Synthesis of High-Purity Few-Walled Carbon Nanotubes from Ethanol/Methanol Mixture," *Chem. Mater.*, vol. 18, no. 24, pp. 5691–5695, Nov. 2006.
- 59) Y. Hou, J. Tang, H. Zhang, C. Qian, Y. Feng, and J. Liu, "Functionalized Few-Walled Carbon Nanotubes for Mechanical," vol. 3, no. 5, pp. 1057–1062, 2009.
- 60) H. Numata, K. Ihara, T. Saito, H. Endoh, and F. Nihey, "Electrical property of printed transistors fabricated with various types of carbon nanotube ink," 2012 12th IEEE Int. Conf. Nanotechnol., pp. 1–4, Aug. 2012.
- 61) Y. Feng, H. Zhang, Y. Hou, T. P. McNicholas, D. Yuan, S. Yang, L. Ding, W. Feng, and J. Liu, "Room temperature purification of few-walled carbon nanotubes with high yield.," *ACS Nano*, vol. 2, no. 8, pp. 1634–8, Aug. 2008.
- 62) B. White, S. Banerjee, S. O'Brien, N. J. Turro, and I. P. Herman, "Zeta-Potential Measurements of Surfactant-Wrapped Individual Single-Walled Carbon Nanotubes," *J. Phys. Chem. C*, vol. 111, no. 37, pp. 13684–13690, Sep. 2007.
- 63) S. B. Chen and D. L. Koch, "Electrophoresis and Sedimentation of Charged Fibers," *J. Colloid Interface Sci.*, vol. 180, no. 2, pp. 466–477, Jun. 1996.
- 64) E. Yariv and O. Schnitzer, "The electrophoretic mobility of rod-like particles," *J. Fluid Mech.*, vol. 719, no. November 2012, p. R3, Feb. 2013.
- 65) P. A. Kralchevsky, K. D. Danov, and N. D. Denkov, "Handbook of Surface and Colloid Chemistry," ch.7, Taylor & Francis Group, 2009.
- 66) D. C. Henry, "The Cataphoresis of Suspended Particles. Part I. The Equation of Cataphoresis," *Proc. R. Soc. A Math. Phys. Eng. Sci.*, vol. 133, no. 821, pp. 106–129, Sep. 1931.
- 67) J. D. Sherwood, "Electrophoresis of rods," *J. Chem. Soc. Faraday Trans. 2*, vol. 78, no. 7, p. 1091, 1982.
- 68) R. Wagner, W. Ellis, "Vapor-liquid-solid mechanism of single crystal growth," *Applied Physics Letters*, vol. 4, no. 89, 1964.

- 69) Y. Wu and P. Yang, "Direct Observation of Vapor - Liquid - Solid Nanowire Growth," no. 22, pp. 3165–3166, 2001.
- 70) J. Hu, T. W. Odom, and C. M. Lieber, "Chemistry and Physics in One Dimension: Synthesis and Properties of Nanowires and Nanotubes," *Acc. Chem. Res.*, vol. 32, no. 5, pp. 435–445, May 1999.
- 71) A.M. Morales and C. M. Lieber, "A Laser Ablation Method for the Synthesis of Crystalline Semiconductor Nanowires," vol. 279, no. January, pp. 7–10, 1998.
- 72) Yang Xu, Zhongrui Li, Enkeleda Dervishi, Viney Saini, Jingbiao Cui, Alexandru R. Biris, Dan Lupuc, Alexandru S. Biris "Surface area and thermal stability effect of the MgO supported catalysts for the synthesis of carbon nanotubes," *J. Mater. Chem.*, vol. 18, 5738-5745, 2008.
- 73) A.Hirsch, "Functionalization of Single-walled Carbon Nanotubes" *Chem. Int. Ed.* vol. 41, pp. 1853-1859, 2002.
- 74) H. Gao, R. Izquierdo, and V.-V. Truong, "Chemical vapor doping of transparent and conductive films of carbon nanotubes," *Chem. Phys. Lett.*, vol. 546, pp. 109–114, Sep. 2012.
- 75) U. N. Maiti, W. J. Lee, J. M. Lee, Y. Oh, J. Y. Kim, J. E. Kim, J. Shim, T. H. Han, and S. O. Kim, "25th anniversary article: Chemically modified/doped carbon nanotubes & graphene for optimized nanostructures & nanodevices.," *Adv. Mater.*, vol. 26, no. 1, pp. 40–66, Jan. 2014.
- 76) X. M. Liu, H. R. Gutiérrez, and P. C. Eklund, "Electrical properties and far infrared optical conductivity of boron-doped single-walled carbon nanotube films.," *J. Phys. Condens. Matter*, vol. 22, no. 33, p. 334213, Aug. 2010.
- 77) L. Wirtz, "Band structure of boron doped carbon nanotubes," *AIP Conf. Proc.*, vol. 685, pp. 402–405, 2003.
- 78) J.-Y. Yi and J. Bernholc, "Atomic structure and doping of microtubules," *Phys. Rev. B.*, vol. 47, p. 1708, 1993.
- 79) Y. Tang, L. Yin, Y. Yang, X. Bo, Y. Cao, H. Wang, and W. Zhang, "Tunable Band Gaps and p-Type Transport Properties of Boron-Doped Graphenes by Controllable Ion Doping," no. 3, pp. 1970–1978, 2012.
- 80) T. Koretsune and S. Saito, "Electronic structure of boron-doped carbon nanotubes," *Phys. Rev. B*, vol. 77, no. 16, p. 165417, Apr. 2008.

- 81) G. Fuentes, E. Borowiak-Palen, M. Knupfer, T. Pichler, J. Fink, L. Wirtz, and a. Rubio, "Formation and electronic properties of BC<sub>3</sub> single-wall nanotubes upon boron substitution of carbon nanotubes," *Phys. Rev. B*, vol. 69, no. 24, p. 245403, Jun. 2004.
- 82) P. L. Gai, O. Stephan, K. McGuire, A. M. Rao, M. S. Dresselhaus, G. Dresselhaus, and C. Colliex, "Structural systematics in boron-doped single wall carbon nanotubes," *J. Mater. Chem.*, vol. 14, no. 4, p. 669, 2004.
- 83) K. McGuire, N. Gothard, P. L. Gai, M. S. Dresselhaus, G. Sumanasekera, and a. M. Rao, "Synthesis and Raman characterization of boron-doped single-walled carbon nanotubes," *Carbon N. Y.*, vol. 43, no. 2, pp. 219–227, Jan. 2005.
- 84) R. Czerw, P.-W. Chiu, Y.-M. Choi, D.-S. Lee, D. . Carroll, S. Roth, and Y.-W. Park, "Substitutional boron-doping of carbon nanotubes," *Curr. Appl. Phys.*, vol. 2, no. 6, pp. 473–477, Dec. 2002.
- 85) D. Carroll, P. Redlich, X. Blase, J.-C. Charlier, S. Curran, P. Ajayan, S. Roth, and M. Rühle, "Effects of Nanodomain Formation on the Electronic Structure of Doped Carbon Nanotubes," *Phys. Rev. Lett.*, vol. 81, no. 11, pp. 2332–2335, Sep. 1998.
- 86) B. Wei, R. Spolenak, P. Kohler-Redlich, M. Rühle, and E. Arzt, "Electrical transport in pure and boron-doped carbon nanotubes," *Appl. Phys. Lett.*, vol. 74, no. 21, p. 3149, 1999.
- 87) S. Ishii, M. Nagao, T. Watanabe, S. Tsuda, T. Yamaguchi, and Y. Takano, "Electrical properties of boron-doped MWNTs synthesized by hot-filament chemical vapor deposition," *Phys. C Supercond.*, vol. 469, no. 15–20, pp. 1002–1004, Oct. 2009.
- 88) Y. Zhang, J. M. Gregoire, R. B. van Dover, and a. J. Hart, "Ethanol-Promoted High-Yield Growth of Few-Walled Carbon Nanotubes," *J. Phys. Chem. C*, vol. 114, no. 14, pp. 6389–6395, Apr. 2010.
- 89) S. V. Deshpande, E. Gulari, S. J. Harris, and A. M. Weiner, "Filament activated chemical vapor deposition of boron carbide coatings," *Appl. Phys. Lett.*, vol. 65, no. 14, p. 1757, 1994.
- 90) V. Domnich, S. Reynaud, R. a. Haber, and M. Chhowalla, "Boron Carbide: Structure, Properties, and Stability under Stress," *J. Am. Ceram. Soc.*, vol. 94, no. 11, pp. 3605–3628, Nov. 2011.
- 91) D. Ghosh, G. Subhash, C. H. Lee, and Y. K. Yap, "Strain-induced formation of carbon and boron clusters in boron carbide during dynamic indentation," *Appl. Phys. Lett.*, vol. 91, no. 6, p. 061910, 2007.

- 92) F. H. Monteiro, D. G. Larrude, M. E. H. Maia da Costa, L. a. Terrazos, R. B. Capaz, and F. L. Freire, "Production and Characterization of Boron-Doped Single Wall Carbon Nanotubes," *J. Phys. Chem. C*, vol. 116, no. 5, pp. 3281–3285, Feb. 2012.
- 93) O. M. Moon, B.-C. Kang, S.-B. Lee, and J.-H. Boo, "Temperature effect on structural properties of boron oxide thin films deposited by MOCVD method," *Thin Solid Films*, vol. 464–465, pp. 164–169, Oct. 2004.
- 94) D. Peak, G. W. Luther, and D. L. Sparks, "ATR-FTIR spectroscopic studies of boric acid adsorption on hydrous ferric oxide," *Geochim. Cosmochim. Acta*, vol. 67, no. 14, pp. 2551–2560, Jul. 2003.
- 95) S. Dike, F. Mindivan, and H. Mindivan, "Effect of B 4 C Content on the Mechanical and Tribological Performances of Polypropylene," *Acta Phys. Pol. A*, vol. 125, no. 2, pp. 396–398, Jan. 2014.
- 96) I. Uslu, H. Da, A. Alta, A. Yayli, O. Atakol, and M. L. Aksu, "Preparation and Characterization of PVA / Boron Polymer Produced by an Electrospinning Technique .," no. 133, pp. 1–6, 2007.
- 97) M. A. Callejas, A. M. Benito, M. Cochet, T. Seeger, A. Anson, and W. K. Maser, "S ensitivity of single wall carbon nanotubes to oxidative processing : structural modification , intercalation and functionalisation," vol. 41, pp. 2247–2256, 2003.
- 98) E. Borowiak-Palen, T. Pichler, G. G. Fuentes, a. Graff, R. J. Kalenczuk, M. Knapfer, and J. Fink, "Efficient production of B-substituted single-wall carbon nanotubes," *Chem. Phys. Lett.*, vol. 378, no. 5–6, pp. 516–520, Sep. 2003.
- 99) D.C. Reigada, F.I. Freire Jr., "Nitrogen incorporation into boron carbide films deposited by dc-magnetron sputtering: film microstructure and tribological properties," *Surf. Coating Technol.*, vol. 889, p. 142, 2001.
- 100) S. Lee, J. Mazurowski, G. Ramseyer, and P. a. Dowben, "Characterization of boron carbide thin films fabricated by plasma enhanced chemical vapor deposition from boranes," *J. Appl. Phys.*, vol. 72, no. 10, p. 4925, 1992.
- 101) W. Han, Y. Bando, K. Kurashima, and T. Sato, "Boron-doped carbon nanotubes prepared through a substitution reaction," no. 299, pp. 368–373, 1999.
- 102) P. Redlich, J. Loeffler, P. M. Ajayan, J. Bill, F. Aldinger, and M. Riihle, " B - C - N nanotubes and boron doping of carbon nanotubes," *Chemical Physica Letters*, vol. 260, pp. 465-470, 1996.

- 103) W. K. Hsu, S. Firth, P. Redlich, M. Terrones, H. Terrones, Y. Q. Zhu, N. Grobert, A. Schilder, R. J. H. Clark, H. W. Kroto, and D. R. M. Walton, "Boron-doping effects in carbon nanotubes," *J. Mater. Chem.*, vol. 10, no. 6, pp. 1425–1429, 2000.
- 104) P. Fischer, "Exploring nanoscale magnetism in advanced materials with polarized X-rays," *Mater. Sci. Eng. R Reports*, vol. 72, no. 5, pp. 81–95, Jun. 2011.
- 105) M. Lazzeri and F. Mauri, "Non-adiabatic Kohn-anomaly in a doped graphene monolayer," Nov. 2006.
- 106) S. Piscanec, M. Lazzeri, J. Robertson, A. C. Ferrari, and F. Mauri, "Optical Phonons in Carbon Nanotubes: Kohn Anomalies, Peierls Distortions and Dynamic Effects," pp. 1–24, Nov. 2006.
- 107) S. Pisana, M. Lazzeri, C. Casiraghi, K. S. Novoselov, a K. Geim, A. C. Ferrari, and F. Mauri, "Breakdown of the adiabatic Born-Oppenheimer approximation in graphene.," *Nat. Mater.*, vol. 6, no. 3, pp. 198–201, Mar. 2007.
- 108) A. C. Ferrari, "Raman spectroscopy of graphene and graphite: Disorder, electron–phonon coupling, doping and nonadiabatic effects," *Solid State Commun.*, vol. 143, no. 1–2, pp. 47–57, Jul. 2007.
- 109) J. Yan, Y. Zhang, P. Kim, and A. Pinczuk, "Electric Field Effect Tuning of Electron-Phonon Coupling in Graphene," vol. 1, no. d, pp. 1–4, Dec. 2006.
- 110) J. Maultzsch, S. Reich, C. Thomsen, S. Webster, R. Czerw, D. L. Carroll, S. M. C. Vieira, P. R. Birkett, and C. a. Rego, "Raman characterization of boron-doped multiwalled carbon nanotubes," *Appl. Phys. Lett.*, vol. 81, no. 14, p. 2647, 2002.
- 111) A. Kumar and C. Zhou, "The race to replace tin-doped indium oxide: which material will win?" *ACS Nano*, vol. 4, no. 1, pp. 11–4, Jan. 2010.
- 112) Z. Chen, B. Cotterell, W. Wang, E. Guenther, and S. Chua, "A mechanical assessment of flexible optoelectronic devices," pp. 202–206, 2001.
- 113) X. Li, Y. Zhu, W. Cai, M. Borysiak, B. Han, D. Chen, R. D. Piner, L. Colombo, and R. S. Ruoff, "Transfer of large-area graphene films for high-performance transparent conductive electrodes.," *Nano Lett.*, vol. 9, no. 12, pp. 4359–63, Dec. 2009.
- 114) S. Bae, H. Kim, Y. Lee, X. Xu, J.-S. Park, Y. Zheng, J. Balakrishnan, T. Lei, H. R. Kim, Y. Il Song, Y.-J. Kim, K. S. Kim, B. Ozyilmaz, J.-H. Ahn, B. H. Hong, and S. Iijima, "Roll-to-roll production of 30-inch graphene films for transparent electrodes.," *Nat. Nanotechnol.*, vol. 5, no. 8, pp. 574–8, Aug. 2010.

- 115) Z. Wu, Z. Chen, X. Du, J. M. Logan, J. Sippel, M. Nikolou, K. Kamaras, J. R. Reynolds, D. B. Tanner, A. F. Hebard, and A. G. Rinzler, "Transparent, conductive carbon nanotube films.," *Science*, vol. 305, no. 5688, pp. 1273–6, Aug. 2004.
- 116) G. Gruner, "Carbon nanotube films for transparent and plastic electronics," *J. Mater. Chem.*, vol. 16, no. 35, p. 3533, 2006.
- 117) H. Wu, L. Hu, M. W. Rowell, D. Kong, J. J. Cha, J. R. McDonough, J. Zhu, Y. Yang, M. D. McGehee, and Y. Cui, "Electrospun metal nanofiber webs as high-performance transparent electrode.," *Nano Lett.*, vol. 10, no. 10, pp. 4242–8, Oct. 2010.
- 118) A. R. Rathmell and B. J. Wiley, "The synthesis and coating of long, thin copper nanowires to make flexible, transparent conducting films on plastic substrates.," *Adv. Mater.*, vol. 23, no. 41, pp. 4798–803, Nov. 2011.
- 119) L. Hu, H. Wu, and Y. Cui, "Metal nanogrids, nanowires, and nanofibers for transparent electrodes," *MRS Bull.*, vol. 36, no. 10, pp. 760–765, Oct. 2011.
- 120) K. Ellmer, "Past achievements and future challenges in the development of optically transparent electrodes," *Nature Photonics*, vol. 6, pp. 809-817, 2012
- 121) S. B. Sepulveda-Mora and S. G. Cloutier, "Figures of Merit for High-Performance Transparent Electrodes Using Dip-Coated Silver Nanowire Networks," *J. Nanomater.*, vol. 2012, pp. 1–7, 2012.
- 122) S. De, P. J. King, P. E. Lyons, U. Khan, and J. N. Coleman, "Size effects and the problem with percolation in nanostructured transparent conductors.," *ACS Nano*, vol. 4, no. 12, pp. 7064–72, Dec. 2010.
- 123) J. van de Groep, P. Spinelli, and A. Polman, "Transparent conducting silver nanowire networks.," *Nano Lett.*, vol. 12, no. 6, pp. 3138–44, Jun. 2012.
- 124) L. Hu, H. S. Kim, J. Lee, P. Peumans, and Y. Cui, "Scalable Coating and Properties of Transparent, Flexible, Silver Nanowire Electrodes," *ACS Nano*, vol. 4, no. 5, pp. 2955–2963, 2010.
- 125) Y. Sun, "Silver nanowires--unique templates for functional nanostructures.," *Nanoscale*, vol. 2, no. 9, pp. 1626–42, Sep. 2010.
- 126) J. Lee, P. Lee, H. Lee, D. Lee, S. S. Lee, and S. H. Ko, "Very long Ag nanowire synthesis and its application in a highly transparent, conductive and flexible metal electrode touch panel.," *Nanoscale*, vol. 4, no. 20, pp. 6408–14, Oct. 2012.
- 127) C. J. Murphy and N. R. Jana, "Controlling the Aspect Ratio of Inorganic Nanorods and Nanowires," *Adv. Mater.*, vol. 14, no. 1, pp. 80–82, Jan. 2002.



- 128) D. Azulai, E. Cohen, and G. Markovich, "Seed concentration control of metal nanowire diameter.," *Nano Lett.*, vol. 12, no. 11, pp. 5552–8, Nov. 2012.
- 129) K.E. Korte, S.E. Skrabalak, Y. Xia, "Rapid synthesis of silver nanowires through a CuCl- of CuCl<sub>2</sub>- mediated polyol process," *Journal of Materials Chemistry*, vol. 18, pp. 437-41, 2008.
- 130) J.-Y. Lee, S. T. Connor, Y. Cui, and P. Peumans, "Solution-processed metal nanowire mesh transparent electrodes.," *Nano Lett.*, vol. 8, no. 2, pp. 689–92, Feb. 2008.
- 131) T. C. Hauger, S. M. I. Al-Rafia, and J. M. Buriak, "Rolling silver nanowire electrodes: simultaneously addressing adhesion, roughness, and conductivity.," *ACS Appl. Mater. Interfaces*, vol. 5, no. 23, pp. 12663–71, Dec. 2013.
- 132) T. Kim, A. Canlier, G. H. Kim, J. Choi, M. Park, and S. M. Han, "Electrostatic spray deposition of highly transparent silver nanowire electrode on flexible substrate.," *ACS Appl. Mater. Interfaces*, vol. 5, no. 3, pp. 788–94, Feb. 2013.
- 133) A. R. Madaria, A. Kumar, F. N. Ishikawa, and C. Zhou, "Uniform, highly conductive, and patterned transparent films of a percolating silver nanowire network on rigid and flexible substrates using a dry transfer technique," *Nano Res.*, vol. 3, no. 8, pp. 564–573, Jul. 2010.
- 134) S. Zhu, Y. Gao, B. Hu, J. Li, J. Su, Z. Fan, and J. Zhou, "Transferable self-welding silver nanowire network as high performance transparent flexible electrode.," *Nanotechnology*, vol. 24, no. 33, p. 335202, Aug. 2013.
- 135) H. a Atwater and A. Polman, "Plasmonics for improved photovoltaic devices.," *Nat. Mater.*, vol. 9, no. 3, pp. 205–13, Mar. 2010.
- 136) K. R. Catchpole and a. Polman, "Design principles for particle plasmon enhanced solar cells," *Appl. Phys. Lett.*, vol. 93, no. 19, p. 191113, 2008.
- 137) C. Battaglia, C.-M. Hsu, K. Söderström, J. Escarré, F.-J. Haug, M. Charrière, M. Boccard, M. Despeisse, D. T. L. Alexander, M. Cantoni, Y. Cui, and C. Ballif, "Light trapping in solar cells: can periodic beat random?" *ACS Nano*, vol. 6, no. 3, pp. 2790–7, Mar. 2012.
- 138) Y. Chiba, A. Islam, Y. Watanabe, R. Komiya, N. Koide, and L. Han, "Dye-Sensitized Solar Cells with Conversion Efficiency of 11.1%," *Jpn. J. Appl. Phys.*, vol. 45, no. No. 25, pp. L638–L640, Jun. 2006.

- 139) N. Koide, A. Islam, Y. Chiba, and L. Han, "Improvement of efficiency of dye-sensitized solar cells based on analysis of equivalent circuit," *J. Photochem. Photobiol. A Chem.*, vol. 182, no. 3, pp. 296–305, Sep. 2006.
- 140) M-G. Kang, T. Xu, H.J. Park, H. X. Luo, L.J. Guo, "Efficiency enhancement of organic solar cells using transparent plasmonic Ag nanowire electrodes," *Adv. Mater.*, vol. 22, pp. 4378–4383, 2010.
- 141) C. Bohren, D. Huffman, "Absorption and Scattering of Light by Small Particles," Wiley-Int. Pub., 1983.
- 142) Khanarian, G., Joo, J., Liu, X.Q., Eastman, P., Werner, D., "The optical and electrical properties of silver nanowire mesh films," *Journal of Applied Physics*, 2013, 114, 024302.
- 143) J. M. Oliva and S. K. Gray, "A computational study of the interaction of light with silver nanowires of different eccentricity," *Chem. Phys. Lett.*, vol. 427, no. 4–6, pp. 383–389, Aug. 2006.
- 144) V. Giannini and J. A. Sánchez-gil, "Calculations of light scattering from isolated and interacting metallic nanowires of arbitrary cross section by means of Green's theorem surface integral equations in parametric form," *America (NY)*, vol. 24, no. 9, pp. 2822–2830, 2007.
- 145) P. B. Catrysse and S. Fan, "Nanopatterned metallic films for use as transparent conductive electrodes in optoelectronic devices," *Nano Lett.*, vol. 10, no. 8, pp. 2944–9, Aug. 2010.
- 146) Y. Xia, P. Yang, Y. Sun, Y. Wu, B. Mayers, B. Gates, Y. Yin, F. Kim, H. Yan, H., "One-Dimensional Nanostructures: Synthesis, Characterization, and Applications," *Adv. Mater.*, vol. 15, p. 3, 2003.
- 147) K. Critchley, B. Khanal, M. Górzny, L. Vigderman, S. Evans, E. Zubarev, N. Kotov, "Near-Bulk Conductivity of Gold Nanowires as Nanoscale Interconnects and the Role of Atomically Smooth Interface," *Adv. Mater.*, vol. 22, p. 2338, 2010.
- 148) Y. Jin, D. Deng, Y. Cheng, L. Kong, and F. Xiao, "Annealing-free and strongly adhesive silver nanowire networks with long-term reliability by introduction of a nonconductive and biocompatible polymer binder," *Nanoscale*, vol. 6, no. 9, pp. 4812–8, May 2014.
- 149) L. Li, Z. Yu, W. Hu, C. Chang, Q. Chen, and Q. Pei, "Efficient flexible phosphorescent polymer light-emitting diodes based on silver nanowire-polymer composite electrode," *Adv. Mater.*, vol. 23, no. 46, pp. 5563–7, Dec. 2011.

- 150) W. Hu, X. Niu, L. Li, S. Yun, Z. Yu, and Q. Pei, "Intrinsically stretchable transparent electrodes based on silver-nanowire-crosslinked-polyacrylate composites," *Nanotechnology*, vol. 23, no. 34, p. 344002, Aug. 2012.
- 151) H. Zhu, Z. Fang, C. Preston, Y. Li, and L. Hu, "Transparent paper: fabrications, properties, and device applications," *Energy Environ. Sci.*, vol. 7, no. 1, p. 269, 2014.
- 152) Z. Fang, H. Zhu, Y. Yuan, D. Ha, S. Zhu, C. Preston, Q. Chen, Y. Li, X. Han, S. Lee, G. Chen, T. Li, J. Munday, J. Huang, L. Hu, "Novel Nanostructured Paper with Ultrahigh Transparency and Ultrahigh Haze for Solar Cells," *Nano Letters*, vol. 14, pp. 765-773 2014.
- 153) H. Zhu, S. Parvinian, C. Preston, O. Vaaland, Z. Ruan, L. Hu, "Transparent nanopaper with tailored optical properties," *Nanoscale*, vol. 5, p. 3787, 2013.
- 154) Z. Fang, H. Zhu, C. Preston, X. Han, Y. Li, S. Lee, X. Chai, G. Chen, L. Hu, "Highly transparent and writable wood all-cellulose hybrid nanostructured paper," *J. Mater. Chem. C*, vol. 1, p. 6191, 2013.
- 155) S. De, T. M. Higgins, P. E. Lyons, E. M. Doherty, P. N. Nirmalraj, W. J. Blau, J. J. Boland, and J. N. Coleman, "Silver Nanowire Networks as Flexible Transparent, Conducting Films: Extremely High DC to Optical Conductivity Ratios," vol. 3, no. 7, pp. 1767–1774, 2009.
- 156) M.-G. Kang, M.-S. Kim, J. Kim, and L. J. Guo, "Organic Solar Cells Using Nanoimprinted Transparent Metal Electrodes," *Adv. Mater.*, vol. 20, no. 23, pp. 4408–4413, Dec. 2008.
- 157) Y. Galagan, J.-E. J.M. Rubingh, R. Andriessen, C.-C. Fan, P. W.M. Blom, S. C. Veenstra, and J. M. Kroon, "ITO-free flexible organic solar cells with printed current collecting grids," *Sol. Energy Mater. Sol. Cells*, vol. 95, no. 5, pp. 1339–1343, May 2011.
- 158) S. Wang, X. Zhang, and W. Zhao, "Flexible, Transparent, and Conductive Film Based on Random Networks of Ag Nanowires," *J. Nanomater.*, vol. 2013, pp. 1–6, 2013.
- 159) M. Nieto-Vesperinas, "Scattering and Diffraction in Physical Optics," World Scientific Publishing Co., 2006.
- 160) D. M. Callahan, J. N. Munday, and H. a Atwater, "Solar Cell light trapping beyond the ray optic limit.," *Nano Lett.*, vol. 12, no. 1, pp. 214–8, Jan. 2012.
- 161) C. K. Carniglia, "Scalar Scattering Theory for Multilayer Optical Coatings", *Opt. Eng.*, vol.18, no. 2, p. 182104, 1979.
- 162) H. A. Macleod, "Thin-film optical filters." Adam Hilger Ltd, Bristol, 2 ed., 1986.

- 163) S. De, T. M. Higgins, P. E. Lyons, E. M. Doherty, P. N. Nirmalraj, W. J. Blau, J. J. Boland, and J. N. Coleman, "Silver Nanowire Networks as Flexible," vol. 3, no. 7, pp. 1767–1774, 2009.
- 164) P. H. Lau, K. Takei, C. Wang, Y. Ju, J. Kim, Z. Yu, T. Takahashi, G. Cho, and A. Javey, "Fully printed, high performance carbon nanotube thin-film transistors on flexible substrates.," *Nano Lett.*, vol. 13, no. 8, pp. 3864–9, Aug. 2013.
- 165) V.K. Sangwan, A. Behnam, V.W. Ballarotto, M.S. Fuhrer, Ant Ural, E.D. Williams, "Optimizing transistor performance of percolating carbon nanotube networks." *Appl. Phys. Lett.* vol.97, p. 043111, 2010.
- 166) C. Preston, Y. Xu, X. Han, J. N. Munday, and L. Hu, "Optical haze of transparent and conductive silver nanowire films," *Nano Res.*, vol. 6, no. 7, pp. 461–468, May 2013.
- 167) C. Preston, Z. Fang, J. Murray, H. Zhu, J. Dai, J. N. Munday, and L. Hu, "Silver nanowire transparent conducting paper-based electrode with high optical haze," *J. Mater. Chem. C*, vol. 2, no. 7, p. 1248, 2014.
- 168) J. B. Li, V. Chawla, and B. M. Clemens, "Investigating the role of grain boundaries in CZTS and CZTSSe thin film solar cells with scanning probe microscopy.," *Adv. Mater.*, vol. 24, no. 6, pp. 720–3, Feb. 2012.
- 169) H. Wang, "Progress in Thin Film Solar Cells Based on  $\text{Cu}_2\text{ZnSnS}_4$ ," *Int. J. Photoenergy*, vol. 2011, no. Figure 2, pp. 1–10, 2011.
- 170) H. Katagiri, K. Jimbo, W. S. Maw, K. Oishi, M. Yamazaki, H. Araki, and A. Takeuchi, "Development of CZTS-based thin film solar cells," *Thin Solid Films*, vol. 517, no. 7, pp. 2455–2460, Feb. 2009.
- 171) D. B. Mitzi, O. Gunawan, T. K. Todorov, K. Wang, and S. Guha, "The path towards a high-performance solution-processed kesterite solar cell," *Sol. Energy Mater. Sol. Cells*, vol. 95, no. 6, pp. 1421–1436, Jun. 2011.
- 172) T. K. Todorov, K. B. Reuter, and D. B. Mitzi, "High-efficiency solar cell with Earth-abundant liquid-processed absorber.," *Adv. Mater.*, vol. 22, no. 20, pp. E156–9, May 2010.

- 173) S. Bag, O. Gunawan, T. Gokmen, Y. Zhu, T. K. Todorov, and D. B. Mitzi, "Low band gap liquid-processed CZTSe solar cell with 10.1% efficiency," *Energy Environ. Sci.*, vol. 5, no. 5, p. 7060, 2012.
- 174) Y. Cao, M. S. Denny, J. V Caspar, W. E. Farneth, Q. Guo, A. S. Ionkin, L. K. Johnson, M. Lu, I. Malajovich, D. Radu, H. D. Rosenfeld, K. R. Choudhury, and W. Wu, "High-Efficiency Solution-Processed Cu<sub>2</sub>ZnSn(S,Se)<sub>4</sub> Thin-Film Solar Cells Prepared from Binary and Ternary Nanoparticles.," *J. Am. Chem. Soc.*, vol. 134, no. 38, pp. 15644–7, Sep. 2012.
- 175) A. Singh, H. Geaney, F. Laffir, and K. M. Ryan, "Colloidal Synthesis of Wurtzite Cu<sub>2</sub>ZnSnS<sub>4</sub> Nanorods and Their Perpendicular Assembly Colloidal Synthesis of Wurtzite Cu<sub>2</sub>ZnSnS<sub>4</sub> Nanorods and Their Perpendicular Assembly," *Sol. Energy*, 2012.
- 176) C. Li, E. Ha, W.-L. Wong, C. Li, K.-P. Ho, and K.-Y. Wong, "A facile arrested precipitation method for synthesis of pure wurtzite Cu<sub>2</sub>ZnSnS<sub>4</sub> nanocrystals using thiourea as a sulfur source," *Mater. Res. Bull.*, vol. 47, no. 11, pp. 3201–3205, Nov. 2012.
- 177) X. Lu, Z. Zhuang, Q. Peng, and Y. Li, "Wurtzite Cu<sub>2</sub>ZnSnS<sub>4</sub> nanocrystals: a novel quaternary semiconductor.," *Chem. Commun. (Camb)*, vol. 47, no. 11, pp. 3141–3, Mar. 2011.
- 178) M. D. Regulacio, C. Ye, S. H. Lim, M. Bosman, E. Ye, S. Chen, Q.-H. Xu, and M.-Y. Han, "Colloidal nanocrystals of wurtzite-type Cu<sub>2</sub>ZnSnS<sub>4</sub>: facile noninjection synthesis and formation mechanism.," *Chemistry*, vol. 18, no. 11, pp. 3127–31, Mar. 2012.
- 179) A. Singh, C. Coughlan, F. Laffir, and K. M. Ryan, "Assembly of CuIn(1-x)Ga(x)S<sub>2</sub> nanorods into highly ordered 2D and 3D superstructures.," *ACS Nano*, vol. 6, no. 8, pp. 6977–83, Aug. 2012.
- 180) P. Absorber, C. Znsnse, J. Li, D. B. Mitzi, and V. B. Shenoy, "Structure and Electronic Properties of Grain Boundaries in Earth-Abundant," no. 11, pp. 8613–8619, 2011.

- 181) J. B. Li, V. Chawla, and B. M. Clemens, "Investigating the role of grain boundaries in CZTS and CZTSSe thin film solar cells with scanning probe microscopy," *Adv. Mater.*, vol. 24, no. 6, pp. 720–3, Feb. 2012.
- 182) Q. Guo, G. M. Ford, W.-C. Yang, B. C. Walker, E. a Stach, H. W. Hillhouse, and R. Agrawal, "Fabrication of 7.2% Efficient CZTSSe Solar Cells Using CZTS Nanocrystals," *J. Am. Chem. Soc.*, pp. 7–9, Nov. 2010.
- 183) Y. B. Kishore Kumar, G. Suresh Babu, P. Uday Bhaskar, and V. Sundara Raja, "Preparation and characterization of spray-deposited  $\text{Cu}_2\text{ZnSnS}_4$  thin films," *Sol. Energy Mater. Sol. Cells*, vol. 93, no. 8, pp. 1230–1237, Aug. 2009.
- 184) H. Wei, W. Guo, Y. Sun, Z. Yang, and Y. Zhang, "Hot-injection synthesis and characterization of quaternary  $\text{Cu}_2\text{ZnSnSe}_4$  nanocrystals," *Mater. Lett.*, vol. 64, no. 13, pp. 1424–1426, Jul. 2010.
- 185) I.V. Pankove, *Optical Processes in Semiconductors*, Dover Inc., New York, 1975, pp. 34–95.
- 186) H. Yoo and J. Kim, "Growth of  $\text{Cu}_2\text{ZnSnS}_4$  thin films using sulfurization of stacked metallic films," *Thin Solid Films*, vol. 518, no. 22, pp. 6567–6572, Sep. 2010.
- 187) G. S. Babu, Y. B. K. Kumar, P. U. Bhaskar, and V. S. Raja, "Effect of post-deposition annealing on the growth of  $\text{Cu}_2\text{ZnSnSe}_4$  thin films for a solar cell absorber layer," *Semicond. Sci. Technol.*, vol. 23, no. 8, p. 085023, Aug. 2008.
- 188) H. Yoo, J. Kim, and L. Zhang, "Sulfurization temperature effects on the growth of  $\text{Cu}_2\text{ZnSnS}_4$  thin film," *Curr. Appl. Phys.*, vol. 12, no. 4, pp. 1052–1057, Jul. 2012.

